Energy Release Processes in Solar Flares

A THESIS

submitted for the Award of Ph.D. degree of

MOHANLAL SUKHADIA UNIVERSITY

in the

Faculty of Science

BY

Arun Kumar Awasthi

Under the Supervision of

Prof. Rajmal Jain

Physical Research Laboratory, Ahmedabad

Department of Physics

MOHANLAL SUKHADIA UNIVERSITY

UDAIPUR

Year of submission: 2013

DECLARATION

I, **Mr. Arun Kumar Awasthi**, S/o Mr. Onkar Nath Awasthi, resident of Room No. 105, PRL Students' hostel, Thaltej Campus, Thaltej, Ahmedabad-380 059, hereby declare that the research work incorporated in the present thesis entitled, **"Energy Release Processes in Solar Flares"** is my own work and is original. This work (in part or in full) has not been submitted to any University for the award of a Degree or a Diploma. I have properly acknowledged the material collected from secondary sources wherever required. I solely own the responsibility for the originality of the entire content.

Date: December 06, 2013

Arun Kumar Awasthi
(Author)

CERTIFICATE

I feel great pleasure in certifying that the thesis entitled, **"Energy Release Processes in Solar Flares"** embodies a record of the results of investigations carried out by Mr. Arun Kumar Awasthi under my supervision. He has completed the following requirements as per Ph.D regulations of the University.

(a) Course work as per the university rules.

(b) Residential requirements of the university.

(c) Regularly submitted six monthly progress reports.

(d) Presented his work in the departmental committee.

(e) Published minimum of one research papers in a referred research journal.

I recommend the submission of thesis.

Date: December 06, 2013

Prof. Rajmal Jain
Professor
Physical Research Laboratory,
Ahmedabad - 380 009.

Countersigned by

Head of the Department

Dedicated to

My Family & Friends

Contents

List of Tables

List of Figures

Acknowledgements

Since the very outset to the accomplishment of my research during PhD, I pay my sincere and deepest gratitude to Prof. Rajmal Jain, my supervisor who has introduced me to the marvelous world of solar physics. His vast experience and knowledge has helped me immensely in learning the subject. He always gave importance to my understandings towards various aspects of subject which gained precision while fruitful discussions with him. I consider myself fortunate to have him as my supervisor.

I thank Prof. J. N. Goswami, Director; Prof. Anjan Joshipura and Prof. A. K. Singhvi, former Deans, and Prof. Utpal Sarkar, Dean of PRL and Prof. T. Chandrasekhar and Prof. P. Janardhan, former and current A&A division chairmen, for providing necessary facilities to carry out research work.

Being a part of an international collaborative project during my PhD, I have seen various crucial dimensions of research. For this I wish to convey my sincere gratitude to Prof. W. Uddin, PI of the project and Acting Director, ARIES, Nainital and Prof. P. K. Manoharan, Head, RAC-TIFR, Ooty. It will be injustice if I do not convey my sincere thanks to Dr. N. V. Nitta, Prof. M. Aschwanden, Prof. N. Gopalswamy, Dr. A. K. Srivastava and Dr. R. Chandra for fruitful suggestions during the project.

I have also imparted significant time of my PhD tenure in the development of a 10 cm aperture optical telescope in Thaltej Campus, PRL. Although I learnt a lot during the development and post-installation exercise of this task, It would have never been a successful without continuous monitoring of the development and effective advices from Prof. Rajmal Jain, my supervisor and my collaborators Prof. Y. Hanaoka, NAOJ, Japan and Prof. Y. Deng, NAOC, China. Moreover, I wish to acknowledge timely support received during installation of telescope from PRL members namely Arvind Rajpurohit, Sharad C. Tripathi, Jayesh Khunt, Raj Laxmi Singh, Pooja D. Gadhiya, Kyaw Min Tint, Arvind Rao, Khushbu Ajmera, V. D. Patel, Vishnu Patel, G. P. Ubale and H. Kaila.

Till masters, we have never undergone through formal courses of Astrophysics which is the foundation of research. This essential need is fulfilled via very effective course work formulation and executing faculties from PRL. In this regard, I sincerely acknowledge the efforts of Prof. R. Ramesh, Dr. R. Rengarajan, Dr. S. Mohanti and Dr. B. Bapat.

I thank academic committee, PRL for critically reviewing my development in research time-to-time and giving me a supportive platform. In addition, I want to pay my special gratitude to Prof. N. M. Ashok, Prof. P. Janardhan and Dr. Bhuwan Joshi who critical reviewed the work conducted by me during thesis whenever needed. Moreover, I specially thank Dr. Sachindra Naik for his farsighted suggestions and critics which always advanced my research.

In this petabyte era of observational capabilities, data handling has been a very crucial but tedious task. In this regard, I thank all the staffs of PRL computer center for providing excellent computational and internet facilities. Especially, I must acknowledge the help received from Jigar Raval, Hitendra, Alok and Tejas, members of computer center and Shashi Prabhakar, student, PRL. In addition, I express my appreciation for the co-operation and help extended ever-willingly by the library and its staff members in general and Ms. Nistha and Pragya in particular.

Administrative matters have been such a relief because of the dedicated support from Mr. Senthil, Mr. Pradeep, Mr. Bharat M. Joshi, K. J. Shah, V. D. Patel, Murli Ji and Bhagirath. I sincerely thank PRL Admin for helping me in associated tasks.

Good company played a very important role in the life. Firstly, I am thankful to Amrendra, Susanta, Vivek, Sid, Sunil, Koushik, Chinmay, Reddy, Abhishek and Yogita, my batch mates, for helping me in keeping pace with research and daily life developments. Specially, mere acknowledgement seems insufficient for the time-to-time company of Amrendra and Raj Laxmi which made my life very systematic and happening. I express my sincere acknowledgments to Medha for showing me the way to the God of music, my tabla teacher. In addition, I thank Sharad and Raj Laxmi for accompanying me and pushing me whenever I seemed to lose my interest in music.

I enjoyed the company of Ram Krishna Da, Blesson, Ashish, Tapas, Vishal, Sunil, Susanta, Tapas, Priyanka, Anjali, Tanmoy C., and Gaurav for the fruitful discussion and suggestions. I enjoyed the company of Ashish, Arvind, Pankaj Sharma, Tanmoy C. and many more during the vollyball and badminton time in thaltej, PRL.

This thesis is incomplete if I do not acknowledge Google, ARXIV, SAO/ADS abstract service as well as open access data policy of several space and ground-based solar observatories. It always made my life easier like a true friend.

Finally last but not the least, I express my whole hearted gratitude to the support in the form of love and affection I got from my parents, my brother, sister, cousins and my family members. This is something beyond acknowledgements. They were always with me and the encouragement I received from them will never fade away.

Arun Kumar Awasthi

ABSTRACT

The study of multi-wavelength emission during solar flares has enormous potential towards understanding the underlying physical phenomena occurring in the solar atmosphere. Our Sun presents nearest laboratory to us where various plasma processes in the extremely severe magnetic environment occur. These processes need complete understanding with the help of continuous monitoring in view of their proximal hazards. Therefore, in general, the focus of this thesis is to understand the open issues in the energy release processes during solar flare using high temporal, spatial and spectral observations from various space and ground-based observatories.

Time evolution of emission from solar flare is categorized in three phases *viz:* precursor, impulsive and gradual. The impulsive and gradual phase of energy release in solar flares are studied in greater detail while the underlying processes causing the precursor phase is not yet explored owing to the lack of high spectral and temporal cadence observations. In order to explore the responsible underlying processes during the precursors and their role in producing impulsive phase, quantitative study is carried out employing multi-wavelength emission from fifty flares occurred during year 2003-2012. We do not find loop-top or foot-point hard X-ray (HXR) signatures during the precursor phase. Moreover, our investigation revealed thermal origin of the emitting plasma. A few of the well observed flares revealed the presence of coronal soft X-ray (SXR) sources during the precursor emission which suggests thermal conduction to be a possible mechanism of energy release. In addition, we find that main phase of all the flares can be fully explained by the CSHKP model. Based on this study, we propose a unified scheme for energy release during the precursor and main phases of emission.

The solar flare plasma is traditionally treated to be of isothermal nature. However, this assumption does not seem to be physically acceptable due to involvement of multiple-loop scenario having multiple temperatures as revealed

from the observations. In this regard, we study high cadence temporal and spectral mode observations of ten M-class flares observed by SOXS to study the isothermal or multi-thermal nature of the plasma. Firstly, we modeled the spectral evolution of the X-ray line and continuum flux during flares by integrating a series of isothermal plasma flux. The differential emission measure (DEM) power-law index of the integrated modeled flux, when compared with that obtained from fitting the observed X-ray spectra revealed flare plasma to be of multi-thermal nature. Moreover, energy-dependent timing delays of temporal evolution of X-ray emission have been studied. This study led to the estimation of thermal to non-thermal photon crossover energy (break energy). Further, as the solar flare plasma cools simultaneously with the heating, we study the effect of cooling on Neupert effect, a causal relationship between SXR and HXR. This enabled us to propose a generalized Neupert relationship involving time-dependent exponentially cooling as previously suggested by Aschwanden (2005).

It has been widely accepted that the surplus energy released at the time of the flare and Coronal Mass Ejection (CME) in an active region is derived from the gradually stored energy from surrounding non-potential magnetic fields. However, the observations do not show any drastic change in the magnetic field at the time of the flare in an active region. Rather it has been revealed that stresses in the coronal magnetic fields may build up in response to the changes taking place at the photospheric level, such as sunspot rotation, flux emergence, submergence and cancellation. In this regard, we carried investigation of multi-wavelengths emission during a flare-CME system occurred on May 12, 1997. We quantify the temporal evolution of magnetic field parameters namely magnetic flux, gradient and sunspot rotation which revealed that free energy was being stored up into the corona several hours prior to the onset of flare. The slow low-layer magnetic reconnection was proposed to be responsible for the storage of magnetic free energy in the corona and the formation of a sigmoidal core field or a flux rope leading to the eventual eruption. Further, magnetic-field gradient and sunspot rotation have shown continual increase till the flare event and then later decreased. Based on the observations and analysis we propose a qualitative model suggesting the mass ejections, filament eruption, CME and subsequent flare to be connected with one another in the framework of a solar eruption.

Akabane (1956) found the statistical behavior of power-law distribution of flare frequency versus respective energy released was found to be scale-invariant (see also, Dennis, 1985) etc. Jain and Bhatnagar (1983) correlated temporal evolutions of photospheric magnetic-field evolution with related X-ray and Hα emission and suggested a "Magnetic Complexity Number" as a cut-off magnetic field for flares of various intensities. As individual solar flare originates from a completely independent magnetic-field configuration from other flare, the aforesaid statistically independent behavior of flares has been posing questions on the understanding. Lu and Hamilton (1991) explained this by proposing solar coronal magnetic field which produces flare happens to be in a state of self-organized criticality (SOC; Bak et al., 1987). As the magnetic-field parameters are found to be a good proxy for build-up and trigger of flare energy release, we explore the SOC occurrence in the corona by employing photospheric magnetic-field and coronal X-ray flux. Firstly, we explored long-duration statistical photosphere-corona coupling through studying the active region independent full-disk magnetic-field parameters and co-temporal disk-integrated coronal X-ray flux. In addition to this, the relationship between flare-associated active region's magnetic flux and coronal X-ray flux has been investigated. We found a strong power-law relationship between the photospheric magnetic flux and coronal X-ray flux in the former case. In the latter case also, power-law relationship between photospheric magnetic flux and coronal X-ray flux is found to hold. In addition, we have also noticed a photospheric magnetic flux over which the flare X-ray flux undergoes avalanche. This magnetic flux is termed as critical magnetic flux.

LIST OF PUBLICATIONS

1. Publications related to the thesis work

A. Referred Journal

1. **Awasthi, A. K.**; Jain, R., Gadhiya, P. D., Aschwanden, M. J.; Uddin, W.; Srivastava, A. K.; Chandra, R.; Gopalswamy, N.; Nitta, N. V.; Yashiro, S.; Manoharan, P. K.; Choudhary, D. P.; Joshi, N. C.; Dwivedi, V. C.; Mahalakshmi, K., "*Multi-wavelength Dignostics of the Precursor and Main phases in M1.8 flare on 2011 April 22*", `MNRAS`, 2013, In Press, DOI: 10.1093/mnras/stt2032.

2. Bhatt, N. J.; Jain, R.; **Awasthi, A. K.**, "*The energetic relationship among geoeffective solar flares, associated CMEs and SEPs*", `Research in Astronomy and Astrophysics`, 2013, 13, 8, 978-990.

3. Jain, R.; **Awasthi, A. K.**; Chandel, B.; Bharti, L.; Hanaoka, Y.; Kiplinger, A. L.,"*Probing the Role of Magnetic-Field Variations in NOAA AR 8038 in Producing a Solar Flare and CME on 12 May 1997*", `Solar Physics`, 2011, 271, 1-2, 57-74.

4. Jain, R.; **Awasthi, A. K.**; Rajpurohit, A. S.; Aschwanden, M. J., "*Energy-Dependent Timing of Thermal Emission in Solar Flares*", `Solar Physics`, 2011, 270, 1, 137-149.

B. Conference Proceedings

1. **Awasthi, A. K.** & Jain, R., "*Probing the Solar origin of energy build-up and release in Solar Energetic Particles*", `Solar and Astrophysical Dynamos and Magnetic Activity, Proceedings of the International Astronomical Union, IAU Symposium`, 2012, 294, 539-540.

2. **Awasthi, A. K.** & Jain, R., "*Generalization of the Neupert effect over the Solar Flare Plasma Cooling*", `Solar and Astrophysical Dynamos and Magnetic Activity, Proceedings of the International Astronomical Union, IAU Symposium`, 2012, 294, 541-542.

3. Jain, R.; **Awasthi, A. K.**, "*Energy-dependent nature of thermal emission in solar flares*", `BASI, Conference Series`, 2011, 3, 101.

4. **Awasthi, A. K.**; Jain, R., "*Multi-wavelength Dignostics of Precursor phase emission in Solar Flares*", `BASI, Conference Series`, 2011, 3, 297-305.

5. Jain, R.; Rajpurohit, A. S.; Aggarwal, M.; Jamwal, R.; **Awasthi, A. K.**, "*Time-Varying Thermal Emission in Solar Flares*", `Astrophysics and Space Science Proceedings`, 2010, 465-470

2. Other Publications

1. Choudhary, P.; Jain, R.; **Awasthi, A. K.**, "*Periodicities in the X-ray Emission from the Solar Corona*", `Astrophysical Journal`, 2013, 778, 28.

2. Choudhary, D. P.; Gosain, S.; Gopalswamy, N.; Manoharan, P. K.; Chandra, R.; Uddin, W.; Srivastava, A. K.; Yashiro, S.; Joshi, N. C.; Kayshap, P.; Dwivedi, V. C.; Mahalakshmi, K.; Elamathi, E.; Norris, M.; **Awasthi, A. K.**; Jain, R. , "*Flux emergence, flux imbalance, magnetic free energy and solar flares*", `Advances in Space Research`, 2013, 52, 8, 1561-1566.

3. Joshi, N. C.; Uddin, W.; Srivastava, A. K.; Chandra, R.; Gopalswamy, N.; Manoharan, P. K.; Aschwanden, M. J.; Choudhary, D. P.; Jain, R.; Nitta, N. V.; Xie, H.; Yashiro, S.; Akiyama, S.; Makela, P.; Kayshap, P.; **Awasthi, A. K.**; Dwivedi, V. C.; Mahalakshmi, K., "*A multiwavelength*

study of eruptive events on January 23, 2012 associated with a major solar energetic particle event", Advances in Space Research, 2013, 52, 1, 1-14.

4. Gopalswamy, N.; Xie, H.; Makela, P.; Yashiro, S.; Akiyama, S.; Uddin, W.; Srivastava, A. K.; Joshi, N. C.; Chandra, R.; Manoharan, P. K.; Mahalakshmi, K.; Dwivedi, V. C.; Jain, R.; **Awasthi, A. K.**; Nitta, N. V.; Aschwanden, M. J.; Choudhary, D. P., "*Height of shock formation in the solar corona inferred from observations of type II radio bursts and coronal mass ejections*", Advances in Space Research, 2013, 51, 11, 1981-1989.

5. Jain, R.; **Awasthi, A. K.**; Tripathi, S.C.; Bhatt, N. J.; Khan, P.A., "*Influence of solar flare X-rays on the habitability on the Mars*", ICARUS, 2012, 220, 2, 889-895.

Chapter 1

Introduction

1.1 The Sun

"It is impossible for any sensitive person to look at a star-filled sky without being stirred by thoughts of creation and eternity. The mystery of the origin and destiny of the universe haunts us throughout our lives" said by Herbert Friedman in `The Amazing Universe`. Therefore, the study of evolution of universe and the solar system, in which we live though vast, possess a wonderful legacy of information. The scientific progress in the field of astronomy has revolutionized long back since year 1926 when the structure of stars has been put forth by Sir Arthur Eddington. It attracted the attention of world because it revealed the fate of stars. Similarly, studying the nearest star, our Sun, has been "icing on the cake" as a wealth of information is available in the form of observations which assist the proposed theories. We live in the era where technology is assisting at its best to unravel behavior of the Nature.

About 4.6 billion years ago, in a distant spiral arm of our Milky Way galaxy, a small cloud of gas and dust began to compress under attractive gravitational collapse. Particles within the clouds center (core) became so densely packed that they fused following collisions. This process released enormous heat and light which exerted in the form of a force opposing to the gravitational compression and eventually reached in equilibrium. This is the process by which the closest to the earth and most interesting star, the Sun, is formed. Based on the luminosity and size, the Sun is categorized as main sequence G2V type star in the Hertzsprung-Russell (H-R) diagram. Since last 4.5 billion years, the Sun has been providing us with its radiant energy and it is expected to continue to do so for another next 3 to 4 billion years. Sun is a source of light and heat which, in turn, provides life on Earth. Thus, being the most valuable star for mankind, every detail of the Sun is worthy of observations and study. The Sun happens to readily available virtual laboratory where various plasma processes are continuously going on in the extremely severe conditions which is very hard to reproduce in any ground/space based observatory. The study of these processes also opens a window of information for the stars away from us and therefore hard to observe with such a fine detail. The study of the Sun, based on the information of various processes, is subdivided in the two topics viz. internal structure of the Sun and solar atmosphere as discussed in following sections.

1.1.1 The Solar Interior

The study of interior of the Sun is subdivided in four regions, namely, the core, the radiative zone, the interface layer (Tachocline), and the convection zone, based on the energy generation/transfer processes occurring there. Figure 1.1 shows the well-studied structure of the solar interior and the atmosphere.

1.1.1.1 The Core

The Sun's core is extended from the center of the Sun to $\sim$ 0.25 $R_\odot$. The temperature at the core is $\sim$ 15 MK, density $\sim$150,000 kg m^{-3}, and a pressure of $\sim$ 233 billion bar. The core is the place where the source of the energy generation via nuclear reactions in the form of p-p and higher order chain reactions take place and enormous amount of energy is released. In the process of p-p chain reaction, 6 hydrogen nuclei, one at a time, undergo nuclear fusion to form one helium and two hydrogen nuclei. In this process, $\sim 0.7\%$ mass-loss occurs which is completely converted into 19.78 MeV of energy which diffuses outward by radiation (mostly γ-rays and X-rays) and makes the Sun shine.

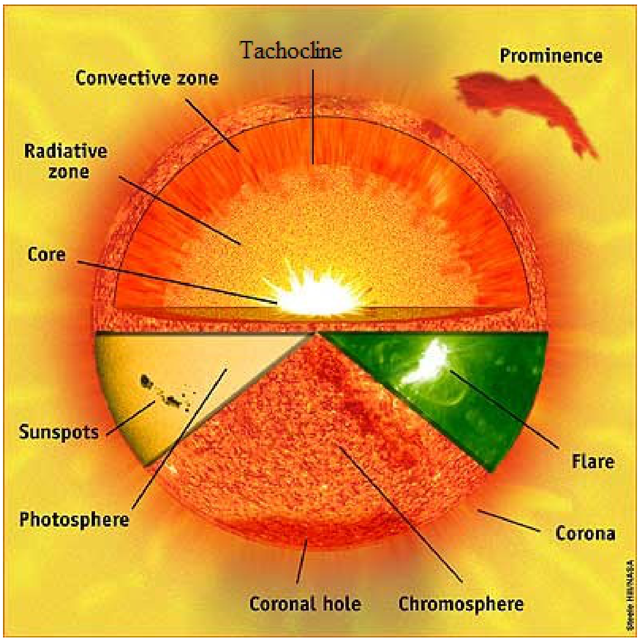

Figure 1.1: Overview of solar structure and associated processes. The three major structural areas, i.e. the core, radiative zone and the convective zone are shown in the upper hemisphere while the lower hemisphere shows the three atmospheres, i.e. photosphere, chromosphere and the corona. (Image courtesy: Solar and Heliospheric Observatory)

1.1.1.2 The Radiative zone

The energy generated in the core of the Sun can transfer to the surface of the Sun through the processes viz. conduction, convection or radiation. Energy transfer in solids is through conduction and is irrelevant for stars. Thus, the radiative zone is the region in the interior of the Sun where the dominating process of energy transfer is radiation. It extends outward from ~ 0.25 to 0.7 solar radii, from the outer edge of the core to the interface layer or the tachocline at the base of the convection zone. The high energy gamma rays generated in the core are carried by light (photons) that bounces from particle to particle through the radiative zone. These photons, though transferred with the speed of light, make countless collisions on their way with electrons and atomic nuclei. This process gradually increases the photon flux in lower energies, from gamma rays to the X-rays and then to visible as they diffuse outwards.

1.1.1.3 The Interface Layer (Tachocline)

While the photosphere is the optical (visible) surface of the sun, the solar interior cannot be observed directly. It is possible to understand the solar interior in a better way by a systematic study of Global oscillations from the solar interior popularly known as Helioseismology. Helioseismic investigations are useful to study the internal rotation of the Sun. A distinct "bump" in the sound speed (corresponding to temperature also) profile at the base of the convection zone between 0.6 and 0.7 solar radii has been discovered from Helioseismic study of oscillations data observed by MDI instrument onboard SOHO spacecraft. This bump is corresponding to increase in temperature and density, a shear region near 0.67 solar radius develops, which is known as 'tachocline'. This region has become interesting in recent years as it has important consequences related to the dynamo theory for generation of magnetic fields in the Sun. The changes in fluid flow velocities across the layer can stretch the magnetic field lines of force and make them stronger. This change in flow velocity gives this layer an alternative name-the Tachocline. There also appears to be sudden changes in chemical composition across this layer. Employing the GONG and MDI data, (Basu and Antia, 2003) observed that in a tachocline layer, the rotation rate increases with radial distance at low latitudes, while at high latitudes the rotation rate decreases with radial distance. They further suggested the possibility of the tachocline comprising of two parts, one at low latitudes and the other at high latitudes, which are located at different depths and have different widths, but there may be no variation in position and width within each of these regions.

1.1.1.4 The Convection zone

The convection zone is the outermost layer of the solar interior and energy transferred in this zone is through convection. It extends up to the visible surface of the Sun. Temperature reaches up to ~ 2 MK at the base of the convection zone. Thus, this is suitable layer for the heavier ions (such as carbon, nitrogen, oxygen, calcium, and iron) to hold onto some of their electrons. This ionized state of matter thus becomes completely opaque and the energy gets trapped in this layer. The material in the convection zone starts to bubble in response to this input 'dumping' of energy. The whole system becomes locally unstable, leading to turbulent convection as the opaque gas, which is blocking the radiation, is forced to rise upwards through the Sun to cooler layers. This is convection and happens to be a highly efficient way of energy transfer in this zone.

1.1.2 The Solar Atmosphere

The solar atmosphere is defined as that part of the Sun extending outwards from the surface of the Sun, from where energy generated at the Sun's core begins to escape into space in the form of radiation. Based on the plasma properties viz. plasma β parameter $[nkT/(B^2/8\pi)]$, density, temperature, pressure etc., the atmosphere of the Sun is subdivided into three regions namely Photosphere, Chromosphere and Corona. Further, there exists a region sandwiched between chromosphere and corona, termed as transition region. I present a brief detail of various observable and physical phenomena taking place at different layers of the atmosphere as following:

1.1.2.1 The Photosphere

The photosphere can be regarded as the Sun's surface. More precisely it is a thin layer. The definition of the base of the photosphere (and therefore thickness) depends on the wavelength of the radiation. In general, it is defined as the depth where the optical depth τ, i.e. the integral of the absorption coefficient over path length, is unity for radiation of wavelength 5000 Å (Phillips et al., 2008). The effective temperature of the photosphere is $\sim$ 5800 K ranging from a temperature of about 6400 K at its base to about 4400 K at the top of the photosphere. The coolest layer of the Sun is known as temperature minimum region (TMR), situated at $\sim$ 500 km above the photosphere, having a temperature of $\sim$ 4100 K. Solar photosphere is an interesting area of research due to the fact that a number of features can be observed in the photosphere with a simple telescope. These features include the dark sunspots, the bright faculae, and granules etc.

1.1.2.1.1 Sunspots : Sunspots are associated with strong magnetic fields emerging through the solar surface with magnetic field strengths of the order of 2000 to 4000 Gauss and appear as dark spots on the surface. Temperatures in the dark centers of sunspots drop to about 3700 K (compared to about 5700 K for the surrounding photosphere). Sunspots vary in size and shape, lasting from a few hours to several weeks and months. Sunspots usually come in groups with two sets of spots. One set will have positive or north magnetic field polarity while the other set will have negative or south magnetic field polarity. Mostly each sunspot has two regions: Umbra and penumbra. Umbra is the darker central part of the sunspot where the magnetic field is strongest. Penumbra is lighter part and filamentary around the edges where the magnetic field is weaker and more horizontal. Figure 1.2 shows full-disk as well as high-resolution observation of sunspots on the photosphere observed on June 5, 2012 from Thaltej Solar Flare Telescope (TSFT) and Helioseismic magnetic imager (HMI) onboard Solar Dynamic Observatory (SDO) respectively.

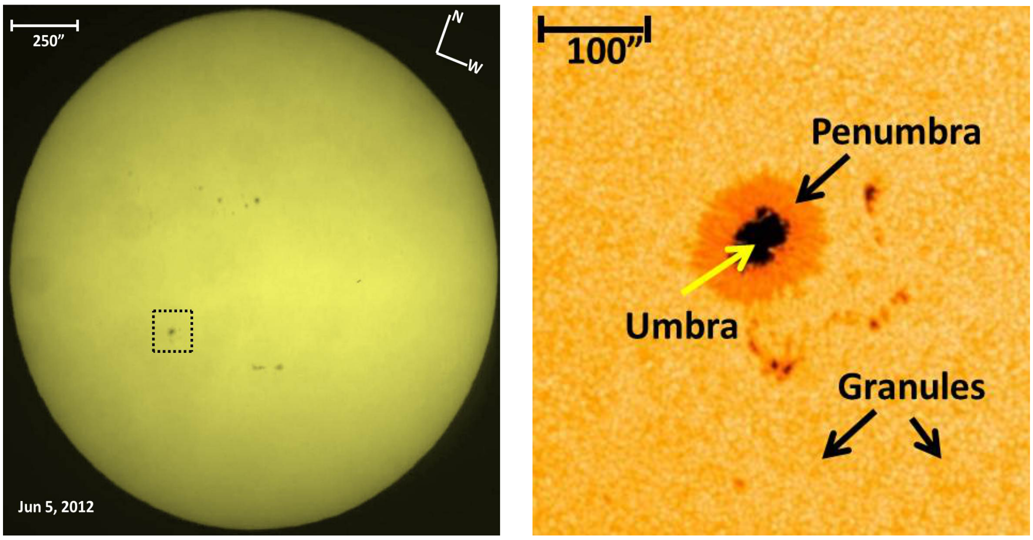

Figure 1.2: Left Panel- Photosphere of the Sun observed from Thaltej Solar Flare telescope (hereafter TSFT) on June 5, 2012. The high resolution view of the sunspot of the same day taken by Helioseismic magnetic imager (HMI) onboard Solar Dynamic Observatory (SDO) mission is shown in the right panel.

Moreover, there are other interesting features observed on photosphere. Faculae are other bright features seen in regions surrounding the sunspots. With respect to sunspots, the magnetic field is less concentrated in facular regions. Further granules which are spread all over the photosphere, manifest the evidence of the bubbling motion of hot gases. Granules are created by the hot bubbles of gas rising from the interior and reaching the solar surface as shown in Figure 1.2. These cellular features are the top of convection cells and cover the entire Sun except the areas covered by sunspots.

1.1.2.1.2 Active Regions : Active regions span over a small fraction of the total solar surface area harboring most of the solar activity. They are located in areas of strong magnetic field concentrations and are visible as sunspot groups in optical wavelengths or magnetograms. Active regions are mainly composed of closed magnetic field lines owing to the bipolar nature of sunspot groups. Dynamic processes such as plasma heating, flares and coronal mass ejections (CMEs) occur in the active regions due to the permanent magnetic activity. Plasma heating in the chromosphere gives rise to upflows into coronal loops. Thus active regions appear as many filled loops. These loops are comparatively hotter and denser than the surrounding coronal plasma. They produce soft X-ray and EUV emission.

1.1.2.2 The Chromosphere

Discovered during a solar eclipse observation, the chromosphere lies above the photosphere. It is $\sim$ 2500 km thick layer where the temperature rises with altitude from about 4400 K to $\sim$ 20000 K at the top of the layer. The chromosphere is most commonly observed in 6563 Å (Hα) wavelength. Figure 1.3 - left panel shows the full disk solar chromosphere observed in Hα line by TSFT and various observable chromospheric phenomena viz. active regions, filaments, prominences etc. in the high resolution image in the right panel.

The chromosphere can also be observed at other spectral lines, for example, the violet K line of calcium with a wavelength of 3934 Å. The chromospheric features are filaments, spicules, mottles, plage, surges and sprays.

1.1.2.2.1 Filaments/Prominences : A filament is a current system above a magnetic neutral line that builds up in several days. A filament can remain in a quiet state for days or weeks and then erupts prior to or during a flare or CME (Aschwanden, 2005). Filaments were first detected in Hα wavelength on the solar disk. It has also been also traced in He 10830 Å and in other wavelengths. Filaments and prominences are same features but differ in nomenclature due to their location on the solar disk and thus brightness. Filaments are observed on the disk while prominences are observed above the limb of the Sun. Observations from TSFT show these features as in Figure 1.3.

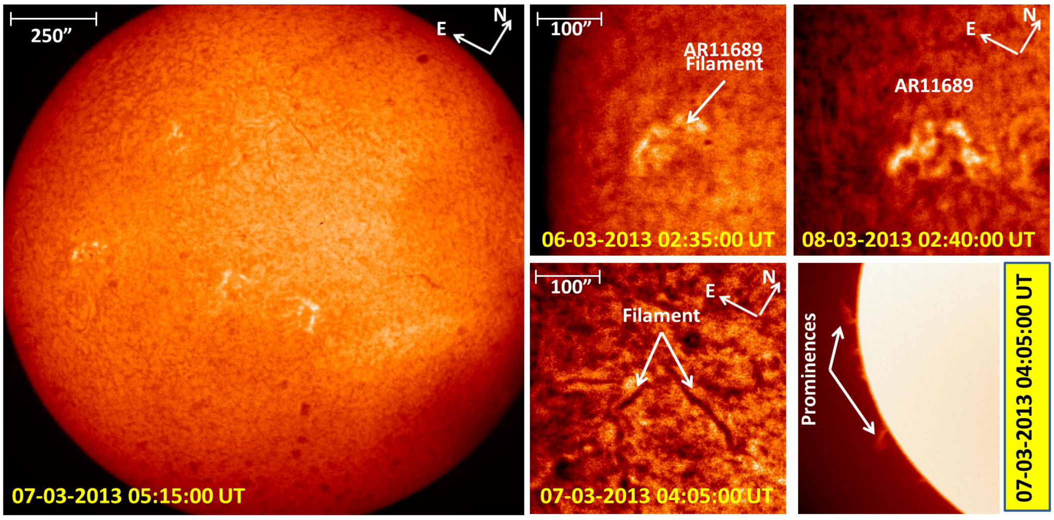

Figure 1.3: left panel shows the full disk image of the solar chromosphere observed in Hα by TSFT and various observable chromospheric phenomena viz. active regions, filaments, prominences etc. in the high resolution image in the right panel

1.1.2.3 The Transition region

The transition region is a thin zone ($\sim$100 km) lying above the chromosphere. It separates the hot corona from the much cooler chromosphere. The cause of occurrence of this zone is the heat flow down from the hot corona into the relatively much cooler chromosphere (Bhatnagar and Livingston, 2005). In the transition region, temperature changes drastically from $\sim$ 20000 K at the top of the chromosphere to $\sim 10^6$ K in the corona. This abrupt shift from the continuous evolution of the plasma parameters of solar atmosphere has been one of the key problems for solar physicist. Wikstol et al. (1997) have proposed a dynamic model for explaining the underlying physical processes occurring in such a thin section having a large temperature gradient. He suggested that this region is affected by the shock waves produced due to innumerable nanoflares occurring at magnetic loop tops in the solar atmosphere.

1.1.2.4 The Corona

The corona is the outermost layer of the solar atmosphere having a kinetic temperature of ∼1 MK. The exact source of this high temperature in the solar corona (coronal heating) is still an open question in astrophysics. Several mechanisms have been proposed namely heating by sound waves which are generated in the convection zone; magneto-seismic waves which would give rise to shock waves; or the Alfven waves travelling along coronal magnetic field (Withbroe and Noyes, 1977; Hollweg, 1985; Heyvaerts and Norman, 2001). Study based on observations from SoHO and HINODE missions suggest that the coronal heating originates from the uninterrupted heated jets driven from chromosphere to corona (De Pontieu et al., 2009). Further, Gupta et al. (2008) proposed micro and nanoflares to be the possible source of coronal heating based on the X-ray and simultaneous Hα observations. According to them the microflares are perhaps the result of the interaction of electrons that accelerated during magnetic reconnection process with ambient plasma in the low lying coronal loops, and they also interact with the chromospheric material while moving down along the loops and thereby produce Hα bright kernels.

The features observed in the corona are active regions, coronal holes, helmet streamers, loop arcades, soft X-ray jets, post flare loops, and cusp shaped loops, multiple arcades, sigmoid structures, flares, coronal mass ejections and solar wind.

1.2 Magnetic Phenomena on the Sun

1.2.1 Magnetic-field

The magnetic field of earth, although significantly small in strengths (≤ 1 Gauss), produces a shield to avoid the stream of charged particles in the form of solar wind and solar energetic particles. Magnetic fields of the strengths of $\sim 10^5$ G are produced in the interior of the Sun and estimated to be several

1000 G in sunspots. The strong magnetic fields are concentrated in sunspots or active regions, while the weaker fields form of magnetic networks are spread over the entire solar disk.

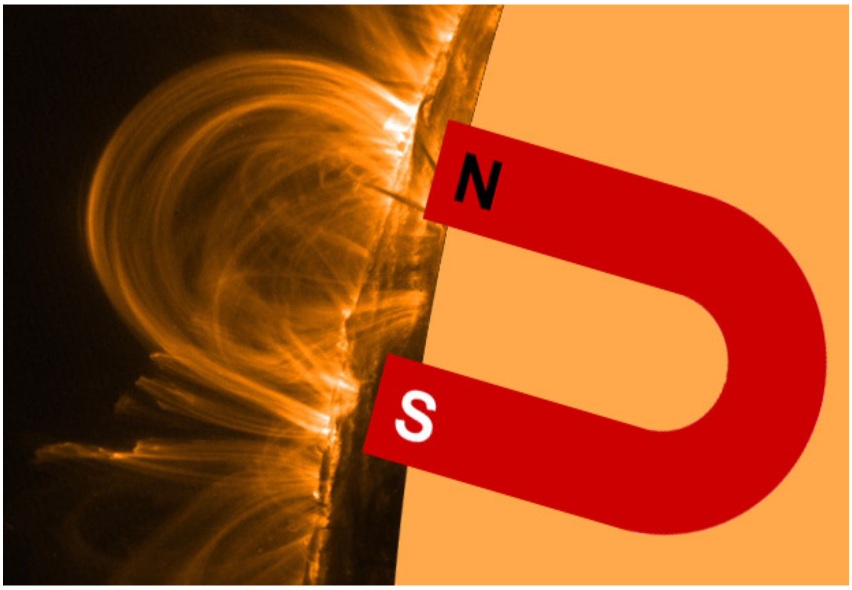

Figure 1.4: Solar magnetic field presented in the form of magnet in the interior of the Sun and by multiple loop system as observed by TRACE mission above the solar surface. (Image courtesy: Randy Russell and TRACE Team)

The origin of eruptive phenomena occurring in the solar atmosphere namely solar flares, CMEs is energized by the stressed (i.e. non-potential) magnetic-fields. For example, a steady prominence is balanced and suspended in the solar atmosphere with the tension force of magnetic fields as shown in the schematic diagram in Figure 1.4. Other than magnetic energy, many other possible sources viz. thermal energy and gravitational energy had been proposed earlier (Tandberg-Hanssen and Emslie, 1988). However, based on the observed atmospheric temperatures, the estimated thermal energy is $\sim 3 \times 10^{28}$ erg which is insufficient to explain all but the smallest of the flare energy. On the other hand, the gravitational energy which is estimated to be equal to the thermal energy (virial theorem for an atmosphere in hydrostatic equilibrium) is not enough to give rise to big flares. Therefore the magnetic energy is the only possible candidate, which can store ample amount of energy enough to produce solar activities.

The morphological and quantitative study of the solar magnetic field is an inevitable step towards exploring the energetic phenomena occurring on the Sun. The magnetic field, in general, is measured through the Zeeman Effect. As the energy level of atoms are splitted into more than one level in the presence of a magnetic field. By measuring their circular and linear polarization, in terms of, Stokes parameters, I, Q, U, V, the strength and direction of the magnetic field can be determined using Stokes inversion (Skumanich and Lites, 1987). Besides Zeeman effect, the Hanle effect is another useful tool to diagnose chromospheric magnetic fields, especially the fields in filaments (Faurobert, 2000).

Further, we know that the probability of flare occurrence in an active region increases with the spot area, the rate of growth of sunspots in the region and the magnetic complexity (Giovanelli, 1939). However, in contrast to dependence of flare occurrence on the spot area, Jain and Bhatnagar (1983) showed quantitatively strong dependence on magnetic complexity index [Mj] which is defined by employing various magnetic classifications.

The magnetic complexity of the sunspot groups is designated progressively by Greek letters α, β, γ and δ with large flares most likely to occur in $\gamma\delta$-spot groups. This classification of the sunspot group is based on the Mount Wilson Sunspot Magnetic Classification[1]. Classification of the magnetic character of sunspots according to rules set forth by the Mount Wilson Observatory in California is as following:

- Alpha (α): A unipolar sunspot group.
- Beta (β): A sunspot group having both positive and negative magnetic polarities (bipolar), with a simple and distinct division between the polarities.
- Gamma (γ): A complex active region in which the positive and negative

[1] `http://www.spaceweather.com/glossary/magneticclasses.html`

polarities are so irregularly distributed as to prevent classification as a bipolar group.

- Beta-Gamma ($\beta\gamma$): A sunspot group that is bipolar but which is sufficiently complex that no single, continuous line can be drawn between spots of opposite polarities.
- Delta (δ): A qualifier to magnetic classes indicating that umbrae separated by less than 2 degrees within one penumbra have opposite polarity.
- Beta-Delta ($\beta\delta$): A sunspot group of general beta magnetic classification but containing one (or more) delta spot(s).
- Beta-Gamma-Delta ($\beta\gamma\delta$): A sunspot group of beta-gamma magnetic classification but containing one (or more) delta spot(s).
- Gamma-Delta ($\gamma\delta$): A sunspot group of gamma magnetic classification but containing one (or more) delta spot(s).

Complexity in the photospheric magnetic-field increases as the active region evolves on the solar disk. It may be either present from the initial emergence or form by the "collision" between separate simpler magnetic bipoles (Zirin and Liggett, 1987).

In the pre-solar activity phase specially prior to flares and/or CMEs, the magnetic-field undergoes through the two crucial steps *viz.* the build-up of energy at coronal site and an initial release in a flare precursor or flare trigger phase. Now, it is widely accepted that solar flares, eruptive prominence, coronal mass ejections (CMEs) and solar energetic particles are three different manifestations of a single energy release process in the solar atmosphere, and that the energy driving the eruption is stored in the coronal magnetic fields prior to the eruption (Jain et al., 2010, 2011a; Bhatt et al., 2013). The magnetic energy available to the energy release processes comes from the kinetic energy of the random motion of the magnetic flux-tubes in the photosphere and the convection zone which builds up the stress in the coronal magnetic field. Observational signatures suggest that as the stress exceeds a critical threshold, the stable equilibrium in the magnetic field turns to unstable leads to eruption. This mechanism is referred to as “storage” model of energy release (e.g. Forbes and Priest, 1995; Priest and Forbes, 2002; Lin and Forbes, 2000; Lin and Rhessi Team, 2003).

Observational evidences of the flare-associated changes in the photosphere include asymmetric evolution of the leading and following polarities in the photospheric line-of-sight (LOS) magnetic field (Cameron, 1999; Wang et al., 2002; Spirock et al., 2002), flux emergence (Wang et al., 2004), rapid changes of the sunspot structure associated with flares (Liu et al., 2005; Deng et al., 2005), decrease in the photospheric magnetic field during solar flares (Uddin et al., 2004; Jain et al., 2011a) etc. The study of magnetic-field observations indicates that the persistent and abrupt changes in the line-of-sight magnetic fields might be a good proxy of the eruption process. On the other hand, investigation of the variations of the non-potentiality in the magnetic field during the eruption have also been carried out (Hagyard, 1984; Ambastha et al., 1993), which indicated that shearing angle of the photospheric field relative to the inversion line can be more effective proxy for large flares.

Therefore, the photospheric parameters though possess strong potential to be the candidates of the probe of solar activity, have not been explored enough in a qualitative as well quantitative sense. The study of temporal evolution of magnetic-field parameters such as gradient, rotation of the sunspots, and magnetic flux may provide a probe in understanding the energy build-up, trigger and release scenario during solar flares. In this context, I study the proxies for flare energy build-up; trigger and release by examining magnetic-field parameters in Chapter 3 and 5 of this thesis.

1.2.2 Magnetic reconnection

The magnetic activities in the solar corona are led due to several reasons. The dynamo process in the interior of the Sun generates magnetic flux constantly. This magnetic flux moves towards the photosphere owing to buoyancy force and emerges in the form of sunspots. Another cause is the differential rotation as well as convective motion of the magnetic flux tubes at the solar surface which continuously twist the coronal field. Further, the magnetic field originated from the interior of the Sun is connected all the way from Sun to the interplanetary space. This connectivity needs to re-structure in due course in order to release excessive magnetic stress which leads to potential (minimum energy) magnetic topology. Thus, magnetic restructuring is inevitable which is termed as magnetic reconnection.

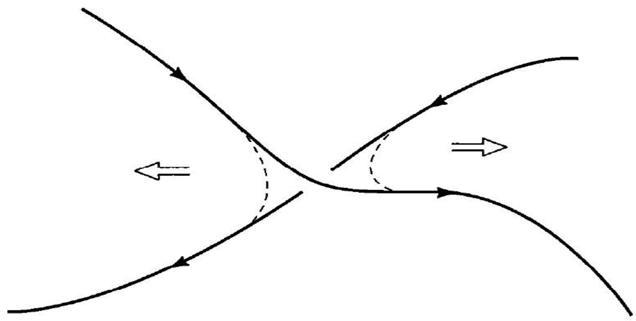

Figure 1.5: Elementary picture of field line reconnection: relaxation of magnetic tension and plasma acceleration by a local change of field-line connectivity. (Picture courtesy: Book "Magnetic reconnection", Author - D. Biskamp)

"The basic picture of the magnetic reconnection is that of two field lines being frozen in and carried along with the fluid, until they come close to each other at some point where, due to weak non-ideal effects in Ohm's law, they are cut and reconnected in a different way" (Biskamp, 2005). Previously, magnetic reconnection was also known as field-line merging(Biskamp, 2005). Figure 1.5 shows the elementary picture of magnetic field-line reconnection and relaxation of magnetic tension and plasma acceleration by a local change of field line connectivity.

Topological changes in the form of magnetic reconnection always release free (non-potential) energy, which is converted into heating and acceleration of the coronal plasma. Magnetic reconnection process is understood by categorizing it among steady 2D, unsteady/bursty and 3D magnetic reconnection scenarios. A steady 2D type magnetic reconnection is understood by the reconnection of magnetic fields which enables the coronal plasma to dissipate magnetic energy, a process that has been proposed to yield direct plasma heating of the corona (Parker, 1963) or to supply direct plasma heating in flares (Sweet, 1958; Sturrock and Coppi, 1966). In this process, when a newly emerging magnetic flux system is moved towards a pre-existing old magnetic flux system, a new boundary is formed where the magnetic field is directed in opposite directions at both sides of the boundary which allows the scenario of magnetic reconnection (see Figure 1.5). The balance between the magnetic and thermal pressure across the neutral boundary layer yields a higher thermal pressure in this layer (B=0 region), than on both sides with finite field strengths (Figure 1.6).

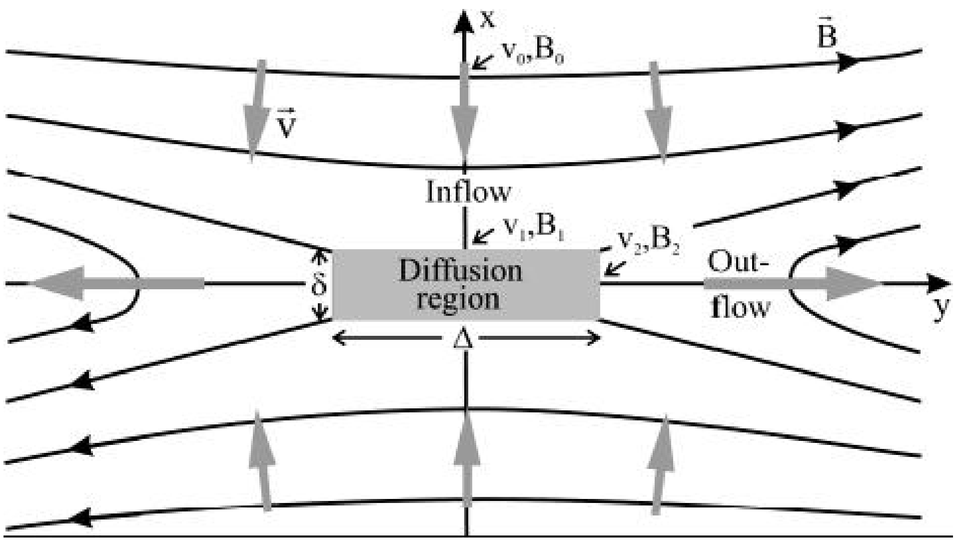

Figure 1.6: 2D steady magnetic reconnection scenario. Two oppositely directed inflows are driven during reconnection which intersect in the diffusion region and create outflows in perpendicular direction. The central zone (grey box) is known as the diffusion region.

The plasma-β parameter is defined as ratio of thermal to magnetic pressure. In the diffusion region, as the magnetic-field approaches to zero value owing to continuity condition, plasma-β in this region becomes > 1 and the plasma can flow across the magnetic field lines. Thereafter, the diffused plasma is guided into the outflow regions along the neutral boundary. Outside the diffusion region, β again drops below unity and the magnetic flux follows frozen-in condition. In the outflow region, highly pointed magnetic field lines experience a large curvature force that tries to minimize the cusps in the outflow region until magnetic tension force is balanced by the magnetic pressure force and thermal pressure. This process is also termed as the sling-shot effect, which explains the conversion mechanism of magnetic into kinetic energy.

1.2.2.1 Sweet-Parker and Petschek Models

The steady-state situation of magnetic reconnection with the analytical solutions was first proposed in Sweet-parker model (Sweet, 1958; Parker, 1958). In this model, it was assumed that the diffusion region is much longer in comparison to its width. With this model, the estimated Sweet-Parker reconnection rate was estimated to be too slow $\sim 10^{-4}$ - 10^{-6} to be able to explain the rate of energy release during a typical flare. In this regard, Petschek (1964) proposed a faster reconnection model which involved reducing the size of the diffusion region to a very compact area. The main aim behind keeping the current sheet much shorter is because of lesser propagation time through the diffusion region and therefore faster reconnection which can explain the flare energy release rate. The Sweet-Parker and Petschek models describe steady-state reconnection, but do not address the circumstances under which it occurs. Furth (1969) showed that a magnetic field can be unstable to small perturbations leading to tearing modes instability.

1.2.3 Particle acceleration

To understand principal mechanism for conversion of magnetic energy into charge particle acceleration is a major area of study. In this, essentially charged particles gain energy when subjected to an electric field in their rest frame. Such an electric field may be a large-scale externally-imposed field, or a v×B field associated with particles crossing magnetic field lines, or a collective effect of Coulomb field and/or a field associated with a plasma wave energy (Fletcher et al., 2011). One of the basic mechanisms is the Dreicer field generation during reconnection (Chen, 1974). The equation of motion for a particle in such a field (in one dimension) is

$$\frac{dv}{dt} = eE/m - f_c v$$

Here m and e are the electron mass and (absolute value of) charge, f_c is the collision frequency, and v is the velocity. Since for Coulomb collisions $f_c \sim v^{-3}$ (Chen, 1974), this model however, is meant for large-scale electric fields generated in the form of Super and/or Sub-Dreicer field.

The acceleration scenario during magnetic reconnection process depends on the magnetic field topology and physical parameters. Further, it is possible, or even likely, that all the acceleration processes discussed above play some role in solar flares and elsewhere in astrophysics which constitutes the central idea of the study energy release processes during precursor phase as presented in Chapter 3.

In the preset section, we have given a brief introduction on magnetic-field generation in the solar interior and its manifestations in the solar atmosphere. Further, magnetic-reconnection which serves as a source of energy build-up and release for solar activities and magnetic-field parameters as a probe to the solar activity has also been presented. In this thesis, magnetic-field evolution turns out to be central part of the study which may lead to a better prediction of activities such as solar flares, CMEs etc.

1.3 Eruptive phenomena in the solar atmosphere

1.3.1 Solar Flares

Solar flares are the most powerful magnetic events in the solar system. In tens of minutes they can release in excess of 10^{32} erg of energy. They emit radiation across the entire electromagnetic spectrum, from radio to γ-rays, and are also causally associated with the acceleration of particles into interplanetary space and with coronal mass ejections. The radiation from solar flares may be continuous emission in some parts of the spectrum, line emission in others, or a combination of both (Svestka, 1976).

The first solar flare recorded in literature was on September 1, 1859 when two scientists, Richard C. Carrington and Richard Hodgson, independently observed an unusually large caterpillar shaped burst in the white light emission. The early idea of the shape, location and intensity of solar flares (Svestka, 1976) was formed from the observations taken at optical wavelength primarily in 6563 Å. Meter-wave radio emissions from flares were recorded in 1942 during military radar operations and revealed the presence of non-thermal electrons in the corona (Hey, 1983). The UV/EUV radiation in the solar atmosphere originates in the chromosphere - corona transition region and in the upper atmosphere. EUV emissions have shown that the flare energy heats the plasma of coronal loops to temperatures from 1.5 MK to beyond 30 MK (Benz, 2008). Thus, solar flares, though of very short time duration, cover almost entire electromagnetic spectrum and leave a large impact on the atmosphere of the sun which consequently affects the earths atmosphere too in the form of coronal mass ejections (CMEs), solar energetic particles (SEPs) events and disturbed storm time (DST) etc. As the solar flare energy release is very impulsive in nature, the energetic particle released from major solar flares can also affect the earth environment drastically.

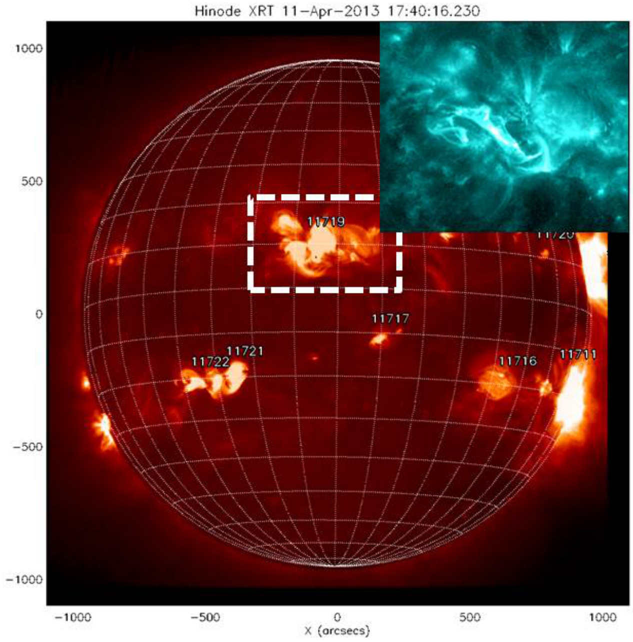

Figure 1.7: This image, from the X-ray Telescope onboard HINODE (Solar-B), shows X-ray flare emission of the solar corona on April 11, 2013. The effective wavelength is about 10 Å, or 1 keV, and the resolution is $\sim$ 1 arc sec. Top right corner represents the zoomed image of the flaring loops in AIA/SDO 131 Å during M6.9 flare occurred on April 11, 2013 at 06:57 UT.

Further, X-rays and UV radiation emitted by solar flares can affect Earth's ionosphere and disrupt long-range radio communications. Direct radio emission at decimetric wavelengths may disturb operation of radars and other devices operating at these frequencies. This damage can be avoided only when the extensive study of particle and radiation budget produced during a flare is completely derivable from the observables. Multi-wavelength study of photosphere is extensively done to reach this objective due to ease of availability of many lines and continuum emission in comparison to higher atmosphere but mere the observations of photospheric changes (most effectively magnetic field observations) are not sufficient (Jain et al., 2011a). The study of multi-wavelength evolution of solar flare emission is inevitably necessary to understand the underlying physical process. We present the observational aspect followed by the mechanism of energy release in solar flares in the following subsections.

1.3.1.1 Solar flares in Soft X-rays

The soft X-rays ($\sim$ 0.1-10 keV) emitted during the solar flares are thermal radiation, released by the virtue of the intense heat and dependent upon the random thermal motions of very hot electrons. The fast variation in SXRs from ARs is mostly associated with solar flares. A typical flare-associated SXR burst has a time profile roughly similar to the time development of the Hα intensity in the brightest point of the flare and similarly, is characterized by a fast rise and a much slower decay as shown in the multi-wavelength intensity profile of April 11, 2013 flare in Figure 1.7. Figure shows the solar flare observed by XRT/HINODE in soft X-rays.

1.3.1.1.1 Solar Flares in Hard X-rays : Solar flare hard X-ray (HXR) emission above $\sim$ 20 keV is a continuum emission. Hard X-rays represent high energy process mostly originated by non-thermal plasma during the process of thick-target bremsstrahlung. The HXR can't be directly imaged similar to SXR and therefore indirect methods of imaging employing observations from RHESSI mission are adapted for the same. The image synthesis technique is discussed in chapter 2 of this thesis.

1.3.1.1.2 Flare Classification : As solar flares vary in area and intensity, the classification of solar flares in X-rays is made by employing 1 - 8 Å peak X-ray intensity measured by the Geostationary Operational Environmental satellites (GOES). Table 1.1 shows the intensity class with respective radiated flux. With this, we may note that an X-class is the most hazardous class of flares due to its large radiated energy. This classification is widely used in solar flare web forecasts.

Table 1.1: The X-ray Flare Classification

Classification	Peak Flux (ϕ) measured in (1-8 Å) (W m^{-2})
A	$\phi < 10^{-7}$
B	$10^{-7} \geq \phi < 10^{-6}$
C	$10^{-6} \geq \phi < 10^{-5}$
M	$10^{-5} \geq \phi < 10^{-4}$
X	$\phi \geq 10^{-4}$

1.3.1.1.3 Solar flares in Hα wavelength : Flares seen on the solar disk frequently show two areas of emission on either side of the magnetic inversion line, because energy released anywhere in a flux tube will rapidly heat the surface at its two foot-points where it meets the surface. When many lines of force are involved, two ribbons of emission (Twin Ribbon Flare) appear. In large flares, the brightening rapidly elongates on either side of the neutral line and separates at a speed of 5-20 km/sec while narrow flare loop prominences form to connect them, rising higher in the corona. If one ribbon is near a sunspot, it will be small and bright, because many flux lines converge there. The ribbons will not cross the spot since the other side involves magnetic field lines connected away from the flare. In the late stages, the strands evolve into two thin lines formed by the intersection of a thin shell of hot coronal material with the surface. Since reconnection means that two tubes of force interchange their end points, one expects four areas to brighten, and in larger flares these often can be picked out. A few flares will sometimes display only one or even three distinct ribbons instead of two or four, although the reason for this is unclear.

Solar flares are ranked in importance by optical, X-ray, or radio flux. Soft X-ray intensity is measured in the 1-8 Å range monitored by the GOES weather satellites (cf. Table 1.1). Optically, flares are classified on the basis of area at the time of maximum brightness in Hα.

- Importance 0 (Subflare): $\leq$ hemispheric square degrees
- Importance 1: 2.1-5.1 square degrees
- importance 2: 5.2-12.4 square degrees
- Importance 3: 12.5-24.7 square degrees
- Importance 4: $\leq$ 24.8 square degrees

Here, one square degree is equal to $(1.214 \times 10^4 \text{ km})^2 = 48.5$ millionths of the visible solar hemisphere. A brightness qualifier F, N, or B is generally appended to the importance character to indicate faint, normal, or brilliant.

Though observed from photosphere to corona in different wavelength, these observations represent a unique energetic process in the solar atmosphere. Therefore, the multi-wavelength manifestations of solar flare as presented above must be explained via the standard model of energy release in solar flares.

1.3.1.2 Temporal Evolution of flare energy release

In general, 10^{32} ergs of energy is being released in tens of minutes from a solar flare. This energy release rate from a very small part of solar atmosphere can be considered very large in comparison to the full-disk observed total solar luminosity i.e. 4×10^{33} erg/s. The total flare energy is estimated to be comparable with the amount of magnetic "free" energy (Metcalf et al., 1995; Schrijver et al., 2008; Jing et al., 2008) which is defined as the energy stored in the magnetic field that is over and above the energy of the potential magnetic field configuration. Further, it is found that the free energy is comparable with that of large flares. In addition, the energy budget is difficult to explain from other possible coronal or chromospheric energy sources (Hudson, 2007). The conversion of stored magnetic energy becomes inevitably the only process at the heart of the flare process and to understand the physical processes causing this much energy release in a very short duration is very crucial in order to explore the plasma conditions on the Sun during solar flares. In this regard, the study of temporal evolution of multi-wavelength flare emissions needs greater attention.

The time evolution of a flare emission is characterized by different timescales for visible to different wavelengths e.g. X-ray, UV and Radio bands etc. In the SXR range, following a rise phase which lasts for a few minutes, the evolution is slow. The label-off of this thermal emission to its pre-event levels is a slow process. On the other hand, the (lower-frequency) radio spectrum exhibits impulsive transient profile also known as type III bursts, with a high brightness temperature, rapid drift rate (frequency decreasing with time) and time duration $\sim$ millisecond (Aschwanden et al., 1995a,b). In general, these are prominent in the decimetric regime and in the microwave band. Further, optical flare variations are typically impulsive, similar to that in HXR lightcurves. UV and EUV also show mixed impulsive and slow variations. During the HXR impulsive phase, soft-hard-soft spectral pattern of the spectral index of the non-thermal part of the photon spectrum is seen which becomes harder as the non-thermal flux increases (Battaglia and Benz, 2006; Fletcher et al., 2011).

Based on specific and different temporal evolution in different wavelength, it can be said that the apparent characteristics of solar flare depend strongly on the frequency of the observed radiation. Though, there are large variations in the characteristic emission of solar flare from one to other, certain broad characteristics of solar flares can still be deduced from the observed time variation of electromagnetic radiation. Kane (1974) categorized the temporal evolution of emission during solar flares in three phases viz: precursor, impulsive and gradual. Figure 1.8 shows the various phase of emission in flare event occurred on February 26, 2004. The impulsive and gradual phase of energy release in solar flare are studied in greater detail but the underlying processes of energy release in the precursor phase is not yet fully established owing to high spectral and temporal cadence observations. The extensive study of this phase, due to its importance in view of understanding the physical processes occurring in the pre-flare plasma which may be responsible for main phase of energy release in solar flares is very necessary. With this study, the complete picture of pre-flare plasma conditions will be obtained which further enable us to predict the impulsive and gradual phase of solar flares. In addition, this study may be helpful to understand the origin and forecast of long duration events *viz:* CMEs, SEPs etc.

1.3.1.2.1 The Precursor Phase : Preceding the impulsive burst of emission, there appears relatively small slow increase in the radiation indicating a possible occurrence of the impulsive and/or gradual phase within following 10 minutes (see Figure 1.8). These initial signs of activity are termed as preflare phase. This term covers both preflare activity, which refers to the very earliest stages of the flare before the impulsive phase radiation is detectable, and the flare precursor events, which are small-scale brightening in UV to SXR wavelengths happening some tens of minutes before the flare (Fletcher et al., 2011). Recent studies employing the spatially resolved observations during the precursor phase suggest that flare precursors often do occur in the neighborhood of the source location from where majority of the flare radiation will subsequently occur (Fárník et al., 1996, 2003; Fárník and Savy, 1998; Warren and Warshall, 2001). Pre-flare brightenings have also been linked to the destabilization of the magnetic structure that will lead to a CME (Harrison et al., 1985; Sterling and Moore, 2005) or a filament eruption (Fárník et al., 2003; Chifor et al., 2007; Liu et al., 2009). Further, the onset of pre-flare activity, in the form of weak SXR emission, precedes the onset of impulsive HXR emission by around 3 minutes in the vast majority of flares, regardless of their total energy or duration (Veronig et al., 2002).

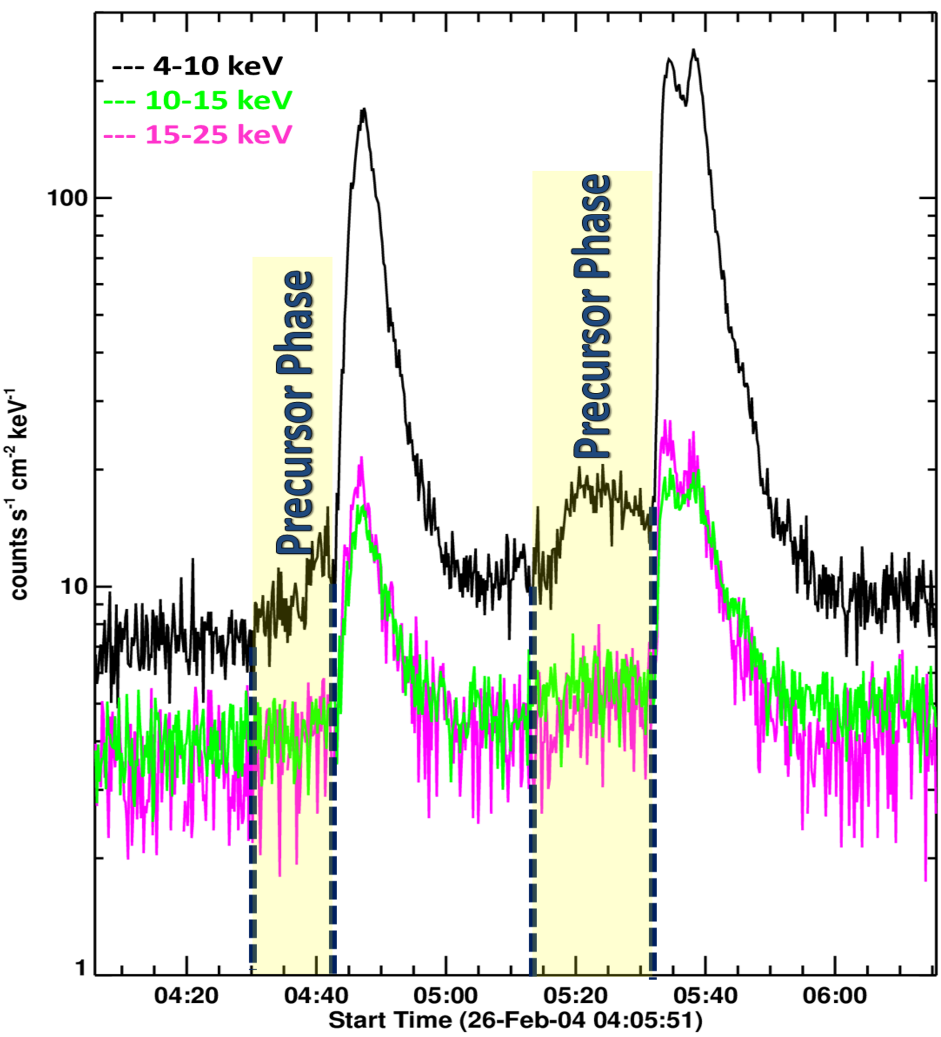

Figure 1.8: Intensity profile of X-ray emission in 4-10, 10-15 and 15-25 keV energy bands during February 26, 2004 flares observed by SOXS. Yellow shaded region represents the precursor phase for respective flares.

Spectral line broadening has been observed in the pre-flare phase (Harra and Sterling, 2001; Harra et al., 2009) starting minutes to hours before the impulsive phase, consistent with nonthermal effects such as plasma turbulence. However, in the recent developments on the pre-flare phase study, non-thermal effects have been reported by analyzing RHESSI observations by Falewicz et al. (2011) and by microwave observations from Nobeyama radio polarimeter (NoRP) by Altyntsev et al. (2012). On the contrary, Battaglia et al. (2009) found thermal conduction to be the energy transfer process during precursor phase emission. Therefore, the current studies do not seem to be settling upon concrete solution to the problem of origin of precursor phase emission originating whether resulted by the process of thermal conduction or by non-thermal beam-driven chromospheric evaporation. Therefore, in this thesis, we have carried out an investigation of fifty flare events observed from various ground based and space based instruments to find out energy release processes as presented in Chapter 3.

1.3.1.2.2 The Impulsive Phase : The primary energy release occurs during the impulsive phase of the flare emission. This phase of flare activity is characterized by most rapid increase in the radiation flux having a lifetime of tens of seconds to tens of minutes after a slow rise in the emission during pre-flare phase. Observationally, this phase is characterized by HXRs, γ-rays, non-thermal (synchrotron) microwaves and white-light continuum emission, indicating strong acceleration of both electrons and ions. These radiations are accompanied also by strong enhancements in chromospheric line and continuum emission, ultraviolet and extreme ultraviolet radiation, and bulk plasma upflows in the EUV and SXRs at speeds on the order of 100 km s^{-1} coupled with downflows in cooler lines such as Hα (Zarro et al., 1988; Milligan et al., 2006). Figure 1.8 shows the temporal evolutions during impulsive phase emission of February 26, 2004 flare.

The impulsive-phase flare spatial signatures in the lower solar atmosphere include “foot-points” or “ribbons”. Further to this, recent high resolution observations from SDO has extracted many more signatures of impulsive phase and magnetic reconnection process (Asai et al., 2004). Early in the impulsive phase, flare HXR foot-points tend to be concentrated around the neutral line, and move with respect to it as the flare evolves. In the later phase of a flare strong Hα and UV emissions in the form of ribbons are visible which move outward from the polarity inversion line. The importance of flare ribbons and footpoints in visualizing the regions of changing magnetic connectivity is now well established (Mandrini et al., 1991). The large-scale reconnection model in two dimensions (Kopp and Pneuman, 1976) was originally developed to explain the spreading Hα ribbons and the Hα arcade that appears in the gradual phase of a flare. The outer edges of the ribbons show the chromospheric projection of the interface (magnetic separatrix surface) between the post-reconnection ("post-flare) arcade fields, and the field that is yet to be reconnected. These may therefore provide a tool to estimate the magnetic reconnection rate as well as reconnection electric field during the impulsive phase (Forbes and Lin, 2000). The reconnection electric-field have been studied in to estimate reconnection rate of May 12, 1997 flare-CME event which is presented in Chapter 5 of the thesis.

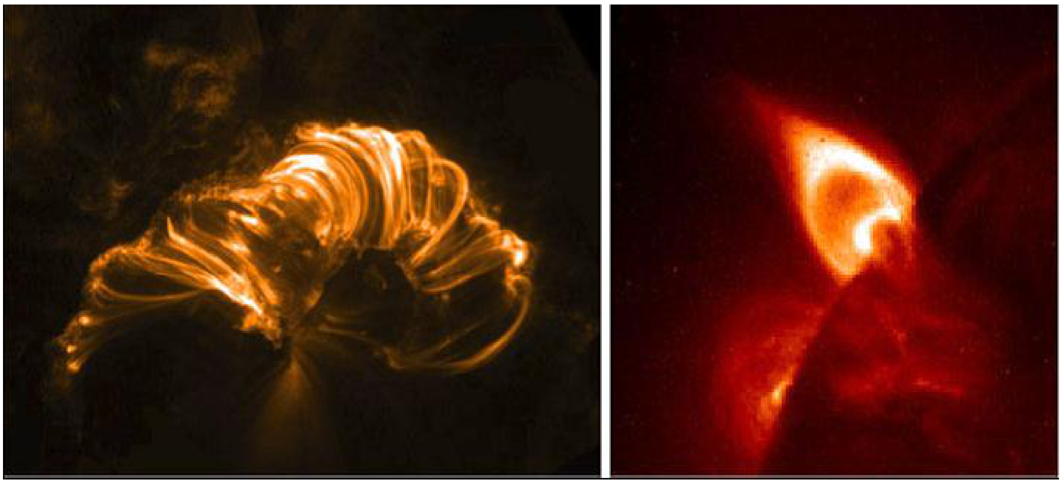

Figure 1.9: Left panel: Flare arcade observed by TRACE in 171 Å wavelength of an X2.3 class flare on April 10, 2001. Right panel: a large post-flare cusp structure observed several hours after the impulsive peak of flare occurred on March 18, 1999 (Image courtsey: TRACE, Yokoyama et al., 2001).

The impulsive phase has been observed and interpreted in greater detail and various models discussed in section 1.3.1.4. Though the impulsive phase have been studied in greater details, only very few studies (Chifor et al., 2006, 2007; Joshi et al., 2011) have been performed during recent years to understand the association/correlation of precursor phase emission with the impulsive phase.

Chifor et al. (2007), based on eight flare event observed in multi-wavelength concluded that slow-rise of the filament is associated to the precursor phase while the fast eruption of the filament gives rise to impulsive phase burst. However, the reason for slow-rise has not been very clear. Further, Joshi et al. (2011) have studied the pre-flare activity and magnetic reconnection during evolutionary stage of an eruptive white light flare. He found the signatures of opening of magnetic-field lines in the localized EUV/UV brightening associated with the filament during the initiation phase which represent the plasma heating and particle acceleration to be taking place. However, the main phase emission has been following the standard flare model. Therefore, one of the motivation of the thesis to study impulsive phase in conjunction to the precursor phase energy release scenario is for the understanding the complete picture of the emission during these phases.

1.3.1.2.3 The Gradual Phase : The gradual phase of a solar flare is identified by relatively slow decaying SXR and microwave signatures than that during the impulsive phase. Flaring loops and loop arcades emitting in SXRs and EUV form and appear to grow, filled by chromospheric plasma forced to expand into the corona as the chromosphere is rapidly heated by particle energy deposition or thermal conduction. This expansion is known as chromospheric evaporation (Aschwanden, 2005). The pressure inside these flaring coronal loops can increase from ~ 0.1 dyne cm^{-2}, typical of the quiet corona, to $>10^3$ dyne cm^{-2} (Machado et al., 1980) which is caused due to the growth of density in the loops. Further during this phase, the loops show multi-thermal plasma. Geometrically, the outermost loops becomes the hottest (Forbes and Acton, 1996) and sometimes exhibit a “cusp” (Figure 1.9) shaped structure (Tsuneta et al., 1992; Yokoyama et al., 2001; Hara et al., 2008). These flaring loops can be observed in EUV and Hα (Schmieder et al., 1995) after they start cooling. Cooling occurs by both conduction and radiation, depending on the flare loop length and plasma parameters. As the loop plasma cools during this phase, it falls back along the field lines (Zarro et al., 1988; Czaykowska et al., 1999; Brosius, 2003). The gradual phase may last for several hours, depending on the magnitude of the flare. It has also been suggested from the estimation of cooling timescales that an additional energy source in the form of ongoing slow reconnection and its associated heating is available during the gradual phase (MacCombie and Rust, 1979; Forbes et al., 1989; Svestka et al., 1982; Forbes and Acton, 1996).

Thus, the study of temporal evolution of the gradual phase can lead to a wonderful opportunity to understand the cooling of the flare plasma and its association to the impulsive as well as precursor phase. The rise phase of ten M-class flares observed by Solar X-ray Spectrometer (SOXS) mission have been used to estimate the conduction cooling time scale and presented in Chapter 4. Further, the evolution during gradual phase has been studied to generalize the Neupert effect, a causal relationship between the SXR and HXR emissions in solar flares as presented in chapter 4 of the thesis. Brief introduction on the cooling of solar flare plasma and its relationship with Neupert effect follows.

1.3.1.2.4 Cooling of the Solar flare plasma : During a solar flare, hot and dense plasma is found to confine within a coronal loop or multiple loops. Observations from several missions namely YOHKOH, TRACE, SOHO, SOXS and RHESSI indicate that flaring plasma temperatures and densities can reach as high as tens MK and $10^{11} cm^{-3}$ during the impulsive phase. Such hot plasma tends to cool to a background temperature after the flare heating stops. Cooling of flare loops is one of the less understood phenomenon mainly affected by conductive and radiative cooling (Culhane et al., 1970; Svestka et al., 1987; Culhane et al., 1994), chromospheric evaporation (Antiochos and Sturrock, 1978), and betatron heating (Karlický and Kosugi, 2004; Veronig et al., 2005).

1. Radiative cooling with the timescales

$$\tau_r = \frac{3nkT}{n^2\phi(T)}$$

2. Conduction cooling with the timescales

$$\tau_c = \frac{3nkT}{KT^{7/2}/L^2}$$

3. Hydrodynamic cooling with the timescales

$$\tau_h = \frac{L}{(kT/m_p)^{1/2}}$$

Here ϕ(T) is the optical thin radiative loss function (Raymond and Smith, 1977). Depending on the flare loop, either the conduction or radiative cooling time scale will be dominating; the hydrodynamic timescale acts only for redistribution of energy and for variation of the density. Multi-strand loop modeling (Hori et al., 1998; Warren et al., 2002; Reeves and Warren, 2002) may help in obtaining cooling time profiles. The energy release from the flare loops, as suggested by Tandberg-Hanssen and Emslie (1988) on a timescale $\tau = (\tau_c^{-1} + \tau_r^{-1})^{-1}$. Therefore, cooling occurring by both conduction and radiation usually depends on the flare loop length and plasma parameters (Culhane et al., 1970; Cargill et al., 1995; Aschwanden and Alexander, 2001). Observational studies have shown that heated plasma cools by conduction during the rise phase of the flare (Culhane et al., 1994) which may then be followed by dominant radiative cooling (Aschwanden and Alexander, 2001). Several models take into account thermal energy redistribution throughout the loop due to conduction, and the gentle chromospheric evaporation in order to understand cooling (Cargill et al., 1995). Therefore, cooling of the flare plasma directly affects the thermal parameters, such as temperature, emission measure (EM), and thermal energy. After the flare onset, both the heating and cooling processes start which results into time delay between the peak value of the flaring temperature, emission measure, and thermal energy (Ning, 2008a,b). However, the domination of conductive cooling in the rise phase and radiative in the decay phase suggests the proposed time-scale to be modified in the current scenario and this is addressed in the Chapter 4 of the thesis. Further, only very recently it has been possible to identify the cooling process during the precursor phase which is presented in Chapter 3 of the thesis.

1.3.1.2.5 Neupert effect in Solar flares : According to the thick-target bremsstrahlung model, hard X-ray emission reaches a peak when most of the non-thermal electrons hit the chromosphere and cause impulsive heating during their energy loss. As a consequence, the heated chromospheric plasma evaporates into the corona due to the local overpressure, which is detectable in the form of soft X-ray emission from the heated plasma that fills the coronal parts of the flare loops. The peak of soft X-ray emission, therefore, lags the peak of hard X-ray emission, due to this causal relationship. In fact, if all non-thermal energy was converted into heating, the energy in soft X-rays should actually represent the time integral of the energy deposition rate of hard X-rays (Aschwanden, 2005). In practice, however, there also occur conductive and radiative energy losses during the heating and evaporation process. The "time integral effect" may remain unaffected only when cooling time scales are much longer than impulsive heating time scales.

This effect was first pointed out by Werner Neupert in 1968, who noticed that time integrated microwave fluxes closely resembles the rising portions of soft X-ray emission curves, which was later termed as Neupert effect by Hudson (1991). Figure 1.10 shows the time-profile of the count flux observed from SOXS mission for the flare event of August 03, 2005 and September 17, 2005 in the left and right panel respectively. It may be noted that temporal evolution of Soft X-ray flux do not show small-scale variations however the time-derivative of SXR flux depicts similar temporal fluctuations as that in hard X-ray intensity profile.

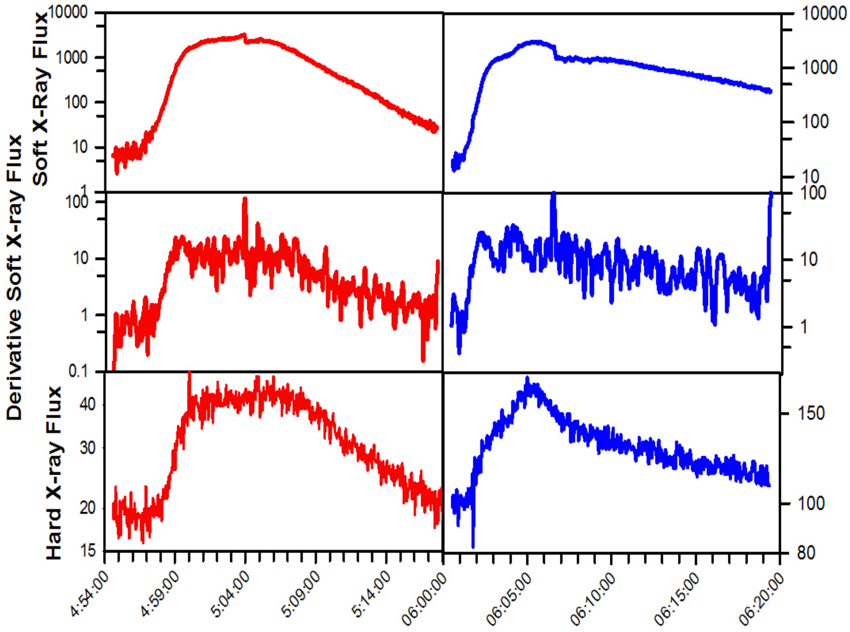

Figure 1.10: Left panel is the stacked plot for light curve of Soft X-Ray in 4-12 keV band ,Time derivative of Soft X-ray in the same band and the light curve of Hard X-ray in 30-50 keV energy band for the flares occurred on August 03, 2005 and September 17, 2005 in the left and right panels, respectively.

The above timing relationship have been found to hold in $\sim$ 80% of several large events studied by Dennis and Zarro (1993). Further, Veronig et al. (2002) performed a timing study of the SXR peak compared to the HXR impulsive phase in more than 1000 events and found that 50% of events were consistent with Neupert-like timing behavior, 25% were inconsistent, with SXR emission peaking substantially after the end of the HXR emission, and the remaining 25% were unclear. Li and Gan (2006) proposed that for the flares which show inconsistency with the Neupert timing behavior, the SXR peaks when the heated plasma, through the process of chromospheric evaporation, reaches to the loop-top. This results in a geometrical dependence of the time lag and a longer time lag is expected for larger flare loops. At the present time, the discrepancies between observed and theoretical Neupert effects are probably within the observational limits, but hints of different physics from the standard ideas that hot thermal emission is coronal and non-thermal emission mostly chromospheric should of course not be ignored. Further, this relationship is expected only for the asymptotic limit of very long cooling times which is not physically accurate assumption. A general Neupert effects is therefore expected to include the effect of cooling as a function of time which is never been attempted (Holman et al., 2011). In this regard, we study the cooling of the solar flare plasma whether conductive or radiative by employing observations from SOXS and RHESSI missions as presented in Chapter 3 and 4.

In addition to the study of temporal evolution of solar flare emission, spectral study of solar flare possesses the capability of estimating the plasma conditions during the flare emission. We present a brief scenario of spectroscopy as a tool of investigation of the flare plasma parameters in the following section.

1.3.1.3 Spectral evolution in Solar flares

The emission spectra of solar flares, especially in the SXR range, represent the most direct information of the flaring coronal plasmas estimated through remote sensing. Many instruments viz. YOHKOH, RHESSI, SOXS, CORONAS missions touch on this domain via its capability for measuring the thermal free-free and free-bound continua, as well as to detect the K-shell emission lines of highly ionized Fe around 6.7 keV and Fe/Ni complex around 7.8 keV. These spectral features appear commonly in a wide variety of astrophysical sources, such as active galactic nuclei, stellar flares, and supernova remnants. The flare plasma parameters thus include electron temperature, emission measure, and information about elemental abundances. Further, the flare thermal spectrum observed $<$20 keV energy range consists of free-free (bremsstrahlung) and free-bound (recombination) continuum emission. The contributions made by these continua vary with energy and temperature (Phillips, 2004). In general, thermal free-free radiation is predominant at lower energies and higher temperatures (Culhane, 1969; Gronenschild and Mewe, 1978).

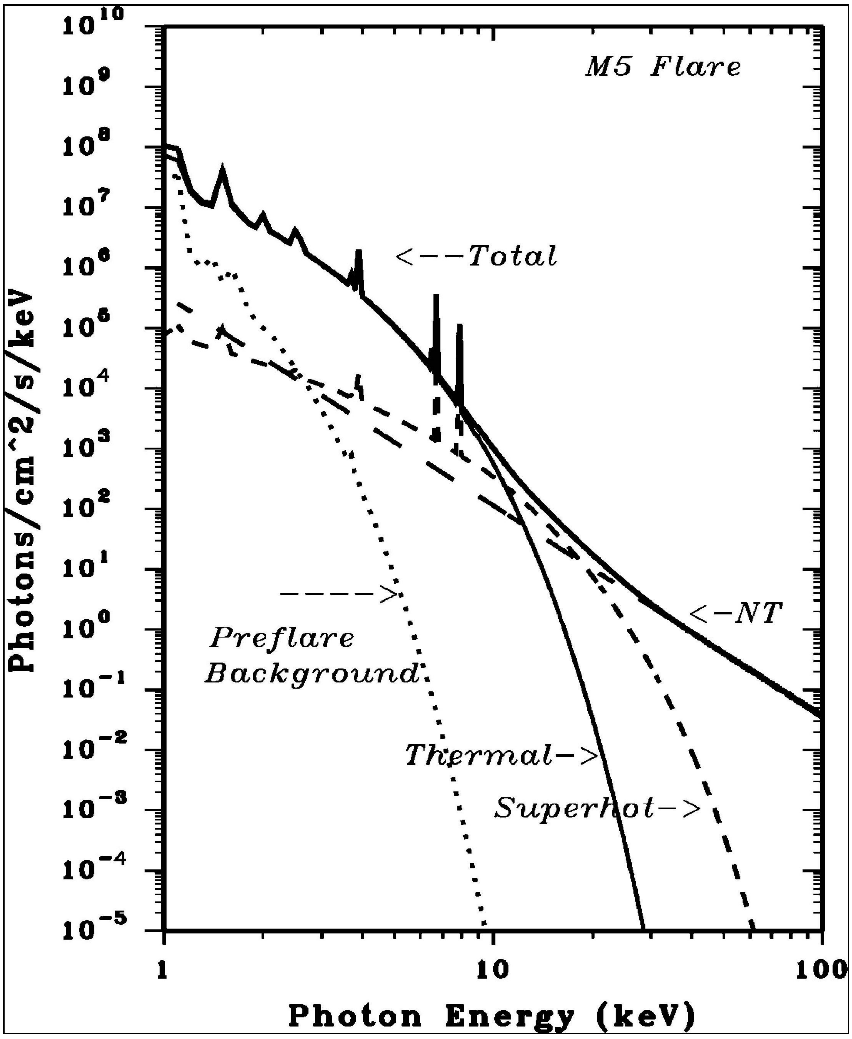

Figure 1.11: Simulation of full-disk integrated X-ray photon emission spectrum from the Sun in the energy range 1-100 keV for quiet and M5 solar flare conditions. The dotted line indicates preflare background; thin solid line the thermal component; medium dashed line the superhot hard X-ray component; long dashed line the non-thermal hard X-ray spectrum while the solid thick line is total flux of thermal and non-thermal components.

Shown in Figure 1.11 is a simulation of full-disk integrated photon spectrum from 1 to 100 keV energy range (Jain et al., 2005, 2006) considering temperature (in MK) and EM (in cm^{-3}) pair to be [4, 10^{49}], [13, $10^{49.5}$] and [40, 10^{47}], representing preflare background, thermal and superhot components of the spectra. Further, nonthermal-spectral index is considered to be -3.5 (ranging between -2.5 to -4.5) and flux at 20 keV = 10 photons $cm^{-2}s^{-1}keV^{-1}$. The dotted line shows the preflare background; thin solid line indicates the thermal component of the flare. The superhot hard X-ray component is shown by a medium dashed line while the long dashed line represents the nonthermal hard X-ray spectrum. The solid thick line is total flux from all these assumptions. It may be noted that iron and iron-nickel complex lines appear only when flare occurs, and there is a break in energy from one to the other spectrum.

The study of spectral evolution of solar flares yield a tool to estimate plasma parameters viz. Temperature (T), emission measure (EM), non-thermal plasma parameters etc. Though the study and the tool well evolved, there are certain assumptions for fitting the plasma parameters which results in various ranges of interpretations from even a single observation. For example, there is a big debate on flare plasma isothermal or multi-thermal treatment. Further, the break energy/ turn-over energy between thermal to non-thermal emission turns out to be never ending problem which I will be discussing in the next few sections. Further, we have studied these debates employing observations from state-of-the-art instruments as discusses in Chapter 4.

1.3.1.3.1 Thermal and Non-thermal contributions to a solar flare X-ray flux : The underlying physical processes of energy release which give rise to the emission in the flare consist of thermal and non-thermal processes. The thermal contribution of the flare emission is known to be originating the processes viz. plasma heating at the magnetic reconnection site; the ablation (or evaporation) of the chromosphere as a consequence of bombardment of the accelerated charged particles to relativistic limit produced due to magnetic reconnection process into the chromosphere, thermal conduction of plasma propelled by high temperature gradients etc. Further, non-thermal contribution of the emission comes mainly from the thick-target bremsstrahlung of the highly accelerated charge particle (mainly electrons) during magnetic reconnection processes. These processes, when combined, form a basis for "The standard model of Solar flares". The X-ray emission is associated with the physical process of Bremsstrahlung. This continuum is the non-thermal power-law like part of the photon spectrum. The thermal and non-thermal radiation mechanism can be described with the help of two processes: Thick-target Bremsstrahlung and thin-target Bremsstrahlung (Brown, 1971). The effectiveness of these processes in producing flare emission solely depends on the bremsstrahlung cross-section. Thick- and thin-target emissions represent the HXR and SXR emission process respectively. The thermal and non-thermal energy estimation critically depends on the input parameters of the model functions. The same is employed for estimating the energy budget during various phases of emission in solar flares as presented in Chapter 3.

1.3.1.4 Models of energy release in Solar flare

It is well established that during solar flare emission, though the primary energy release process in the form of magnetic reconnection takes place in the corona, the dominant radiative energy of a flare, in the form of both thermal and non-thermal emission has been observed from the lower atmosphere (Chupp et al., 1973; Hudson and Ohki, 1972; Kane et al., 1979; Lemaire et al., 2004; McIntosh and Donnelly, 1972; Woodgate et al., 1983). Therefore, the flare energy generated during conversion of magnetic energy into the kinetic energy via the process named as magnetic reconnection at the energy storage site must be transported into the chromosphere, there to be dissipated by radiation and flows of the energetic particle. The magnetic reconfiguration that allows the rapid release of stored magnetic energy in a flare is generally agreed to occur somewhere above the chromosphere in the corona. The main theoretical argument for a coronal energy release is that the corona provides adequate volume for storing the energy required for a flare (Fletcher et al., 2011).

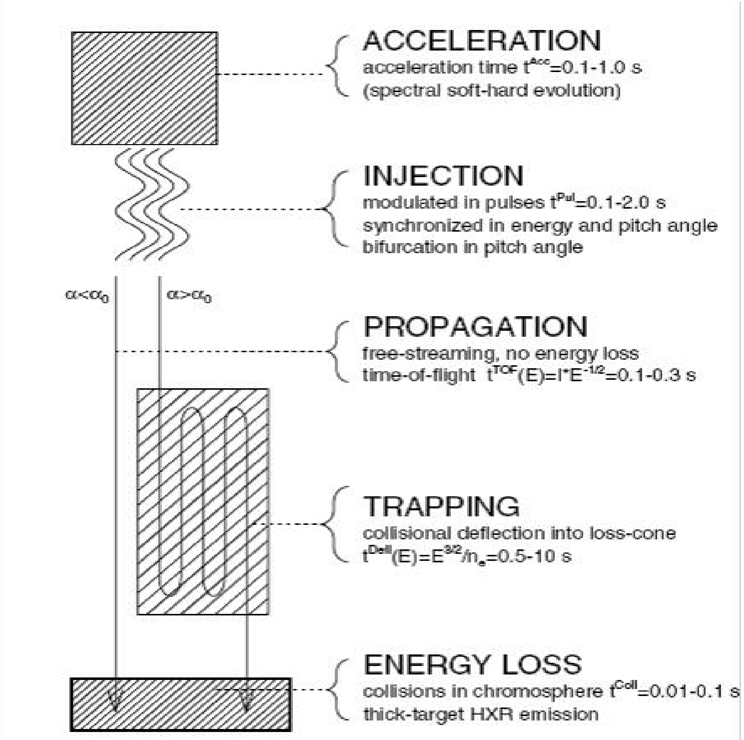

Figure 1.12: Physical processes during solar flares (Figure Courtsey: Aschwanden et al., 1998; Aschwanden, 2005).

Observationally, coronal manifestations such as large SXR and Hα flare loops, HXR looptop sources, and coronal mass ejections have almost universally been interpreted in a framework involving large-scale coronal magnetic reconnection. Non-linear force-free reconstructions of the magnetic field find that the energy is concentrated low in the corona in a newly emerged active region, and can be sufficient for flaring activity (Régnier and Priest, 2007; Schrijver et al., 2008) whereas in an older decaying active region it is stored higher in the corona. Therefore, based on the observational combined with theoretical aspects, many eminent physical models for flare and CME processes have been established, which all involve magnetic reconnection. Although not all flares can be explained by a single model, it is justified to establish a standard model that fits most of the observations and has a well-understood theoretical foundation. Figure 1.12 shows the conceptual breakdown of emission process in solar flares in five steps (Aschwanden et al., 1998; Aschwanden, 2005) which any model must explain. In this regard, the most widely accepted standard model for flares is the 2D magnetic reconnection model that evolved from the ideas of Carmichael (1964), Sturrock and Coppi (1966), Hirayama (1974), Kopp and Pneuman (1976), called the "CSHKP model" according to the initials of these five authors. This has been further elaborated by Tsuneta (1997) and Shibata et al. (1995) based on the modeling of Yohkoh observations.

1.3.1.4.1 CSHKP model : According to the standard flare CSHKP model, the initial driver of a flare process is a rising filament (or prominence) above the neutral line. The rising filament stretches the overlying field lines. This results in the formation of the current sheet above a neutral line where they reconnect, prone to Sweet-parker or Petschek reconnection scenario.

In the model of Sturrock and Coppi (1966), a helmet streamer configuration was assumed to exist at the beginning of a flare, where the tearing-mode instability (induced by foot-point shearing) near the Y-type reconnection point triggers a flare, accelerating particles move in a downward direction and producing shock waves and plasmoid ejection in an upward direction.

Hirayama (1974), in the preflare phase, modeled a rising prominence above a neutral line (between oppositely directed open magnetic field lines), which carries an electric current parallel to the neutral line and induces a magnetic collapse on both sides of a current sheet after eruption of the prominence. The magnetic collapse is accompanied by lateral inflow of plasma into the opposite sides of the current sheets. The X-type reconnection region is assumed to be the location of major magnetic energy dissipation, which heats the local coronal plasma and accelerates non-thermal particles. These two processes produce thermal conduction fronts and precipitating particles which both heat the chromospheric footpoints of the newly reconnected field lines. As a result of this impulsive heating, chromospheric plasma evaporates and fills the newly reconnected field lines, with over-dense heated plasma, which produces soft X-ray emitting flare loops with temperatures of $\sim$ 10 - 40 MK and densities of $\sim 10^{10}$ - 10^{12} cm^{-3}. Figure 1.13 shows the Hirayama (1974) model of flare emission scenario.

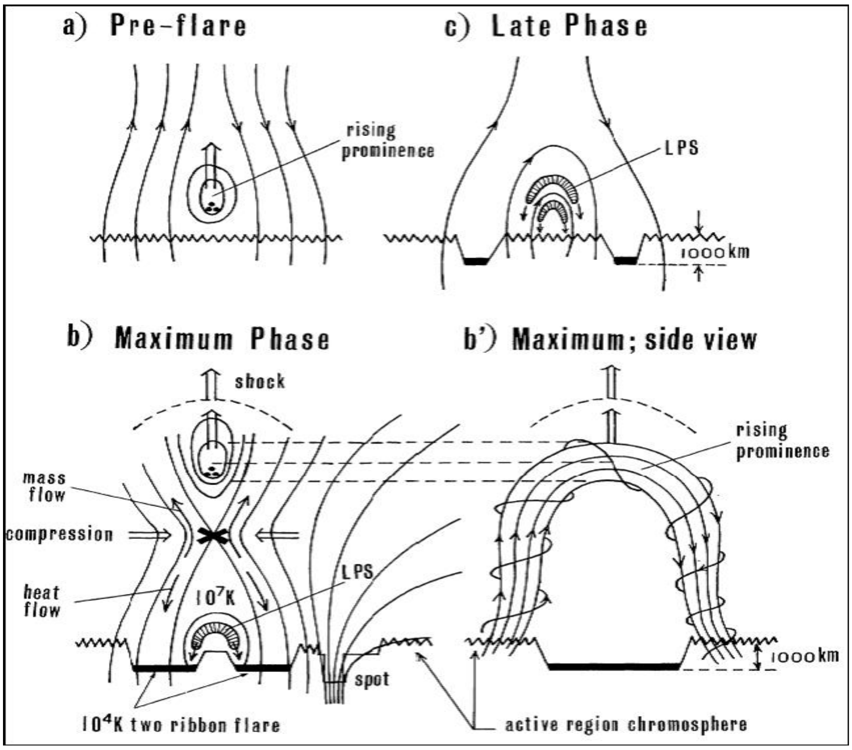

Figure 1.13: Temporal evolution of a flare, starts from a rising prominence (a), triggers X-point reconnection beneath an erupting prominence (b), shown in side view (b'), and ends with the draining of chromospheric evaporated, hot plasma from the flare loops (c) (Hirayama, 1974). (Figure courtesy: Aschwanden, 2005)

According to the general flare scenario, the accelerated electrons spiral down the magnetic field lines to the chromosphere. In the chromosphere, they suffer collisions with the ions in the ambient plasma and produce Bremsstrahlung. They lose energy through Coulomb collisions, which leads to heating the chromospheric plasma upto several MK, which is also known as chromospheric evaporation. This hot plasma expands and fills up the coronal flare loops emitting soft X-rays. The temperature of the flare plasma decreases slowly and returns gradually to its original state due to flare plasma cooling processes. This standard model of the flare energy release though its overall elegancy, does not incorporate the description of the precursor phase changes and emission which needs to be studied and incorporated. Chapter 3 and 4 of the thesis are dedicated to either refining or augmenting the model of energy release in Solar flares.

Further, chromospheric plasma heating during the flare, which occurs when, accelerated particles or thermal conduction fronts during their downward propagation hit the transition region and chromosphere. Because of the large density gradient at this interface, this secondary heating process produces far more heated flare plasma than any of the primary heating mechanisms that operate in the corona (Aschwanden, 2005). There are two competing agents for chromospheric heating, non-thermal particles (termed as beam-driven) versus thermal conduction fronts (conduction-driven), which both seem to be important in flares. In the next section, we present the current understanding of both the processes and their relevance during various phases of emission in solar flares.

1.3.1.5 Conduction and Beam-driven chromospheric evaporation

The magnetic reconnection process at the site of energy storage represents the origin of non-thermally accelerated particles as well as of heat up the local plasma, to temperatures as high as T $\sim 10^7$ K. This overpressure in the heated plasma will cause an expansion, with thermal conduction fronts that have a steep temperature gradient at the leading edges. The leading edge is expected to propagate with the ion-sound speed (Smith, 1979), leading to an anomalous heat flux. Though the anomalous flux suffers limitations in the form of saturated heat flow capability of thermal-gradient induced propagation, this has motivated a dissipative thermal flare model (Brown et al., 1979; Smith, 1979), where the impulsively heated coronal plasma is confined by the relatively slowly moving conduction fronts. A substantial fraction of the observed soft X-rays are then produced by thermal bremsstrahlung of the bottled-up electrons. A number of observational tests have been performed for this model, where a proportionality between the hard X-ray rise time and the (microwave) flare size was found, which was interpreted in terms of a constant source expansion speed (Batchelor, 1989). Another argument in favor of the conduction-front model was brought forward for a flare that showed all signatures of chromospheric evaporation upflows but a lack of ($>$ 15 keV) hard X-ray emission (Czaykowska et al., 2001). Further, numerical MHD simulations of magnetic reconnection processes include heat conduction and reproduce the evolution and propagation of conduction fronts in detail (Yokoyama et al., 2001). The 2D simulations of Yokoyama et al. (2001), including the effects of anisotropic heat conduction and chromospheric evaporation, revealed that the energy transported by heat conduction causes an increase in temperature and pressure of the chromospheric plasma. Thus, these MHD simulations confirm that chromospheric evaporation can also be produced by heat conduction fronts, which is important for flares without detectable hard X-rays. In flares with detectable hard X-rays, both drivers (i.e., particle precipitation and heat conduction) may compete in spawning chromospheric evaporation. Recently, a study of precursor phase emission of four RHESSI observed flares by Battaglia et al. (2009) also supported the conduction-driven chromospheric evaporation. On the other hand, studies by Falewicz et al. (2011), Altyntsev et al. (2012) found the signature of beam-driven chromospheric evaporation. In this regard, though the generally accepted model of energy release in solar flare suggests beam-driven chromospheric evaporation as “the model” however, the observationsof precursor phase emission in SXR without the presence of HXR emission originates the possibility of conduction-driven chromospheric evaporation too. In this regard, we study the existence of thermal and non-thermal signatures in greater detail in Chapter 3 to delineate the dominating model during precursor phase and main phase of the flare emission. In the next section, mechanism of trigger of energy release during the flares is discussed.

1.3.1.6 Trigger mechanisms of energy release during solar flares

Solar flare occurs as a consequence of magnetic instability. The magnetic instability condition is triggered prior to the state when the magnetic field configuration loses its equilibrium and subsequently leads to a equilibrium of a lower energy state. To understand this mechanism, a physical model explaining the trigger mechanism is essential. In this Section, we present a brief discussion on various such models existing in the literature as also presented in Figure 1.14.

1.3.1.6.1 Random motion of photospheric magnetic field : The random motion of magnetic flux tubes at the photospheric height is driven by the convective motions of the plasma governing the magnetic fields. This motion results in the tangled and braided coronal magnetic field lines (Parker, 1988). Thus the magnetic-field lines lead to a non-potential state and become prone to magnetic reconnection. This process is understood to release magnetic energy $\sim 10^{24}$ erg (Parker, 1988). Due to the released energy being small in comparison to that estimated during typical flares, this process was accounted for the occurrence of nanoflares. This process is also capable of accelerating nonthermal electrons.

1.3.1.6.2 Shearing of magnetic field : The coronal magnetic field may experience shearing due to the oppositely-directed photospheric flows on both sides of a neutral line. Hagyard et al. (1984) found that multiple co-spatial flares occurred as soon as the photospheric shear angle reached a critical value of 80°. In addition, large shears are found to be the origin of large flares with the emission reaching upto gamma rays (Hagyard et al., 1990). Numerical models were also proposed based on the effect of shear angle on the length of the current sheet associated with magnetic reconnection (Karpen et al., 1991, 1995, 1998). Thus, magnetic shearing in coronal zones seems to be a very favorable condition to trigger magnetic reconnection and particle acceleration.

1.3.1.6.3 Emergence and cancellation of magnetic flux : Small-scale magnetic flux-tubes emerge through the photosphere and chromosphere which interact with the pre-existing overlying coronal field. Due to this process, the heating of the newly formed current sheet and increase of resistivity occurs which lead to subsequent reconnection (Heyvaerts et al., 1977). The source of emerging magnetic flux is understood to be the convection in the solar interior (Fisher et al., 1991). Leka et al. (1996) had shown the evidence of current-carrying nature of emerging flux. Observational evidence for emerging flux prior to flares and CMEs has been reported by Canfield and Reardon (1998); Jain et al. (2011b). In-spite of this causal relationship, the emerging flux is not direct proxy of flare events (Nitta et al., 1994). In this regard, although flux emergence contributes to enhance flaring, the detailed trigger that leads to the rapid energy release is not known.

In addition to the flux emergence, the submergence of a magnetic fluxtube leading to the disappearance of a photospheric dipole has also been associated with the role of a flare trigger (Wang and Tang, 1993; Zhang et al., 2001). Further, Priest and Forbes (2002) proposed a converging flux model which triggers magnetic reconnection leading to flares. The slow magnetic reconnection in the chromosphere driven by flux emergence and/or cancellation may lead to the global instability responsible for filament destabilization in major flares.

1.3.1.6.4 Kink Instability driven filament eruption : Eruption of the filament is often accompanied with the flare. The cause of this eruption is suggested to be the kink instability which is driven by excess magnetic twist in the flux tube (Hood and Priest, 1979; Cheng, 1977). Observational evidence for helically kinked magnetic flux ropes have been found in several observations of Yohkoh/SXT data (Rust and Kumar, 1996).

1.3.1.6.5 Tether Cutting : The onset and growth of the solar eruptions may be understood to be caused by tether-cutting reconnection (van Ballegooijen and Martens, 1989; Moore et al., 2001a). Tether-cutting mechanism is a consequence of an interplay between magnetic pressure and tension forces. Prior to the eruption, the magnetic pressure force remains in balance with the magnetic tension force. Although the magnetic pressure keeps the magnetic bipole configuration inflated, the tension opposes the same keeping field tied down/tethered to the photosphere. During the eruption, the reconnection within the core of the sigmoid progressively cuts more and more of the tethers, allowing the core field to expand upward. Internal and external tether-cutting (Figure 1.14 Moore et al., 2001a) are the mechanism which can act as a trigger a filament to erupt which is sustained by a sheared core field in the central lobe of a quadrupolar magnetic field configuration.

1.3.1.6.6 Magnetic Breakout Model : Antiochos et al. (1999) proposed a sheared arcade model which requires magnetic reconnection to trigger the eruption. In this model the magnetic field configuration has spherically symmetric quadrupolar geometry, rather than dipolar geometry. The model has three polarity inversion lines on the photosphere and four distinct flux-systems (Lin et al., 2003), as may be noted from Figure 1.14. Aulanier et al. (2000) made a generalized extension of reconnection scenario in 2D-quadrupolar magnetic configuration proposed by Antiochos et al. (1999) to the case of 3D reconnection. In this, he involved a coronal null point above an active region of δ configuration and defined magnetic breakout as the opening of initially low-lying sheared fields, triggered by reconnection at a null point. In this multipolar magnetic topology, reconnection between the sheared arcade and the adjacent arcade reduces the shear and thereby supports the core flux to reconnect which may lead to filament eruption.

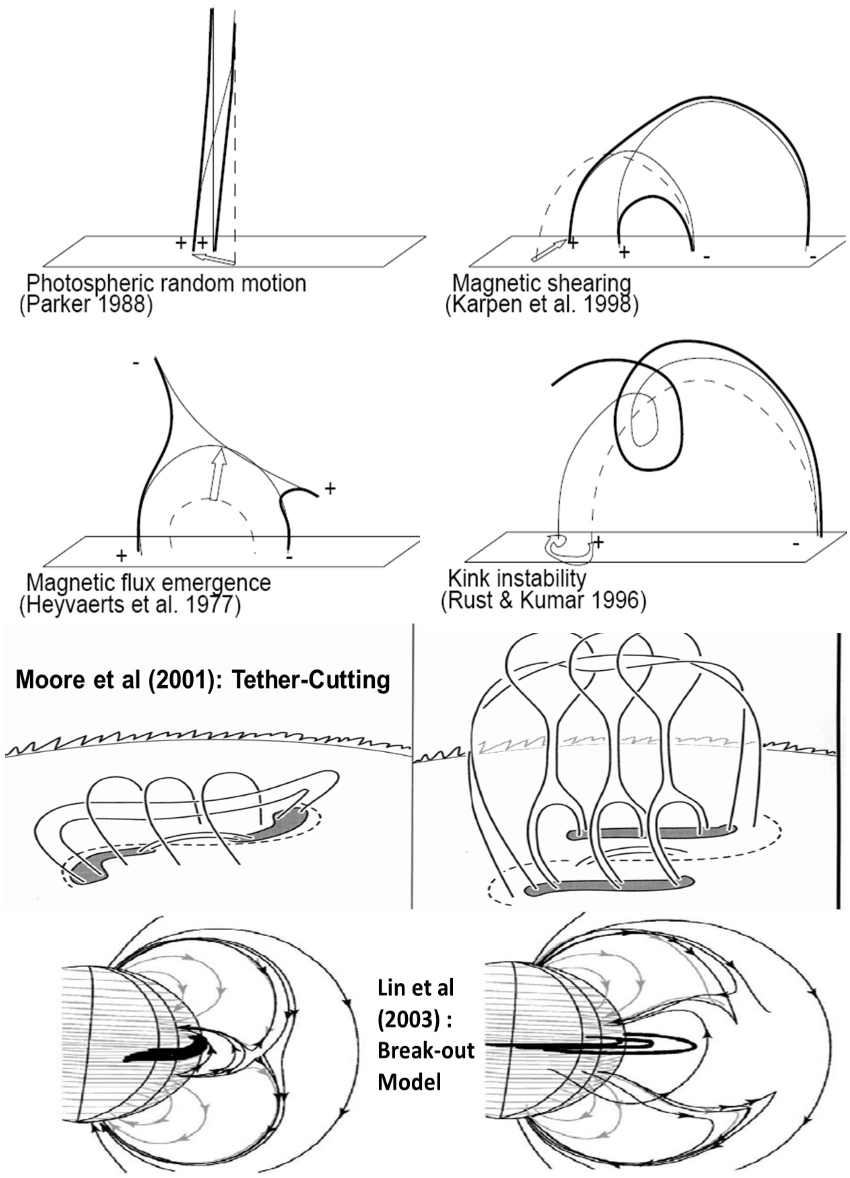

Figure 1.14: Schematics of various mechanisms of trigger of solar flare. (Figure courtesy : Moore et al., 2001a; Lin et al., 2003)

1.3.1.6.7 Reconnection Inflows : Through the identification of converging flows toward the magnetic X-point above a cusp-shaped soft X-ray flare loop, Yokoyama et al. (2001) revealed the evidence of reconnection in-flows in a solar flare. The momentum of the inflowing mass or the difference in magnetic pressure high up in the corona may act as a trigger of the magnetic reconnection process. Blackman and Chou (1997) proposed the particle acceleration during reconnection inflow case as that the rate of accelerated particles in the fast shocks of the down streaming outflows is directly related to the angle of the inflow field and the velocity of the slow shocks.

As discussed above, each flare can be associated with certain type of magnetic-field topology and respective trigger mechanism. This enables us to infer the reconnection topology of an observed flare trigger mechanism, or vice versa. We discuss various trigger mechanisms associated with flares and CMEs in Chapter 3 and 5 of the thesis.

1.3.2 Coronal Mass Ejections (CMEs)

The dynamic phenomena on the Sun known as Coronal Mass ejections (CMEs) occur as a consequence of reconnection of magnetized loops in the corona, which, however, accelerates magnetized plasma beyond the escape speed. Therefore, the CMEs are generally associated with a release of magnetic energy in the solar corona. CMEs occur with a frequency of few events per day and carry a bulk of plasma with mass ranging from 10^{14} to 10^{16} g. As the CMEs propagate outward from the Sun into the interplanetary space, they expand in size and carry a frozen-in magnetic flux. A CME aimed towards the earth is called a Halo-CME or an Earth-directed CME event. Figure 1.15 shows image of the halo CME observed by COR2 onboard STEREO-A satellite on November 03, 2012.

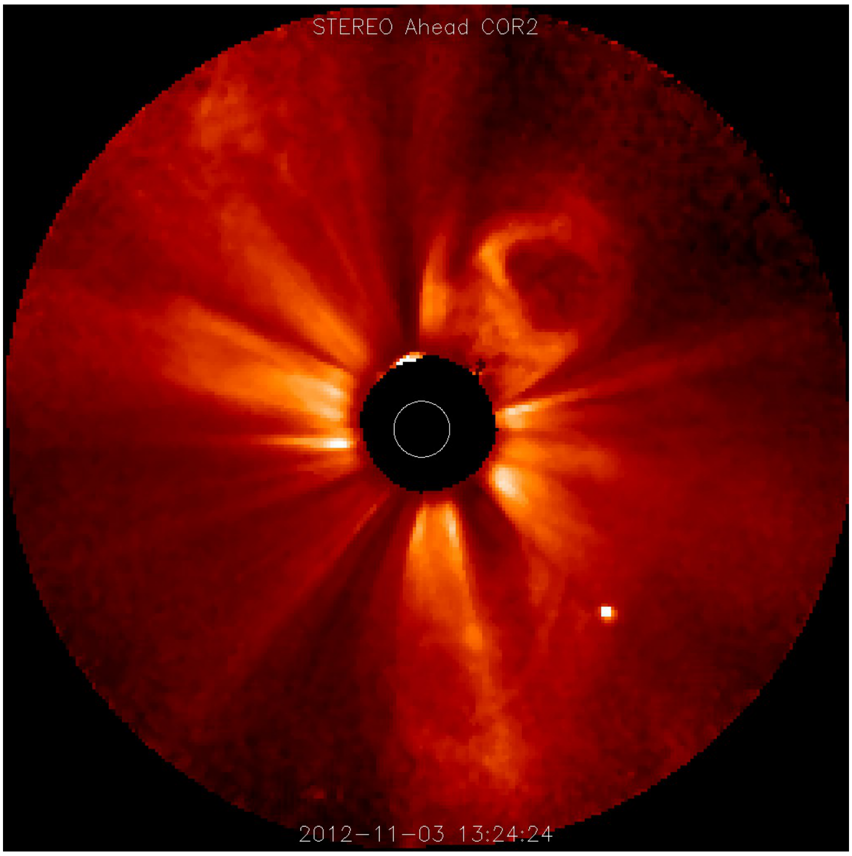

Figure 1.15: A halo coronal mass ejection observed by COR2 onboard STEREO-A satellite on November 03, 2012 (Image courtsey: STEREO-A).

Coronagraphs measure mainly photospheric light scattered by coronal electrons (Thomson scattering). An increase in brightness means that the integrated density along the line-of-sight is increased which provides us with a white-light image against the plane of the sky. A typical morphology of many CMEs is the three-part structure consisting of a bright leading edge (or frontal loop) and a dark cavity surrounded by a bright core. Employing the LASCO observations of CME, Krall et al. (2000) showed that the magnetic field geometry of a CME is that of a flux rope. They further explained that LASCO observations are consistent with a two-dimensional projection of a three-dimensional magnetic flux rope with legs that remain connected to the Sun.

The density distribution in a CME is very inhomogeneous. The first determination of true mass of CMEs observed with SECCHI-COR2 on STEREO-A and B was made by Colaninno and Vourlidas (2009). They demonstrated that it is possible to simultaneously derive the direction and true total mass of the CME by assuming that the same mass should be observed in COR2-A and B.

Based on the velocity and acceleration profiles observed with SOHO/LASCO over the distance range of 2Rs to 30 Rs, it was proposed that there exist two distinct classes of CMEs (Sheeley et al., 1999): gradual CMEs and impulsive CMEs. When prominences and their cavities rise up from below coronal streamers, gradual CMEs are formed. They typically attain slow speeds (v $\sim$ 400 - 600 km s^{-1}) with clear signs of gradual acceleration (3 - 40 m s^{-2}) at distances R $<$ 30Rs. Impulsive CMEs are often associated with flares and Moreton waves on the visible disk. They have velocities $\geq$ 750 - 1000 km s^{-1}. When first seen in coronagraphs, observations show that they either have a constant velocity or they decelerate at distances R $\geq$ 2Rs.

Typical total energy of CMEs ranges between $\sim$10^{29} - 10^{32} erg, comparable with the flare energy. Using the direct measurements of the mass, velocity, and dimensions of CMEs observed by LASCO on SOHO, Vourlidas et al. (2000) found that the potential and kinetic energies increase at the expense of the magnetic energy as the CME moves out, keeping the total energy almost constant. Jain et al. (2010) studied the relationship between the CME velocity and plasma temperature of the solar flare employing SOXS (CZT) data and obtained a correlation of 0.82. This suggests that, when the free magnetic field energy in the active region is converted pre-dominantly to heating the flare plasma near the energy release site, the associated outgoing CMEs move faster initially. This also suggests that the source of the energy release of CME and flare events, when associated, is the same.

Owing to the space weather effects of CMEs, it is extremely important to understand their speed profiles, propagation direction and 3D configuration so that their arrival time can be accurately predicted. A better understanding in this context is now possible with the launch of STEREO spacecraft in 2006. The purpose of the STEREO Mission is to understand the causes and mechanisms of coronal mass ejection (CME) initiation and to follow the propagation of CMEs through the inner heliosphere to Earth (Kaiser et al., 2008). Mierla et al. (2010) suggested that the propagation direction and the 3-D structure of coronal mass ejections may be inferred using data from the SECCHI coronagraphs onboard the STEREO mission. They described different techniques that were used to model the 3-D configuration of CMEs in the coronagraph field of view (up to 15Rs). They estimated the most probable CME propagation direction at the outer boundary of the corona (observed in coronagraph images) to within $\sim 10^0$.

Various models have been proposed to understand and explain the theoretical concepts of a CME. Some of the major CME models are thermal blast model, Dynamo model, and storage and release model, tether-cutting or flux cancellation model and magnetic breakout model. The thermal model proposed that a CME is driven outward by a greatly enhanced thermal pressure produced by a flare (Dryer, 1982).

1.3.2.1 Flare-CME relationship

CMEs and flares may be produced by quite different mechanisms (Feynman and Hundhausen, 1994) or the same mechanism but two different components of explosive magnetic-energy release (Jain et al., 2010). The flare-CME relationship has been studied by Zhang et al. (2001), Chen and Zong (2009), Jain et al. (2010) and many other researchers. Jain et al. (2010) showed that the speed of CMEs increases with X-ray flare plasma temperature (r =0.82). They proposed that initiation and speed of CMEs perhaps depend upon the dominant process of conversion of the magnetic field energy of the active region to either heating or accelerating the coronal plasma in the reconnected loops. Aarnio et al. (2011) found that CME mass increases with flare flux. Temmer et al. (2010) found that the CME acceleration profile and the flare energy release as evidenced in the hard X-ray (HXR) flux evolve in a synchronized manner. To probe the energy release in eruptive and confined events, Wang et al. (2007) investigated X-class flares. Employing the potential field source-surface model, they found that a stronger overlying arcade field may constraint energy releases in the lower corona from being eruptive, resulting in flares, without CMEs. In order to study the properties of solar source regions which produced fastest front side CMEs, they derived a set of parameters characterizing the size, strength, morphology, complexity, and free energy of ARs. Their results suggest that larger and stronger active regions with more complex magnetic configuration are more likely to produce an extremely fast CME. Similarly, Liu et al. (2007) also concluded that the ambient magnetic field structure plays a role in determining the speed of halo CMEs. However, the ultimate question still remains open, how and in what forms, the flare emission is associated with the CME in the timing study as well as in the energy budget. Therefore, in chapter 5, we probe the magnetic-field parameters in association with UV and Hα emission to understand the flare-CME relationship.

1.4 Motivation and outline of the thesis

The central theme of my thesis is to understand the energy release processes in various phases of flare emission and its association with the CMEs. The plan of the thesis formulates as following:

In chapter 2, we present the brief introduction of the instruments employed for ground and space based observations of multi-wavelength emission from solar flares employed for study in the thesis. The data analysis technique for the respective instrument is also discussed.

Chapter 3 deals with the multi-wavelength diagnostics of precursor phase emission in solar flares and its association to the main phase emission. In this theme, we discuss temporal and spectral evolution of thermal and non-thermal emission. In addition, we also present a detailed study on the role of filament during precursor and main phase.

In chapter 4, we present our study on the nature of solar flare plasma in view of isothermal or multi-thermal. The flare plasma nature has been under great debate in view of isothermal or multi-thermal nature and the data unavailability in the energy <10 keV prior to SOXS era has been one of the major issues which poses challenge to solve the issue.

Chapter 5 deals with probing the role of magnetic-field parameters viz. magnetic-field gradient, in producing flare-CME event occurred on May 12, 1997. Most interestingly, we estimated the rotation of the leading polarity which led us to critically review the association of it with the free energy and thereafter its role towards the destabilization of flare-CME system.

In chapter 6, we present preliminary study of the causal relationship between coronal X-ray and photospheric magnetic-field observation. The study led us to new insights on the phenomena of "Self-Organizing criticality in the corona".

Chapter 7 focuses on the conclusions, discussions and future aspects of the aforesaid study. The research never stops and that happened here too as we have many more unsolved questions with us than the ones we solved. In here, we wish to augment our work on cooling of the solar flare plasma in generalizing Neupert effect by employing Hα observations from the TSFT in conjunction to the other ground-based observatories. Further, we also look forward to model multi-thermal solar flare plasma employing more precise weighted temperature analysis.

During my research fellowship, I have been involved in the development of a dedicated solar flare observing facility at Astronomy & Astrophysics Division, Thaltej, PRL. This is named as Thaltej Solar Flare Telescope (TSFT). In Appendix A, we present a detailed description on its installation, specification and observing summary.

Chapter 2

Instrument and Data Analysis Techniques

2.1 Introduction

Solar flares are understood to be one of the most hazardous events occurring in the atmosphere of the Sun. Typically 10^{32} ergs of energy is released in 1000 s from a solar flare. It has been widely established that this gigantic energy comes from the magnetic flux evolving at sub-photospheric level and being transferred to corona. The random motion of magnetic flux tubes which transfer the energy from photosphere to corona for storage, which later release in the form of flare emission, can be studied through observing the magnetic-field of the active region (AR). Similarly, the trigger of the stored energy in the form of filament activation can be mapped from the observations in red-wing of the visible electromagnetic spectrum. Following the magnetic reconnection process, energized electrons traverse from corona to chromosphere while gyrating along the magnetic field-lines which can be imaged in radio waveband. Further, as the accelerated charged particles hit the relatively denser chromosphere, X-ray emission is produced in the process of thermal and non-thermal bremsstrahlung. Thus solar flare energy release is observed from microwave to

Gamma rays covering almost entire electromagnetic spectrum. This suggests that observing the phenomenon of solar flares with multi-wavelength eyes is necessary. Therefore in this thesis, we have carried out the investigation of solar flares employing multi-wavelength observations starting from X-rays to visible waveband over the electromagnetic spectrum. We probe X-ray waveband using the observations from Solar X-ray spectrometer (SOXS; Jain et al., 2005) and Reuven Ramaty High Energy Solar Spectroscopic Imager (RHESSI; Lin et al., 2002) missions. Emission in EUV wavebands is obtained from Atmospheric Imaging Assembly (AIA; Lemen et al., 2012) and photospheric magnetic-field observations by Heliospheric Magnetic Imager (HMI; Scherrer et al., 2012) onboard Solar Dynamic Observatory (SDO; Pesnell et al., 2012). We have also used photospheric line-of-sight magnetic-field observations from Michelson Doppler Imager (MDI; Scherrer et al., 1995) instrument onboard Solar and Heliospheric Observatory (SoHO; Domingo et al., 1995) mission and EUV observations from EUV Imaging Telescope (EIT; Delaboudinière et al., 1995) onboard SoHO and Transition Region and Corona Explorer (TRACE; Strong et al., 1994) mission for the flares occurred prior to SDO launch (i.e. February 2010). Filament dynamical and morphological evolutions have been studied by using high temporal and spatial resolution Hα observations from: (i) 15-cm Solar Tower Telescope installed in ARIES, Nainital, (ii) GONG Hα Network (GHN) which is consisted of multiple solar telescopes around the globe for uninterrupted observations, and (iii) recently installed 10-cm aperture Thaltej Solar Flare Telescope (TSFT) in Astronomy & Astrophysics Division, PRL. In the following sections, we present the brief descriptions of various instruments as well as data product specifications. As we have used the all observations available from archives of the aforesaid instruments, we will also present the post-processing technique employed for science outcomes of this thesis. We organize instrument description in this chapter in accord to the solar atmospheric layers. We first discuss the instruments used for observations of solar photospheric features then chromosphere and at the end we brief the instruments used for observation of emission originated from solar corona.

2.2 Instruments and Analysis techniques

2.2.1 Instruments for observing emission from photosphere

The study of the evolution of the physical observables from solar photosphere is essential to study the underlying energy release processes in solar flares. Photospheric magnetic-field, optical intensity, and sunspot evolutions are some of the major areas of observations of this part of solar atmosphere.

2.2.1.1 Michelson Doppler Imager (MDI) onboard SoHO and Helioseismic Magnetic Imager (HMI) onboard SDO missions

Magnetic non-potential fields are the source of various physical processes occurring in the flux tubes, coronal holes, flares and CMEs. Therefore, measurement of magnetic-field of the solar photospheric disk is of fundamental importance. Therefore, line-of-sight (LOS) magnetograms, used in this thesis, are taken from the Michelson Doppler Interferometer (MDI; Scherrer et al., 1995) onboard the SoHO (Domingo et al., 1995). MDI obtains high-resolution synoptic observations of full-disk LOS magnetic field every 96 minutes in narrow band centered around 6767.8 Å wavelength on a 1024×1024 CCD camera with 4 arcsec spatial resolution.

Key parameters of MDI observations are shown in Table 2.1. Calibrated level 1.8 MDI observations are archived from 1996 till 2008 at Stanford SOI project page[1] which are a-priori corrected for instrument artifacts such as dark current, flat field etc. The magnetograms are further corrected for foreshortening using `map_carrington.pro` procedure available in SolarSoftWare (SSW), a repository of algorithms developed in Interactive Data Language (IDL). More

[1] `http://soi.stanford.edu/data/`

Table 2.1: Key Parameters of MDI/SoHO and HMI/SDO

S. N.	Property	HMI/SDO	MDI/SoHO
1	Central wavelength	6173.3 ± 0.1 Å	6767.8 ± 0.2 Å
2	Filter bandwidth	76 m Å	94 m Å
3	Field of view	∼2000 arcsec	34 × 34 arcmin
4	Angular resolution	∼1.5 arcsec	
5	Spatial resolution	0.50 ± 0.01 arcsec	4 arcsec
6	Cadence	45 s	96 minute (synoptic)
			3 seconds (capability)

detailed description of SSW is given in Section 2.2.1.2 and at LMSAL SSW description page[2]. After April 2010, Helioseismic Magnetic Imager (HMI; Scherrer et al., 2012) instrument flown onboard Solar Dynamic Observatory SDO (Pesnell et al., 2012) has superseded observations from MDI/SoHO. HMI observes the full solar disk at 6173 Å with a spatial resolution of 1 arc-second. It consists of a refracting telescope, a polarization selector, an image stabilization system, a narrow band tunable filter and two 4096 × 4096 pixels CCD cameras with mechanical shutters and control electronics. Images are obtained in a sequence of tuning and polarizations at a 4-second cadence for each camera. One camera is dedicated to a 45s Doppler and line-of-sight magnetic-field component while the other to 90s vector magnetograms. All of the images are processed at the HMI/AIA Joint Science Operations Center and archived for science use from where we have obtained the observations of LOS magnetograms employed for investigation in this thesis. Table 2.1 shows the key parameters of MDI/SoHO and HMI/AIA. The study of magnetic-field evolution is made using HMI observation for the flares analyzed in this thesis which belong to SDO era of observation.

[2]http://www.lmsal.com/solarsoft/

2.2.1.2 SolarSoftWare(SSW)

SolarSoftWare (SSW) is an integrated package containing software libraries, instrument data bases and many other utilities which are necessary to analyze multi-wavelength observations obtained from various ground and space-based instruments. The SSW consists of Astronomical Libraries[3], analysis package for Yohkoh, SoHO, SDO and several other space and ground-based observatories. Detailed description of SSW can be found at LMSAL[4]. We have employed SSW repository to read, display, analyze and plot the evolution of various spatial, spectral and temporal characteristics of solar flares. The observations from most of the solar observatories are distributed in the form of universally accepted flexible image telemetry system (fits) format. FITS files are easily readable using fits library package provided in SSW. Several algorithms provided in SSW are used to display 2-D images, plot contours of multi-wavelength co-spatial flare emissions and make movies of ARs and flares. Additionally, we employ Object Spectral Executive (OSPEX) package provided in SSW to analyze spectral observations obtained from SOXS and HESSI missions (*cf.* section 2.2.3.1 and 2.2.3.2) in order to estimate flare plasma parameters. OSPEX is described in section 2.2.3.3.

2.2.2 Instruments for observing emission from chromosphere

Solar filaments, consist of cool plasma, are usually observed at chromospheric temperature. As solar filaments are one of the leading candidate understood as a trigger of the flare, the observations of solar chromosphere attained immense interest in solar physics community. We have used instruments described in this section for the topological and morphological study of filament evolution.

[3]http://idlastro.gsfc.nasa.gov/homepage.html

[4]http://www.lmsal.com/solarsoft/sswdoc/local_copy/references/crossroads.html

2.2.2.1 GONG Hα Network (GHN)

The Global Oscillation Network Group (GONG) is a program to understand the underlying physical processes occurring from solar interior to the solar atmosphere. A network of instruments around the world has been developed in GONG program to obtain un-interrupted observations of the Sun. Although GONG network was primarily designed to study solar interior through helioseismology and been operational since May 1995, GONG has started regular observation of the full disk Sun in Hα at six sites around the world starting from April 2010 (Harvey et al., 2011). Basically, the Hα system is an add-on facility to the normal GONG helioseismology instruments. These Hα observations provide a near real-time solar activity monitor. Images are collected with a time cadence of 1 minute on a 2k $\times$ 2k interline transfer CCD camera which are then corrected for dark, smear, and flat-field. These observations are then compressed and archived at NSO page[5] for solar physics community usage. Exposure times for observations are adjusted automatically in order to maintain the quiet disk center at 0.2 times that of full dynamic intensity range to avoid saturation during large flares.

2.2.2.2 Solar Tower Telescope (STT, ARIES/Nainital)

The Hα (λ=6563 Å) observations of some of the flare events analyzed in chapter 3 of this thesis have been made using a 15-cm f/15 Coude type refracting telescope mounted on a tower at ARIES, Nainital, India. The images from this telescope are recorded with a 512 $\times$ 512 pixel 16 bit frame transfer CCD camera. Solar tower telescope (STT) provides high-resolution AR observations with the spatial resolution of 0.6 arcsec per pixel and the temporal cadence is about 2 s (Uddin et al., 2012).

[5] http://halpha.nso.edu

2.2.2.3 Thaltej Solar Flare Telescope (TSFT)-PRL

We installed a 10-cm aperture refracting type telescope to observe full-disk chromosphere of the Sun. This facility is named Thaltej Solar Flare Telescope (TSFT) which is installed at roof-top of Astronomy & Astrophysics division building, PRL. Detailed description and specification of TSFT is given in Appendix-A of this thesis. This facility has been operational for synoptic observation of white-light Sun since April 2012. However, full-fledge Hα observations from TSFT started only since March 2013.

2.2.3 Instruments for observing emission from corona

The mean temperature of the solar corona is $\sim$2 MK, which however exceeds 10 MK during solar flares. The quiet corona emits UV, EUV and soft X-ray waveband but during solar flare, the emission is originated mainly in EUV, X-Ray and Radio waveband due to high-temperature nature of the emission. The study of processes of energy release in solar flares has been made employing X-ray observations from Solar X-ray Spectrometer (SOXS) and Reuven Ramaty High Energy Solar Spectroscopic Imager (RHESSI) missions. The SOXS and RHESSI observations have been used for the spatial, spectral and temporal evolution of X-ray sources. In this section, we describe the instruments employed for observing emission from corona.

2.2.3.1 SOLAR X-Ray Spectrometer (SOXS)

Solar X-ray Spectrometer (SOXS), the first space-borne solar astronomy experiment of India was launched onboard GSAT-2 spacecraft by GSLV-D2 rocket on 08 May 2003. The motivation of the SOXS mission is to improve our current understanding of the physical processes of energy release in solar flares in general and to detect the Fe and Fe/Ni line features as well as to measure the break energy between thermal and non-thermal components in particular. SOXS is comprised of two semiconductor detectors, viz. silicon PIN detector (area 11.56 mm^2) covering the energy range of 4-25 keV and, cadmium-zinc-telluride (CZT) detector (area 25 mm^2) operating in the 4-56 keV energy band. The spectral resolution provided by Si detector is ∼0.7 keV @ 6 keV and ∼0.8 keV @ 22.2 keV. However, the CZT detector provides a moderate energy resolution of ∼1.8 keV in its dynamic energy rage of observations in 4-56 keV. Therefore, these state-of-the-art solid state detectors in SOXS have superb sub-keV energy resolution capabilities and additionally, temporal resolution characteristics, make them most appropriate to investigate the energy transport and acceleration time scales of charged particles during solar flares. This section presents the details of the SOXS instrumentation and characteristics of the observations. For the investigation carried out in chapter 3 and 4 of this thesis, I have used observations from this mission.

Table 2.2: Special Features of the Si and CZT Detectors

1.	Si-PIN and CZT photodiode detectors
2.	Thermoelectric cooler (Peltier cooler)
3.	Cooled FET
4.	Temperature monitor
5.	Beryllium window
6.	Charge sensitive preamp
7.	Hermetic package (TO-8)
8.	Wide detection range
9.	Operation at near room temperature

The SOXS mission consists of four subsystems, *viz.* SOXS Low Energy Detector (SLED) package; SOXS Sun Tracking Mechanism (SSTM); and Front-end electronics which consist of SOXS Low Energy Processing Electronics (SLE) package; and SOXS Common Electronics (SCE) package. The payload, spacecraft and mission characteristics are presented in Table 2.2 and detailed description of the subsystems of SOXS is presented as follows.

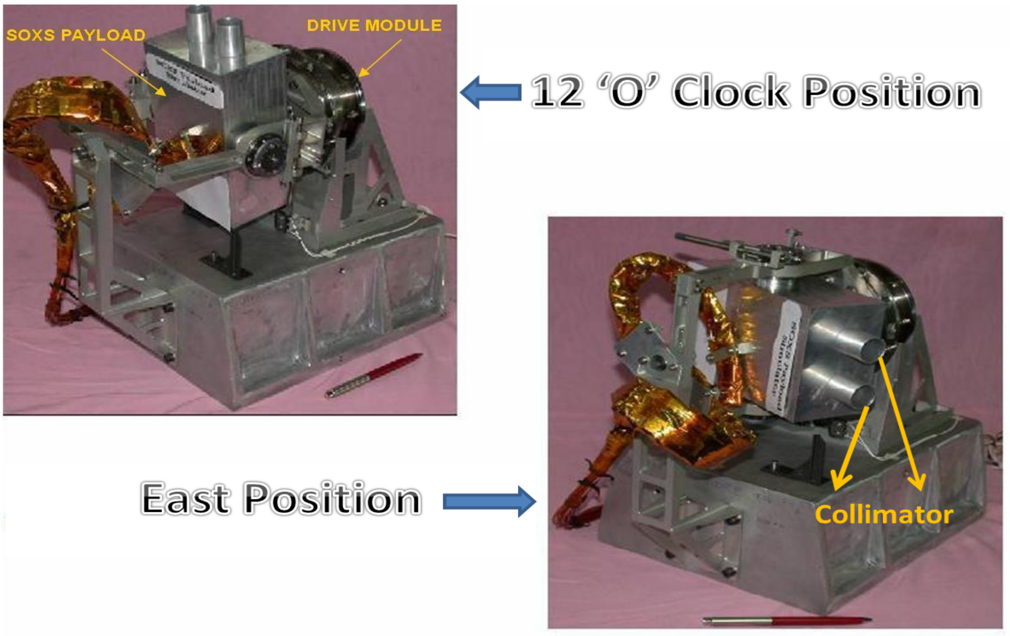

Figure 2.1: The detector package mounted on the SOXS Sun Tracking Mechanism (SSTM). The collimators are seen projecting outside. The FOV is 3.4°. The detector package moves in the line of sight of the Sun within an accuracy of about 0.1°. The SSTM has only one drive motor for correction in right ascension and declination.

2.2.3.1.1 The Solid-state Detectors : For the first time, the state-of-the-art solid state detectors made of viz. Si PIN-type and CZT mixed composition material semiconductor detectors have been used for a dedicated space-borne solar astronomy experiment namely SOXS mission. These high performance X-ray detectors are coupled with a charge sensitive preamplifier and thermoelectric cooler system in order to collect X-ray counts. The FET and the feedback circuits are also coupled with the detector system and positioned on the cooler. The package containing all the aforesaid components is kept approximately at -20°C which is monitored by an onboard internal temperature sensor. The detectors were developed at the Physical Research Laboratory using the hermetic TO-8 package from Amptek, USA. Special features of these detectors, which have been exploited to full potentiality to achieve the science

Table 2.3: Instrument Characteristics of SOXS/SLD

1a. Instrument characteristics :		
Detectors	**Si PIN**	**CZT**
Energy range	4 - 25 keV	4 - 60 keV
Energy resolution (FWHM)	$\sim$700 eV at 5.9 keV,	$\sim$1.5 keV at 5.9keV
	$\sim$ 900 eV at 22.2 keV.	$\sim$1.8 keV at 22.2keV
Temporal Resolution		
Flare	100 ms	100 ms
Quiet	1 s temporal,	1 s temporal,
	3 s spectral	3 s spectral
Field of view	full Sun ($\sim$3.4°)	full Sun ($\sim$3.4°)
Effective area	$\sim 10^{-4}$ cm^2 at 4 keV	$\sim 10^{-4}$ cm^2 at 4 keV
	$\sim 10^{-2}$ cm^2 at 10 keV	$\sim 10^{-1}$ cm^2 at 10 keV
Aspect system	Sun Tracking Mechanism;	Sun centered to $<$0.20
Mass	18 kg	
Power	20 watts	
Telemetry	8 kbps, downlink	
On-board storage	5 MB	
1b. Spacecraft characteristics		
Payload	SLD/SOXS, payload of opportunity	
Spacecraft	GSAT-2, communication satellite	
Orbit	Geostationary	
Altitude	36400 km	
Nominal mission lifetime	5 years	
1c. Mission characteristics		
Launch Date	8 May 2003	
Launch vehicle	GSLV-D2	

goals, are shown in Table 2.3. In Table 2.2 specifications and operating conditions of CZT and Si detectors are presented.

The exhaustive investigation for design, development and characterization of various kinds of Si and CZT detectors exists in the literature. Huber et al. (1995) and Desai et al. (1995) studied the response of high performance thermoelectrically cooled X-ray and gamma ray detectors. They fabricated compact Si and CZT detectors and explored their potentiality for high-resolution X-ray and gamma ray spectroscopy. The system used by them consists of a small cylindrical hybrid circuit including detector, FET and feedback components mounted on a small thermoelectric cooler. Huber et al. (1995) achieved energy resolution (FWHM) $\sim$250 and 350 eV at $\sim$5.9 keV for Si PIN and CZT detectors respectively under all ideal conditions and at operating temperature of -20°C. Later, a detailed response study of CZT detectors to explore them as future spectroscopic detectors for X-ray astronomy was undertaken in a big way by several investigators over the globe (Tousignant et al., 1997; Matteson et al., 1997; Kraft et al., 1998; Lachish, 1999). A detailed design and development study on the application of XR-100CR (Si PIN) and XR-100T-CZT (CZT) detectors from Amptek, USA for the proposed SLD (Soxs Low Energy Detector) payload was carried out by Jain et al. (2000). A prototype model of the detector package was designed and developed at Physical Research Laboratory (PRL), and thereafter characterization of the detectors was successfully carried out by Jain et al. (2000). Later, the flight model was fabricated at Space Application Centre (SAC) of Indian Space Research Organization (ISRO), Ahmedabad, India and pre-flight characterization was done at Dr. Satish Dhawan Space Launching Facility, of ISRO at Shriharikota, India as described in Jain et al. (2003).

Table 2.4: Specifications and Operating Conditions of SLED Characteristics

Characteristics	**CZT**	**Si PIN**
Material	Cadmium-Telluride crystal	N-type silicon wafer
Doping	zinc	P-type material
Size	5×5×2 mm	3.6×3.6×0.3 mm
Be window thickness	0.25 mm	0.025 mm
Energy Resolution	1.2 keV at 5.9 keV	500 eV at 5.9 keV
Dark counts	$< 5\times10^{-3}$ cts/s at 10 keV < E < 1 MeV	$<3\times10^{-3}$ cts/s at 2 keV < E < 150 keV
Preamps	Amptek model A250 with current divider	Amptek model A250 with current divider
Operating Voltage	300 - 400 volts DC	100 volts DC
Temp. Monitor Sensor	1 micro-A/°K	1 micro-A/°K
Operating Temperature	-30°C to -10°C	-30°C to -10°C
Sensitivity	0.73 mV/keV	1 mV/keV
Pedigree	never flown in space	flown on Mars Pathfinder
Pre-Amps Power	±8 volts at 25 mA	±8 volts at 25 mA
Detector Power	+ 400 volts at 1 micro-A	+100 volts at 1 micro-A
Cooler Power	2.1 volts at 0.7A	2.1 volts at 0.7A
Total Power	< 1 watt	< 1 watt

2.2.3.1.2 Collimator and Filter : In order to reduce the background/noise counts, Si and CZT detectors are kept occulted by 0.025 and 0.250 mm thick Beryllium (Be) sheet. Apart from this, as this Be sheet does not provide sufficient cover to the background counts produced at geostationary platform, a collimator and filter/attenuator were designed, fabricated at PRL and employed in order to achieve the S/N ratio >10.

The collimator is made of 1.8 mm thick nickel sandwiched between 1.8 and 3.4 mm thick aluminum tubes. The length of the collimator is 56 and 81.5 mm for Si and CZT detectors respectively which lead to the detector FOV to be 3.4°. It may be noted that angular span of the Sun is 0.50 and therefore detector package is capable of making a disk-integrated solar observations. As shown in Figure 2.1, the detector package is mounted on the SOXS Sun Tracking Mechanism (SSTM) system. A 0.080 mm thick aluminum filter plus 0.15 mm thick kapton polyamide film are mounted on the Be window of the detector. This combination is good enough to eliminate the X-rays below 4 keV (solar and cosmic) and electrons and protons up to 300 keV and 2 MeV respectively that fall directly in the line of sight of the FOV. This enabled us to achieve S/N ratio $\sim$100 in Si and $\sim$50 in CZT. However, due to the 2 mm thick CZT substrate higher noise counts are observed as a function of energy.

2.2.3.1.3 Response Matrix of the SOXS instrument : Response matrix R[i,j] is calculated by multiplying effect of resolution broadening matrix with photopeak response. The construction of the matrix is of the form R[i,j] where index j refers to the energy of the incident photon and the index i refers to the output energy channel. The values of R[i] for a given j are taken from a normalized Gaussian integration where the full width at half maximum (FWHM) is 0.7 keV (for Si) and the centroid is taken at the diagonal element of the square matrix. Further, photopeak response of the detectors is computed from the exposed geometric area through the collimator circle, the absorption from the Be, Al, and Kapton, and then the probability of single photon energy detection in Si and CZT. A correction to the photopeak efficiency was obtained by a second order fit of the detector efficiency data which included the Be window of 1 mil for Si and 10 mil for CZT detector. We therefore group the Be window with the detector and treat the Al and Kapton separately as absorbers. The effective area for Si and CZT detectors is derived using the following equations.

$$\mathrm{EA}_{\mathrm{Si,CZT}} = \exp(-\mu \mathrm{t})_{\mathrm{Al}}.\exp(-\mu \mathrm{t})_{\mathrm{Kp}}.[1 - \exp(-\mu \mathrm{t})_{\mathrm{Si,CZT}}.\exp(-\mu \mathrm{t})_{\mathrm{Be}}].\mathrm{GA}$$

Where μ is the Attenuation Coefficient for corresponding absorber, t is thickness (cm) and GA is geometrical area of the detector.

The aforesaid effective area calculations have been inbuilt in OSPEX/ SolarSoft package using `soxs_photopeak.pro` and `soxs_czt_photopeak.pro` programs for Si and CZT detectors respectively.

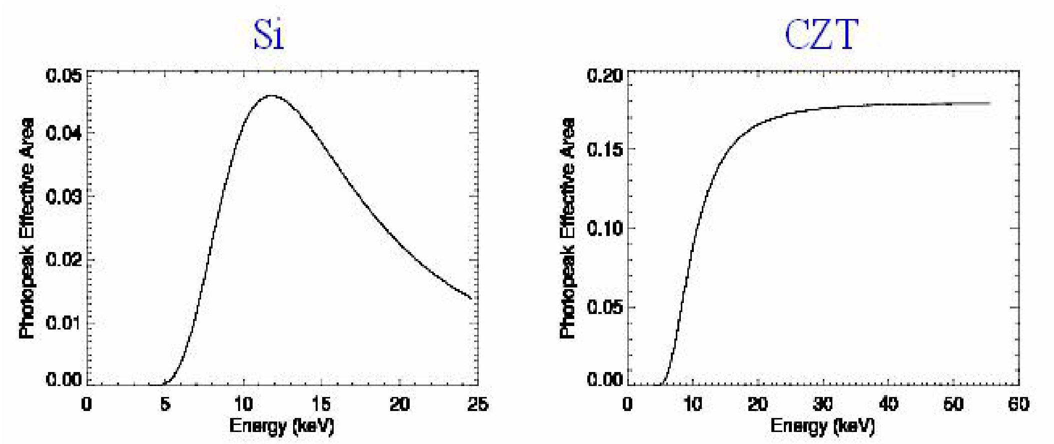

Figure 2.2: The effective area of the Si and CZT detectors of the SLED package. The Si and CZT have 0.025 and 0.25 mm Be windows respectively in front of the detector heads. Additional filters were mounted on the head to reject the background significantly.

Further, detector response is also available in SSW from the programmes *viz.* `soxs_drm.pro` and `soxs_czt_drm.pro` for Si and CZT detectors, respectively. The detector response matrix (DRM) is calculated by using the effective area and the energy resolution function which is a Gaussian resolution function with 2.0 keV (CZT) and 0.8 keV (Si) FWHM for all energies. Shown in Figure 2.2 (left and right) are the effective area for Si PIN and CZT detectors folded over the efficiency of the detector and considering the above design for filter. It may be noted that almost no contribution arrives from X-rays below 4 keV where the Sun remains bright even outside of flare conditions. The design details of collimator and filter may be found in Jain et al. (2003).

2.2.3.1.4 Onboard Radioactive Source : SOXS employs a radioactive source namely Cd^{109} (5 micro curies, half life time 412 days) for onboard calibration. The source emits lines at 22.2 and 25 keV, far from any line expected to occur in flare or in the detector's dynamic range by any varying background. The source is mounted inside the collimator in such a way so as to shine at direct the radiation on the center of the detector. The intensity of the calibration source is attenuated by 2 mm thick aluminum shield on the top of the source so as to reduce its intensity and hence the background during quiet Sun. The calibration is conducted in night time as well as in the day time in the line of sight of the Sun. Similarly, for in-flight calibration of CZT detector, the 25 keV line in addition to the 22.2 keV line is used. The 22.2 keV line from the radioactive source and the 6.7 keV line from Fe XXVI emission during solar flares enable to monitor any energy band shift over the dynamic range of the detector as well as the FWHM as a function of the period elapsed from the launch.

In Figure 2.3, the results of in-flight calibration taken on 05 June 2003 during spacecraft night time for the Si and CZT detectors are shown. It may be noted that the Si detector shows unambiguously 22.2 keV line arising from in-built Cd^{109} radioactive source. However, in the case of CZT we find shift of 14 channels as soon as we turn ON the thermo-electric cooler (TEC). This anomaly is due to grounding scheme adopted for CZT detector, and thereby it reveals both lines from Cd^{109} radioactive source at 22.2 keV and 25 keV shifted to 14 channels. In this view the dynamic energy range for CZT detector has been 4 keV to 56 keV instead of designed energy band of 4 - 60 keV.

2.2.3.1.5 Sun Aspect System SOXS Sun Tracking Mechanism (SSTM)

: The GSAT-2 is a communication satellite and SOXS is a payload of opportunity. The SOXS was mounted on the anti-earth view (AEV) side of the spacecraft enabling the payload to look at the Sun. However considering the limited FOV of 3.4°, an aspect system *viz.* SOXS Sun Tracking Mechanism (SSTM) was designed and developed at Spacecraft Mechanisms Group of ISRO Satellite Centre. The SSTM is unique in terms that it employs only a single drive module and keeps the Sun tracking in both right ascension and declination (Viswanatha et al., 2005). The SSTM consists of one stepper motor drive module with a gear reducer, and attached to it is a frame with the Declination Tilt Mechanism above which the detector package was mounted. The drive module (Figure 2.1) consists of a stepper motor and a pancake type harmonic drive gear reducer. The stepper motor is a two-piece motor, and Duplex pair of angular contract ball bearings fixes on the motor to the input shaft. The motor drives the input shaft in steps of 1°. The input shaft drives the harmonic drive. The fixed gear of the harmonic drive is fixed to the outer housing and the rotating dynamic gear is mounted on a four-point contact ball bearing and the output flange is fixed on the outer side. The gear reducer has 1:157 gear reductions.

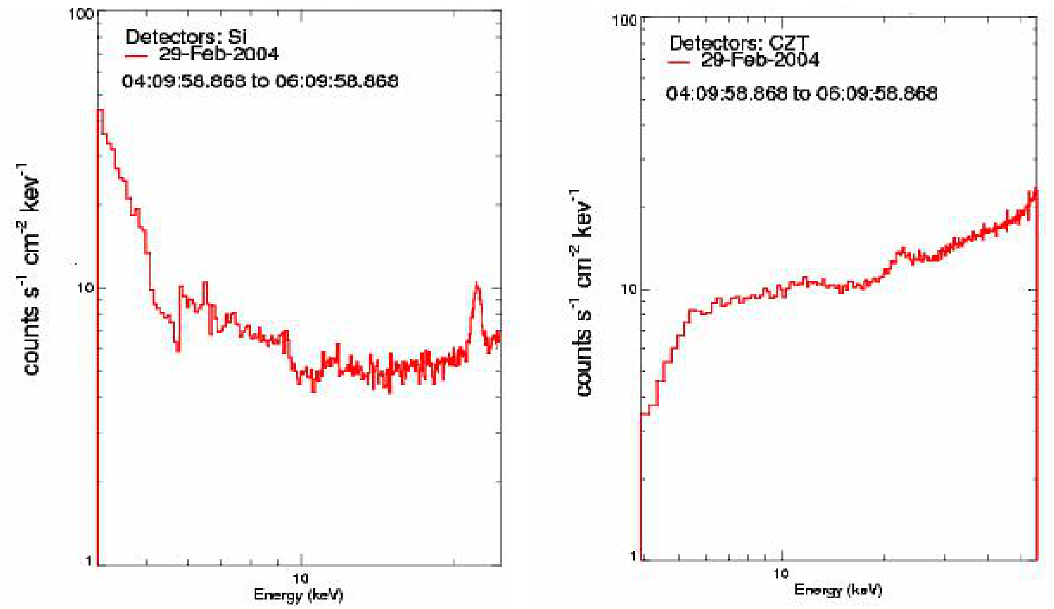

Figure 2.3: In-orbit calibration test of the Si and CZT detectors in left and right hand panels, respectively.

The output flange provides the interface for mounting the main frame. The motor used is SAGEM 35PP 81 04-03-01 redundant winding stepper motor of 1° step angle and the holding torque of 0.6 Nm and drive torque 0.4 Nm. The detailed design specifications may be found in the preliminary design review document prepared by Viswanatha et al. (2005). A Sun sensor is mounted on the payload (SLED) platform to indicate the Sun axis pointing error during payload operation. The sensor does not operate in a close-loop arrangement. The sensor's FOV is ±15° and the accuracy is 0.1° in two axes.

2.2.3.1.6 Electronics : SOXS Front-End Electronics (SFE) : The SOXS front-end electronics (SFE) aims to carry out the tasks of pulse shaping, pulse amplification, peak detection, and digital conversion of the input pulse train from the SLED package. In order to achieve these functions the front-end electronics package includes a linear pulse shaping amplifier, peak detectors, 8-bit ADC, energy window discriminators, telemetry interface for housekeeping (HK) parameters, temperature and corona (high voltage) autoshutoff circuits. It also classifies input energy into nine (four for Si and five for CZT detectors) predefined energy window counters for light curve (temporal mode) observations and flare detection logic. The power supply circuit converts regulated DC voltages from SOXS common electronics (SCE) into required DC voltages for SFE and SLED packages. The package is designed and developed to maintain and reveal detector characteristics viz. sub-keV spectral energy resolution and 100 msec temporal resolution.

Housekeeping parameters : System health is monitored at 1 kHz telemetry rate. 16 housekeeping (HK) parameters are monitored at every 16 s through LBT. These parameters provide the information such as detector temperatures, SFE DC-references and salient threshold voltages. Total events recorded in both detectors are also monitored by telemetry.

Detector Protection Circuits : SFE includes an auto-shut off circuit, which switches off the detector bias voltage as soon as the detector temperature falls out of operating temperature range of -5°C to -30°C so as to protect the detectors from thermal break down. Corona auto-shut off circuit switches off the detector bias when the bias current increases to 50% above the normal value.

Detector Processing Electronics : Detector processing electronics aims to read digital information from the SFE store into onboard memory and upload it to the ground station. The whole data processing electronics are integrated into this package. It consists of 16-bit window counters, ADC interface, and real-time pulse height analysis (PHA) circuits for Si and CZT detectors, 5 MB onboard memory to store flare and HK data, on board timer (OBT) and telemetry-telecommand interfaces. This package was designed and developed at Space Astronomy and Instrumentation Division of ISRO Satellite Centre (ISAC), Bangalore. Onboard 16-bit CPU controls all operations of the processing electronics. The SLD current operating mode is programmable via telecommand. SLD has following operating modes:

- Search, quiet and flare integrated mode.
- Survey/background mode (100 ms and 1 s).
- Memory and electronics checkout mode.
- Readout mode. Search mode is normal operating mode. In this mode a search is going on for flare onset and quiet phase.

Survey mode has been used to study the level of background noise of the quiet Sun. This helps to estimate correct thresholds for flare detection. Memory checkout and read out modes are usable for onboard diagnosis.

2.2.3.1.7 Flare Triggering Logic : The detector operation/observing logic is as follows:

(a) The Survey Mode observes preflare background in the line-of-sight of the Sun and thereby the threshold flux for flare trigger can be determined precisely. However, this default threshold can be modified as and when required through telecommand. This selected threshold flux is equal to 5σ, where σ is measured preflare background during the quiet Sun condition. After completion of Survey Mode during 5-7 June 2003 two default energy windows 10-20 keV for Si and 20-30 keV for CZT detectors were chosen respectively for flare trigger logic. However, out of nine energy windows any two may be selected for flare detection through telecommand.

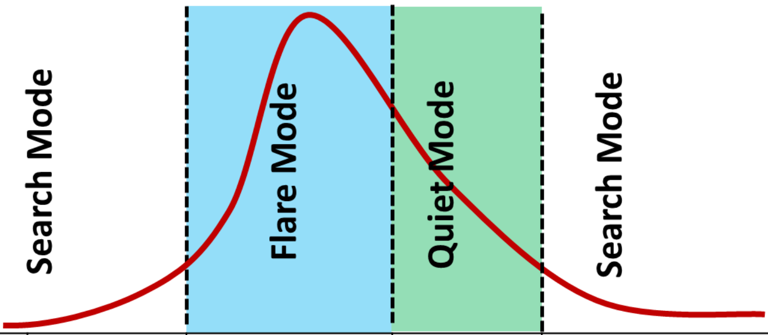

Temporal	1 Sec	100 msec	1 Sec	1 Sec
Spectral	3 Sec	100 msec	3 Sec	3 Sec

Figure 2.4: The operation logic of the SLD payload. The temporal resolution during flare mode is 100 ms.

(b) As shown in Figure 2.4 during normal observing mode, i.e., Search Mode, the observations in these energy window counters (temporal data) are made always at a cadence of 100 ms but recorded at every 1 s.

(c) The Search Mode will turn into flare Mode as soon as five consecutive 100 ms observations in any one out of the two energy windows show the flux threshold that is set in these windows.

(d) The Flare Mode, however, lasts only for 287.5 s, as shown in Figure 2.4, with a temporal resolution of 100 ms for energy windows (temporal) and PHA (spectral). After 287.5 s the logic returns to Quiet Mode, which continues for 2274 s and observations are made at a cadence of 1 and 3 s in windows and PHA respectively irrespective of new flare occurrence during this period. This design is carried out in context to limited on-board memory and telemetry rate as well as keeping in mind the most interesting period for high time resolution observations during the flare is first 5 min. After completion of quiet mode the logic returns to search mode automatically. Both Si and CZT detectors are competent to observe soft and hard X-ray micro flares.

2.2.3.1.8 SOXS Common Electronics (SCE) : The SOXS common electronics (SCE) is truly common for both low energy and high-energy payloads. SCE package provides common interface to all SOXS packages with spacecraft (S/C) bus. It minimizes the chance of damage to the mainframe bus because of any anomaly in the packages. SCE consists of low voltage DC/DC converters, high current ART converters, power electronics, telemetry/telecommand interfaces, base-band data encoder, convolution encoder, pre-modulation filter, Sun sensor and SOXS Sun tracking mechanism (SSTM) drive electronics. This package is also designed and developed at Space Astronomy and Instrumentation Division of ISAC, Bangalore (Sharma et al., 2000).

The SOXS instrument, experimental techniques, and observations are discussed in more detail in Jain et al. (2005). SOXS observations are archived at SOXS data warehouse[6]. These observations are analyzed with the help of OSPEX (Object Spectral Executive) software package inside SolarSoft as discussed in section 2.2.3.3 in order to estimate flare plasma parameters.

2.2.3.2 Reuven Ramaty High Energy Spectral Imager (RHESSI)

The Reuven Ramaty High-Energy Solar Spectroscopic Imager (RHESSI) was designed to investigate particle acceleration and energy release in solar flares, through high resolution imaging and spectroscopy of hard X-ray/gamma-ray continua emitted by energetic electrons, and of gamma-ray lines produced by energetic ions. RHESSI satellite was launched on 5th February 2002 in the series of NASA small explorer mission (Lin et al., 2002) into a nearly-circular, 38° inclination, and low-Earth orbit, and began observations a week later. As of today, it continues to successfully operating with similar observing capabilities as at launch. RHESSI is a solar-pointed spinning spacecraft with a nominal rotation period of ∼4 sec. The detailed mission overview is discussed in this section. Detailed instrument and data characteristics are provided in Lin et al. (2002).

[6] `http://www.prl.res.in/~soxs-data/DataHome.php`

RHESSI satellite facilitates the imaging as well as spectroscopy of X-ray emission from solar flares. RHESSI observations are archived at RHESSI data warehouse[7]. These observations are analyzed with the help of SSW in order to estimate the flare plasma parameters viz. temperature, emission measure and spectral power-law index etc. The spatial evolution of X-ray sources is studied by synthesizing X-ray images of flaring region with the help of image reconstruction algorithms *viz.* PIXON, CLEAN, etc. as discussed subsequently. In this thesis, we have used PIXON and/or CLEAN algorithms for synthesizing X-ray images presented in Chapter-3. In the following section, we provide a brief overview of RHESSI spectrometers.

2.2.3.2.1 RHESSI Imager : The Imaging Telescope Assembly onboard RHESSI consists of the telescope tube, grid trays, Solar Aspect System (SAS), and Roll Angle System (RAS). RHESSI uses nine Rotating Modulation Collimators (RMCs) for imaging, each consisting of a pair of grids mounted on the rotating spacecraft. Figure 2.5 shows a schematic representation of a set of nine double-grid sub-collimators, each consisting of a pair of widely separated grids in front of a corresponding X-ray/gamma-ray detector. Each collimator grid is made of a plane array of equi-spaced X-ray-opaque slats separated by transparent slits. Within each subcollimator, the slits of the two grids are parallel and their pitches are identical. The nominal parameters of the RHESSI grids are listed in Table 2.5. As shown in Figure 2.5, the transmission through the grid pair varies as a function of the direction of the incident X-ray photon as well as the axis of rotation of the imaging assembly. Thus, as the direction of incidence is changed as a function of time, the resultant transmission of the grid pair is modulated in time. Therefore, the X-ray images are synthesized with the help of the time-modulate count rates collected separately with all the nine detectors. With this assembly employed for imaging X-ray sources, RHESSI provides spatial resolution of 2 arcsec at X-ray energies from ∼4 keV

[7] `http://hesperia.gsfc.nasa.gov/hessidata/`

Table 2.5: Grid parameters of RHESSI mission (Hurford et al., 2002)

Subcollimator number	1	2	3	4	5	6	7	8	9
Pitch (mm)	0.034	0.059	0.102	0.177	0.306	0.530	0.918	1.590	2.754
slit width (mm)	0.020	0.035	0.061	0.106	0.184	0.318	0.477	0.811	1.487
FWHM (arc sec)	2.26	3.92	6.79	11.76	20.36	35.27	61.08	105.8	183.2
Max. transmission	0.60	0.60	0.60	0.60	0.60	0.60	0.52	0.51	0.54
Grid thickness (mm)	1.2	2.1	3.6	6.2	10.7	18.6	6.2	6.2	30.0
Slat material	Mo	W	W	W	W	W	W	W	W
Field of view (deg)	1.0	1.0	1.0	1.0	1.0	1.0	4.4	7.5	2.8

to ∼100 keV, and 7 arcsec upto ∼400 keV.

2.2.3.2.2 Image reconstruction algorithms for RHESSI observations : RHESSI data is collected in such a way so as to enable us to extract the spatial information in the form of source location, size and morphology from the non-imaging detectors. The Fourier-transformation is the technique which is employed to the RHESSI time and energy tagged observations available from the nine rotating collimators with angular period 4 s. As the time modulation of the incident flux is the function of the location, size, and intensity of the X-ray source, different Fourier components represent the source angular morphology. Seven image reconstruction algorithms are available in the RHESSI software which models the spatial distribution of photons by employing the observed modulated time profiles, spacecraft roll position as well as pointing. We briefly discuss the algorithms employed on RHESSI observation for X-ray image synthesis in this thesis as following. Complete description of the image synthesis algorithms is given at RHESSI homepage[8].

[8] `http://hesperia.gsfc.nasa.gov/rhessi2/home/software/imaging-software /image-algorithm-summary/`

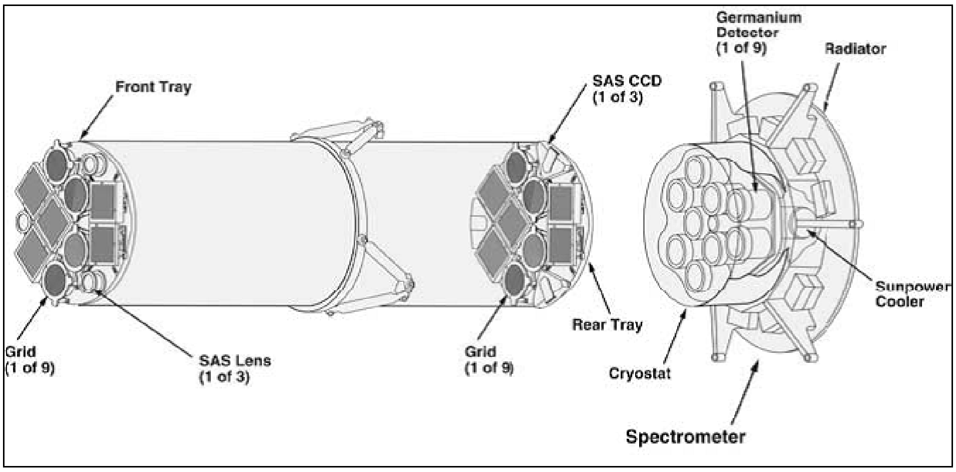

Figure 2.5: Schematics of the RHESSI imager-cum-spectrometer. The principal components are two identical sets of nine grids mounted on front and rear grid trays. A corresponding set of nine cooled germanium detectors is mounted behind the rear grids. The solar aspect system (SAS) consists of three lenses mounted on the front grid tray which focus optical images onto SAS CCDs on the rear grid tray.

1. **Back-projection:** The most basic approach is to synthesize 'back projection' algorithm (Mertz, 1986). In this method, a 2D inverse Fourier transformation of the input RHESSI data is performed (Kilner and Nakano, 1989). This technique is developed from the idea of the Fourier transform of the radio observations, also termed as visibility which enables the synthesis of dirty map which gives an ab-initio-approximation of the source morphology. Back projection can be best explained by mathematical explanation. In this, modulation patterns are estimated for various position of the source and then these are added over time bins and pixels over which the image is to be synthesized. Further, flat-fielding is an essential step of this method which enables in modulating the sensitivity of each pixel of the image to be proportional to respective variance of the modulation profile. Numerical recipes for both of the aforesaid steps involved in this method are developed by Durouchoux et al. (1983). Thus, the intensity I_m of each pixel (m) in the back-projection map is defined by the following linear combination of the observed count rates Ci

$$I_m = \frac{1}{A} \sum_{i=1}^{N} [c_i/\Delta t_i] P_{im}$$

Here A is the effective area (cm^2) of the detector and Δt is the time-bin duration (s). The normalization by A is performed in such a way so as to keep the expectation value at the peak of the dirty map equal to the maximum intensity of the source. This dirty map is employed as an input to the other algorithms as discussed below.

2. **Clean:** Clean algorithm was originally developed for image synthesis in radio astronomy. It employs iterative process for synthesis of images with the assumption that an image can be decomposed as a superposition of contributions from multiple point sources (Hogbom and Brouw, 1974). In this method, the observed dirty map is postulated to convolution of a multiple point sources with the instrument Point Spread Function (PSF). With this PSF convolution, a cleaned image as well as a residual image is synthesized. Followed to this, iteratively the image is cleaned until either the number of iteration exceeds its limit or residual map leads to negative maximum. Further, this method is performed in the polar coordinates and the resultant image is converted into the rectangular coordinates for further use.

3. **PIXON:** The Pixon method is another method which is employed extensively for image synthesis from RHESSI observations. As we know that the dirty map synthesized by back-projection technique has spurious side lobes of the image. PIXON is employed to remove these side lobe patterns. In this regard, this method synthesizes a model for the image consistent with the data with the help of least χ^2 fitting. The model is constrained by the observation and therefore possesses reliability in the output parameters (Metcalf et al., 1996). A model is chosen from the family of multi-resolution basis functions (Pixons) which statistically fits the data.

In this thesis, we have used the aforesaid algorithms for the synthesis of X-ray images. In addition to the above algorithms, many other algorithms are supported for image synthesis namely maximum entropy method (Sato et al., 1999), Forward-fitting (Aschwanden, 2002) and UV smoothing (Masson et al., 2009).

2.2.3.2.3 RHESSI Spectrometer : The RHESSI spectrometer package is composed of nine cryogenically cooled coaxial germanium detectors (GeD) (Smith et al., 2002). A cutaway of the Spectrometer showing the numbered location of the germanium detectors is presented in Figure 2.6. The very important fact about the super-cooled ultra-pure germanium at cryogenic temperatures is that no electron-hole pairs in the conduction band is produced other than when a hard X-ray or gamma-ray photon interacts in the crystal which enables the release of many energetic electrons which create free pairs. If there is a high electric field ($\sim$1000 V cm^{-1}) across the crystal, the electrons and holes will be pulled to each electrode, creating a current pulse that can be amplified and digitized by suitable electronics.

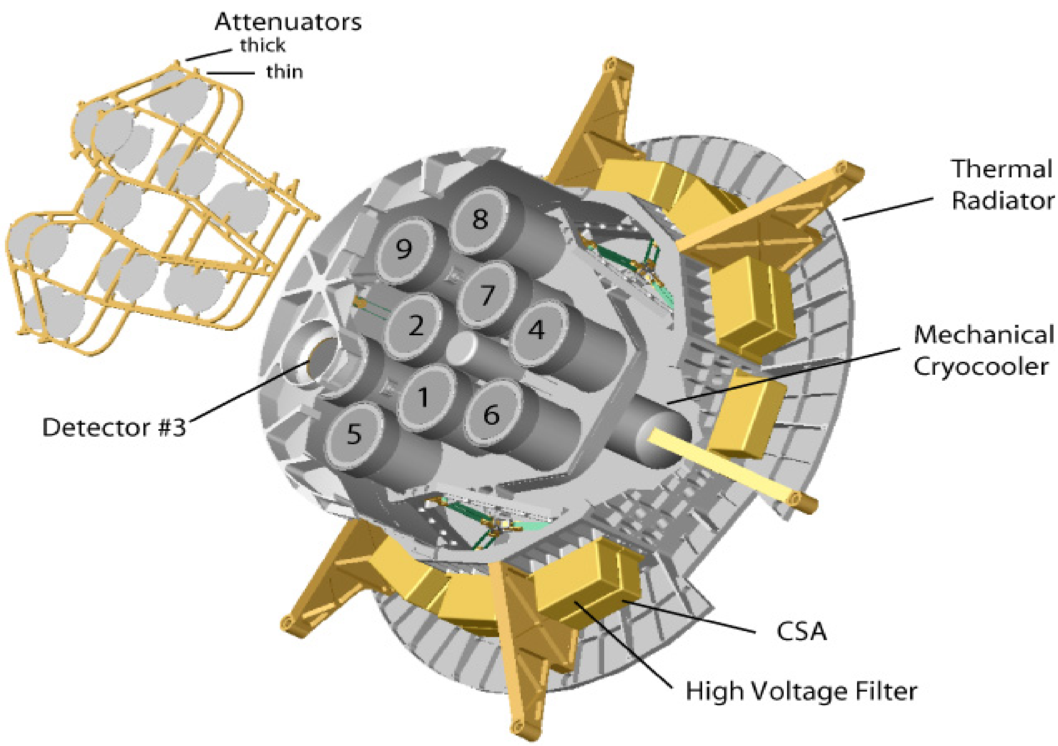

Figure 2.6: A cutaway of the Spectrometer showing the location of the germanium detectors (by number). (Lin et al., 2002).

Figure 2.6 shows schematics of detector package of RHESSI. A special arrangement of the electrodes and the field lines allows a single germanium detector to be operated as two segments, a front segment and a rear segment. X-rays (primarily below ~200 keV) have shallow penetration in Ge and are measured primarily in the front segment, while higher-energy gamma rays penetrate more deeply and are measured in the rear segment. RHESSI spectrometer is uniquely designed for achieving high-spectral resolution which allows for the accurate measurement of even extremely steep power-law spectra. Energy resolution of the front detectors is about 1 keV (for 3-100 keV). For the rear detectors, it is around 3 keV (for higher energies up to 17 MeV). Photons from 3 keV to 17 MeV can be detected.

2.2.3.2.4 Attenuators : RHESSI employs attenuators during the flare to avoid saturation. As we may note from Figure 2.6 that two light weight movable frames are placed on the top of each of the nice nine germanium detectors, each holding nine aluminum discs - thin and thick attenuators. As the flare emission is dominated by lower-energy photons, attenuating the SXR flux reduces detector dead time and pulse pileup, maintaining accurate spectroscopy for higher-energy photons above $\sim$ 6 keV even during periods with high incident SXR fluxes. The centers of the attenuators are made thinner to preserve some low-energy response - the transmitted flux is reduced by 1/e below $\sim$15 and $\sim$25 keV for the thin and thick attenuators, respectively. Consequently, the detector resolution below $\sim$10 keV is improved in attenuator states A1 and A3 (to $\sim$0.75 keV FWHM, compared to $\sim$1 keV nominally), as the low-energy photons are then detected only at the center of the GeDs, where the electric fields are strongest, charge travel distance is smallest, and charge collection is fastest. Although all attenuators of a given type (thin or thick) move together, the thin and thick attenuators can be inserted independently. In practice, only three of four modes are used, in order of increasing attenuation: A0 no attenuators (when both sets of attenuators are held out of the detector lines of sight to the Sun); A1 thin attenuators only (when the X-ray counting rate from a flare increases above a prescribed level); and A3 thin and thick attenuators engaged (if the emission increases still further to another prescribed count rate level). The on-board computer automatically engages the appropriate attenuators as the detector-averaged live time drops below specified thresholds ($\sim$92% for A0, $\sim$90% for A1). When the live time remains above 99% for $\sim$4 minutes, the most recent attenuator is disengaged. If the unattenuated rates are still sufficiently high so that the live time falls below the threshold, the attenuator is reinserted, and the process repeats; the data collected during these successive attenuator changes is generally omitted during spectral analysis.

2.2.3.3 Object Spectral Executive (OSPEX)

We use the OSPEX (Object Spectral Executive) software package inside SSW to analyze the X-ray data. The OSPEX is an object-oriented interface for X-ray spectral analysis of solar data. It is the next generation of SPEX (Spectral Executive) written by R. Schwartz in 1995. OSPEX enables us to read and display the input data (from SOXS and RHESSI) and to select and subtract background. OSPEX also enables us to make time-binned X-ray spectra and to select time intervals of interest. The selected spectrum is then described by employing a combination of photon flux model components which uses forward fitting of those components to the spectrum. During the fitting process, the instrument response matrix is used to convert the photon model to the model counts to compare with the input count data. The OSPEX subroutines have been updated to undertake detailed temporal and spectral data analysis of Si and CZT detectors of SLD/SOXS mission. The raw data for spectral mode SOXS observations was first corrected for any spurious or false flare as well as for pre-flare background. For the analysis of observations from SOXS, response matrix is in-built in the OSPEX package. On the other hand, for RHESSI observations, spectral response matrix (SRM) from the X-ray observations is synthesized using HESSI graphical user interface package provided in SSW a-prior to the spectral analysis. This SRM files serve as input with spectrum to the object spectral executive (OSPEX) package for estimation of flare plasma parameters. In each time-bin, OSPEX enables us to estimate the T, EM, power-law index by forward-fitting the observed count spectra with the model count spectra generated by the in-built model functions viz. thermal, line emission, multi-thermal, and non-thermal functions which use CHIANTI database (Dere et al., 1997; Landi et al., 2012). The resulting time-ordered fit parameters are stored and can be displayed and analyzed with OSPEX. The entire OSPEX session can also be saved in the form of a script and the fit results are stored in the form of a FITS file.

2.2.3.4 GOES

We use the X-ray observations provided by Geostationary Operational Environmental Satellites (GOES) for the investigation of temporal evolution of flare. GOES has been developed for National Oceanic and Atmospheric Administration (NOAA) by the National Aeronautics and Space Administration (NASA). It measures solar radiation in the X-ray and EUV region and the in-situ magnetic field and energetic particle environment at geosynchronous orbit, providing real-time data to the NOAA Space Weather Prediction Center (SWPC). GOES satellites provide un-interrupted observations of the Sun and therefore extensively used for temporal evolution studies in solar flare X-ray emission. The Space Environment Monitor (SEM) subsystem onboard GOES consists of four instruments: An energetic particles sensor (EPS), high energy proton and alpha detector (HEPAD), X-ray sensor (XRS) and two redundant three-axis magnetometers. HEPAD monitors the incident flux density of protons, alpha particles, and electrons over an extensive range of energy levels. XRS monitors the X-ray emission from the solar atmosphere. Two redundant three-axis magnetometers operate one at a time to monitor earths geomagnetic field strength in the vicinity of the spacecraft. The SEM instruments are capable of ground command-selectable, in-flight calibration for monitoring on-orbit performance and ensuring proper operation.

2.2.3.5 Transition region coronal explorer (TRACE)

TRACE mission (Strong et al., 1994) was designed to observe corona with unprecedented high spatial resolution of $\sim$1" (with 0.5"/pixel size). The TRACE telescope was launched in April 1998 and remained operational till April 2010 after which its successor, SDO mission has become fully operational. It consists of a 30-cm Cassegrain type telescope with a field of view (FOV) of 8.5 $\times$ 8.5 arc minutes. TRACE used to provide images in three coronal EUV wavelengths (171 Å, 195 Å and 284 Å) and also covered other wavelengths viz. 1216 Å, 1550 Å, UV continuum (1600 Å), and white light (5000 Å). These wavelengths were aimed to observe the evolution of features in the solar atmosphere with the temperatures from 6000 K to 10 MK. We have used TRACE observations for studying precursor phase emission from solar flares as presented in Chapter-3 as well as to visualize the evolution of flare-CME system as presented in Chapter-5.

2.2.3.6 Atmospheric Imaging Assembly (AIA)

The Atmospheric Imaging Assembly (AIA; Lemen et al., 2012) onboard the Solar Dynamics Observatory (SDO; Pesnell et al., 2012) is designed to observe solar atmosphere in high-resolution through multi-wavelength window and launched on 11 February 2010. AIA records images with FOV of 1.3 solar diameters in multiple wavelengths nearly simultaneously with the help of 4096 $\times$ 4096 detectors, at a resolution of $\sim$1 arcsec and at a temporal cadence as good as 12 s. AIA consists of four telescopes which are used to observe Sun in seven extreme ultraviolet (EUV) narrow band band passes centered on specific lines: Fe XVIII (94 Å), Fe VIII,XXI (131 Å), Fe IX (171 Å), Fe XII,XXIV (193 Å), Fe XIV (211 Å), He II (304 Å), and Fe XVI (335 Å). In addition to the aforesaid lines, One telescope simultaneously observes the Sun in two UV lines viz. C IV (1600 Å) and in the continuum (1700 Å). Further to this, it also records white light Sun in order to enable co-alignment with images from other telescopes. The temperature diagnostics of the EUV emissions cover the range from 6×10^4 K to 2×10^7 K. We have used the EUV/UV observations from AIA instrument in chapter-3 in order to quantify the spatial evolution of flare plasma in various temperatures. Further to this, the EUV channels of AIA possess the capability of estimating temperature and emission measure of the active-region and full-disk Sun with unprecedented spatial and temporal resolution as discussed in the following section.

2.2.3.7 Automated technique for synthesis of temperature and emission measure 2D map

In this section, we discuss the technique established by Aschwanden et al. (2013) for estimation of plasma parameters using the AIA data, recorded in six coronal temperature wavelengths viz. Fe XVIII (94 Å), Fe VIII,XXI (131 Å), Fe IX (171 Å), Fe XII,XXIV (193 Å), Fe XIV (211 Å), and Fe XVI (335 Å), covering the temperature range from 0.6 - 10 MK (Nitta et al., 2013). The analysis tools employed in this technique are developed in IDL with the use of routines available in SSW. This technique enables us to retrieve physical parameters viz. DEM distributions, electron temperatures, and electron densities, for solar active regions and coronal loops, as well as some geometric parameters of coronal loops.

In order to synthesize T and EM maps from this technique involves several steps. First step is a perfect ($\sim$ 0.5 pixel) alignment between the images in different wavelengths. The coalignment of AIA images in the aforesaid six EUV channels is carried out by fitting limbs of the Sun in various wavelengths. Generally, the solar limb in EUV wavelength appears a few thousand kilometers above the photospheric altitude level, which amounts to $\sim$ 5-10 AIA pixels. Therefore, the coalignment accuracy is verified using the EUV limb offset to the optical limb. This co-aligned set of images is used for the synthesis of T and EM maps. As the observed EUV intensities at a particular pixel F_λ[x, y] (in the units of data number per second DN S^{-1} pix^{-1})are related to the EM[x,y] through the following equation,

$$\mathrm{F}_\lambda(\mathrm{x},\mathrm{y}) = \int \frac{\mathrm{dEM}(\mathrm{T},\mathrm{x},\mathrm{y})}{\mathrm{dT}} \mathrm{R}_\lambda(\mathrm{T})\mathrm{dT}$$

where $\mathrm{R}_\lambda(T)$ is the filter response matrix. As this technique employs the set of EUV intensities of particular pixel, the above equation when ran over the pixels of interest produce the DEM distribution map. Thus the estimated differential emission measure distribution from the aforesaid equation is employed in synthesizing the T-map by employing following equation.

$$\frac{\mathrm{DEM}(\mathrm{T},\mathrm{x},\mathrm{y})}{\mathrm{dT}} = \mathrm{EM_p}(\mathrm{x},\mathrm{y})\mathrm{exp}(-\frac{[\log(\mathrm{T}) - \log(\mathrm{T_p}(\mathrm{x},\mathrm{y}))]^2}{2\sigma_{\mathrm{T}}^2(\mathrm{x},\mathrm{y})})$$

where σ_T is the width of the Gaussian function employed to fit the array of DEMs. Synthesized T and EM map using the aforesaid technique is used in chapter-3 of this thesis to visualize the effect of heating on the filament.

We acknowledge the scientific teams of the mission and instruments for providing the observations. Employing the multi-wavelength observations from aforesaid instruments, the underlying physical processes of energy release in solar flares are studied as presented in this thesis.

Chapter 3

Multi-wavelength Diagnostics of the Precursor and Main phases of Solar Flares

3.1 Introduction

The "standard model" of energy release in solar flares suggests the acceleration of the charged particles (mostly electrons) following to the reconnection of the overlying magnetic field lines. These accelerated electrons lose most of their energy through Coulomb collisions in the chromosphere and emit thick-target hard X-rays (HXRs) (In detail: Chapter 1). As a consequence, the chromosphere is heated up, which enhances the local pressure and thereby drives the heated plasma up into the coronal loops which appear in the form of soft X-rays (SXRs) as a result of thermal bremsstrahlung within the loop plasma. Following this mechanism, non-thermal emission (mostly in HXR energy band) must precede or at least accompany the SXR thermal emission (Jain et al., 2000, 2005, 2011a; Shibata and Yokoyama, 2001; Shibata and Magara, 2011), which, however, has not been observed. On the contrary, in most of flares observations, a low energy and slow rising soft X-ray (SXR) component has been found at the onset of the flare and preceding the HXR component. Markeev et al. (1983) showed the appearance of a pre-maximum phase a few minutes before the impulsive phase, termed later as precursor phase and studied by several authors e.g. Fárník and Savy (1998), Veronig et al. (2002), Battaglia et al. (2009), Falewicz et al. (2011), Awasthi and Jain (2011), Altyntsev et al. (2012).

Based on multi-wavelength observations, the time evolution of a solar flare has been categorized into three phases *viz.* precursor, impulsive and gradual. Figure 3.1 shows the precursor phase emission in multi-wavelength observations during the flare event of April 22, 2011.

Though, the impulsive and gradual phases (together termed as main phase) of solar flares have been studied in greater detail, the underlying processes of energy release in the precursor phase and their relation to the main phase have not been fully established owing to lack of high spatial, spectral and temporal resolution observations during the precursor phase. Further, the physical processes occurring during the precursor phase emission do not form a part of the standard model of energy release in solar flares (Shibata, 1999; Shibata and Magara, 2011) and therefore leaves a missing link in the understanding of energy release processes during this phase. The aim of the study presented in this chapter is to understand the energy release process in the precursor phase and its association with the main phase.

The precursors to the flare are identified based on the disk integrated X-ray emission (Fárník and Savy, 1998). The precursor phase study with spatially resolved observations has revealed interesting insights on the physical processes occurring during this phase and their relation to the main phase. From the spectral analysis of X-ray emission during the precursor phase, Battaglia et al. (2009) found that the precursor emission is of thermal origin and suggested that chromospheric evaporation during this phase is occurring due to the conduction driven saturated heat flux. On the contrary, Altyntsev et al. (2012), in their study of precursor events used microwave observations and found the evidences of non-thermal electrons during this phase even though the HXR emission was found absent. They suggested microwave observations to be better proxy of non-thermal processes during solar flares than the HXRs. Falewicz et al. (2011) found that the energy required to produce precursor SXR emission can be completely derived from the energy available with non-thermal electrons while discarding the need of any other heating mechanism. However, their analysis is constrained to a single loop model. Therefore, currently, different schools of thoughts are being proposed to explain the origin of precursor phase emission. Further, in search of a driver of the instability during the precursor phase, Chifor et al. (2006, 2007) have found slow-rise of the filament that temporally and spatially associated with the precursor brightening (Joshi et al., 2011). Therefore, the origin of precursor phase and its relation to the main phase has been an open issue demanding the need of a quantitative study employing multi-wavelength observations to address the issues of its energy characteristics *viz.* thermal and/ or non-thermal and the triggering mechanism.

During a typical solar flare energy release, both the thermal and non-thermal emissions are usually observed (Jain et al., 2000, 2005). The non-thermal emission is an indication of the particle acceleration, while the thermal emission is a signature of chromospheric heating produced either by non-thermal charge particle beam-driven or by conduction-driven plasma (Fisher et al., 1985; Fisher, 1989; Brosius and Holman, 2012). Nishio et al. (1994), in their study of thermal and non-thermal energetics of solar flare using radio and soft X-ray observations found that the heated plasma observed during the impulsive and gradual phases can only be maintained from continuous bombardment of accelerated charge particles for $\sim$1000s.

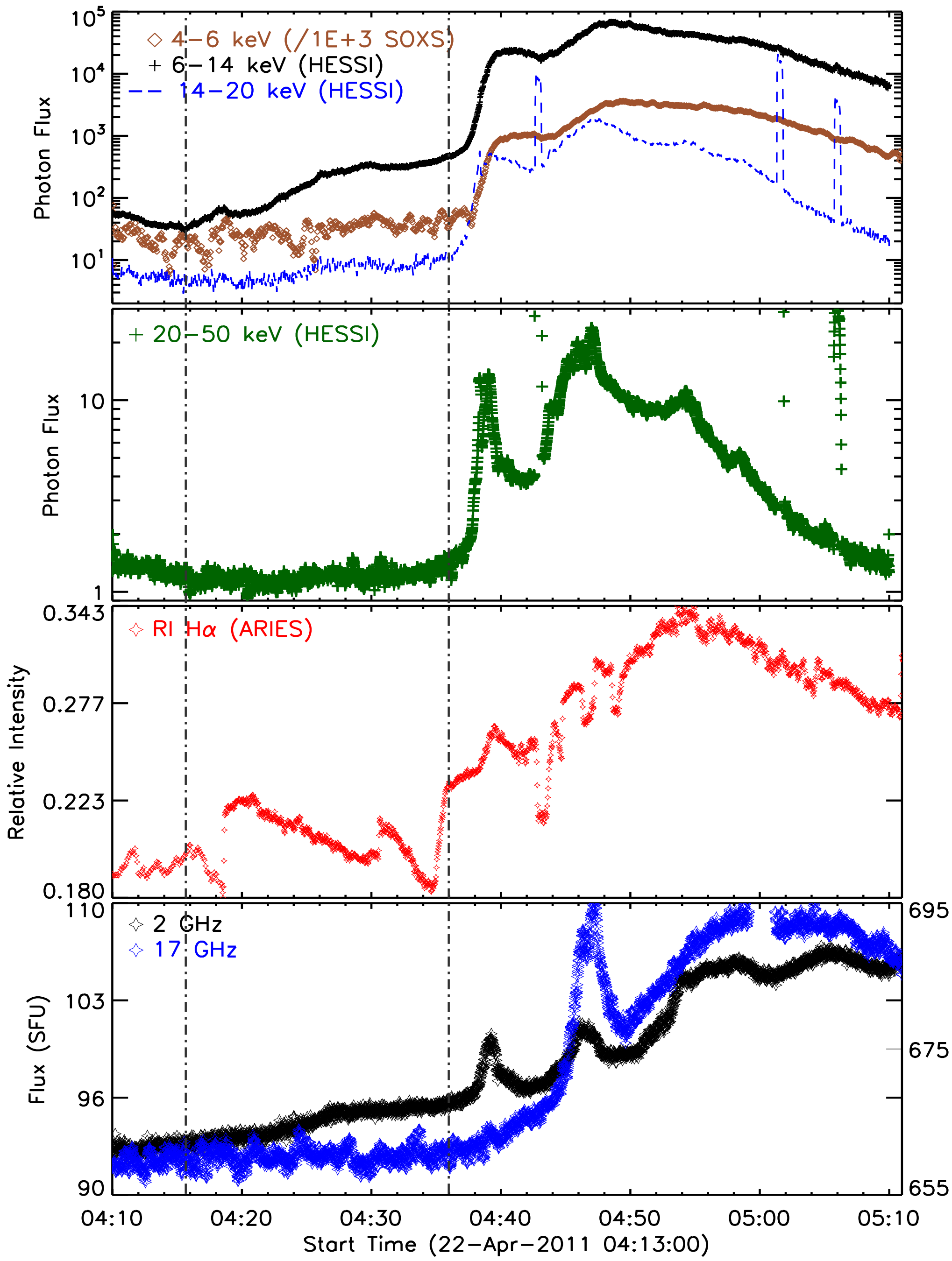

Figure 3.1: Temporal evolution of multi-wavelength emission during various phases of April 22, 2011 flare. Panel (a) represents the soft X-ray (SXR) emission in 4-6 keV observed by SOXS mission and 6-20 keV from RHESSI mission. Panel (b) represents the co-temporal evolution of HXR emission in 20-50 keV waveband. Panel (c) represents the temporal evolution of Hα emission from ARIES/Nainital observations and microwave emission in 2 and 17 Ghz in shown in panel (d).

Jain (1985) conducted the statistical study of 1885 Hα flares associated with microwave emission and suggested that two-ribbon (TR) flares and associated impulsive microwave bursts are produced as a consequence of the interaction of non-thermal electrons with ambient plasma embedded in strong magnetic field near lower atmosphere. Using SDO/AIA observations, Brosius and Holman (2012) found that chromospheric evaporation is driven via thermal conduction front which is energized by magnetic reconnection. Li et al. (2005) analyzed spectral observations from RHESSI and found that during the gradual phase, only 20 per cent of the energy transported to the chromosphere has been contributed due to the non-thermally accelerated charged particles, however, the rest came from the charged particles driven through thermal conduction. Radziszewski et al. (2011) performed a correlation study on Hα observation of high cadence with the respective X-ray emission and suggested that longer time-delays between Hα and HXR emission of $\approx$20 s correspond to a slow-chromospheric response associated with heating through conduction whereas short delays $\approx$1-2 s are consistent with energy transfer through beam-driven evaporation. Therefore, a correlation study of Hα and X-ray emission provides a better opportunity to understand the principle mechanisms of energy transfer in various phases of solar flares. Therefore the spatial, spectral and temporal evolutions of thermal and non-thermal sources is the focus of current study in order to understand the underlying physical processes of energy release in various phases of emission.

In this chapter, we present a detailed study of temporal, spatial and spectral evolution of the flare parameters using multi-wavelength observations. In Section 3.2, we brief the observations used for this study. Section 3.3 deals with the data analysis and results where we present statistical survey as well as case study. Section 3.4 presents the discussion and conclusion drawn from the study performed in this chapter.

3.2 Observations

The study of spatial, spectral and temporal evolution of X-ray emission provides excellent insights to physical processes. In this regard, we investigate the X-ray emission of 30 flare events (Table 3.1) observed by the Si detector onboard "Solar X-ray Spectrometer (SOXS)" mission (Jain et al., 2005) revealing clear-cut precursor signatures. SOXS was launched on-board the Indian GSAT-2 spacecraft on 2003 May 8 and has been successfully operational till 2011 May 2. A detailed instrumentation and observations techniques of the SOXS mission have been presented in Chapter 2 of the thesis.

Generally, the precursors to the flare are identified from the temporally correlated full disk-integrated X-ray emission. This terminology, however, may be misleading as the flares from two or more different regions may occur within the ~30 min and they might fall in the criteria of the precursors. In this regard, in addition to the study of temporal and spectral mode observations from Solar X-ray Spectrometer (SOXS), we also performed the study of spatial evolution of the X-ray sources using the observations from Ramaty High Energy Solar Spectroscopic Imager (RHESSI) in 6-100 keV energy band. The RHESSI facilitates X-ray imaging as well as spectroscopy of solar flares (Lin et al., 2002). We have also carried out multi-wavelength investigation of 15 flare events observed during 2010-2012 (Table 3.2) from the state-of-the-art and high-resolution instruments *viz.* Solar Dynamic Observatory (SDO) and Global High Resolution H-alpha Network (GHN/GONG). In order to explore the spatial correlation of multi-wavelength emission with photospheric magnetic-field observations, we use observations from Helioseismic Magnetic Imager (HMI; Scherrer et al., 2012) instrument onboard the Solar Dynamic Observatory (SDO) mission. It provides full-disk magnetograms at wavelength 6173 Å with spatial resolution of 0.5" per pixel and temporal cadence of 45 s. We also employ EUV observations in Fe XVIII (94 Å), Fe VIII, XXI (131 Å), Fe IX (171 Å), Fe XII, XXIV (193 Å), Fe XIV (211 Å), He II (304 Å), and Fe XVI (335 Å) taken by Atmospheric Imaging Assembly (AIA; Lemen et al., 2012) onboard Solar Dynamic Observatory (SDO) in close simultaneous with the RHESSI observations to restore the structure and investigate the plasma characteristics of emitting source. The spatial and temporal resolution of these observations is 0.6" per pixel and 12s respectively. We investigate the spatial evolution of temperature (T) and emission measure (EM) synthesized from EUV observations taken by SDO/AIA in 6 wavelength channels *viz.* 94, 131, 171, 193, 211, 335 Å which cover the temperature range of 0.6 to $\sim$16 MK. Further, we study the temporal evolution of Hα emission and spatial evolution of filament using observations from Solar Tower Telescope installed at Aryabhatta Research Institute of Observational Sciences (ARIES), Nainital, India (Uddin et al., 2006) as well as from GONG Hα Network (GHN) monitor. The 15-cm, f/15 Hα telescope observes active regions on the Sun with superb time cadence (up to 2s). The images are recorded by a 16 bit 1K$\times$1K pixel CCD camera system having a pixel size of 13 μm with a spatial resolution of 0.58" per pixel. This provides unique opportunity to investigate the correlation of temporal evolution of Hα emission in various phases of a flare.

Though, the precursor emission is very common feature during X-ray emission from several flares (Fárník and Savy, 1998; Veronig et al., 2002) but non-availability of high temporal, spatial and spectral multi-wavelength observations of flares restricted their detailed statistical and physical study until 2002 when space observations era started with RHESSI, SOXS, Hinode and SDO etc.

In order to characterize the statistical as well as physical parameters during the precursor phase and study their relationship with that during the main phase emission, we selected the flares occurred during year 2003-2012 in X-ray waveband by RHESSI as well as SOXS missions mainly because of the availability of high resolution spectral and temporal mode observations. We undertook the investigation of the flares which follow the criteria as follows and presented in Table 3.1 & 3.2.

- SXR emission within $\sim$30 mins prior to the onset of impulsive X-ray emission,
- Precursor emission to be spatially associated with the location of source of the impulsive phase within $\sim$20 arcsec,
- Availability of multi-wavelength (Hα, X-ray and UV) observations,
- The source of the precursor and impulsive phases of the flare should lie within $\pm 60^\circ$ from the center of the solar disk (for proper study of the filament and LOS magnetic-field observations).

Several flares have qualified one or more of the above criteria but we have selected only those events which followed all of the aforesaid criteria. In this regard, we have selected fifty flares with precursors for the study carried out in this chapter. These observations are analyzed with the help of SolarSoftWare (SSW), a software with a repository of codes and graphical user interfaces (GUIs) written in the interactive data language (IDL). Shown in Figure 3.1 is the intensity time profile of the flare in 4-6 keV (SOXS) and in 6-20 as well as in 20-50 keV (RHESSI) revealing the precursor, impulsive and gradual phases. We may note a small bump predominantly in SXR waveband prior to the impulsive emission which can be observed across full electromagnetic spectrum as presented in Figure 3.1.

3.3 Multi-wavelength diagnostics of solar flare emission

3.3.1 Temporal and Spectral study of X-ray emission

We study in great detail the temporal and spectral evolution of flare plasma parameters during various phase of flare events presented in Table 3.1 and 3.2 and then we conduct a statistical investigation of the derived temporal and spectral parameters. Table 3.1 contains the flare events observed by Solar X-ray Spectrometer (SOXS; cf. Chapter 2). In Figure 3.1, we plot the intensity time profile of the flare event occurred on April 22, 2011 in 4-6 keV (SOXS), 6-14 and 14-20 keV (RHESSI) representing SXR in panel (a), in 20-50 keV (RHESSI) representing HXR in panel (b), relative intensity in Hα waveband in panel (c) and in 2 and 17 Ghz from Nobeyama Radio Polarimeter (NoRP) observations in panel (d). The two vertical dashed lines on the graph show the duration of the precursor phase. We may note from Figure 3.1 that the precursor phase is pronounced in the SXRs, Hα and low-energy radio wavebands. In contrast, HXR and high-energy radio emission do not show clear signature of precursor while they are observed clearly during the main phase. Further, there are several spikes present in the RHESSI light curve which correspond to the change of attenuators during the observations.

We study the temporal evolution of the flare plasma parameters *viz.* temperature (T), emission measure (EM), density (n_e) and non-thermal photon spectral index using the observations from SOXS and RHESSI missions in X-ray waveband for the flare events listed in Table 3.1 and 3.2. We employ OSPEX (Object Spectral Executive) software package of SolarSoft for the analysis of the data used in the current investigation. OSPEX is an object-oriented interface developed to analyze solar X-ray spectral observations. OSPEX is a powerful tool which enables us to read and display the spectral and temporal mode observations from SOXS, selection and subtraction of background. During the fitting process, the instrument response matrix is used to convert the photon model to the model counts to compare with the input count data. For the analysis of spectral mode observations obtained from SOXS mission, the response matrix is incorporated in OSPEX itself (Jain et al., 2008).

Table 3.1: Time characteristics and plasma parameters during various phases of flares during Year 2003-2005

Date	Precursor Phase			Main Phase			Peak Temperature		Peak EM		Location
	Start	Peak	End	Start	Peak	End	T_p	T_m	EM_p	EM_m	(arcsec)
	Time (in UT)						MK		$(\times 10^{49} cm^{-3})$		
10-Jul-2003	04:23:48	04:27:36	04:33:54	04:33:54	04:41:15	04:58:10	10.32	11.252	0.07	0.20	(909, 239)
17-Nov-2003	04:55:04	05:09:52	05:18:00	05:18:00	05:22:56	05:46:45					(-959, 172)
26-Feb-2004-I	04:28:36	04:40:23	04:42:44	04:42:44	04:47:12	05:01:36	9.28	11.72	0.02	0.23	(277, 340)
26-Feb-2004-II	05:14:04	05:21:50	05:31:49	05:31:49	05:34:22	06:03:23	10.09	12.412	0.03	0.26	(277, 340)
05-Apr-2004	04:52:29	05:02:38	05:32:33	05:32:33	05:47:15	06:35:26	9.28	12.76	0.03	2.74	(-535, -197)
28-Jun-2004	B03:54:46	04:10:25	04:10:25	04:15:1	04:42:11		10.09	12.76	0.05	0.55	(947, -151)
13-Jul-2004-I	04:21:35	04:31:17	04:31:17	04:38:47	04:56:23		10.44	11.6	0.01	0.15	(-916,-191)
13-Jul-2004-II	05:20:08	05:22:24	05:26:10	05:26:10	05:32:09	05:35:16	11.25	12.41	0.04	0.80	(689, 188)
19-Jul-2004	04:11:23	05:09:15	05:23:53	05:23:53	05:30:32	A05:34:31	10.21	12.06	0.08	21.54	(70, -272)
10-Jan-2004-I	04:01:14	04:15:21	04:18:20	04:18:20	04:25:32	04:39:31	11.37	12.53	0.02	0.82	(511, -164)
10-Jan-2004-II	04:53:45	05:07:58	05:10:48	05:10:48	05:13:05	05:36:11	12.06	14.85	0.02	0.72	(511, -164)
22-Mar-2004	04:27:18	05:54:45	06:08:57	06:08:57	06:14:25	06:43:56	9.86	12.53	0.02	0.92	(47, 46)
14-Jul-2004	04:30:59	05:06:21	05:17:54	05:17:54	05:22:23	05:34:52	10.21	12.06	0.09	21.54	(820, 198)
21-Jul-2004	04:07:30	04:57:28	05:11:10	05:11:10	05:18:29	05:34:23	11.02	12.18	0.02	1.05	(-474, -74)
14-Aug-2004-I	03:57:43	04:05:37	04:12:22	04:12:22	04:14:17	04:30:50	8.70	12.41	0.07	9.47	(451, -310)
14-Aug-2004-II	05:32:26	05:37:47	05:37:47	05:43:31	06:04:32		10.44	12.64	0.01	64.50	(451, -310)
01 Jul 2005	04:53:21	04:55:04	04:57:09	04:57:09	05:01:22	05:16:08	10.79	12.18	0.01	0.41	(-681, -296)
03-Aug-2005	04:03:56	04:29:18	04:53:11	04:53:11	05:05:08	05:42:57	10.79	13.11	0.01	5.99	(-623, -310)
08-Jul-2005	04:58:49	05:08:01	05:16:38	05:16:38	05:19:51	05:30:48	10.79	11.02	0.19	5.72	(768, -95)
09-Sep-2005-I	03:55:29	04:18:13	04:37:17	04:37:17	04:52:11	05:23:32	10.67	11.02	0.18	5.53	(-861, -244)
09-Sep-2005-II	05:23:20	05:27:42	05:31:09	05:31:09	05:38:59	06:17:13	10.67	11.02	0.27	31.05	(-861, -244)
10-Sep-2005	05:15:00	05:37:43	05:50:52	05:50:52	06:14:13	06:20:09	11.48	11.83	0.26	12.73	(-778, -266)
12-Sep-2005	04:44:14	04:52:14	04:52:14	04:59:14	05:39:30		11.02	11.95	0.03	2.90	(-459, -317)

15-Jan-2005-I	04:08:04	04:09:51	04:10:47	04:10:47	04:15:30	04:24:27	11.60	11.14	0.18	76.02	(-109, 295)
15-Jan-2005-II	04:24:46	04:27:14	04:28:22	04:28:22	04:30:39	05:17:52	12.06	11.14	0.17	74.37	(-109, 295)
15-Jan-2005-III	05:32:28	05:36:56	05:42:04	05:42:04	06:24:42		10.09	11.60	0.06	27.62	(-109, 295)
17-Jan-2005	04:42:09	05:20:08	06:05:50	06:05:50	06:09:11	06:25:40					(312, 267)
17-Sep-2005	04:11:00	04:44:10	06:00:26	06:00:26	06:04:54	A06:19:45					(630, -269)
19-Jan-2005	04:25:29	04:48:03	05:17:12	05:17:12	05:22:22	05:48:13	9.86	12.30	0.13	0.47	(732, 308)
23-Jan-2005	04:28:12	04:34:52	04:43:20	04:43:20	05:01:29	05:46:33	9.63	11.25	0.03	9.65	(958,251)

Table 3.2: Time characteristics and plasma parameters during various phases of flares during Year 2010-2012

Date	Precursor Phase			Main Phase			Peak Temperature		Peak EM		Location
	Start	Peak	End	Start	Peak	End	T_p	T_m	EM_p	EM_m	(arcsec)
	Time (in UT)						MK		($\times 10^{49} cm^{-3}$)		
16-Oct-2010	18:52	18:59	19:07	19:07	19:12	19:15	16.472	20.648	0.0002	1.23	(410, -404)
22-Apr-2011	04:15	04:28	04:35	04:35	04:57	05:14	18.56	23.316	0.002	0.09	(-611, -227)
30-Jul-2011	01:56	–	02:04	02:04	02:09	02:12	8.12	21.46	0.01	2.84	(-518, 171)
15-Feb-2011	01:27	01:34	01:44	01:44	01:56	02:06	12.064	29	0.02	2.68	(196, -231)
09-Mar-2011	22:39	22:55	23:13	23:13	23:23	23:29	15.08	19.72	0.02	10.0	(191, 277)
01-Jun-2011	02:27	—	02:38	02:38	02:42	02:52A	12.18	13.572	0.005	0.17	(-686, 284)
08-Jul-2011	11:23	—	11:41	11:41	11:49	11:50A	6.96	9.28	0.03	0.6	(-294, -370)
08-Jul-2011	14:53	—	14:58	14:58	15:01	15:03A	9.28	11.6	0.06	0.04	(-261, -371)
10-Oct-2011	06:53	—	07:03	07:03	07:18	07:30A	9.86	11.02	0.03	38	(-176, -341)
06-Jul-2012	01:12	—	01:36	01:36	01:38	02:00	20.532	29	0.005	2.0	(591, -331)
13-Nov-2012	05:27	—	05:40	05:40	05:47	06:09	8.468	26.68	0.05	0.35	(-605, -455)
14-Nov-2012	03:51	—	03:56	03:56	04:03	04:26	8.236	19.488	0.01	0.32	(-406, -435)
18-Nov-2012	03:14	—	03:55	03:55	04:08	04:08A	9.396	11.6	0.05	25	(355, 97)
20-Nov-2012	18:50	—	19:17	19:17	19:26	19:30A	8.352	11.02	0.003	1.9	(-266, 64)
21-Nov-2012	05:58	—	06:42	06:42	06:52	06:57A	6.96	17.4	0.002	2.0	(-187, 66)

For analyzing RHESSI spaectral observations, we synthesize the spectrum and spectral response matrix (SRM) files from the observations which serves as a input to OSPEX. The energy resolution for the RHESSI spectra and SRM synthesis is kept to be 0.3 and 1 keV over the energy band of 6-15 and 15-50 keV, respectively. The raw data for spectral mode observations has been corrected for any spurious or false flare as well as for pre-flare background. Later, the spectrum at a given time is made by integrating the spectra over an interval of 180 s during the precursor phase interval while over 60 s interval during the main phase for the events observed by SOXS. Similarly, we integrate the RHESSI observations for 60 s and 32 s for the precursor and main phases, respectively. In each time-bin, we use OSPEX to estimate the flare plasma parameters *viz.* T, EM, non-thermal power-law index etc. by forward-fitting the observed count spectra with the model count spectra. Model count spectra is generated from the inbuilt functions *viz.* iso/multi-thermal, line gaussian, and non-thermal functions which employ CHIANTI atomic database (Dere et al., 1997; Landi et al., 2012). The SXR emission is believed to be originated either from isothermal or multi-thermal plasma, while the HXR emission via non-thermally excited electrons during magnetic reconnection. As there is no straight forward demarcation energy between thermal and non-thermal emission, it is estimated by forward fitting the observed spectra with thermal and non-thermal model photon functions, simultaneously. The spectral fitting is carried out by iterative adjustment of the free functional parameters by least square fit method keeping $\chi^2 \sim 1$, which enables us to estimate the flare plasma parameters from the best fitting of modeled counts over the observed counts. Figure 3.2 and 3.3 show the photon flux spectrum of a few flares that occurred during year 2003-2005 and observed by SOXS.

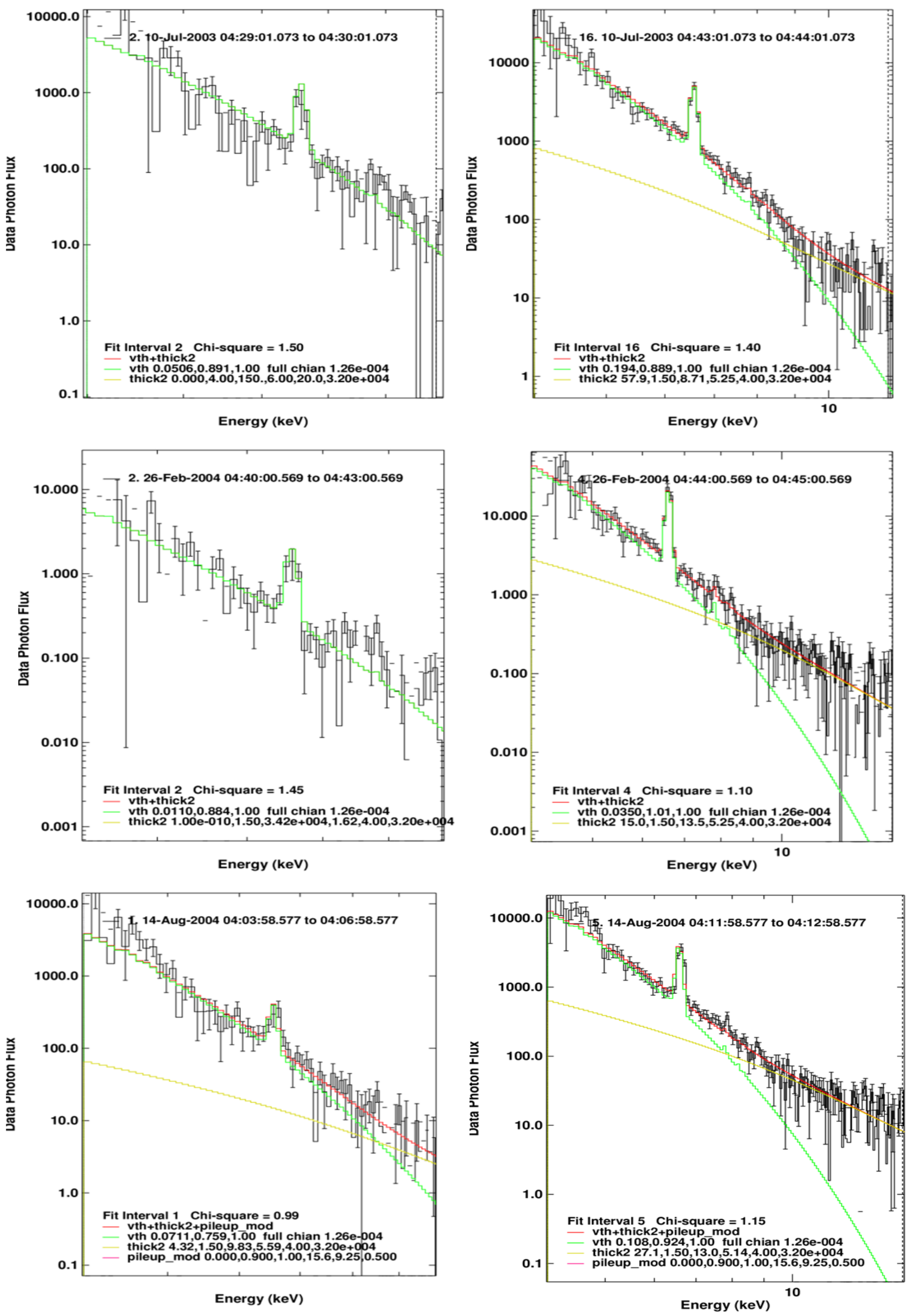

Figure 3.2: Photon spectra (black line) during the precursor and impulsive phases in the left and right panels, respectively for July 10, 2003, February 26, 2004 and August 14, 2004 flares. The spectral fit is done using isothermal (green line) + thick2 (yellow line) photon models while total model flux is shown by the red line.

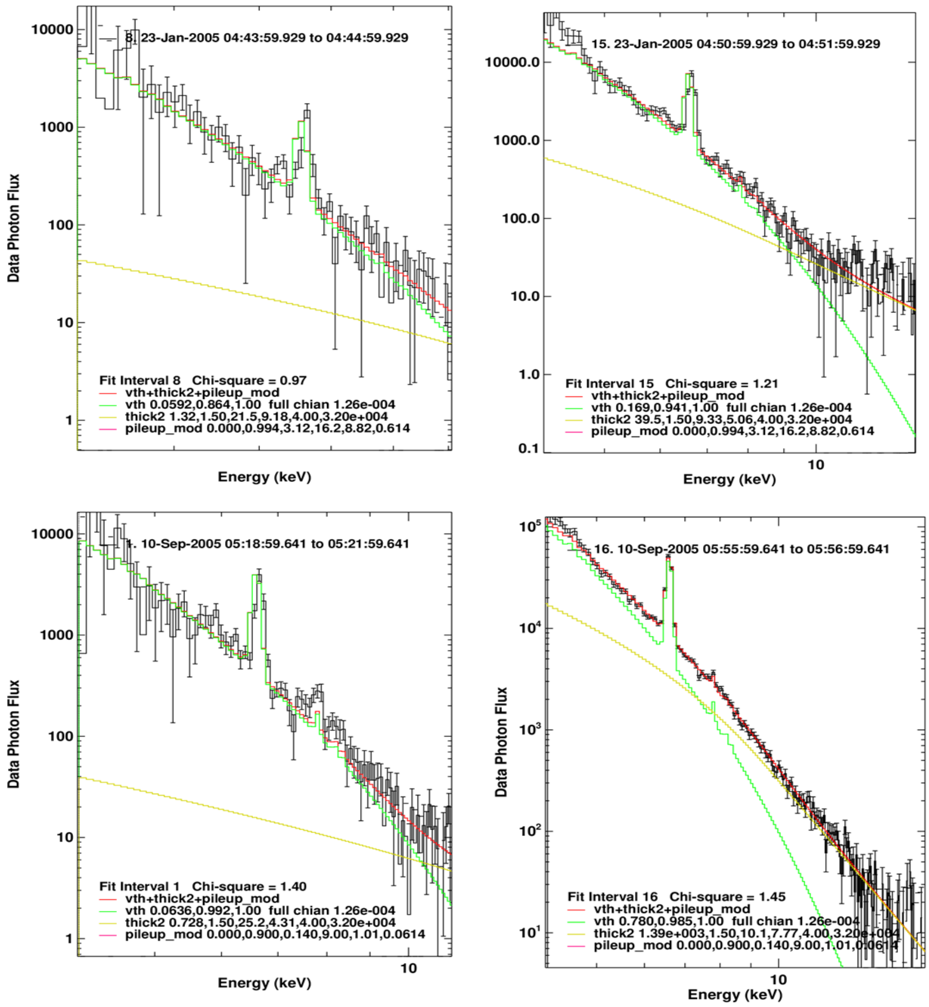

Figure 3.3: Photon flux spectra (black solid line) of the precursor and impulsive phases in the left and right panels, respectively for January 23, 2005 and September 10, 2005 flares. Spectral fit is done using isothermal (green line) + thick2 (yellow line) photon models with goodness of fit represented by χ^2 in each panel. The total model photon flux spectrum is shown by the red line.

We have analyzed the spectra of all the flares listed in Table 3.1 & 3.2 and deduced various flare plasma parameters which are also presented in the tables. This analysis is comprised of the study of 50 flares out of which 30 have been observed by SOXS and RHESSI however rest of the 20 flares have been observed only by the RHESSI. We analyzed on average about 40 spectra of each flare and thus the flare plasma parameters deduced here represent a significant statistics of 1620 sets of plasma parameters. We found temperature (T) during the precursor phase to be varying in the range of 8.7-11.5 MK while that in the main phase between 11-14 MK. Similarly, the emission measure is found to be ranging between 0.002 - 0.02 and 0.01 - 0.27 $\times$ 10^{49} cm^{-3}, respectively during the precursor and main phases. From this study, we learnt that the X-ray emission during the precursor phase is solely originated from physical processes of thermal origin while during the main phase both thermal and non-thermal processes play significant role. Further, this study revealed that although the count rate of X-ray emission during the precursor phase is $\sim$ 1% of the main phase, the temperature attains a value $\sim$ 80 % of that during the main phase. In contrast, the emission measure during the precursor phase is estimated to be $\sim$ two orders less than that during the main phase. The estimated temperature suggests the initiation of precursor phase as a result of plasma heating. On the other hand, significant low value of the EM does not permit the onset of the chromospheric evaporation, which, however, enhances the volume of the source and the density so as to fill up the flaring loops. In the following section, we present the statistics of plasma parameters deduced from the spectra observed during the precursor and main phase of the flares.

3.3.2 Statistical study of flare plasma parameters in the precursor and main phases

We attempt to make a comparative study of the flare plasma parameters *viz.* Temperature and Emission Measure during both precursor and main phases. For this study the 1620 sets of plasma parameters that estimated above have been considered. These parameters have been separated according to the phase. Thus, we have two sets of both T and EM values *i.e.* during the precursor phase and during the main phases of all the flares listed in Table 3.1 and 3.2. Figure 3.4 shows the normalized frequency histogram of T and EM with the binning of 0.1 MK and 0.01 $\times$ 10^{49} cm^{-3}, respectively.

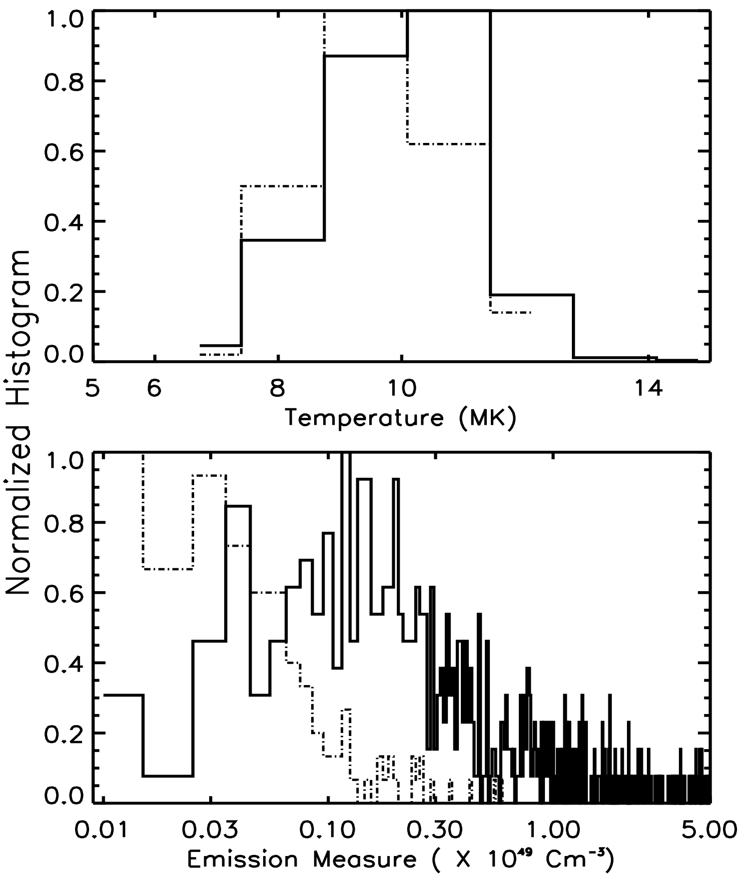

Figure 3.4: Normalized frequency histogram of the temperature and emission measure, respectively in the top and bottom panel during the precursor and main phases. The dotted line represent the histogram of T and EM during the precursor phase while solid line represents that during the main phase.

From the top panel of the Figure 3.4 which represent the histogram of temperature, it may be noted that the temperature during the precursor phase (shown by dotted line) is peaked at 9 MK while that during the main phase is peaked at ~11 MK. The normalized histogram of EM during the precursor and main phases is shown in the bottom panel of Figure 3.4. We may note that the emission meaure during the precursor phase remains ~ two orders lower during the precursor phase than that during the main phase with a peak occurrence at 0.01 and 0.2×10^{49} cm^{-3}, respectively.

Further, we also explore the scaling law between T and EM during the various phases of emission in solar flares. In this regard, we plot the T versus EM during the precursor and main phases as presented in Figure 3.5.

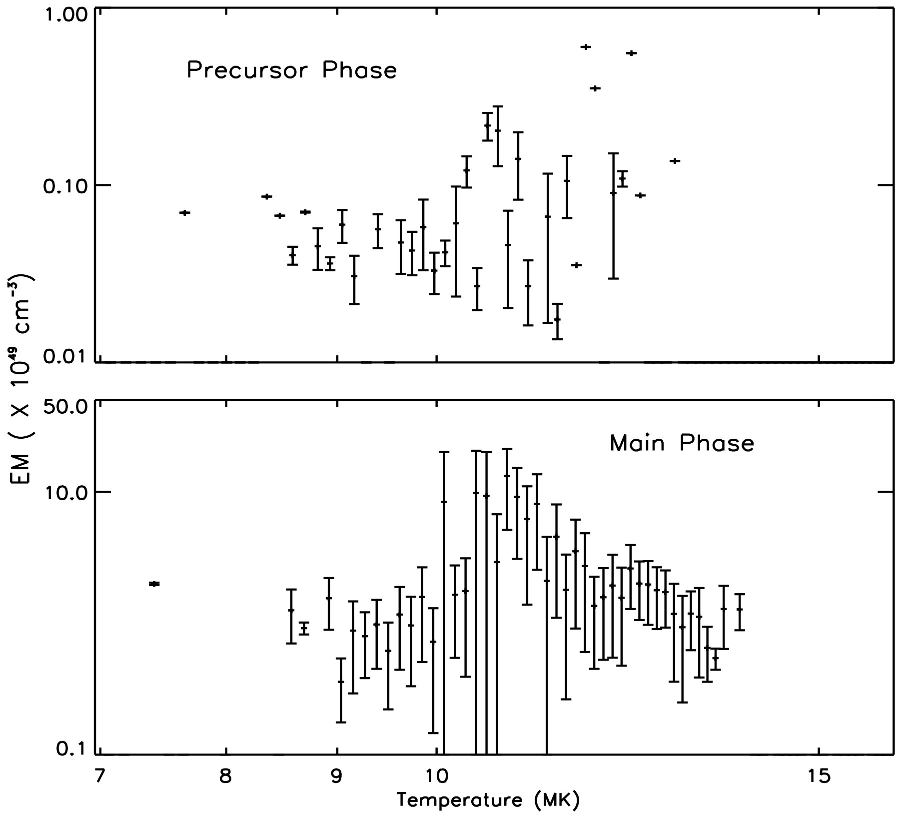

Figure 3.5: Top and bottom panels represent the T versus EM plotted during the precursor and main phases, respectively.

From Figure 3.5, we found T-EM relationship follows a power-law during both the precursor phase. During the main phase, this relationship tends to deviate from the power-law at high temperature. In theoretical investigations, Shibata (1999) and Shibata and Yokoyama (2001) found a universal power-law relationship between T and EM. Thus, this study inarguably shows power-law relationship between T and EM to be invariant of the phase of emission. We further investigate the timing study of the temperature and emission measure in the following section.

3.3.3 Timing analysis of flare Temperature and Emission measure

Study of causal relationship in the flare plasma parameters is an excellent tool to investigate the underlying mechanisms. In the case of solar flares, timing studies have been a great advantage in order to understand the several processes such as energy release mechanism (Aschwanden et al., 1998; Veronig et al., 2002), heating and cooling of the flare plasma (Aschwanden, 2007; Jain et al., 2011a) etc. Therefore, we investigate the timing delay between peak of the temporal evolution of temperature (T) and emission measure (EM) of the analyzed flares. Figure 3.6 shows the temporal evolution of T and EM for the August 03, 2005 flare observed by SOXS mission.

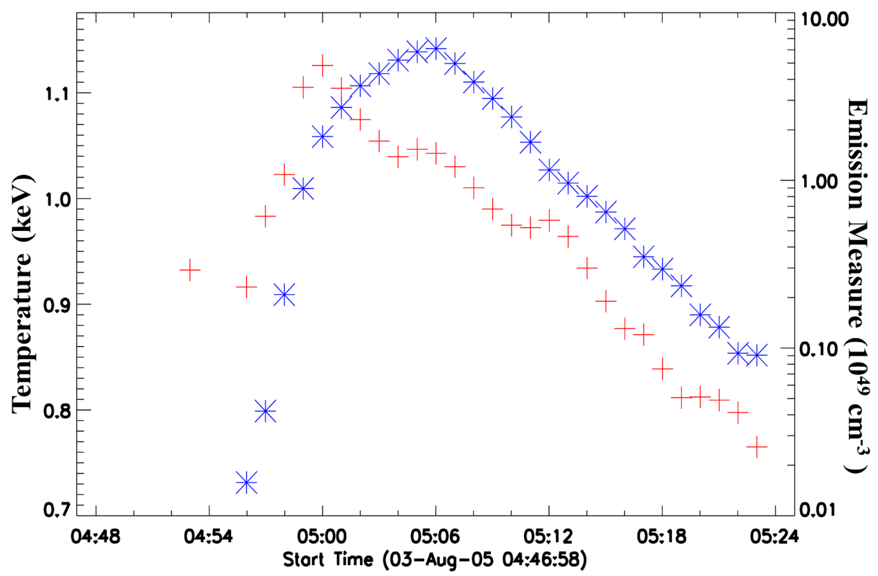

Figure 3.6: Temporal evolution of T and EM for the August 03, 2005 flare observed by SOXS mission drawn by red and blue symbols, respectively.

From Figure 3.6, we note the T profile peaks earlier than EM profile. The physical reasoning for this causal relation is associated with the chromospheric evaporation followed by reconnection driven charge particle bombardment onto chromosphere. We have estimated this timing delay for all 50 flares analyzed under current investigation. Figure 3.7 shows the normalized histogram of estimated delays. The delay histogram is best-fitted with a gaussian profile with a peak at 190 seconds.

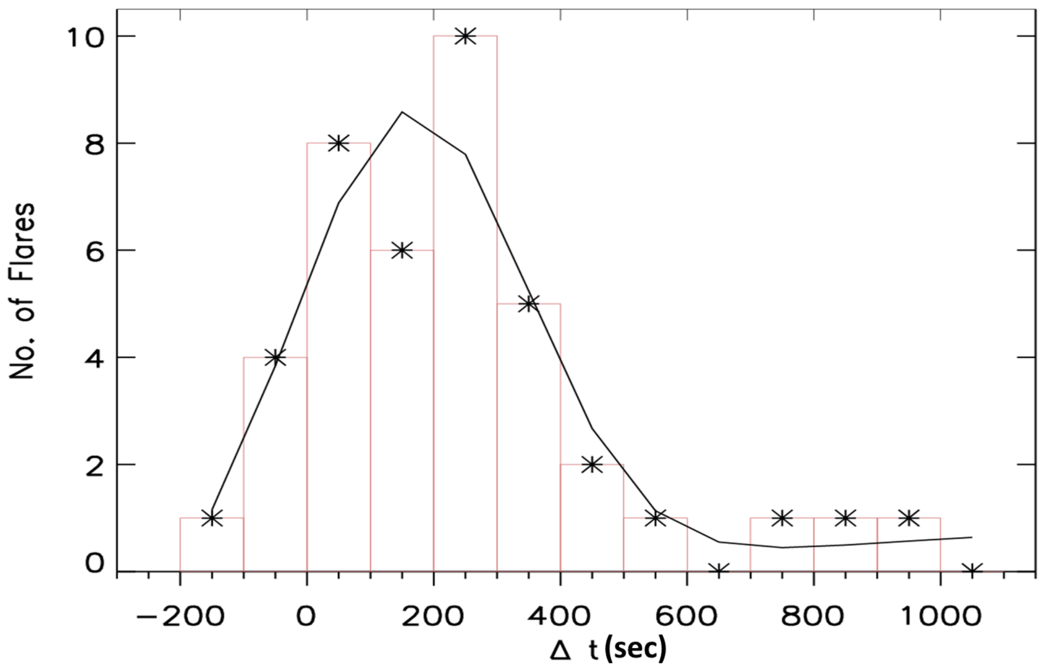

Figure 3.7: Histogram of time-delay (Δt) (in sec) between the peak of temperature (T) and emission measure (EM) profile. The histogram is fitted with Gaussian profile with the peak at 190 sec.

The delay obtained in such a way enable to estimate the length of the flaring loop. As we estimated 190 s to be the average delay between T and EM, flaring plasma moving up owing to the effect of chromospheric evaporation with a typical speed of $\sim$ 400 km/s (Ning et al., 2009) will travel $\sim$ 80,000 km. This length may be considered as a average half-loop length for the flare events investigated in this study. This study also enables us to have an indirect measure of flaring volume and thus the average density of the flaring region.

Further, in order to investigate the source of emission during the precursor and main phases, we study the spatial evolution of multi-wavelength emission during various phase of flare as presented in the following section.

3.3.4 Spatial Evolution of multi-wavelength emission during the precursor and main phases

The physical processes occurring during various phases of the emission in solar flares can be unraveled through the multi-wavelength study of topological and morphological evolution of sources. In this study, we considered only those precursor events in which the SXR source happened to be within $\sim$ 20 arcsec from the location of SXR source during the main phase as also mentioned previously in the criteria of selection of events. To do this, we synthesized X-ray images in various energy bands from RHESSI observations. We further undertake the study of source evolution in EUV waveband observed from TRACE and SDO/AIA satellites and filament evolution by using the observations from the Global High resolution Hα network (GHN) as well as from ARIES/Nainital observing facility. In the following sections, we present the spatial evolution of sources in multi-wavelength emission.

3.3.4.1 Morphological study of X-ray emission

In order to establish spatial relation between the sources during the precursor phase and main phases, we synthesize X-ray images using RHESSI (Lin et al., 2002, Chapter 2) observations. The images have been synthesized with spatial resolution of 1 arcsec/pixel from the observations integrated over 30s duration. The energy bands employed for synthesizing X-ray images are: 6-14, 14-20 and 20-50 keV from the counts collected in RHESSI sub-collimators 2F, 3F, 4F, 5F, 6F, 8F and 9F. We employ the CLEAN imaging algorithm (Hurford et al., 2002) for synthesis of X-ray images throughout the study as this is fast and reconstructs source structures reliably.

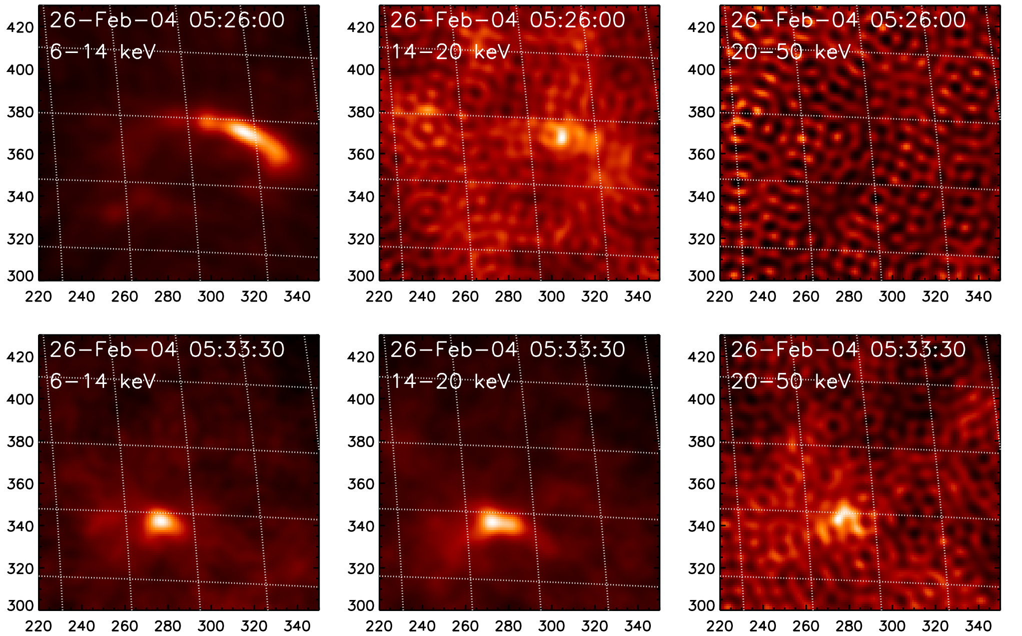

Figure 3.8: Time series of images at the peak of the precursor and main phases *i.e.* at 05:26:00 and 05:33:30 UT in 6-14, 14-20 and 20-50 keV energy bands for the flare occurred on February 26, 2004.

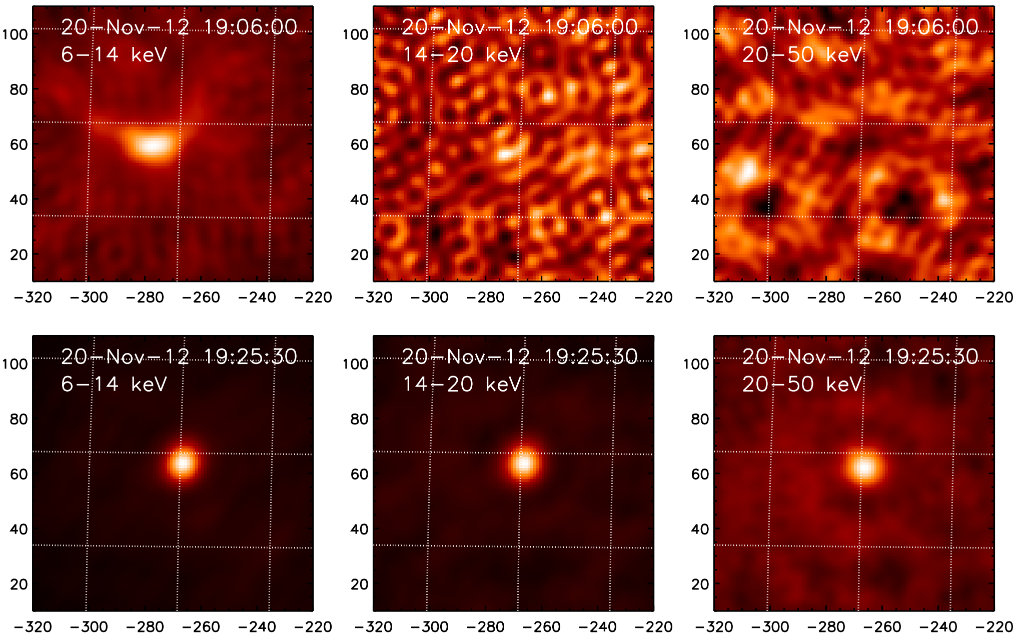

Figure 3.9: Time series of images at the peak of the precursor and main phases *i.e.* at 19:06:00 and 19:25:00 UT in 6-14, 14-20 and 20-50 keV energy bands for the flare occurred on November 21, 2012

Shown in Figure 3.8 and 3.9 is the series of images for the flare occurred on February 26, 2004 and November 20, 2012, respectively, at the time of peak of precursor and main phase emission in 6-14, 14-20 and 20-50 keV energy bands. From Figure 3.8 and 3.9, we see that the source of emission in SXR during the precursor phase were extended in area in comparision to that during the main phase. Further, during the precursor phase, the estimated EM is $\sim$2 orders lesser than that during the main phase and the source of emission is extended. This leads to the fact that density of the emitting region associated with the precursor emission was very small. Thus combining the aforesaid outcomes namely high enough temperature while low plasma density suggest different mechanism of heating than that operates during the main phase emission. It may be proposed that intensive heating (high temperature) produced during the precursor phase results in gentle evaporation in contrast to explosive evaporation occurring during the main phase. Consequently, the principal mechanism of plasma heating during the precursor phase seems to differ from that operating in the main phase such as conduction front driven plasma heating which mainly results in a gentle evaporation (Battaglia et al., 2009) is a possible candidate.

Further, the study of evolution of X-ray sources revealed that the precursor phase emission is originated from AR having multi-loop system with complex magnetic-field topology. We do not find a single case of where a single-loop structures AR is the origin of precursor emission prior to the main phase. In addition, we also note the change of loop configuration as may be noted from Figure 3.8 and 3.9 where precursor phase is originated either from a low-lying loop or from one foot-point of the loop-system which is involved in the main phase emission. This suggests the possibility of the magnetic-field restructuring from the precursor to the main phase emission in which the magnetic-field topology becomes more complex during the main phase than that during the precursor phase. In this regard, we perform a detailed study of magnetic-field topology in the following section.

3.3.5 Evolution of Photospheric magnetic field

To investigate the energy build-up and trigger of the flare, we study the evolution of magnetic-field parameters *viz.* signed and unsigned flux, gradient and rotation angle of the sunspot polarities. For this study, we have used magnetic-field observations from Michelson Doppler Imager (MDI) onboard SOHO spacecraft for the flare events listed in Table 3.1 and from Helioseismic Magnetic Imager for the events listed in Table 3.2. Here we present a detailed study of the flare occurred on April 22, 2011. The observations were obtained from the URL: `http://jsoc.stanford.edu`. These magnetograms are then processes with the standard procedures discussed in Chapter-2 of this thesis. Shown in Figure 3.10 is a sequence of a few high resolution magnetograms of NOAA AR 11195 during April 20-23, 2011. The AR magnetic field evolution during April 20-23, 2011 has been studied using the techniques discussed in (Jain et al., 2011b) and Chapter 5 of this thesis.

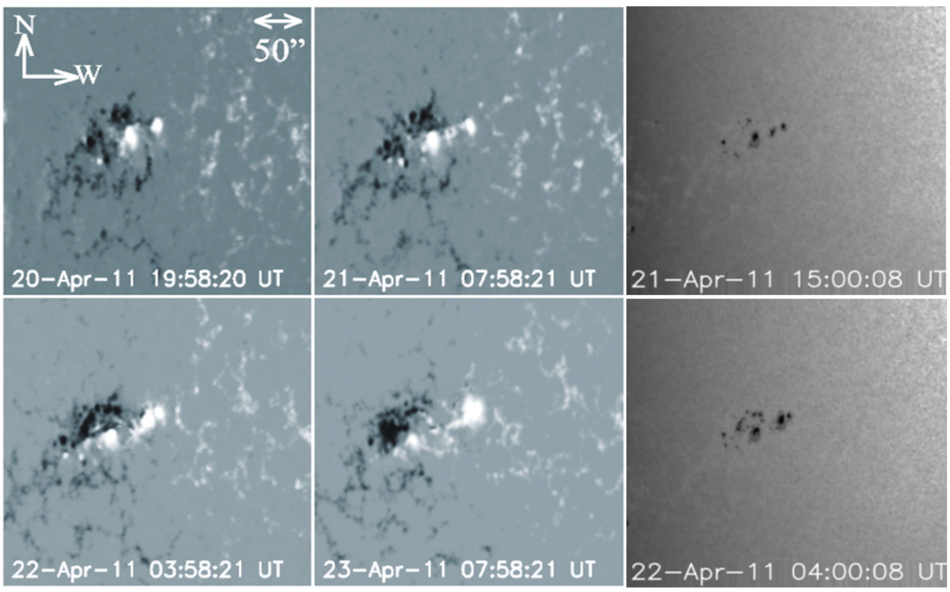

Figure 3.10: Rotation corrected time sequence of a few selected high-resolution magnetograms of NOAA AR 11195 obtained by SDO/HMI for the period 20-23 April 2011. Right Top and bottom images show the evolution of sunspots in SDO/AIA 4500 Å images

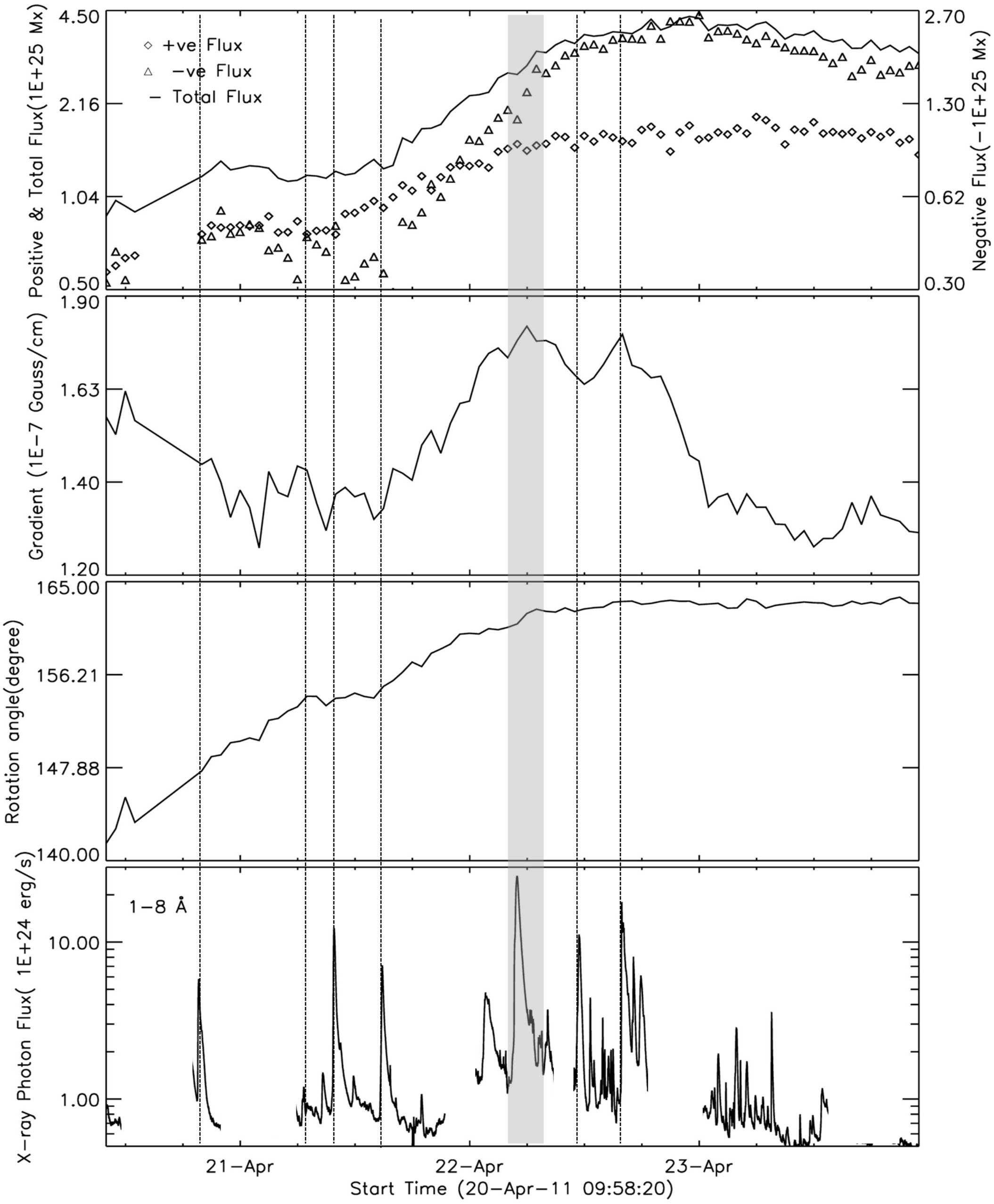

Figure 3.11: Temporal evolution of one hour cadence magnetic fluxes of leading and following polarities as well as total flux of NOAA 11195 (a), the gradient (b), and the rotation angle of active region 11195 (c) and energy loss rate in 1-8 Å observed by GOES mission (d). The shaded area represents the 2011 April 22 flare and the dotted lines facilitate the correlation of other flares with the magnetic-field parameters from AR11195.

3.3.5.1 Measurement of magnetic flux

The magnetic flux [Φ] is estimated as the product of magnetic-field strength [H] and area [A] of a given active region. $\Phi = H.A$ where H is obtained from HMI/AIA synoptic observations. The magnetic flux is estimated separately for leading and following polarities. Pixels having positive magnetic field strength constitute leading polarity region. Similarly, pixels with the negative magnetic field strength represent the following polarity region. The size of one pixel is 2.0172 arcsec and therefore the area occupied by both the polarities is then estimated separately by total number of pixels multiplied by area of single pixel, *i.e.* $725^2\times$ 2.0172 $\times$ 10^{10} cm^2. The magnetic flux for each polarity is then estimated using above relation and plotted for 20-23 April 2011 as shown in panel (a) of Figure 3.11. Total flux is also derived and plotted in the same panel. The gradient (panel b), shear angle (panel c) and GOES X-ray energy loss rate in 1-8 Å obtained during the flare events reported to be associated from NOAA AR11195 (panel d) during 20-23 April 2011 are also shown in Figure 3.11. Grey shaded region corresponds to the flare evnt occurred on April 22, 2011.

3.3.5.2 Measurement of the magnetic field gradient

The separation (dz) between the leading and following polarities is obtained from the distance between their respective centers of masses. The center of mass coordinates (x_c, y_c) of both the polarities are obtained as:

$$\mathrm{x_c} = \frac{\sum_{\mathrm{i,j}} \mathrm{x(i,j)B_{los}(i,j)ds}}{\sum_{\mathrm{i,j}} \mathrm{B_{los}(i,j)ds}}$$

$$\mathrm{y_c} = \frac{\sum_{\mathrm{i,j}} \mathrm{y(i,j)B_{los}(i,j)ds}}{\sum_{\mathrm{i,j}} \mathrm{B_{los}(i,j)ds}}$$

Where B_{los}(i,j) is the line-of-sight magnetic field strength corresponding to the pixel with coordinate [x(i,j), y(i,j)] and ds = dx • dy is the area of each pixel. The aforesaid sum runs over the all the pixels from region of interest

(ROI). The estimated center of masses of leading and following polarities is then employed to get dz from:

$$\mathrm{dz} = \sqrt{(\mathrm{x_{cl}} - \mathrm{x_{cf}})^2 + (\mathrm{y_{cl}} - \mathrm{y_{cf}})^2}$$

Here, (x_{cl}, y_{cl}) are the coordinates of the center of mass of the leading polarity and (x_{cf}, y_{cf}) are of the following polarity. The magnetic field gradient is then estimated as dH/dz. The variation of dH/dz during the disk passage of the active region (20-23 April 2011) is shown in panel (b) of Figure 3.11.

3.3.5.3 Measurement of shear angle of the active region

The shear angle (θ) of the active region has been defined as the angle between line joining the center-of-masses of the leading and the following polarities and the equator in the clockwise sense. The shear/rotation angle of the active region is shown in panel (c) of Figure 3.11.

Figure 3.11 - panel (a) shows that the positive and negative magnetic fluxes have been increasing and varying between (0.5 - 1.5) $\times$ 10^{25} and - (3 - 6) $\times$ 10^{24} Mx, respectively during 20 April 09:00:00 UT - 22 April 04:00:00 UT. This variation suggests that the energy build-up process in the corona has started since 2011 April 20. The dH/dz and θ vary in the ranges 1.3 - 1.7 $\times$ 10^{-7} Gauss/cm and 140 - 163°, respectively during 20 April 2011 09:00:00 UT - 22 April 2011 04:00:00 UT (see Figure 3.11 panel b,c). As we note from the temporal evolution of dH/dz that it has been increasing until the onset of the flare and then decreased. The same trend of evolution in dH/dz has been noted for the folllowed M1.2 flare from the same AR during 15:47 - 16:11 UT. This suggests to the first approximation that the evolution of dH/dz serves a good proxy for the trigger of stored energy to release in the flare events in general and for the M-class and higher flares in particular. Further, θ, which may represent the free energy available in the AR, shows continuous increase in the clock-wise sense, but saturates after the flare. Therefore, the temporal evolution of magnetic field parameters suggest that the magnetic flux along

with shear have been responsible for the energy build-up while the gradient, when reached to a critical value, serves to trigger the stored energy so as produce the flare.

Although the photospheric magnetic-field parameters reveal a good proxy for trigger of main phase emission in solar flares, however, we still lack in the understanding how photospheric magnetic-field play a role in the energy release processes during the precursor and main phases. In this regard, we have also carried out the study of photospheric magnetic field parameters from the magnetic field observations with temporal resolution as high as of 45 s obtained from HMI/SDO instrument. We estimate the evolution of magnetic field parameters for the events listed in Table 3.2 from the aforesaid technique. In addition to this, we also tracked the spatial evolution of high cadence magnetic-field evolution for the flares. We do not find the significant magnetic flux emergence, submergence or cancellation prior to- or during the precursor phase. In addition, the study of temporal evolution of photospheric magnetic-field parameters also did not undergo noticeable change. Therefore, this study suggests that although the photospheric magnetic field parameters are very good proxy of the energy build-up, they do not play significant role in producing the precursor phase emission. This rule out the possibility of flux emergence, submergence or cancellation to be the underlying mechanism of energy release during the precursor phase as previously suggested by Tandberg-Hanssen and Emslie (1988). However, this exercise does not rule out the role of coronal magnetic-field restructuring as the possible candidate for energizing the precursor emission.

3.3.6 Kinematics and Morphology of filament

In the previous section, we studied the role of photospheric magnetic field as a proxy of the trigger for the energy release during either of the precursor or main phases in solar flares. The magnetic field acts as a bed to the cool plasma known as the filament. We pursue the study of filament morphology and kinematics in various phases of flare emission employing multi-wavelength observations in this section. The study of the morphological evolution of the filaments for the flare events listed in the Table 3.1 has been carried out employing Hα observations mainly from various ground based observatories operated by National Astronomical Observatory of China (NAOC) and Japan (NAOJ). In addition to this, we have also used the 304 Å wavelength observations from Extreme Ultraviolet Imaging Telescope (EIT) onboard Solar and Heliospheric Observatory (SOhO) spacecraft whenever available. On the other hand, the detailed kinematics of the filament is performed for the flare events presented in Table 3.2 from the observations available from Global High Resolution Hα Network (GHN) for uninterrupted observation of the Sun in Hα wavelength (see Chapter 2). Further, we also use high temporal resolution observations in 304 Å from AIA/SDO mission and 15 cm high resolution Hα telescope installed in ARIES-Nainital for few events.

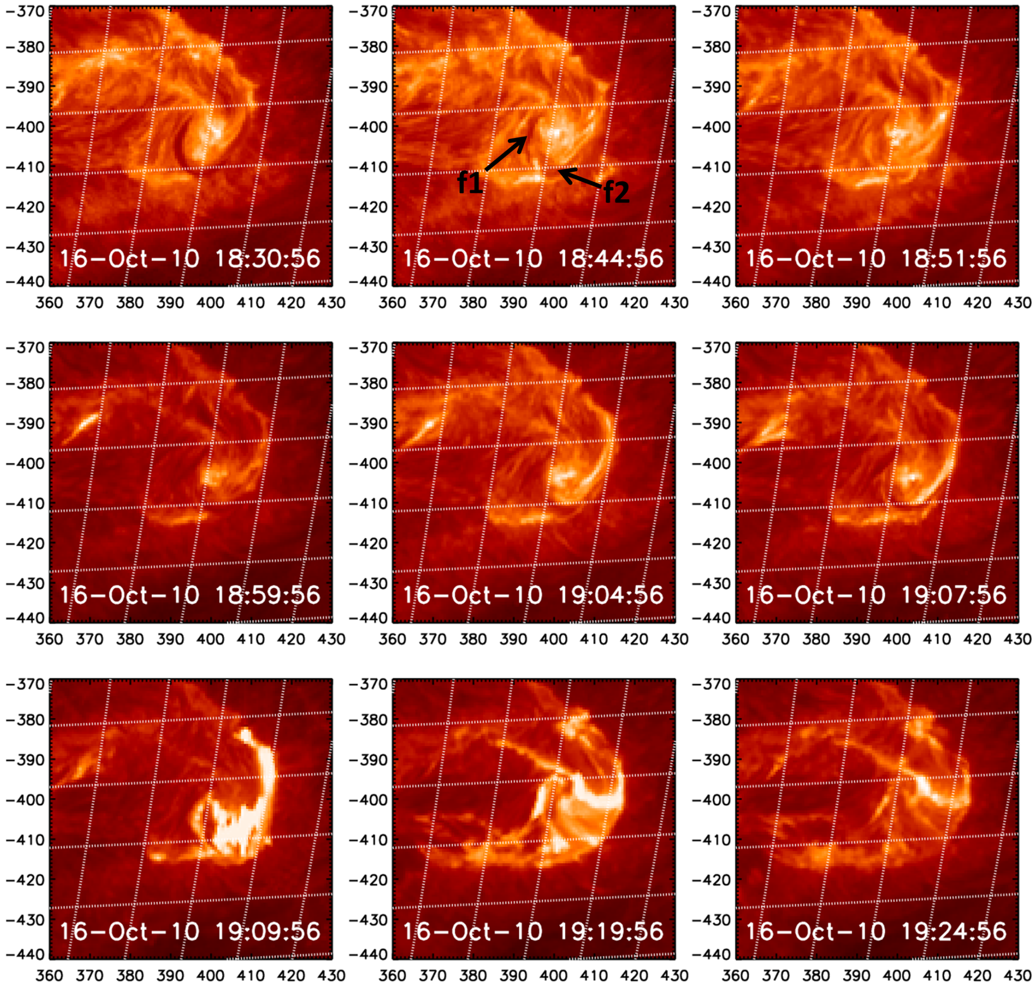

Figure 3.12: Time series of 304 Å wavelength emission during the flare occurred on October 16, 2010 from AIA/SDO observations. Top panel represent the filament evolution during the pre-precursor phase, middle panel represent the evolution during the precursor phase and the bottom panel represents the same during main phase emission.

Figure 3.12 shows the filament dynamics in various phases of the flare occurred on October 16, 2010. Top, middle and bottom panels of the figure represent the evolution of the filament prior to the onset of the precursor phase, during the precursor phase and during the main phase, respectively. The filament structure prior to the onset of the precursor emission (top panel) can be characterized by a 'U' shape. The rightmost image in the top panel shows the disruption of the filament as designated by ‘f1’ and ‘f2’. Later ‘f1’ erupted at the onset of the precursor emission at 18:51:56 UT, and ‘f2’ started to slowly rise as may be noted from the middle panel of the Figure 3.12. Finally the eruption of ‘f2’ at 19:07:56 UT has led to the onset of the main phase emission. Another important aspect is the enhanced emission in the vicinity of the filament during the precursor phase which may suggest the ongoing reconnection underneath the filament. We have carried out such an investigation for all the flares events enlisted in Table 3.2. We find onset of the precursor phase of 8 flares out of total 15 to be associated with the partial eruption of the filament. Rest of the flares were showing slow-rise of the filament associated with the precursor phase. Therefore, we find that filament activity plays a dominating role in the energy release during the precursor and main phase emission.

Thus, from the above study performed on a large dataset, we learnt that precursor emission is either co-spatially associated or lies in the vicinity of the source of the main phase emission. Further to this, this study also revealed that no drastic changes of the magnetic-field in the form of emergence/submergence or collision have been observed as a proxy of the precursor phase. However, the study of filament morphology led us to conclusive evidences. We find slow-rise of the filament accompanied by either the partial eruption or increasing complex structure of the filament during the precursor phase. A detailed study of multi-wavelength evolution of the aforesaid proxies is inevitable in order to lead to conclusive remarks. In this regard, in the following section, we present case study of the flare occurred on April 22, 2011 using multi-wavelength observations.

3.3.7 Thermal and non-thermal characteristics of the precursor and main phases of April 22, 2011 M1.8 flare: A case study

The active region (AR) 11195 located at (S17, E31) on 2011 April 22 first appeared at the south-east limb on 2011 April 19. It produced 6 flares of GOES C-class and 2 M-class during 2011 April 20-22. The M1.8 flare that occurred on 2011 April 22 is the subject of current investigation because this event shows very clear precursor enhancement before the impulsive phase as observed in multi-wavelength emissions. In order to investigate the various phases of the flare, we use X-ray observations in 4-6 keV during 04:00:00 UT - 05:10:00 UT from the Si pin detector onboard the Solar X-Ray Spectrometer (SOXS) mission. The Si detector provides high spectral resolution ($\sim$0.8 keV) in the 4 - 25 keV energy range. The temporal cadence of observations is 100 ms but data is recorded only at an interval of 3 s for the quiet time, while it is recorded at a cadence of 100 ms during flare activity for 287 s based on the on-board automatic flare detection algorithm after which, however, the observing mode returns to 3 s. The data have been archived on the SOXS website `http://www.prl.res.in/~soxs-data`. In addition, we use X-ray observations made by the RHESSI mission in the 6-50 keV energy band from 04:09:00 UT to 05:05:00 UT as the observations were not available during 04:00:00-04:09:00 UT due to RHESSI night time. The RHESSI facilitates X-ray imaging as well as spectroscopy of solar flares. These observations are analyzed with the help of SolarSoftWare (SSW), a software with a repository of codes and graphical user interfaces (GUIs) written in the interactive data language (IDL). Shown in Figure 3.13 is the intensity time profile of the flare in 4-6 keV (SOXS) and in 6-20 as well as in 20-50 keV (RHESSI) revealing the precursor, impulsive and gradual phases. We note several spikes in the RHESSI light curve which correspond to the change of attenuators during the observations. The event history is summarized in Table 3.3.

In order to explore the spatial correlation of multi-wavelength emission with photospheric magnetic-field observations, we use observations from SDO/HMI. We further use EUV observations in 94 and 131 Å wavelengths observed from SDO/AIA combining with the RHESSI observations to restore the structure of emitting source. We investigate the spatial evolution of temperature (T) and emission measure (EM) synthesized from EUV observations taken by SDO/AIA in 6 wavelength channels *viz.* 94, 131, 171, 193, 211, 335 Å which cover the temperature range of 0.6 to ∼16 MK.

Table 3.3: Timeline of activities during the precursor and main phases of flare

S.N	Time (UT)	Observations/Events
1	04:12:34 - 04:13:50	Eruption of the South-West leg (L1) of the filament
2	04:15:18	Onset of the precursor phase in 4-6 and 6-14 keV emission
3	04:18:26	First SXR peak during the precursor phase (P_{x1})
4	04:20:40	First $H\alpha$ peak during the precursor phase (P_{h1})
5	04:27:14 - 04:36:00	Heating in the vicinity of the filament and enhanced ambient density
6	04:35:00	Onset of the filament eruption
7	04:36:00	Onset of impulsive phase in 20-50 keV (HXR) emission
8	04:39:16/04:39:26	First Peak in HXR and RI in $H\alpha$ time profile after onset of Impulsive phase represented in Fig. 1 by P_{x2} and P_{h2}, respectively
9	04:45:00	$H\alpha$ plage brightening in the south-east of the AR 11195
10	04:54:20	Commencement of the Gradual Phase
11	04:54:30	Peak emission in $H\alpha$ as denoted by P_{h3} in Fig. 1
12	05:14:00	End of the Gradual/Decay phase

We study the temporal evolution of Hα emission and spatial evolution of filament using observations from Solar Tower Telescope installed at Aryabhatta Research Institute of Observational Sciences (ARIES), Nainital, India (Uddin et al., 2006). The 15-cm, f/15 Hα telescope observes active regions on the Sun with superb time cadence (up to 2s) and with a spatial resolution of 0.58” per pixel. This provides unique opportunity to investigate the correlation of temporal evolution of Hα with multi-wavelength intensity in various phases of flare.

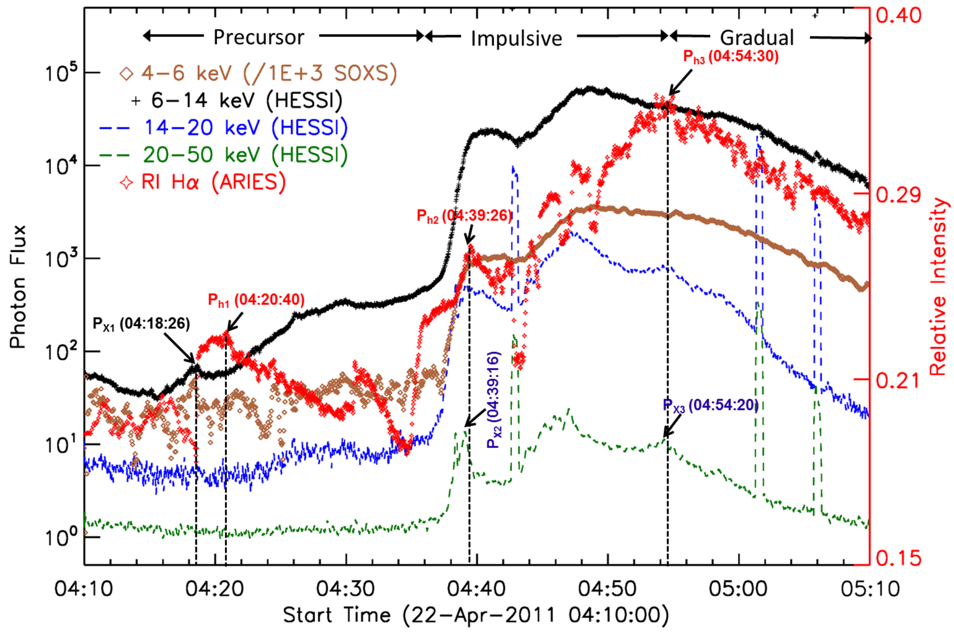

Figure 3.13: Temporal evolution of multi-wavelength emission during M1.8 flare on 2011 April 22. Relative intensity estimated from $H\alpha$ observations from ARIES/NAINITAL is plotted by red color's symbol. 4-6 keV emission observed by *SOXS* as well as 6-14, 14-20 and 20-50 keV emission by *RHESSI* shown by brown, black, blue and green symbols, respectively. $P_{x1,2,3}$ and $P_{h1,2,3}$ represent the corresponding peaks during precursor, impulsive and gradual phases in X-ray and $H\alpha$, respectively.

3.3.7.1 Evolution of Multi-wavelength emission in the precursor and main phases

The precursor phase is identified by the enhanced X-ray emission in SXR (<20 keV) 10-20 minute prior to the onset of the impulsive phase. Figure 3.13 shows temporal evolution of multi-wavelength emission during M1.8 flare on 2011 April 22. 4-6 keV emission observed by *SOXS* as well as 6-14, 14-20 and 20-100 keV emissions observed by *RHESSI* are shown by brown, black blue and green symbols, respectively. Relative intensity of the $H\alpha$ emission observed by $H\alpha$ telescope at ARIES/NAINITAL is estimated from the following equation.

$$RI = (I_f \text{ - } I_b)/I_b$$

Here I_b represents the background intensity estimated from a rectangle of 10×10 pixel away from the flare location and I_f represents mean of the intensities of the region in the frame having intensities above I_b for respective frames. Temporal evolution of RI of $H\alpha$ emission during the flare event is plotted by red color's symbol in Figure 3.13. $P_{x1,2,3}$ and $P_{h1,2,3}$ represent the corresponding peaks during precursor, impulsive and gradual phases in X-ray and $H\alpha$ intensity profile, respectively.

From Figure 3.13, we may note that the emission in 4-6 and 6-14 keV energy band (from *SOXS* and *RHESSI* observations respectively) has commenced on 04:15:18 UT and kept on increasing till 04:36:00 UT in the several steps. In contrast, the HXR (>20 keV) emission has been absent during the precursor phase while commenced at 04:36:00 UT in the form of impulsive burst almost simultaneous to impulsive SXR emission. Thus, we consider impulsive phase onset at 04:36:00 UT that lasted till 04:54:30, after which, gradual phase has commenced. The absence of the HXR emission in the precursor phase of this flare motivates us to probe the origin of the SXR emission. To understand this question, we study the spatial, spectral and temporal evolution of thermal and non-thermal emission in various phases of the M1.8 flare occurred on April 22, 2011.

3.3.7.1.1 Spatial analysis In order to study the spatial evolution of X-ray sources during the precursor and main phases, we synthesize X-ray images of the active region during the flare interval 04.08:30 - 05:05:30 UT on April 22, 2011 using *RHESSI* observations. *RHESSI* observes X-ray emission from the full solar disk in a wide energy range (3 keV - 17 MeV) with high temporal and energy resolution as well as with high signal sensitivity. Such observations enable us to synthesize the 2D images and spectra in the X-ray band, which provide valuable data for investigation of topological evolution of the thermal and non-thermal sources during flares. We employ CLEAN algorithm (Hurford et al., 2002) to synthesize the X-ray images during the precursor and main phases. Using the sub-collimators 3F, 4F, 5F, 6F, and 8F, the images are synthesized with spatial resolution of 1" and integrated over 60 s duration in 4 energy bands *viz.* 6-10, 10-14, 14-20 and 20-50 keV. The purpose of synthesizing the images in the aforesaid energy bands is to study the morphological evolution of sources of thermal and non-thermal emission. Generally, 6-10 and 10-14 keV emissions are dominated by thermal processes. Further, 14-20 keV emission may be considered to be an intermediate energy band between thermal and non-thermal processes and may be dominated by one component on the other over the evolution of the flare (Jain et al., 2005, 2011a; Aschwanden, 2007). However, >20 keV emission is considered to be originated mainly from the population of accelerated electrons and represent non-thermal source morphology. Further, in order to clearly visualize the source topology, we complement the synthesized X-ray images with the observations of *SDO/AIA* 131 Å. The temperature response of the 131 Å channel peaks ∼10 MK (Nitta et al., 2013) and therefore represents very hot plasma produced during the flare heating due to thermal processes which are also the origin of SXR (<10 keV) emission. Figure 3.14 shows a sequence of images in 131 Å wavelength observed by SDO overlaid by the contours of 30, 50 and 80 per cent intensity (drawn by red, blue and yellow lines respectively) of the maximum emission in co-temporal 6-10 keV energy band during the precursor phase and main phases. Panel (a) of Figure 3.14 shows 131 Å images at 04:09:09, 04:12:09 and 04:14:45 UT which represent the topology of AR and loops prior to the precursor phase commencement.

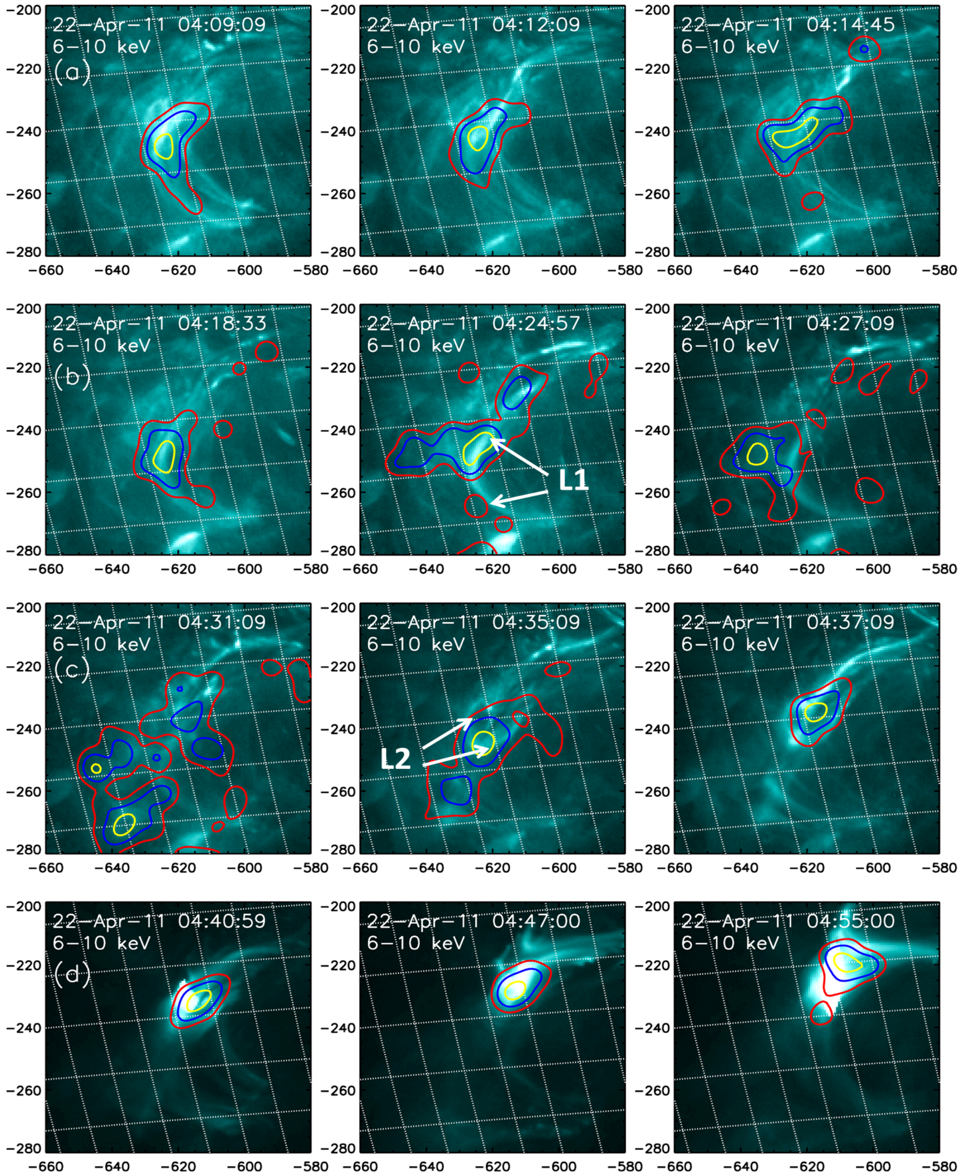

Figure 3.14: *RHESSI* X-ray contours of 30, 50 and 80 per cent intensity of the maximum of 6-10 keV energy band in each frame over plotted on the *SDO/AIA* observations in 131 Å wavelength. The three contours levels are drawn by red, blue and yellow colors' lines respectively. Panel (a) and (b) represent the evolution of thermal emission during the precursor phase while (c) and (d) represent the same during precursor to main-phase transition and main phase, respectively. The flaring loop during the precursor and impulsive phases is denoted by 'L1' in panel (b) and by 'L2' in the panel (c), respectively.

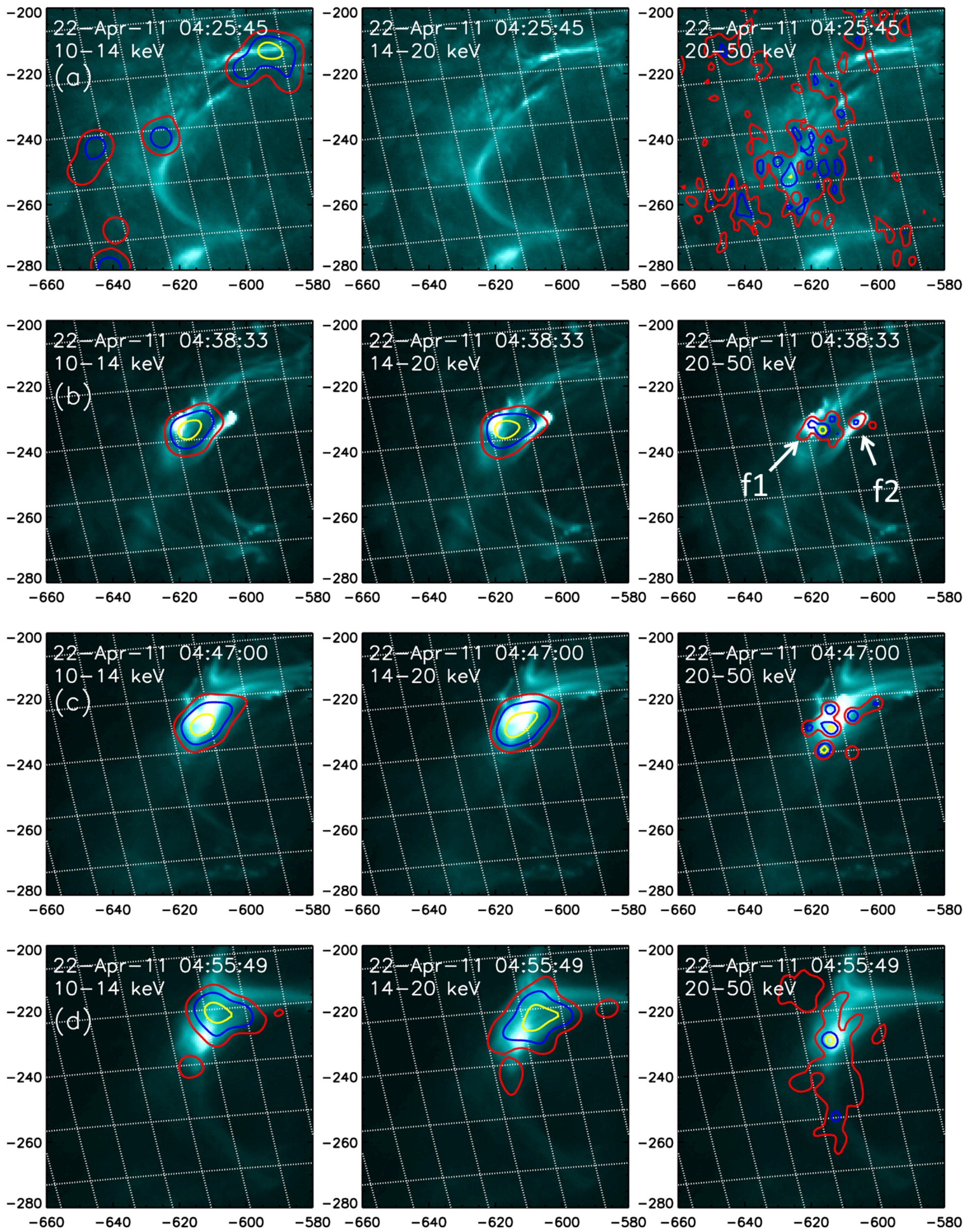

Figure 3.15: *RHESSI* X-ray contours of 30, 50 and 80 per cent intensity of the maximum of 10-14 and 14-20 and 20-50 keV energy bands during the precursor and main phase over plotted on the 131 Å emission observations from *SDO/AIA* as shown from top to bottom panels respectively. The contours levels are drawn by red, blue and yellow blue colors' lines, respectively. The foot-points revealed by the X-ray images are denoted by 'f1' and 'f2'.

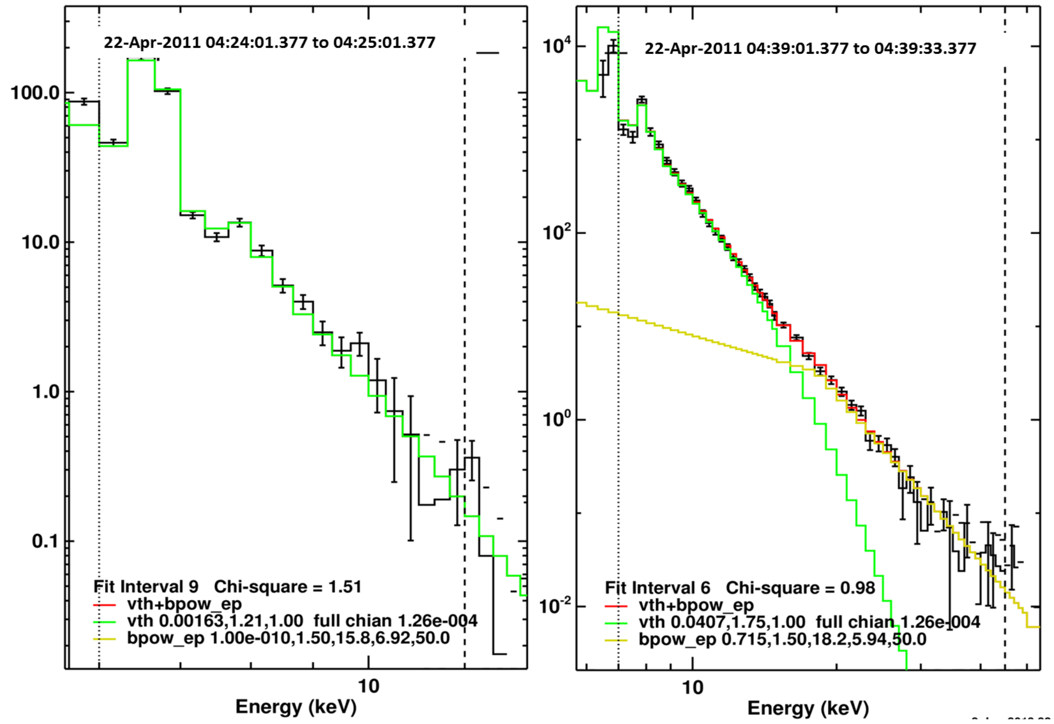

Figure 3.16: Photon flux spectrum of 2011 April 22 flare observed during 04:24:01-04-25:01 UT and 04:39:01-04:39:33 UT in the left and right panels, respectively shown by the black line. The spectral fit in the left panel is performed employing isothermal photon model function (green line) and that in the right panel employing isothermal (green line) + broken-power-law (yellow line) photon models with goodness of fit represented by $\chi^2 = 1.51$ and 0.98, respectively. The total model photon flux spectrum in the right panel is shown by the red line.

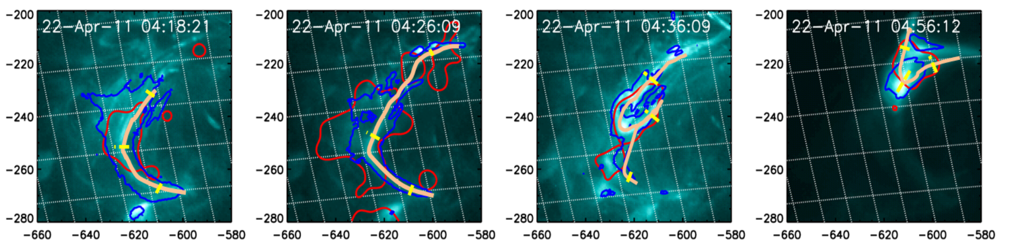

Figure 3.17: A sequence of images in 131 Å overlaid by contours of 30 per cent of the maximum intensity of co-temporal 6-10 keV energy band as well as in 94 Å wavelength drawn by red and blue colors, respectively. Traced loop is drawn by light orange color line while the diameter of the loop is shown by yellow line.

We may note from panel (a) that the loop-top appears to be brightened which may refer to the onset of heating at the coronal location of the loop and energizes the transfer of coronal plasma towards the chromosphere through conduction. Panel (b) shows the precursor phase emission evolution at 04:18:33, 04:24:57 and 04:27:09 UT, respectively. Panel (c) shows the images at 04:31:09, 04:35:09 and 04:37:09 UT representing the topological changes during precursor to main phase emission changeover and panel (d) represents the spatial evolution of sources during main phase at 04:40:59, 04:47:00 and 04:55:00 UT. From the panel (b), we may note a uniformly brightened loop 'L1' with a cusp shaped structure. Further, from panel (c) and (d), it may be noted that as the impulsive phase has commenced, the loop which is brightened during the precursor phase has faded and another loop 'L2' located close to northern foot-point of 'L1' started emission. From panel (d), we also note the systematic movement of X-ray emission as well as loops towards the north-west side. This kind of systematic motions in SXR source appears to be associated with the phenomena of asymmetric eruption as already reported for an X2.6 event on 2005 January 15 by Liu et al. (2010).

Further, we present the evolution of 10-14, 14-20 and 20-50 keV (HXR) emissions during the precursor and main phase in Figure 3.15. It is noteworthy that the X-ray intensity profile (*cf.* Figure 3.13) did not show the emission in HXR (>20 keV) energy band during the precursor phase which, however, has commenced at 04:36:00 UT, the onset of the impulsive phase. Panel (a), (b), (c) and (d) of the fig. 3 represent the *SDO/AIA* images in 131 Å wavelength at 04:25:45, 04:38:33, 04:47:00 and 04:55:49 UT, respectively overlaid by contours of 30, 50 and 80 per cent of the intensities in 10-14, 14-20 and 20-50 keV drawn by red, blue and yellow color's lines, respectively. It may be noted from panel (a) of the Figure 3.15 representing the images during the precursor phase at 04:23:45 UT that we do not see signatures of foot-point emission. However, during the impulsive phase, as shown in panel (b) and (c), we note the foot-points as marked by 'f1' and 'f2'. Further, during the evolution of emission in gradual phase, as shown in panel (d), the foot-point separation has increased in comparison to that during impulsive phase which may suggest the rising of reconnection region. Further, the source morphology in both 14-20 and 20-50 keV during the impulsive phase (panel b & c) reveal foot-point like structure which suggests that 14-20 keV energy band is dominated by non-thermal emission during this phase of the flare.

3.3.7.1.2 Spectral and temporal evolution of the X-ray emission

We study the temporal evolution of the flare plasma parameters *viz.* temperature (T), emission measure (EM) and density (n_e) employing the *RHESSI* observations. First, we synthesize the spectrum and spectral response matrix (SRM) files from the X-ray observations during 04:15:00 to 05:10:00 UT of 1 m and 32 s time cadence during the precursor and main phases, respectively. The energy resolution is kept to be 0.3 and 1 keV over the energy band of 6-15 and 15-50 keV, respectively. This spectrum and SRM files serve as input to the object spectral executive (OSPEX) package provided in SSW. The OSPEX is an object-oriented interface for X-ray spectral analysis of solar data. In each time-bin, we used OSPEX to estimate the T, EM, power-law index by forward-fitting the observed count spectra with the model count spectra generated by the inbuilt model functions *viz.* thermal, line emission, multi-thermal, and non-thermal functions which use CHIANTI database (Dere et al., 1997; Landi et al., 2012). The SXR emission is originated either from isothermal or multi-thermal plasma, while HXR emission is considered to be originated via non-thermally excited electrons (during reconnection). As there is no clear-cut demarcated energy between thermal and non-thermal emission, it is estimated by forward fitting the observed spectra fitting simultaneously employing thermal and non-thermal model photon functions. The spectral fitting is carried out by iterative adjustment of the free parameters leading to χ^2 close to 1, which enable us to estimate the flare plasma parameters from the best fitting of modeled counts over the observed counts.

We obtained best fit of the observed flux during the precursor phase considering isothermal function. Left panel of Figure 3.16 shows the spectral fitting of the X-ray emission in the 6-15 keV energy band (shown by dotted lines) observed during 04:24:01 - 04:25:01 UT, the time of precursor emission. The observed photon flux spectrum (black line) is fitted with the isothermal model (green line) with the goodness of fit represented by χ^2=1.51. The estimated temperature and emission measures are 1.21 keV (≈14 MK) and 0.0016 × 10^{49} cm^{-3}, respectively. The aforesaid technique is applied to the 1 minute and 32 s integrated spectra during 04:15 - 04:36 UT and 04:36 - 05:10 UT, respectively covering all phases of the flare. In this way, we estimated the temporal evolution of the temperature (T) and emission measure (EM) as shown in Fig. 6 panels (a) and (b), respectively. We also show the evolution of density in the panel (b) of Figure 3.18. The density is estimated by employing the relation

$$n_e = \sqrt{EM/V}$$

where EM is the emission measure and V is the volume of flaring region. The temporal evolution of EM has already been estimated from the forward-fitting performed on the observed spectra. The volume of the flaring region is estimated from the loop morphology. The loop morphology is very clear throughout the precursor and main phases, which enables us to estimate the volume, considering cylindrical shape of the loops, by $\pi r^2 l$ where r is the radius and l is the length of the flaring loop. The length of the loops have been estimated by manually tracing the same from the composite of the observation in 131 Å wavelength overlaid by contour of 30 per cent of the maximum intensity of co-temporal 6-10 keV energy band and of 94 Å wavelength drawn by red and blue colors, respectively. The traced loop has been shown by light orange color. The diameter of the traced loop is also calculated from these images by averaging the diameter estimated at three different positions of the visible loop as drawn by yellow line in Figure 3.17. The first-two images of the Figure 3.17 represent the shape of the loop during the evolution of emission in precursor phase at 04:18:21 and 04:26:09 UT. The rest of the two images represent the loop topology during impulsive phase at 04:36:09 and gradual phase at 04:56:12 UT respectively.

The non-thermal component in spectral observations during the impulsive phase is fitted considering the broken-power law photon model function as shown by the yellow line in the right panel of the Figure 3.16. The broken-power law function provides us the photon turn-over energy (ϵ_{to}), power-law index (γ) above and below the ϵ_{to} and normalization value at 50 keV (F_{50}). The power-law index below ϵ_{to} is fixed to the value of 1.5 (Saint-Hilaire and Benz, 2005). The temporal evolution of the non-thermal power-law index (γ) and the HXR flux in 20-50 keV is plotted in the panel (c) and (d) of Figure 3.18, respectively. We find T, EM and γ to be varying in the range of 12.4 - 23.4 MK, 0.0003 - 0.6 $\times$ 10^{49}cm^{-3} and 5 - 9.0, respectively. Further, the photon turn-over energy (ϵ_{to}) is found to be varying in the range of 14-18 keV. This break energy suggests that the emission above $\sim$ 14 keV is dominated by non-thermal emission which is consistent with the non-thermal X-ray source morphologies in 14-20 and 20-50 keV energy bands during the main phase emission as discussed in section 3.3.7.1.1. From the temporal evolution of non-thermal power-law index (γ) (cf. panel (d) of Figure 3.18), we may note that γ remains steady during impulsive phase (04:47:10-04:54:30 UT) to the value of $\sim$7.0. This suggests continuous bombardment of non-thermally accelerated charged particles which may be noted from the panel (d) of the Figure 3.18. We may further note the double peaks in the HXR intensity profile at 04:39:16UT and 04:47:10 UT followed by a plateau region during 04:47:10-04:54:30 UT. This suggests the involvement of multi-loop configuration followed by their systematic destabilization and activation which is consistent with the movement of the centroids of the X-ray as well as EUV 131 Å sources as revealed from the spatial study of multi-wavelength sources in Section 3.3.7.1.1.

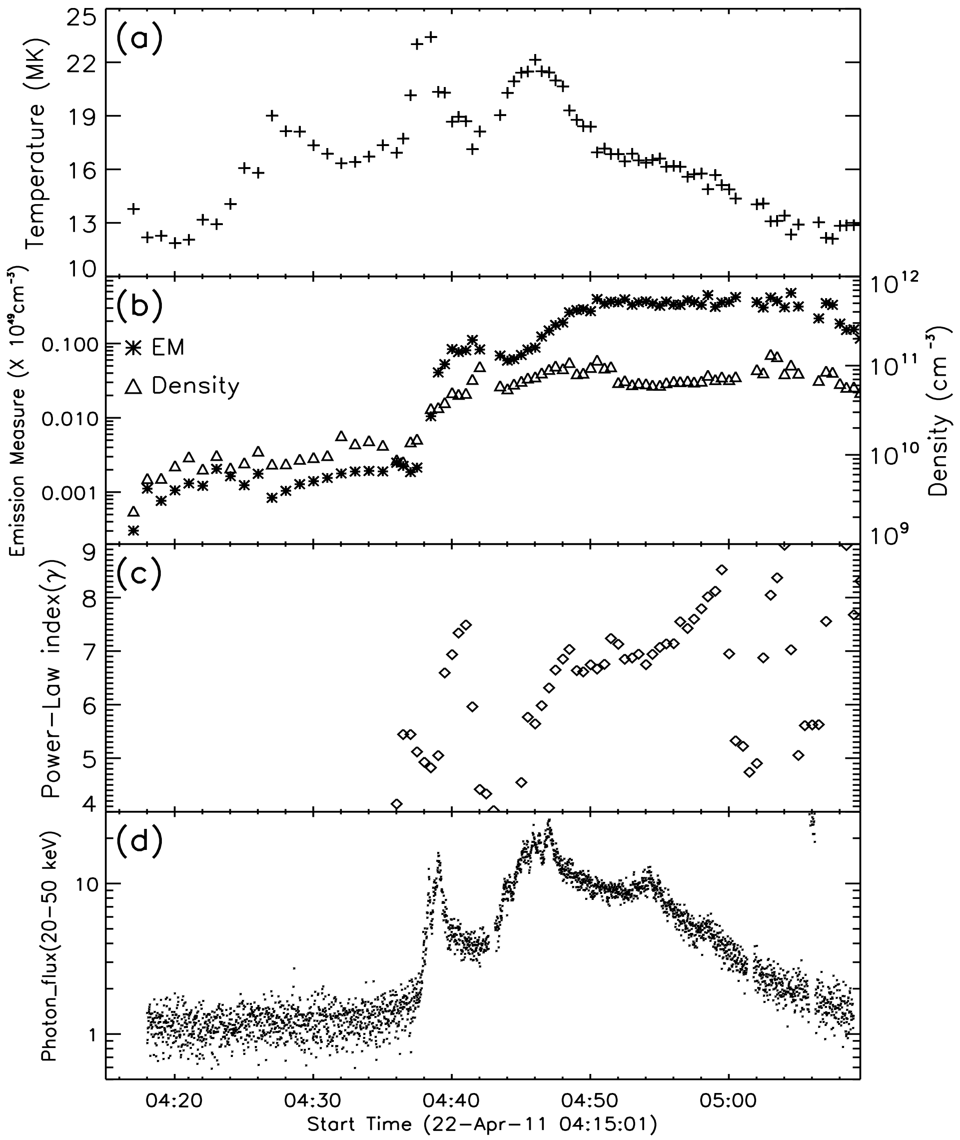

Figure 3.18: Panel (a): Temporal evolution of temperature (T), Panel (b): Left - EM; Right- density, Panel (c): negative non-thermal power-law index (γ) and Panel (d): Intensity profile of emission in 20-50 keV from *RHESSI* observations.

Further, this study has enabled us to perform a comparative study of the evolution of flare plasma parameters during the precursor and the main phase. The peak temperature during the precursor phase has been estimated to be 19.1 MK, ∼80 per cent of that attained during the impulsive phase (∼23.0 MK). It may be noted that the rate of increase of EM during the precursor phase has been insignificant in comparison to that during the impulsive phase.

On the other hand, the estimated density has remained almost constant to the value of $\sim 10^{10}$ cm^{-3} during the precursor phase and increased rapidly after the commencement of impulsive phase to the value $>10^{11} cm^{-3}$. The above analysis shows slow evolution of T and n_e suggesting gradual heating during the precursor phase. This result is in agreement to Battaglia et al. (2009). The temporal evolution of n_e as plotted in panel (b) of Figure 3.18 shown slow evolution with a rate of during the gradual phase very similar to that during the precursor phase. During the precursor phase, the density varied between 1 - 8 $\times$ 10^9 cm^{-3} with a rate of change $\sim$ 5.5 $\times$ 10^6 cm^{-3} - s^{-1}. On the other hand, the rate of change of density during the impulsive and gradual phase phase were $\sim$ 1 and $\times$ 10^8 cm^{-3} - s^{-1} and $\sim$ 6.1 and $\times$ 10^6 cm^{-3} - s^{-1}, respectively. This suggests the possibility of common physical origin of the precursor and gradual phases dominated by thermal processes.

3.3.7.2 Thermal and Non-thermal Energetics

We estimate the thermal and non-thermal energies available during the precursor, impulsive and gradual phases of the flare evolution from the technique employed in Saint-Hilaire and Benz (2005). For estimating thermal energy, we employ following equation.

$$E_{th} = 3k_b T \sqrt{EM.V.f} \tag{3.1}$$

where T and EM represent temperature and emission measure of flare plasma estimated from fitting the spectral observations in Section 3.3.7.1.2. V represents the volume of the flaring region and estimated by cylindrical approximation of the loops as discussed in Section 3.3.7.1.2. f represents the filling factor and assumed to be 1 which gives an estimation of upper limit of the thermal energy available in the flare. The thermal energy release rate is estimated to be varying in the range of 0.1- 4 $\times$ 10^{29} ergs/s as shown in Figure 3.19. The total thermal energy released during the flare is estimated to be $\sim$ 1.3 $\times$ 10^{31} ergs out of which $\sim$2 per cent energy was released during the precursor phase and is estimated to be 2 $\times$ 10^{29} ergs.

Further, we estimate non-thermal kinetic power considering the turnover model of electron flux from the following equation

$$P_{nth} = \int_{E_{min}}^{E_{to}} A_e E_{to}^{-\delta} dE + \int_{E_{to}}^{\infty} A_e E^{-\delta} dE \tag{3.2}$$

Here, δ is the power-law index of the incident electron spectra and is estimated from the fitted power-law index γ by δ=γ+1. E_{min} is the minimum energy for the electron flux and considered to be 6 keV for the current study. E_{to} is the electron turn-over energy and estimated by the photon turn-over energy (ϵ_{to}) and electron power-law index (δ) employing the relation of fraction ϵ_{to}/E_{to} versus δ as derived in Saint-Hilaire and Benz (2005). They estimated that the fraction ϵ_{to}/E_{to} varies between 0.4-0.6 for the values of δ ranging 3 to 8. With this relation, we estimate the interpolated value of aforesaid fraction for each δ to estimate E_{to} corresponding to each ϵ_{to}. Thus, E_{to} is found to be varying in the range of 24-35 keV. Further, A_e is obtained from the relation

$$A_\epsilon = \frac{A_e}{4\pi D^2} \overline{z^2} \frac{\kappa_{BH}}{K} \frac{B(\delta-2,1/2)}{(\delta-1)(\delta-2)}$$

where Aϵ is the normalization index defined as

$$I_{thick}(\epsilon) = A_\epsilon \epsilon^{-\gamma}$$

The non-thermal kinetic power (P_{nth}) for this flare is estimated which varies in the range of 0.01- 2 $\times$ 10^{30} ergs/s and shown in Figure 3.19. Further, total non-thermal energy released is estimated to be $\sim$ 4 $\times$ 10^{31} ergs.

We perform a comparative study of the energy released during various phases of emission. The total (thermal+non-thermal) energy (E_{tot}) released during the flare is estimated to be $\sim$ 5.3 $\times$ 10^{31} ergs. During the precursor phase, only $\sim$1 per cent of E_{tot} has been released which is originating from thermal processes. Further, during the impulsive phase, the rate of release of non-thermal energy is $\sim$ 1- 10 order higher than that of thermal energy (*cf.* Fig. 7). However, after the onset of the gradual phase, the rate of release of non-thermal energy has been superseded by the thermal energy release rate and the ratio of non-thermal to thermal energy release rate Q_f reduces to $\sim$ 0.2, in agreement to Li et al. (2005).

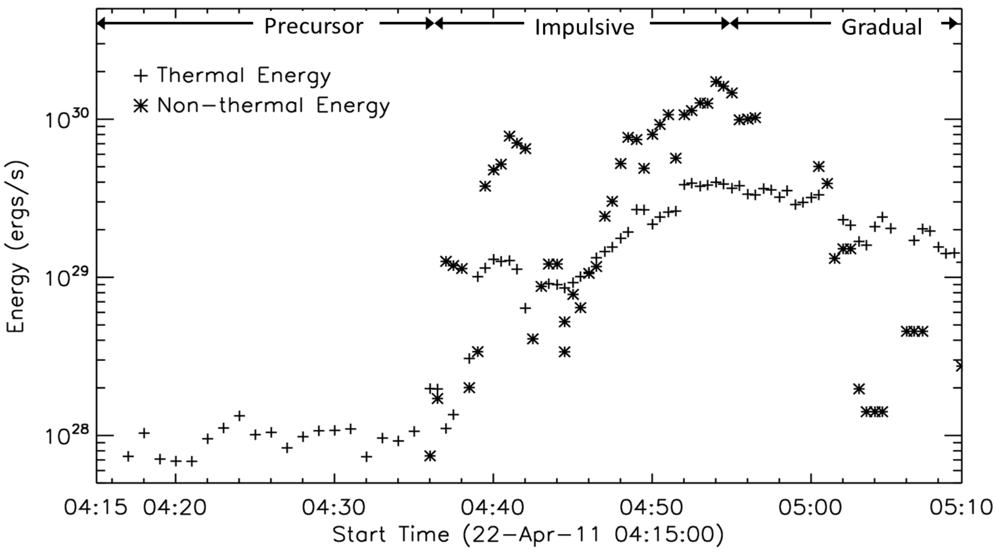

Figure 3.19: Temporal evolution of thermal and non-thermal energy release rate during various phases of the 2011 April 22 flare.

3.3.7.3 Temperature and Emission Measure evolution

We further study the spatial and temporal evolution of temperature (T) and emission measure (EM) employing multi-wavelength observations. We synthesize T and EM maps using the technique established by Aschwanden et al. (2013). The T and EM maps over the active region are synthesized using observations from the 6-channels of EUV *viz.* 94, 131, 171, 193, 211, 335 Å wavelengths. Firstly, the alignment of the co-temporal images obtained in 6 wavelengths with an accuracy of ∼1 pixel is performed by fitting the solar-limb detection algorithm[1]. The perfectly aligned images give a set of 6 EUV intensities at each pixel location over the AR which serves as input for forward-fitting modeled by Gaussian function to estimate emission measure-weighted temperature for a given pixel. This fitting is performed pixel-by-pixel to synthesize

[1] `http://www.lmsal.com/~aschwand/software/aia/aia_dem.html`

temperature and emission measure maps of the flaring region. We employ the aforesaid steps to the AIA observations obtained during 04:10:00 - 05:10:00 UT to synthesize the maps. The observations from *SDO/AIA* during the precursor phase were not saturated which allow us to restore the spatial evolution of the T and EM without any limitation. Although the observations happened to saturate for some intermediate frames during the impulsive phase, the automatic exposure control onboard *SDO/AIA* is programmed in such a way so as to deliver every second image to be unsaturated. We estimate peak temperature in the duration of synthesized map to be varying in the range of 5.7 - 10 MK. We overlay the contours of 80 per cent of the maximum intensity of 6-10, 10-14, 14-20 and 20-50 keV energy band on the T and EM maps as drawn by lines of green, blue, khaki and light orange colors, respectively as shown in Figure 3.20. The top panel of Figure 3.20 represents the spatial evolution of temperature at 04:05:03, 04:12:14, 04:19:26 and 04:38:14 UT, respectively. We further overlay the contour levels of 30 and 70 per cent of the maximum positive and negative magnetic-field observations from *SDO/HMI* over the T-map to track the polarity inversion line (PIL). The contours corresponding to positive and negative magnetic-fields are drawn with cyan and black lines respectively. It may be noted from the T-map synthesized at 04:05:03UT that the heating has started co-spatial to the polarity inversion line prior to the onset of SXR enhancement during the precursor phase. We further plot the EM-map in the middle and bottom panels of Figure 3.20 during the precursor and main phases, respectively.

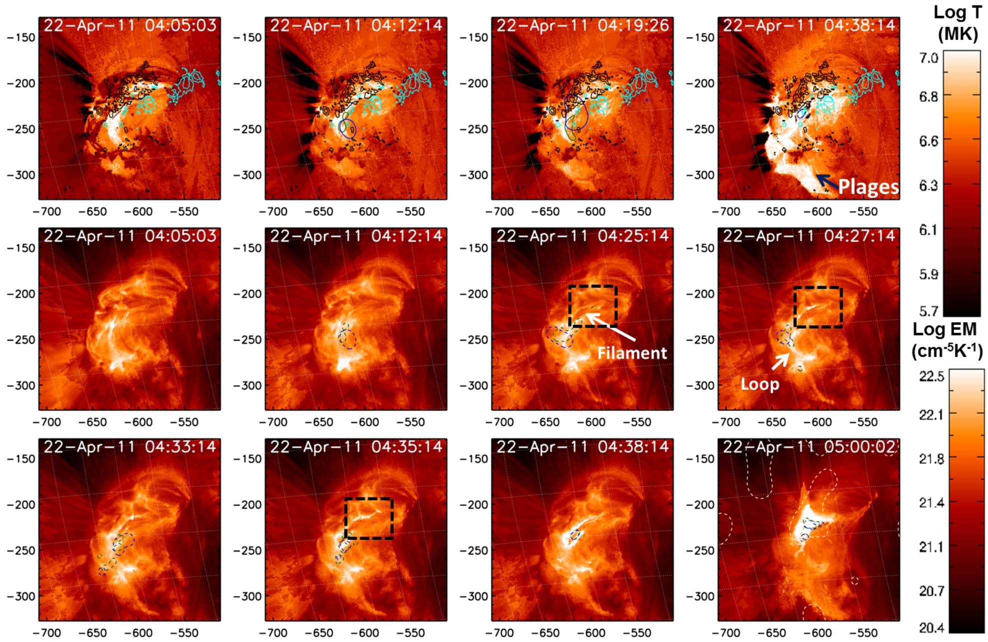

Figure 3.20: Temperature (top) and Emission measure (middle and bottom panel) maps. The temperature map is overlaid by HMI contours of leading and following polarities as represented by cyan and black colors respectively. The box in the middle and lower-panels represent the region of enhanced intensity prior to the eruption of the filament.

The study of spatial evolution of the temperature with the time cadence of 12 s led us to various salient features: 1) The existence of heated plasma co-spatial to the polarity inversion line (PIL) during precursor phase; 2) Heated area has been found to be substantially increased during the impulsive phase in comparison to that during precursor phase; and 3) Plage brightening associated with the main phase with the peak temperature ∼10MK. Similarly from the synthesized EM maps we have been able to trace the filament and morphological evolution of T and EM in its vicinity.

Further, as previously mentioned, the loop-shape structure co-spatial to the SXR contours visible during the precursor phase can be observed in the middle panel of Figure 3.20. We have noticed enhanced density in the vicinity of the north-west leg of the filament first appeared at 04:27:14 UT as highlighted in the dashed box in the middle panel of Figure 3.20. In addition, we have also noted slow rise of the filament prior to the eruption, however almost parallel to the line-of-sight of the observations imposing the restriction on estimating the speed of eruption. Further, it is noteworthy that the area of heated dense region enhanced at 04:35:14 UT, ~60 s before the onset of impulsive phase emission. This suggests that the small scale magnetic reconnection underneath the filament and associated heating have been going on prior to the accelerated eruption (Liewer et al., 2009) and the onset of impulsive phase of the flare. We further study the morphological evolution of the filament in conjunction to the synthesized T and EM maps in the following section.

3.3.7.4 Hα emission and Filament morphology

We use $H\alpha$ observations from ARIES/Nainital to study the role of the filament in the energy release during various phases of emission. Shown in Figure 3.21 is a sequence of Hα images during various phases of emissions of the flare. The top panel shows a series of images representing the filament activity prior to the onset of the precursor phase at 04:01:15, 04:04:36, 04:05:52 and 04:10:54 UT respectively. We denote the filament legs into the southern as well as eastern direction as L1 and L2 respectively. It may be noted that the L1 started sequential movement towards east as marked in top panel of the Figure during 04:05:52 - 04:10:54 UT. Further, L1 possibly erupted prior to the onset of emission in the precursor phase and disappeared as may be seen in the frame at 04:15:05 UT in the middle panel. In addition to the partial eruption of the filament, we have also noticed the filament activity in the form of sigmoidal shape and a clear appearance of other leg during 04:29:48 - 04:36:00 UT as represented by L3 in the middle panel. The bottom panel of the Figure 3.21 represents the time sequence of $H\alpha$ filtergrams during main phase of the flare at 04:36:04, 04:37:45, 04:40:07 and 04:56:02 UT, respectively. We note that the enhanced emission visible at 04:37:45 UT which expanded later during the gradual phase.

The study of the spatio-temporal evolution of the filament reveals the role of the partial filament eruption in triggering the precursor phase emission and later the whole filament system has been destabilized prior to the onset of the main phase emission. In order to probe the cause of destabilization of the filament we investigate the morphological evolution of filament in conjunction to the T and EM maps.

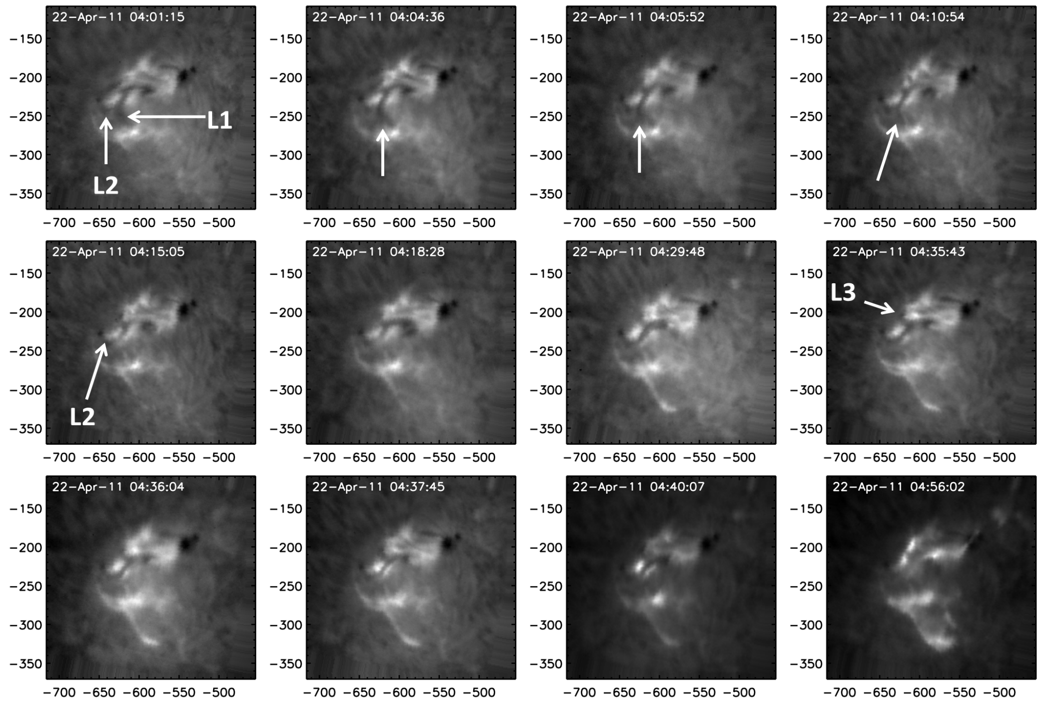

Figure 3.21: Top panel - Sequence of images representing the filament activity prior to the onset of precursor phase at 04:01:15, 04:04:36, 04:05:52 and 04:10:54 UT, respectively. Middle and bottom panels represent the evolution of filament during the precursor and main phases, respectively.

Figure 3.22 shows the time series of $H\alpha$ observations from ARIES/Nainital overlaid by the contours of log T= 6.8 and log EM= 22.5 drawn by red and green colors, respectively. We may note the heating of the filament from the top panel of Figure 3.22 which represents the evolution of T and EM with H-alpha intensity during precursor phase at 04:10:54, 04:18:28 and 04:29:48 UT respectively. Further, the heating remains co-spatially associated with the filament during the whole precursor phase which, however, followed an expansion during the main phase after the destabilization of the filament. In addition, contours representing EM evolution in the top panel clearly depict the loop-shaped structure during the precursor phase. The evolution of loop emission during precursor phase has also clearly been visible in 131 Å.

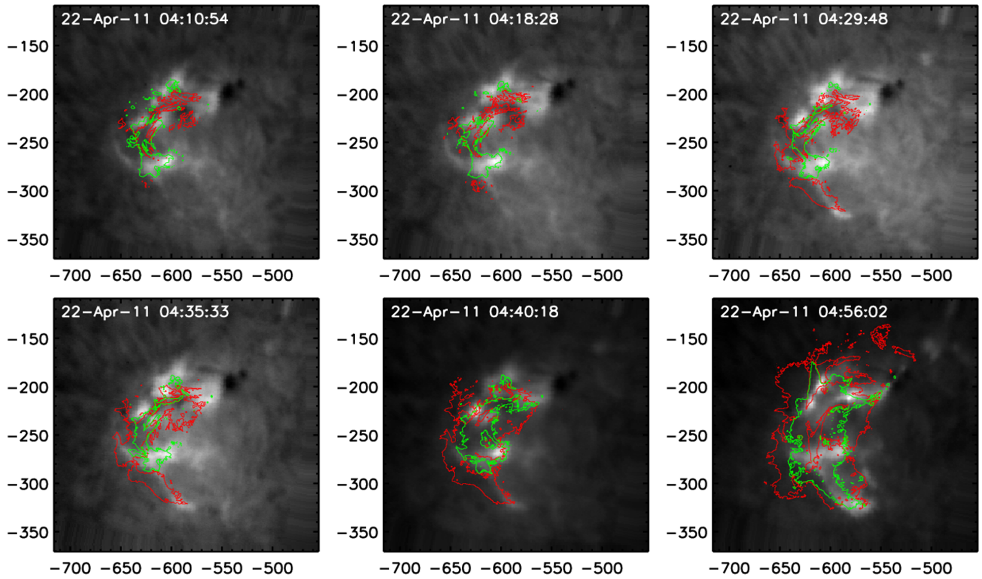

Figure 3.22: Sequence of $H\alpha$ images (ARIES/Nainital) overlaid by the contours of log T=6.8 and log EM=22.5 drawn by red and green lines, respectively.

3.4 Discussion, Summary and Conclusions

We investigate the temporal, spatial and spectral evolutions of multi-wavelength emission during the precursor phase of 50 solar flares to understand the physical processes occurring during this phase. We also aim to understand the association of physical processes occurred during this phase with those occurring in the well-understood main phase emission. In this regard, we performed statistical and quantitative characterization of the flare plasma parameters during the precursor as well as main phase in order to to visualize their association during the main phase. In addition to the analysis of the large dataset, a case study of an M1.8 flare occurred on 2011 April 22 in NOAA AR 11195 has also been carried out. In this section we combine the results obtained from multi-wavelength analysis and interpretations to propose a unified scheme of energy release during the precursor and main phases. We present the key results of the study and associated implications as following:

3.4.1 Flare plasma parameters during various phases of emission

We estimated the flare plasma parameters *viz.* Temperature, Emission measure, non-thermal spectral index, and thermal non-thermal break energy employing a large dataset consisting of 50 flares attributing precursor as well as main phase. From this study, we have found that although the peak intensity count flux during the precursor phase is $\sim 10\%$ of that during the main phase, the estimated temperature during the precursor phase attains substantially high value *i.e.* $\sim 80\%$ of the peak temperature attained during the main phase. On the other hand, the estimated emission estimated is ~ 2 orders lesser than that attained during the main phase. In this regard, we propose very high temperature plasma giving rise to the precursor phase without pronounced HXR emission. Although recent attempts to explore the origin of the precursor phase emission by Altyntsev et al. (2012); Falewicz et al. (2011); Battaglia et al. (2009) put forth a debate on the existence of thermal and non-thermal emission signatures during the precursor phase, they do agree on the existence of high temperature plasma during this phase which is in agreement to the current study. Further, spectral analysis of X-ray emission carried out during the precursor phase studied in this thesis clearly reveal thermal dominated distribution of the plasma responsible for the precursor emission.

The trigerr of this gradual energy release/leakage of energy in the form of precursors prior to impulsive explosion was still less explored. In this regard, we further explored the scenario of energy release during the precursor and main phases of twenty flares employing multi-wavelength observations. We carried out the investigation of the temporal and spatial evolution of photospheric magnetic-field parameters *viz.* signed and unsigned flux, gradient and shear. Although we noted small scale magnetic-field activities, no substantial evidences of magnetic-field emergence, submergence and/or cancellation was temporally associated with the precursor phase emission. This result is not in complete agreement ot the implications by Tandberg-Hanssen and Emslie (1988); Chifor et al. (2007) who suggested significant signatures of mageticfield evolution during the precursor emission. In contrast, we found large scale flux cancellation during impulsive and gradual phase as previously suggested by Jain et al. (2011a); Chandra et al. (2011) etc. Moreover, we carried out the investigation of spatial and temporal evolution of E/UV emission in conjuction with synthesized temperature and emission measure maps and filament evolution. We found conslusive evidence of filament slow-rise and/or partial eruption co-temporally associated with the precursor phase emission. In addition to this, we also noted the enhanced heated plasma as well as emission measure in the vicinity of the filament following polarity inversion line. This manifestation lead us to the scenario of filament activation joining both the phases of emission. We propose that during the precursor phase, small-scale magnetic reconnections in the vicinity of polarity inversion line heat the plasma which destabilizes the filament for eruption lately trigerring the main phase emission.

We present the implications from multi-wavelength investigation of various phases of emission during April 22, 2011 M1.5 class event as following.

1. The study of spatial evolution of multi-wavelength emission during the precursor and main phases has been performed. We note a brightened loop in X-ray and UV emission, specially in 131 Å during the precursor phase whereas no foot-point emission was observed during this phase. Therefore, the appearance of coronal source heating prior to the precursor emission suggests the possibility of conduction-driven chromospheric

heating during this phase. In contrast, the foot-point HXR sources in addition to the SXR loops have been pronounced during the main phase which can be explained by the standard model of energy release in solar flares.

2. The spectral fitting has been performed on the *RHESSI* observations over the flare duration to study the evolution of flare plasma parameters *viz.* temperature, emission measure and power-law index. The estimated temperature during the precursor phase attained its peak value of $\sim$ 10 MK in comparison to that in the impulsive phase of $\sim$ 12 MK. We have also estimated the T and EM values from *SDO/AIA* observations for the events listed in Table 3.2. We note that the T values estimated from *RHESSI* are twice as high as from SDO/AIA differential emission measure peak temperature. This difference in the temperature values may be attributed to the fact that current investigation employs isothermal photon function for estimating the flare plasma temperature from *RHESSI* observations which leads to the overestimated values of T as demonstrated in the recent studies by Ryan D. F. et al. (Private Communication) and (Aschwanden and Shimizu, 2013).

3. The spectral fitting has also revealed that the EM is $\sim$ 2 orders lesser than that attained during the main phase. Further to this, the rate of increase of EM during the precursor phase has been slow in comparison to that during the main phase. The synthesized X-ray images revealed extended source during the precursor phase in comparision to that during the main phase. This suggests that significant density enhancement in comparision to that during the precursor phase. In the case study performed for April 22, 2011 flare, the estimated density (n_e) has remained almost constant at $\sim 10^{10}$ cm^{-3} during the precursor phase however increased drastically to $\sim 10^{11}$ cm^{-3} after the commencement of the impulsive phase. Thus the temporal evolution of EM and n_e suggests a

relatively slow heating of the flare plasma most likely to be due to gentle evaporation by conduction front, which has also been suggested by Battaglia et al. (2009).

4. The study the temporal evolution of relative intensity of several $H\alpha$ brightening within the flaring region and its correlation with the X-ray emission have been carried out for the flare occurred on April 22, 2011 as presented in the multi-wavelength light curve in Figure 3.13. The onset of the precursor phase emission in $H\alpha$ at 04:18:24 UT is unambiguous. Further, the first peak in the $H\alpha$ emission P_{h1} is delayed by $\approx$ 134 s relative to that in 6-20 keV emission denoted by P_{x1}. Theoretically, the delay of the peak in $H\alpha$ intensity profile with respect to the corresponding peak in the X-ray intensity profile represents the response time of the chromosphere which is heated either by the accelerated electrons or by the conduction front produced during magnetic reconnection. Considering the fact that this heating is produced by the non-thermal particles' interaction with the chromosphere, the delay is short ($\sim$10 s) which, on the other hand, turns out to be $\sim$20 s in case of conduction-driven chromospheric evaporation (Radziszewski et al., 2011). The extra-ordinary long delay of 134 s may point towards the phenomena of slow response of the chromosphere undergoing through gentle evaporation originated by conduction-front during the precursor phase. We estimate the half loop-length (L_{loop}) from 131 Å image during the precursor phase to be $\sim$ 30,000 km which suggests the conduction front speed ($v_{cond} = L_{loop}/\Delta t$) $\sim$ 450 km/s. This estimated velocity may provide direct evidence to the numerically estimated speed of the conduction front ranging between 450 and 600 km/s by Guidoni and Longcope (2010). On the contrary, during the impulsive phase, P_{h2} has been delayed by $\sim$10 s with respect to P_{x2} which indicates non-thermal interaction with the chromosphere during this phase.

5. To understand the source of the energy made available during the precursor phase, we undertook the study of filament kinematics during the precursor and main phases. We noticed the partial eruption of the filament prior to the onset of precursor phase. We also find gradual but continuous reformation of the filament leading to a complex (sigmoid) shape. This suggest that after the partial filament eruption leading to the precursor phase emission, the magnetic-field restructuring has occurred which led to a more complex field-line connectivity. Thus the filament underwent heating and slow-rise throughout the precursor phase caused by magnetic reconnection underneath the filament (Liewer et al., 2009) and the main phase emission has been triggered by the eruption of the unstable filament. We also note the enhancement of UV emission the vicinity of the of the filament before the onset of filament eruption which assist the scenario presented here for the eruption of the filament.

Based on the 50 flare events and the results drawn from them, we propose that the plasma heating during the precursor phase is originating via the conduction front triggered by the partial filament eruption/slow-rise of the filament. Next, the heated filament undergoes slow rise and heating due to magnetic reconnection during the precursor phase and finally erupts to produce main phase emission.

Chapter 4

Energy-dependent Heating and Cooling of the Solar Flare Plasma

4.1 Introduction

X-ray emission from solar flares has been traditionally treated as well as shown to be isothermal in nature (Landi and Chiuderi Drago, 2003; Landi and Phillips, 2005; Landi et al., 2006; Phillips et al., 2003; Caspi, 2010), particularly while simulating spectral line and continuum intensities using CHIANTI atomic database (Landi and Klimchuk, 2010; Phillips et al., 2010). The analysis of Fe-line emission in flare spectra to derive the flare Fe/H abundance ratio (Phillips et al., 2006) was based on the assumption that the emitting plasma was isothermal. This conflicts with the appearance of flares with multiple loops, in which each loop may have a different Temperature. Further, the fact that the plasma is heated at different temperatures (multi-thermal plasma), and the emission measure varies as a function of temperature emphasizes the crucial need to study the X-ray spectra with high energy and temporal resolution. In spite of this, the isothermal approximation appears to apply to many flares, even including long-duration flares observed spectroscopically from Yohkoh in S XV and Ca XIX lines (Phillips et al., 2005). Such flares have obvious multiple-loop structures. The isothermal fits suitably apply to RHESSI spectra at low energies. However, for the rise phase of many flares, fits to RHESSI spectra are not so satisfactory, even for spectra which appear not to have any non-thermal component in the low-energy continuum (Fletcher et al., 2011).

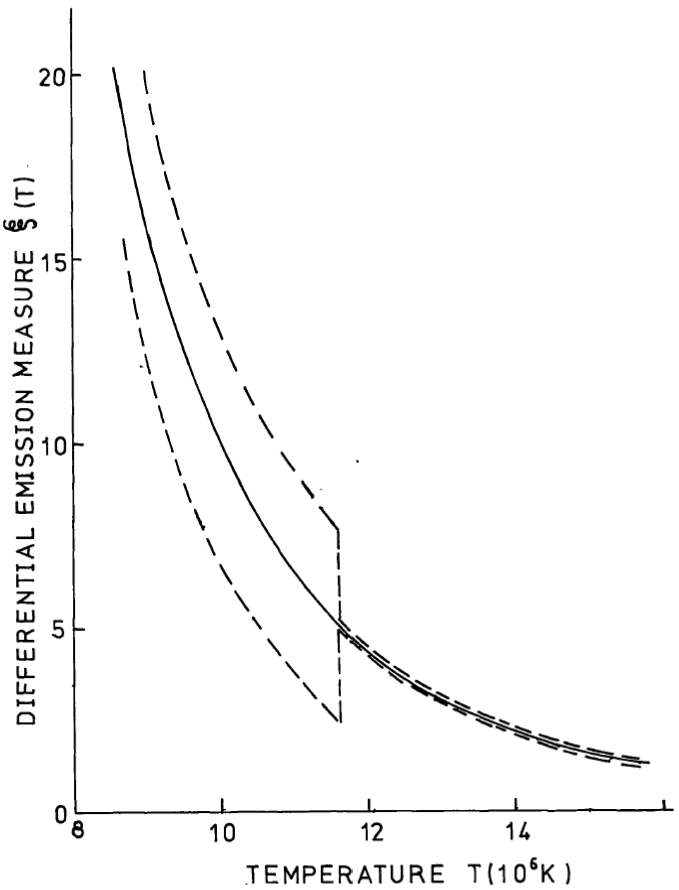

Figure 4.1: Illustration of the insensitivity of bremsstrahlung spectrum to the temperature of the source plasma. The region within the dashed line shows that any set of DEM and T within that will yields the same spectrum as obtained from the solid line to within 10% uncertainties. Figure courtesy: Craig and Brown (1976)

However, Craig and Brown (1976) formulated the concept of multi-temperature plasma in the flare considering differential emission measure (DEM). They concluded that there exists a large uncertainties in the analysis which is inevitable due to the calculations involve inversion of the spectra to the parent distribution. Figure 4.1 illustrates the insensitivity of bremsstrahlung spectrum to source temperature structure. Any distribution function whatever within the dashed line will yield the same spectrum as the solid line to within 10% over the entire range of energy.

Although limitations exist, a more physically based description would involve a set of nearly isothermal components reflecting the multiple loops each in its own cooling equilibrium, so that the DEM parameters α or temperature-epivot would characterize the distribution of the components needed. Therefore, Aschwanden (2007), for the first time, investigated the nature of X-ray emission in solar flares with the help of modeling the spectral-temporal hard X-ray flux in terms of multi-temperature plasma. In his quantitative model, he has characterized the multi-temperature differential emission measure distribution (DEM) and non-thermal spectra with power-law functions. By fitting this model to the spectra and energy-dependent time delays on the RHESSI flare observations, he suggested the flare X-ray emission to be multi-thermal in nature. As the RHESSI instrument's response function below 10 keV is highly uncertain he restricted his work up to 10 keV only. It is believed that thermal emission is mostly pronounced in the energy below 10 keV which is still not addressed in this context. Therefore, Jain et al. (2011a) has employed observations in the energy range 4-25 keV observed by Solar X-ray Spectrometer (SOXS) mission as presented in this chapter.

Jain et al. (2008) showed that the X-ray bursts associated with solar flares above 25 keV come mostly from the non-thermal bremsstrahlung while the X-ray emission between 10 and 25 keV in principle includes both thermal and non-thermal contributions. Both types of X-ray emission occur during solar flares and the clear demarcation line between the two processes is essential for quantitative estimation of energy release by thermal and non-thermal processes in solar flares. Break energy is defined as a demarcation energy after which non-thermal emission dominates the thermal emission. In literature, low-energy cutoff or turn over energy is also the term used to separate the thermal and non-thermal contribution in the flare spectra. Aschwanden (2007), ignoring possible low-energy cutoff, has found the thermal-non-thermal crossover energy 18 $\pm$ 3.4 keV using the power law approximation of X-ray emission. On the other hand, Gan et al. (2002) estimated the low energy cutoff (E_c) of the non-thermal emission by fitting the hard X-ray spectra obtained from BATSE/CGRO. They found E_c varies between 45 and 97 keV with an average of 60 keV for 44% of the events considered for investigation. For another 44% events they suggested that E_c could be lower than 45 keV due to non-availability of data below 45 keV. Further, for 11% of events, the hard X-ray spectra could not be explained by a beam of power-law electrons with low-energy cutoff, which supports the break-energy concept and that could be on the lower side (Jain et al., 2000; Aschwanden, 2007). Sui et al. (2005) found 24 ± 2 keV as the low-energy cutoff (E_c) to ensure that always thermal emission dominates over non-thermal emission in low energy. On the other hand, Saint-Hilaire and Benz (2005) considering 20 keV as the turnover energy of non-thermal electrons (E_{to}) estimated available energy to be $\approx 2 \times 10^{30}$ ergs, almost the same value as Sui et al. (2005) found for an M1.2 class flare. In principle, the low-energy cutoff seems physically not realistic as such a configuration leads to plasma instability. Therefore, the turnover of break energy appears to be more physically realistic and needs to be measured as precisely as possible. In this chapter, we also present a detailed study of break-energy estimation by characterizing flare plasma up to 25 keV with high spectral resolution observations.

The time-profile of the flare emission in several energy bands shows a sequential delay in the timings of respective peak emission with smallest energy emission peak is delayed most. Aschwanden (2007) modeled the energy-dependent delay by a cooling time scale and suggested conduction cooling to be operating in the rising phase of the flare. The characteristic times for heating and cooling of the X-ray emitting plasma in solar flares are estimated by modeling temporal evolution of temperature and the emission measure of the thermal X-ray burst, and the over-all length scale of the flare- heated plasma at thermal X-ray maximum. Culhane et al. (1970) treated the problem of flare produced plasma cooling by examining three cooling processes: Coulomb collisions of hot electrons with lower-temperature ions, conductive cooling, and radiative cooling. They concluded that the first process is unimportant because it is not applicable to solar flares (Somov, 1978), and that radiative cooling, which varies as the square of the electron density, is ineffective below particle density 10^{11} cm^{-3} (during rise phase of the flare). Based on observed flare parameters, Antiochos and Sturrock (1978); Culhane et al. (1994) and Aschwanden and Alexander (2001) suggested thermal conduction to be the dominating cooling mechanism in high-temperature soft X-ray loops during the rise or impulsive phase, while radiative cooling in the gradual phase when the flare loop-density exceeds 10^{11} cm^{-3}. We model the energy-dependent cooling delays which enabled us to estimate the break-energy, for the first-time, in the time domain without spectroscopic study of the flare emission. We also study the effect of cooling on the well-known Neupert effect (Neupert et al., 1969; Dennis and Zarro, 1993). According to the standard model of solar flares, the reconnection accelerated charged particles stream along field lines toward the dense chromosphere where as a consequence the hard X-ray emission (HXR hereafter) is produced and chromosphere evaporation begins to produce soft X-ray (SXR hereafter) emission. Therefore, the time-derivative of SXR should mimic HXR emission (Dennis and Zarro, 1993). However, as the plasma producing SXR cools simultaneously to the heating in the form of HXR emission (Culhane et al., 1970), Neupert effect is strictly only expected for the asymptotic limit of very long cooling times (Holman et al., 2011). Ning (2012) have shown that the radiative and conductive losses added to SXR have very good correlation with the HXR flux. Therefore, in strict sense, the effect of cooling must be convolved in view of generalization of Neupert effect as presented in this chapter. With the motivation of studying the issues discussed above, we have undertaken the investigation of ten M-class flares observed by the Si detector of Solar X-ray Spectrometer (SOXS) experiment onboard the Indian GSAT-2 spacecraft. This chapter is organized as follows. Firstly, we present the modeling of the X-ray emission from solar flares and the estimated plasma parameters are then compared with the observed flare emission. At the end, we study the effect of cooling on solar flare plasma to deriving the break-energy (E_b) and generalizing Neupert effect.

4.2 Modeling the X-ray Flare

The bremsstrahlung spectrum $F(\varepsilon)$ of multi-thermal plasma as a function of photon energy $\varepsilon = h\nu$ and temperature T is given by,

$$F(\varepsilon) = F_0 \int \frac{exp(-\varepsilon/k_B T)}{T^{1/2}} \frac{dEM(T)}{dT} dT, \tag{4.1}$$

where $F_0 = 8.1 \times 10^{-39}\ keV s^{-1} cm^{-2} keV_{-1}$ (Culhane, 1969; Craig and Brown, 1976) and dEM/dT specifies the temperature sensitivity of the differential emission measure in the volume element dV with temperature T and electron density n_e as,

$$\left[\frac{dEM(T)}{dT}\right] = n_e^2(T) dV \tag{4.2}$$

Jain et al. (2005) and Jain et al. (2008) simulated the full-disk integrated photon spectrum $F(\varepsilon)$ from 0.01 keV to 1000 keV, considering a three-temperature emission measure (EM) distribution of the coronal plasma, including quiet (pre-flare) and various flare components of the M5 class flare. Based on the results from Yohkoh observations, they employed T = 4MK, EM = $10^{49} cm^{-3}$ for the pre-flare background, T = 13 MK and EM = $10^{49.5} cm^{-3}$ for the thermal component, and T = 40 MK and EM = $10^{47} cm^{-3}$ for the superhot component. They also considered a non-thermal component with a spectral index (γ) = -3.5 (whose range is between -2.5 and -4.5) and a flux of 10 photons

$cm^{-2}s^{-1}keV^{-1}$ at 20 keV.

In this chapter, we simulate the multi-thermal flux by integrating the series of isothermal photon flux considering line and continuum emissions and compare the observations in the energy range 4-15 keV in contrast to Aschwanden (2007). Aschwanden (2007) considered only continuum from 1 to 100 keV, but compared the observations of RHESSI from 10 keV. In order to estimate the flux of isothermal plasma, we employ the temperature (T) and emission measure (EM) of the flare plasma employing the CHIANTI atomic database (Dere et al., 1997). We estimate model photon flux assuming isothermal function by employing *f_vth.pro* function provided in *OSPEX* package of *SolarSoftWare (SSW)*. Shown in Figure 4.2 is the simulated line and continuum X-ray spectra for temperatures of T=11, 14,...34 MK in steps of 3 MK (thin curve) and their sum (dotted). The integrated flux is then fitted with the power-law function (the red line in Figure 4.2), which provides the photon spectral index (γ) of -4.65. However, if the flare plasma is multi-thermal then the photon spectral index of flux (γ) and power-law index of DEM (δ) should be related as $\gamma = \delta$ - 0.5 (Aschwanden, 2007; Klimchuk et al., 2008). This model suggests that for a flare emission produced by multi-thermal plasma, the DEM power-law δ should be -5.15.

4.3 Observations, Analysis and Results

In order to probe the nature of observed solar flare plasma in view of multi-thermal or isothermal nature in comparison with the simulated multi-thermal plasma described in the previous section we study full disk integrated X-ray emission from ten M-class flares observed by Si detector of the SOXS (see Chapter 2) mission. The flare characteristics of the selected ten flares are given in Table 4.1. The start and peak time, and peak flux of the flares are measured in 7-10 keV as observed by the Si detector of the SOXS payload.

The data have been taken from the SOXS website [1].

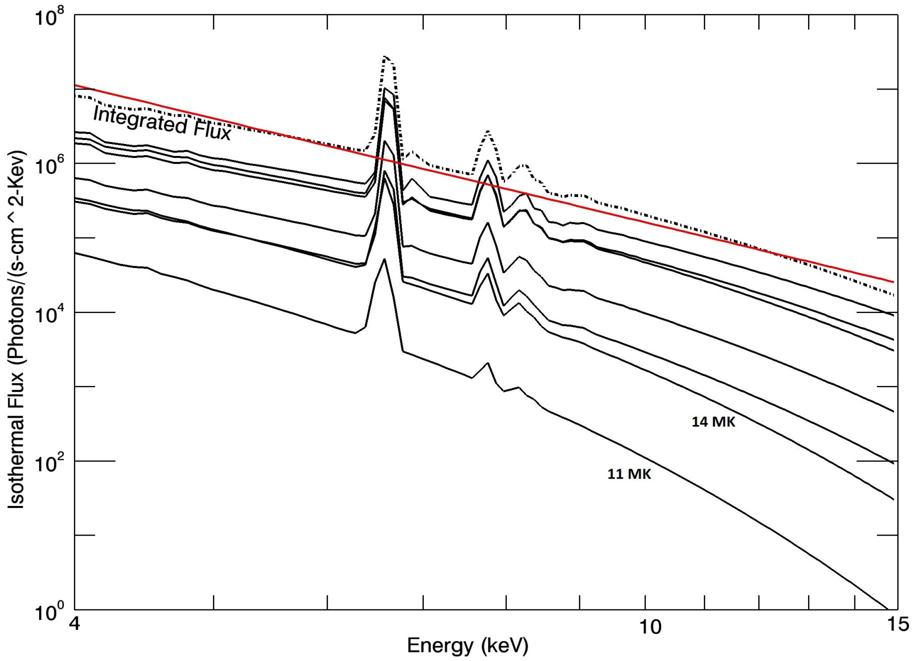

Figure 4.2: Theoretical line and continuum X-ray spectral evolutions of isothermal flux in the energy range 4-15 keV for the temperatures 11-34 MK. The temperatures are in steps of 3 MK (thin curve) and their sum is shown as the dotted curve. The red curve is the best fit considering a power-law function, revealing a power-law index of γ=-4.65

4.3.1 Spectral Analysis

We use the OSPEX (Object Spectral Executive) software package inside Solar-Soft to analyze the data. The OSPEX is an object-oriented interface for X-ray spectral analysis of solar data. It is a new version of the original SPEX (Spectral Executive) code written by R. Schwartz in 1995. Through OSPEX, the user reads and displays the input data, selects and subtracts the background, selects time intervals of interest, selects a combination of photon flux model components to describe the data, and fits those components to the spectrum

[1] http://www.prl.res.in/ soxs-data

in each selected time interval. During the fitting process, the response matrix is used to convert the photon model to the model counts to compare it with the input count data. The resulting time-ordered fit parameters are stored and can be displayed and analyzed with OSPEX. The entire OSPEX session can be saved in the form of a script and the fit results are stored in the form of a FITS file. The OSPEX enables us to look at the temporal evolution, spectrogram and spectral evolution. It also enables us to fit energy spectra using the CHIANTI code (Dere et al., 1997) for flare plasma diagnostics with the application of various thermal, line emission, multi-thermal, and non-thermal functions. Thus to calculate the peak plasma temperature and the DEM we have employed the least-χ^2 fitting to the SOXS X-ray spectra in OSPEX as described earlier by Jain et al. (2008) and Bhatt et al. (2013). However, we have discarded spectra with pulse pile-up to avoid spurious results. In this way, we have analyzed 280 spectra of 10 flares for current investigation. Figure 4.3 shows spectral evolution of the flare event of 19 November 2003 in the energy band of 4-25 keV. The spectral fit is made applying the CHIANTI code with the help of multi-thermal and single power-law functions provided in OSPEX. The modeled flux contribution from the multi-thermal function is shown by the green-colored line and that of the single power-law function with a break-energy point at 12 keV is shown by the yellow line. The total of these two contributions is shown by the red line. The total modeled flux is a good fit over the observed spectra with the goodness of fit evaluated as χ^2=1.84. For this event, we estimate DEM = 0.1×10^{49} cm^{-3} keV^{-1}, peak temperature T=24.4 MK and a power-law index of δ=-4.77 from spectral fitting. The same method is employed for all flare events under consideration and the average of estimated values of DEM and δ is listed in Table 4.1.

Table 4.1: Characteristics of Flare Plasma

Observed Parameters								Estimated Parameters		
Date	Start Time	Peak Time	Peak Intensity[1]	GOES CLASS	DEM Index[2] (δ)	DEM $\times 10^{49}$ (cm^3 keV^{-1})	Peak Temperature[3] (MK)	Loop Length $\times 10^9$ cm	n_e $\times 10^{10}$ (cm^3)	t_c (sec)
19-11-03	03:58	04:02	3.07	M1.7	4.38	0.033	26.38	04.52	10.9	579.85
07-01-04	03:55	04:00	6.50	M4.5	5.10	0.144	21.01	07.38	8.24	1195.59
19-01-04	04:35	04:54	2.45	M1.0	5.37	0.119	25.64	20.30	2.99	2990.58
25-04-04	05:28	05:36	5.80	M2.3	5.39	0.048	25.88	15.60	4.75	2753.94
14-08-04	04:13	04:14	8.80	M2.4	5.32	0.185	21.63	20.20	5.28	1398.03
31-10-04	05:26	05:31	6.04	M2.3	5.69	0.155	26.48	30.80	1.82	4640.42
03-06-05	04:06	04:10	1.70	M1.3	5.15	0.043	16.19	07.79	2.91	295.89
03-08-05	04:57	05:05	5.40	M3.4	5.31	0.119	22.25	20.90	1.77	1817.76
12-09-05	04:31	05:00	1.48	M1.5	5.11	0.079	19.13	08.34	5.88	1099.12
17-09-05	06:01	06:05	14.5	M9.8	5.39	0.092	20.93	04.34	29.3	1676.81

1. The X-ray peak intensity is in unit of 10^4 ph cm^{-2} s^{-1} keV^{-1} and measured for 7-10 keV band.

2. *delta* is the power-law index for DEM dependence on temperature (T).

3. Average of the peak temperatures over the temporal evolution of the flare.

We find the power-law index in the range of -4.4 and -5.7. These values are in good agreement with the expected value of δ = -5.15 (cf. Section 4.2) obtained by the simulation and thereby verify the nature of flare plasma to be multi-thermal.

4.3.2 Temporal Analysis

Figure 4.4 shows the temporal evolution of the 19 November 2003 flare in 13 energy bands. This flare evolved in the beginning via slow plasma heating seen in soft X-rays (4-10 keV), and then through impulsive transport followed by a long-duration thermal component. This figure also reveals a delay of the flare onset at higher energies, however, peaking earlier with respect to the low-energy curves. For example, Figure 4.4 shows that the flux in the highest energy band (20-25 keV) peaked at 03:59:14 UT, while it peaked in the next lower energy band (15-20 keV) at 03:59:30 UT, at a delay of 16 s. Figure 4.5 shows these delays as a function of energy, and demonstrates that the rise time i.e., the time from the onset to the peak emissions, is longer at lower energies. In fact, this explains why the soft X-ray flare is of longer duration than the hard X-ray flare. However, this behavior can also be explained in terms of the conduction cooling time. The electron density (n_e) calculated for all flares ranges between 1.77 and 29.3 $\times$ $10^{10} cm^{-3}$ (cf. Table 4.1) suggests that the conduction cooling of thermal X-ray plasma dominates over radiative cooling in the initial phase of the flare (Culhane et al., 1970). The conduction cooling time is expected to become shorter with higher temperatures ($\tau \propto T^{-5/2}$) as thermal bremsstrahlung involves increasing photon energy with higher flare plasma temperature. Thus longer cooling delays are expected at low energies. Our findings from the analysis of ten flares confirm this scaling law. This suggests that X-ray emission for all analyzed flares can be well explained by the presence of multi-thermal plasma. This is the reason of the delay soft X-ray peaks with respect to the hard X-ray peak. The cause behind the delay essentially could be due to the time delay between chromospheric heating, evaporation, and cooling of flare loops. Thus we may conclude that the multi-temperature components in the flare plasma are due to heating and cooling processes during the flare evolution.

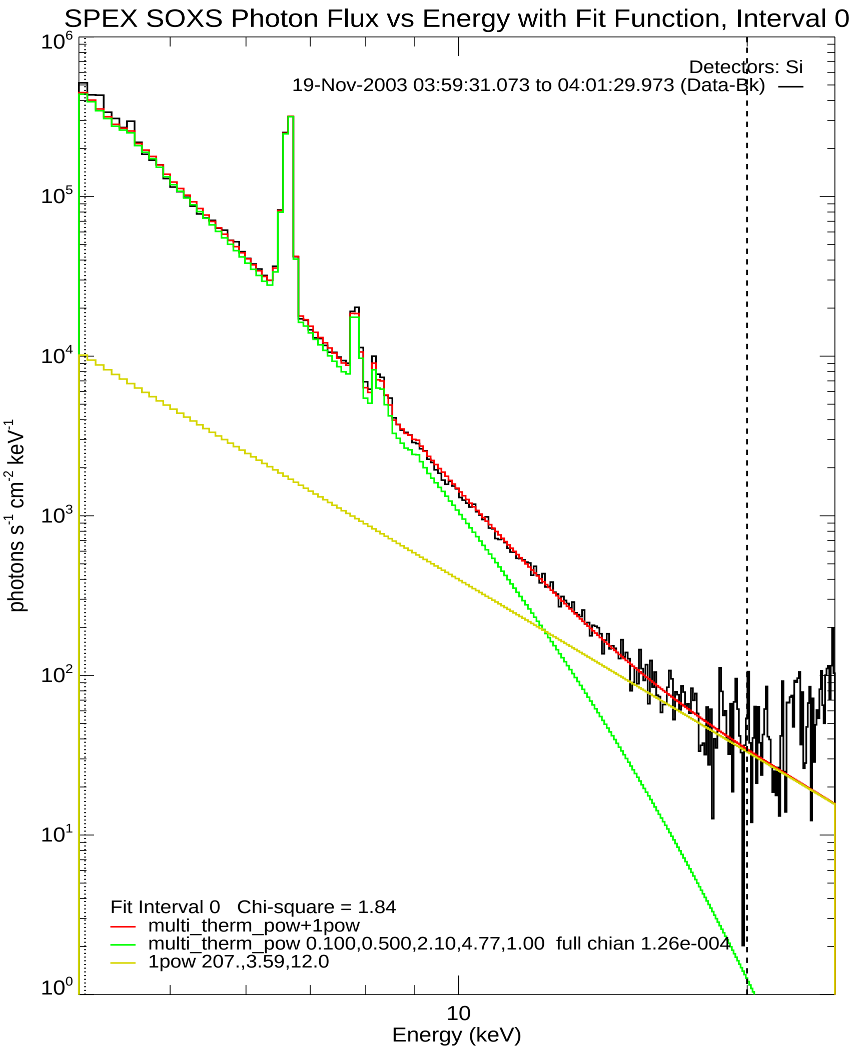

Figure 4.3: Spectral evolution of the 19 November 2003 flare event in the energy range of 4-25 keV as observed by the Si detector onboard the SOXS mission (shown by black line). The spectral fit with the help of multi-thermal, single power-law, and pulse pile-up functions provided in the OSPEX package is shown respectively by green and yellow lines. The goodness of fit of the total modeled flux (red line) over the observed spectra is evaluated to be χ^2=1.84.

On the other hand, Hudson (1991) and Dennis and Zarro (1993) found that the thermal emission often closely resembles the integral of the non-thermal emission, which is known as the Neupert effect. However, it is difficult to know precisely the break-energy (E_B) where thermal contribution ends and non-thermal emission begins, and as well as the fraction of thermal and non-thermal contributions in the total X-ray energy budget (Jain et al., 2005). Therefore, in this investigation we also attempt to measure the thermal-nonthermal crossover energy i.e., the break-energy (E_B) point with the help of the behavior of the relative time delay (Δt) and the conduction cooling time (τ_c). Our time domain technique is new and simpler in contrast to finding the break energy with the help of spectral evolution of flare plasma emission.

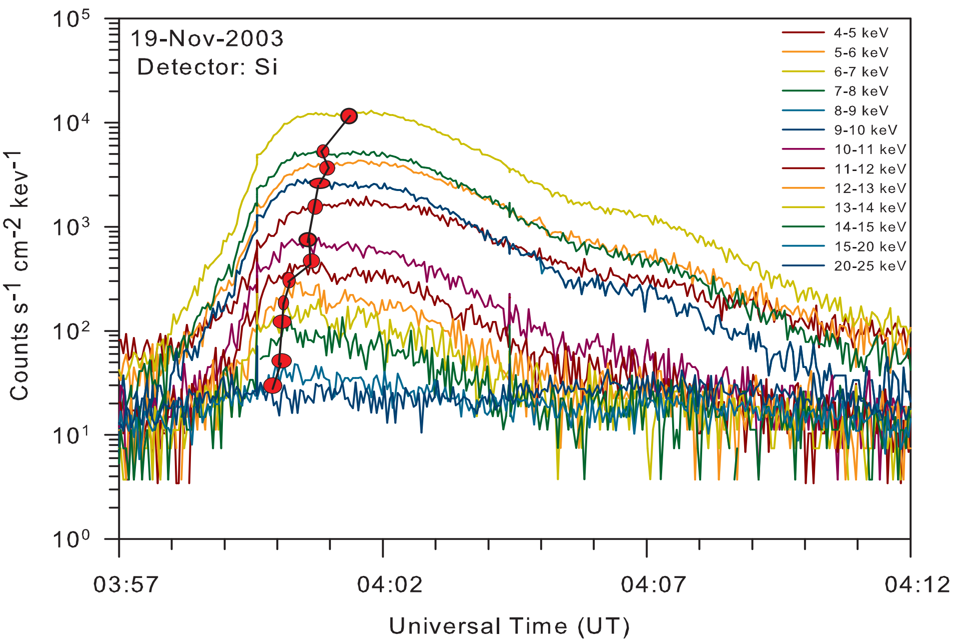

Figure 4.4: Temporal profiles in 13 energy bands (ε = 4-5, 5-6 ...14-15, 15-20, and 20-25 keV) of the 19 November 2003 flare. Each peak time is shown by circle. The curve connecting these circles illustrates the delay in peak time between successive profiles.

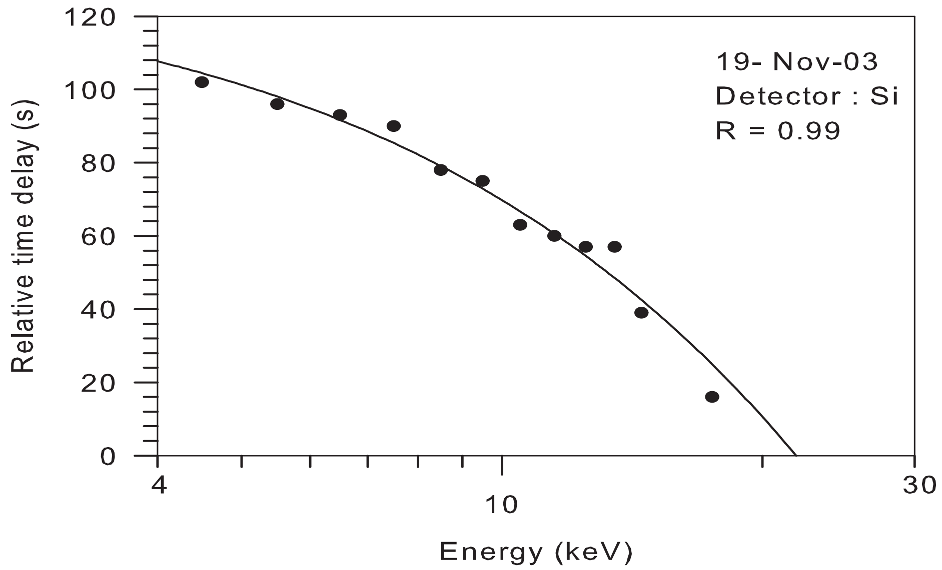

Figure 4.5: Relative time delay of the peak in a given energy band with respect to the reference energy band (20-25 keV) as a function of energy for the 19 November 2003 solar flare. The best-fit χ^2 value is 0.98.

The cooling at a given energy band can be approximated from the time profile of the flare. However, flare plasma cooling at initial high temperatures ($T \geq 10$ MK) is dominated by conduction cooling and is observable in soft X-rays, while the later phase detected in EUV ($T \leq 2$ MK) is dominated by radiative cooling. The conduction cooling time (τ_c) is given by the ratio of the thermal energy to the conductive loss rate, and can be expressed as a power-law dependence on the temperature

$$\tau_c(T) = t_{c0} \left(\frac{T}{T_0} \right)^{\beta} \tag{4.3}$$

Where, T is the flare peak temperature, $T_0 = 11.6$ MK and $\beta = 5/2$, and the thermal conduction cooling time scale τ_{c0} is given by

$$\tau_{c0} = 344 \left(\frac{L}{10^9} \right)^2 \left(\frac{n_e}{10^{11}} \right) \tag{4.4}$$

Where L and n_e are half loop length and electron density, respectively and estimated as follows.

We have estimated the length and the volume of the flaring loops with the help of 171 and 195 Å images from TRACE and EIT observations and Hα images recorded at the Hiraiso Solar Observatory (HSO) in Japan (Akioka, 1998). The EIT and TRACE observations are downloaded from the IAS page[2] and $H\alpha$ full-disk images of HSO are obtained from NICT/Japan[3]. We process the data with the help of routines provided in the *SolarSoft* package in IDL. Firstly, we select the active region in which the flare occurred. This selected region is substantially magnified in order to identify and extract the loop structure. The length of the identified loop structure is measured using a pixel difference method. In this technique the array of pixels is manually selected that cover the loop structure. The pixel array on the spatial image has coordinates viz. $[(x_1, y_1)$, (x_2, y_2), (x_3, y_3),...] in the selected region. The loop length of the identified loop structure is then measured as

$$Loop \;\; Length \quad 2L = \sum_{i=1}^{n} \sqrt{(x_i - x_{i-1})^2 + (y_i - y_{i-1})^2} \quad (in \;\; pixel) \tag{4.5}$$

Where the loop length 2L is in pixels and is converted to arcsec with the help of the pixel scale of the respective instruments. The pixel scales of TRACE, EIT and HSO are respectively, 0.4993, 2.6 and 1.2428 arcsec. The quantity ‘n’ is the dimension of the pixel array. However, in order to estimate the values of τ_{c0} and τ_c we employ the half loop length (L), and volume V estimated by a cylindrical approximation as follows.

$$V = \pi r^2 (2L) \quad (in \;\; cm^3) \tag{4.6}$$

Here, r is the radius of the loop and estimated by the half of the loop diameter D. D is estimated by averaging the observations of the loop cross-section at three different places d_1, d_2, d_3 (cf. Figure 4.6: top left panel) on the loop. The loop length 2L has been estimated from the coronal loop images obtained in either of the instruments TRACE (171 $\mathring{A}$), EIT (195 $\mathring{A}$) or $H\alpha$ at the peak emission period.

[2]http://idc-solar.ias.u-psud.fr/

[3]http://sunbase.nict.go.jp/solar/db/home.html/

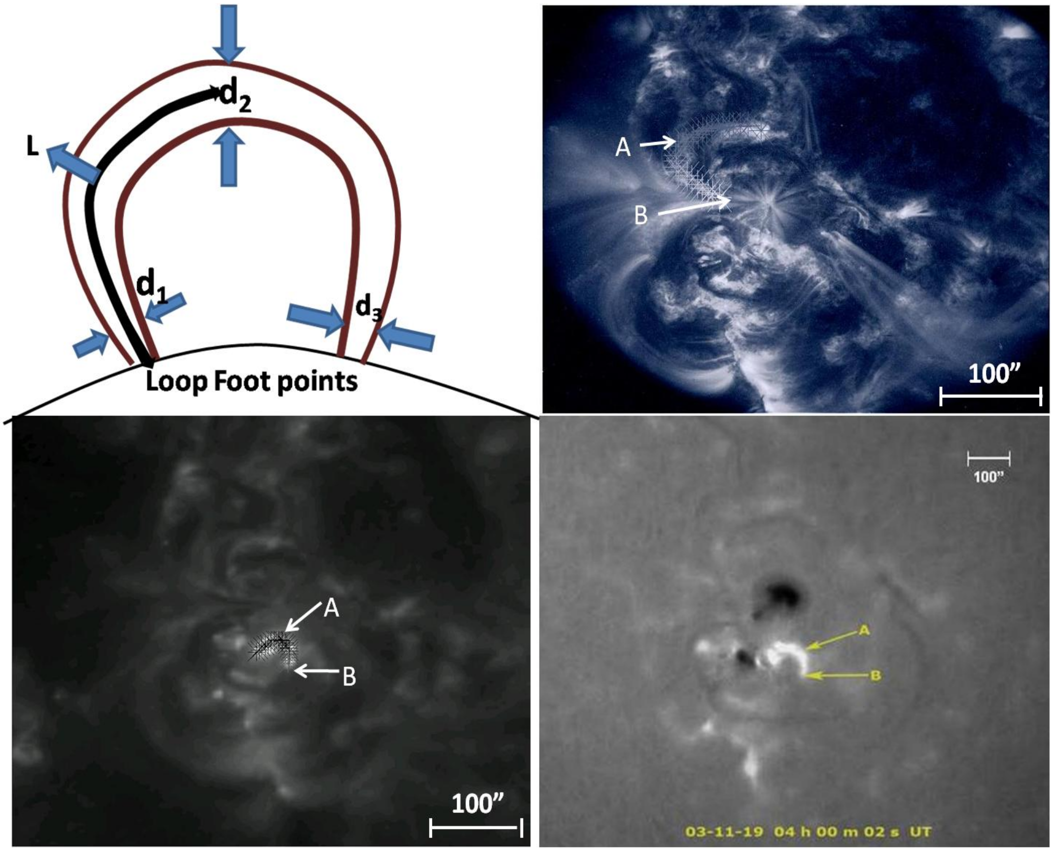

Figure 4.6: (Top left) The schematics of a length and diameter estimations of a typical flare loop. (Top right) Flare event of the 19 November 2003 observed in TRACE 171 $\AA$. The loop is shown in white crosses. (Bottom) EIT and HSO observations of the same event in 195 $\AA$ and in $H\alpha$, respectively. The loop-top and one of the foot-points are shown respectively by points A and B.

For example, shown in Figure 4.5 are the images of the coronal loop emission for the flare event of 19 November 2003 observed in 171 $\AA$ by TRACE at 04:28:59 UT, in 195 $\AA$ by EIT at 04:00:10 UT and in $H\alpha$ by HSO at 04:00:02 UT. The peak X-ray emission for the 19 November 2003 event observed by the Si detector is at 04:00:01 UT, and therefore, for this event, we have considered the EIT image to process for the loop length. Post-flare loops are visible in all wavelengths. The cross symbols on the images represent the identified loop structure. The loop-top and one of the foot-points are shown by A and B respectively. The estimated volume of a flare loop thus enables us to estimate the electron density n_e from the DEM which is estimated by fitting the X-ray spectra (Equation-4.2).

The conduction cooling time as a function of energy is thus estimated with the help of equations (4.3) and (4.7), and the relation between the peak temperature (T) and energy (ε) for which the multi-thermal bremsstrahlung spectrum $F(\varepsilon)$ contributes maximum (Aschwanden, 2007),

$$\varepsilon(T, \delta) = k_B T(\delta + 0.5) \tag{4.7}$$

The energy-dependent conduction cooling time is given as

$$\tau_c(\varepsilon) = \tau_{c0} \left[\frac{\varepsilon}{(\delta + 0.5)} \right]^2 .5 \tag{4.8}$$

where ε is the energy and tau_{c0} is thermal conduction cooling time scale obtained from Equation (4.4). The X-ray time profiles of Gaussian nature, however, without cooling when convolved over the conduction cooling time allows us to compare with the observed time profiles as expressed as,

$$\mathrm{f}(\varepsilon, \mathrm{t}) = \mathrm{F}_0(\varepsilon) \int_{-\infty}^{\mathrm{t}} \exp\left[-\frac{(\mathrm{t}' - \mathrm{t}_0)}{2\tau_\mathrm{g}^2} \right] \exp\left[-\frac{(\mathrm{t} - \mathrm{t}')}{\tau_\mathrm{c}} \right] \mathrm{dt}' \tag{4.9}$$

Here, t' is the time over which the conduction cooling has evolved and t0 is the flare peak time. Therefore, the peak of the observed time profile actually becomes delayed with respect to the peak of the un-convolved Gaussian time profile. The Gaussian width (τ_g) is obtained by fitting the light curve of 20-25 keV energy band with the gaussfit.pro procedure provided in IDL.

The application of L and n_e in Equation (4.4) allows us to estimate the thermal conduction cooling time scale (τ_{c0}) to be 1920 s and using Equation (4.8), we obtain τ_c to be 284 s at energy ε = 12.5 keV for the flare event of 19 November 2003. The analysis of all flare events under current investigation shows that τ_{c0} varies between 1520 and 18600 s, and averaged τ_c between 296 and 4640 s (cf. Table 4.1). Figure 4.7 shows the behavior of the observed time delay ($\Delta t/\tau_g$) normalized with respect to τ_g and the conduction cooling time (τ_c/τ_g) normalized with respect to τ_g for all events under consideration.

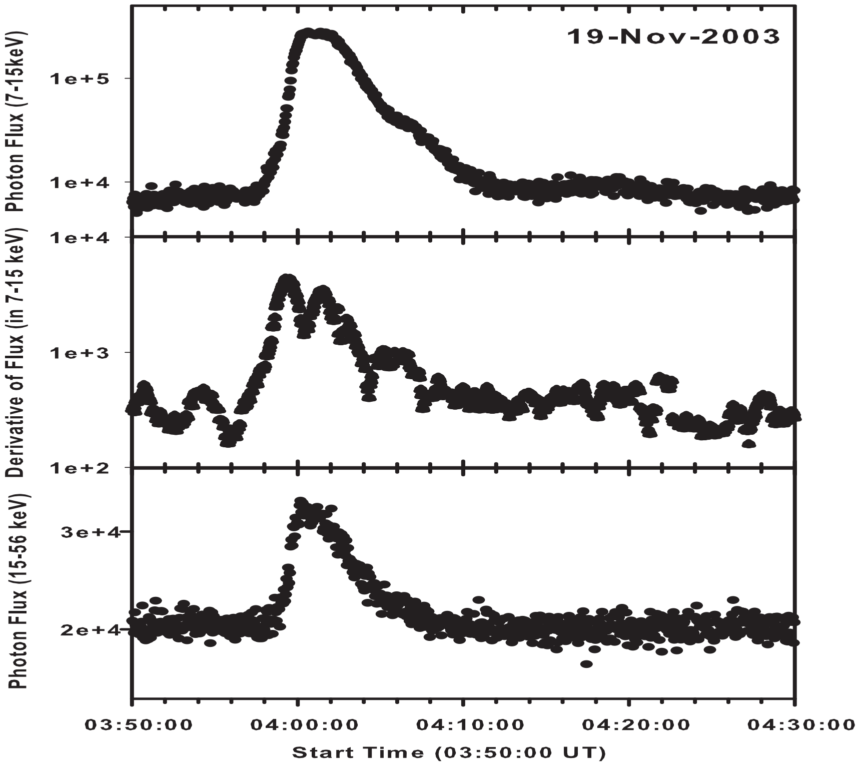

Figure 4.7: Observed time delay normalized with respect to τ_g $\left(\frac{\Delta t}{\tau_g}\right)$ as a function of the conduction cooling time normalized with respect to τ_g $\left(\frac{\tau_c}{\tau_g}\right)$ for the flare events.

Our observations and analysis as shown in figure 4.7 reveal that for a relatively short cooling time, the delay $\frac{\Delta t}{\tau_g}$ vanishes because of the negligible involvement of conduction cooling time, while in the opposite limit the delay $\frac{\Delta t}{\tau_g}$ increases and saturates beyond certain energy in the asymptotic limit of large cooling time for a given flare event. This suggests that the X-ray emission beyond this energy involving longer conduction cooling time is thermal in nature and before this energy is of non-thermal nature. This technique enables us to estimate the thermal-non-thermal crossover energy (break energy) within the energy resolution limits of the Si detector (0.7 keV). We find the break-energy (E_B) point to vary between 14 and 21 $\pm$ 1 keV for the flares considered in this investigation.

4.3.3 Generalization of Neupert effect

According to the thick-target model, the peak of SXR emission should lag the peak of HXR. Further, due to this causal relationship, if all non-thermal energy converts into heating, the derivative of soft X-ray flux ($F_{sxr}(t)$) should mimic the hard X-ray Flux $F_{hxr}(t)$.

$$\frac{\mathrm{d}}{\mathrm{dt}}\mathrm{F_{SXR}(t)} \propto \mathrm{F_{HXR}(t)} \tag{4.10}$$

However, the conductive and radiative energy loss during the heating and evaporation process affects this relationship. Therefore, the relation between the evolution of soft X-ray flux $F_{sxr}(t)$ and hard X-ray Flux $F_{hxr}(t)$ can be modeled with the empirical cooling time (Aschwanden, 2005) as

$$\frac{1}{\mathrm{F_{HXR}}}\frac{\mathrm{d}}{\mathrm{dt}}\mathrm{F_{SXR}(t)} \propto \mathrm{e}^{-\mathrm{t}/\tau_{\mathrm{cool}}} \tag{4.11}$$

We study this relation in the selected ten M-class events as already shown in Table 4.1. In addition to the usual 3 sec spectral and temporal cadence observations used in the study of spectral study of X-ray emission, CZT/SOXS also provides count flux in 5 energy-bands viz. 6-7, 7-10, 10-20, 20-30, 30-56 with time cadence of 1s. We employ photon flux in 7-10 and (10-20 + 20-30) keV energy bands as SXR and HXR flux respectively. Top, middle and bottom panels of figure 4.9 show the F_{SXR}, time derivative of F_{SXR} and F_{HXR}, respectively for the flare event of 19-Nov-03. The correlation co-efficient of the $\frac{dF_{SXR}}{dt}$ and $\frac{dF_{HXR}}{dt}$ is estimated to be varying between 0.3-0.6 for all the flares of current investigation. According to the classical expression of Neupert effect, the coefficient should be close to 1. However this reduced value explicitly reveals the effect of cooling on this relationship.

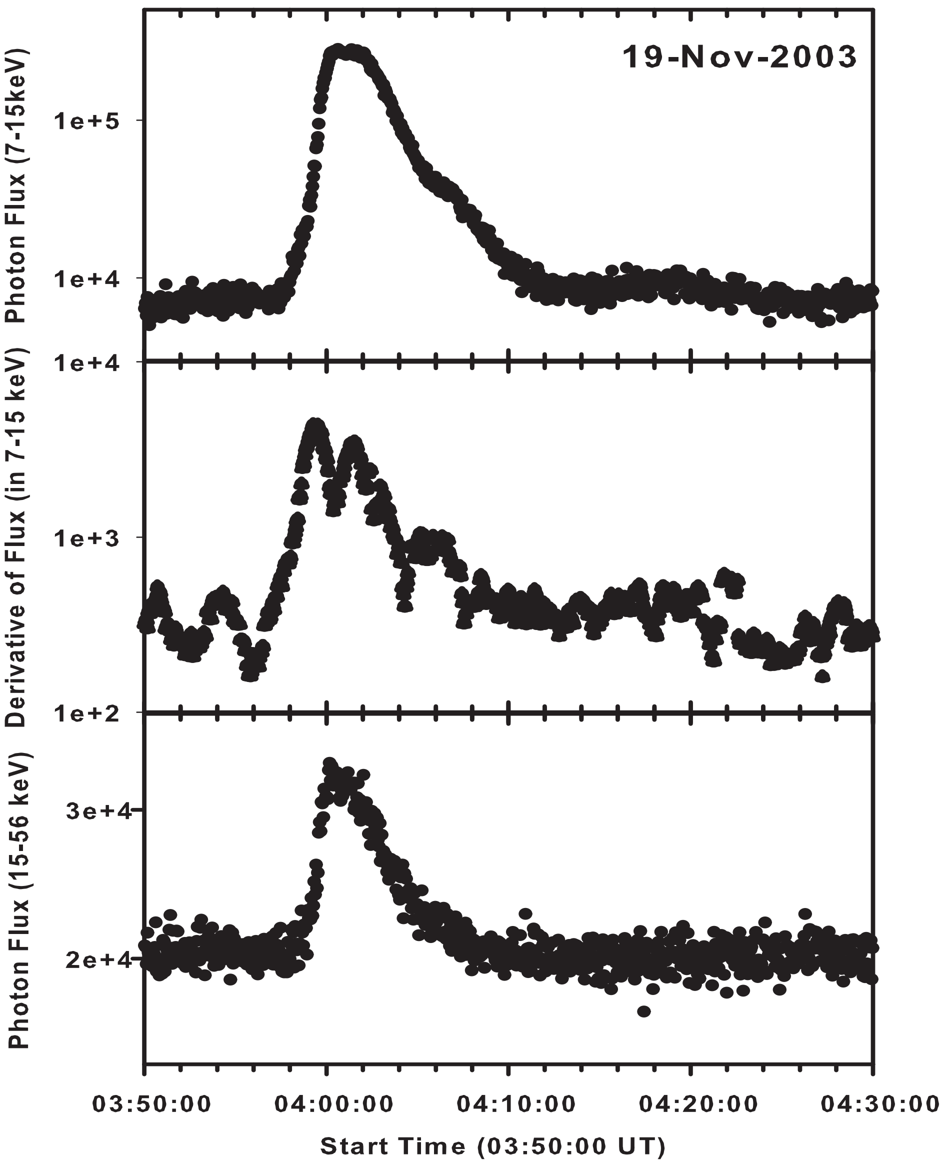

Figure 4.8: The 7-10 keV soft X-ray flux F_{SXR}, time derivative of F_{SXR} and 15-56 keV hard X-ray flux F_{HXR} for the flare event of 19-Nov 2003 plotted in top, middle and bottom panels, respectively.

We further fit the time evolution of the ratio of $\frac{dF_{SXR}}{dt}$ and F_{HXR} by an exponentially decaying function in the rising phase and estimated the empirical cooling scale as shown in Figure 4.9. We estimate this time scale for all flares and found to be varying between 39 and 525 s. Due to its occurrence in rising phase, this scale may be attributed to conduction cooling time scale. This study therefore generalizes Neupert effect over rising phase of the flare where conduction cooling plays significant role. We could not study the functional evolution of radiative cooling as the F_{hxr} diminishes during the gradual phase of the flare.

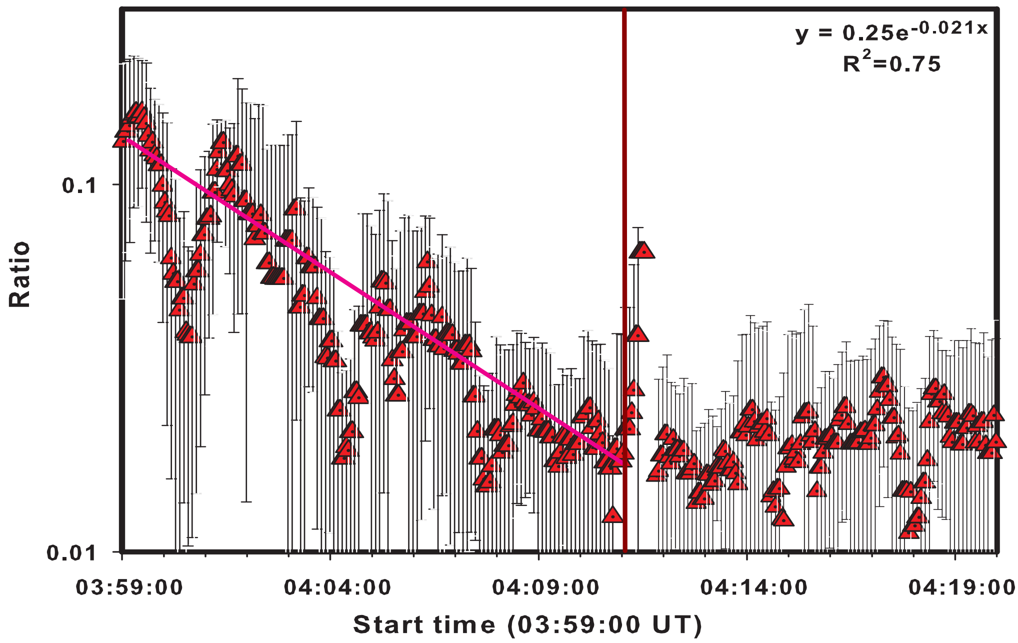

Figure 4.9: Ratio of time-derivative of SXR and HXR plotted and fitted with the exponentially decaying function for 19 Nov-2003 event. The cooling time scale derived is 47 sec. The solid demarcation line may also be interpreted as the crossover of conduction to radiative cooling.

4.4 Discussion

The single temperature approximation has been widely used in the past to investigate X-ray emission from the solar flares. However, the fact that the plasma is heated at different temperatures (multi-thermal plasma), and therefore the emission measure varies as a function of the temperature, emphasizes the crucial need to study X-ray spectra with improved energy and temporal resolution (Aschwanden, 2007, 2008; Jain et al., 2008). The present study of solar flares, in this context, using the Si detector of SOXS with the energy resolution ¡1 keV is a step ahead in this direction. In order to model the multi-temperature X-ray emission from the solar flare, firstly we begin with modeling isothermal plasma flux and then integrate the series of these isothermal plasma fluxes to obtain multi-temperature plasma flux. The integrated flare spectra of individual temperatures has a shape of a power-law and resembles very well the observed spectra, suggesting that the flare X-ray emission up to 25 keV is multi-thermal in nature. Aschwanden (2007) employed 10-50 keV X-ray spectra from RHESSI and fitted the 30-50 keV emission assuming non-thermal contribution, and extrapolated it into the low energy regime. He then subtracted the extrapolated part from the observed flux to deduce pure thermal contribution in the 10-30 keV energy band. Further, we find the multi-thermal nature in all ten flares under investigation during their whole duration, which is in contrast to Phillips et al. (2005) who suggested the isothermal nature of flare plasma during decay phase.

Further, there are strong indications that, in many flares the non-thermal component contains a substantial fraction of the total energy (Jain et al., 2000, 2005; Gan et al., 2001; Lin et al., 2002). The flare-accelerated 10-100 keV electrons appear to contain a significant fraction $\approx$ 10-50% of the total energy, indicating that particle acceleration and energy release processes are intimately linked. How the Sun releases this energy, presumably stored in the magnetic fields of the corona, and how it rapidly accelerates electrons and ions with such high efficiency, and to such high energies, is presently unknown. However, to address these questions, efforts using X-ray techniques have been undertaken with limited resolution. Bursts of bremsstrahlung hard X-rays ($\geq$ 20 keV), emitted by accelerated electrons colliding with the ambient solar atmosphere, are the most common signature of the impulsive phase of solar flares. Provided that the electron energy E_e is much greater than the average thermal energy, kT, of the ambient gas, essentially all of the electron energy will be lost to Coulomb collisions (Jain et al., 2000). Therefore, the non-thermal hard X-ray flux observed in many flares indicates that the energy in the accelerated > 20 keV electrons must be comparable to the total flare radiative and mechanical output (Lin and Hudson, 1976). Thus, the acceleration of electrons to tens of keV may be the most direct consequence of the basic flare-energy release process. High-resolution spectroscopy is the key to understanding the electron acceleration and energy release processes in solar flares. Therefore the precise measurement of the low-energy cut-off of non-thermal emission is an important quantity: not only it is related to the acceleration mechanism, but it also determines the total number of accelerated electrons and the energy they carry (Gan et al., 2001). Usually the low-energy cut-off is assumed to be 20 or 25 keV, which constitutes a main ingredient of the so-called standard picture of solar flares. However, the variation in the low-energy cut-off indicates that a higher low-energy cut-off means that the total energy carried by non-thermal electrons is much less than that is required to explain the flare energy budget. But the great decrease of the total number of accelerated electrons seems to explain the number problem in the standard flare scenario. Thus it would be proper that further studies based on observations with high energy resolution are being carried out (Gan et al., 2001). The low energy cut-off of the non-thermal hard X-ray emission commonly taken to be 20 to 30 keV is in fact not known due to the presence of thermal emission, which in extreme cases can extend to energies > 30 keV. In principle, this lower energy cut-off of power-law electrons (E_c) could be related to the break point energy (E_B). Gan et al. (2002) obtained the probability distribution of E_c, which represents that about half is larger than 45 keV and another half smaller than 45 keV. In order to estimate the break-energy (E_B) between thermal and non-thermal energy release in a solar flare we find that the peak of the observed flare gets delayed from the 20-25 keV Gaussian time profile. However, the delay Δt (cf. Figure 4.7) beyond certain energy (break-energy) in the asymptotic limit of cooling time saturates for a given flare event, suggesting that the X-ray emission beyond this energy is of non-thermal nature. This break-energy (E_B)

point is measured within the energy resolution limits of the Si detector (0.7 keV) and found to vary between 14 and 21 ± 1 keV for the flares considered in this investigation (cf. Figure 4.7) in agreement to the break energy point to be $\approx 18 \pm 3.4$ keV previously obtained by Aschwanden (2007).

Further to this, we attempted to generalize the Neupert effect in solar flares employing the effect of cooling in the plasma. We find the exponentially decaying model function to be fitting well which helps in estimating empirical cooling time. As the F_{HXR} diminishes during the gradual phase, we could only deduce the effect of cooling during the rise phase of the flare which suggests that the parameterized cooling is effectively conduction cooling. This enabled us to estimate the conduction cooling time scale of the events of current study to be varying in the range of 39-525 s. The cooling time scales estimated with this method are in close agreement with that derived by Aschwanden (2007), however, an order less than that estimated previously employing the energy-dependent delays. This overestimation can be attributed to the fact that in the previous technique, we have employed flare density which is estimated by using volume as well as loop-length which may be under/overestimated. In this regard, the cooling time scales estimated by Neupert effects are more accurate and reliable as they do not need manual intervention.

4.5 Conclusions

We analyzed the multi-thermal evolution in solar flares in the energy range of 4-25 keV of ten M-class flares using the high-resolution spectra from the Si detector of SOXS. We model the spectral-temporal evolution of the soft and medium-hard X-ray flux $F(\varepsilon, t)$ in terms of an evolving multi-temperature plasma and found that the resulting photon spectrum is a power-law function of energy. Our observations provide direct evidence of multi-thermal plasma in all ten flares and suggest that the flare X-ray spectra should be fitted with multi-thermal rather than isothermal model. The relative delay measurements show that the rise-to-peak time is longer for lower energy, which further indicates that flares are composed of multi-thermal plasma. We also found that Δt saturates for an asymptotic limit of large cooling time between 14 and 21 $\pm$ 1 keV for the flares considered in this investigation, which suggests that the break-energy point varies between these energy ranges, in agreement to other investigations.

Chapter 5

Probing the Role of Magnetic-Field Variations in Producing Solar Flare and CMEs

5.1 Introduction

It has been widely accepted that the energy released at the time of the flare and Coronal Mass Ejection (CME) in an active region is derived from the gradually stored energy of the surrounding magnetic fields which are in a non-potential state and twisted or sheared magnetic loops (Jain and Bhatnagar, 1983; Martens and Kuin, 1989; Aurass et al., 1999; Schmieder, 2006; Jain et al., 2010). However, the observations do not show any drastic change in the magnetic field at the time of the flare in an active region. Rather they reveal that stresses in the coronal magnetic fields may build up in response to the changes taking place at the photospheric level, such as sunspot motion and emerging fluxes. During the evolution of an active region and passage over the disk many phenomena are observed viz. the motion of an active region around its own axis, moving magnetic features (MMFs), cancellation of active region fluxes, new flux emergence, plage brightening, surge activity, and filament eruptions. Magnetic-field variations have now been well quantified and studied to probe their relationship with energetic phenomena viz. flares, eruptive prominences, and CMEs.

One way to quantify shear in an active region is to measure rotation of the leading and following polarity sunspots around their center of mass known as "Rotation angle" (Zhang et al., 2008). The continuous ongoing processes of emergence and cancellation of flux change the total flux of the active region, which may be quantified by the product of magnetic field strength [H] and area [A] of the region. Complex structures and fast dynamics in an active region result in the formation of structures that can be qualitatively described as twisted, sheared, etc. Such structures provide evidence for a strong departure from potentiality, the stored excess energy in the magnetic field and presence of major current systems in them (Chumak, 2005).

Solar flares have been classified into two types, such as LDE flares vs. impulsive flares, or two-ribbon vs. simple loops. The former has often been thought to be explained by the so called "CSHKP" (Carmichael-Sturrock-Hirayama-Kopp-Pneuman) reconnection model, whereas the latter has been attributed to different models, such as the emerging-flux-reconnection model (Shibata, 1998). Yohkoh, however, has revealed that there are many common features in both types of flares, e.g., the ejection of hot plasma (Shibata et al., 1995; Ohyama and Shibata, 1997); X-type or Y-type morphology suggesting the presence of current sheets or neutral points (Tsuneta et al., 1992; Tsuneta, 1997) and, change of field configuration, etc. In this view, it is now not easy to classify the flares into two types, and thus Yohkoh observations require a more unified view of flares. Shibata et al. (1996); Shibata (1998) introduced a general model, known as the "unified model", to interpret all classes of flares. In his model, reconnection is caused by a plasmoid eruption and is observed in all classes of flares. These plasmoid eruptions may be mass ejections seen in the chromosphere such as a surge, spray, or filament eruption, or CMEs seen in the corona and beyond. However, in a study carried out by Subramanian and Dere (2001) on the source regions of 32 distinctly identified coronal mass ejections, they found that 41% of CMEs are not associated with any prominence eruption; rather they are associated with emergence or cancellation of magnetic fields in the active region. On the other hand 59% CMEs were found to be associated with a prominence eruption in the same or in a remote active region. This may reveal that CMEs may induce reconnection and the observed flares may be a result of such reconnection. However, many flares are not found to be associated with CMEs and thus reconnection through a plasmoid is an unlikely possibility. On the other hand, almost all flares are found to be associated with a small- or large-scale mass eruption, but not necessarily CMEs. Thus we may conclude that the primary energy for these manifestations is derived from the magnetic field of the active region but it is not known what kinds of magnetic-field variations are responsible for triggering such energetic phenomena. Therefore in this chapter we wish to address this question by studying the NOAA Active Region 8038 for the interval 07 to 13 May 1997 during which it produced a flare and associated CME on 12 May 1997. The observations, analysis, and results are presented in section 5.2. We discuss results in section 5.3 and conclude the investigation in the section 5.4.

5.2 Observations, Analysis and Results

5.2.1 Magnetic field evolution

Shown in Figure 5.1 is a sequence of a few high resolution magnetograms of NOAA Active Region 8038 made by the MDI instrument onboard the SOHO mission during 11–12 May, 1997. A detailed study of the evolution of magnetic field in the active region using a movie of in total 60 re-registered magnetograms during 10–13 May, 1997 was conducted and presented earlier by

Bharti et al. (2005). Therefore in this investigation we briefly describe salient features of the magnetic field evolution as follows.

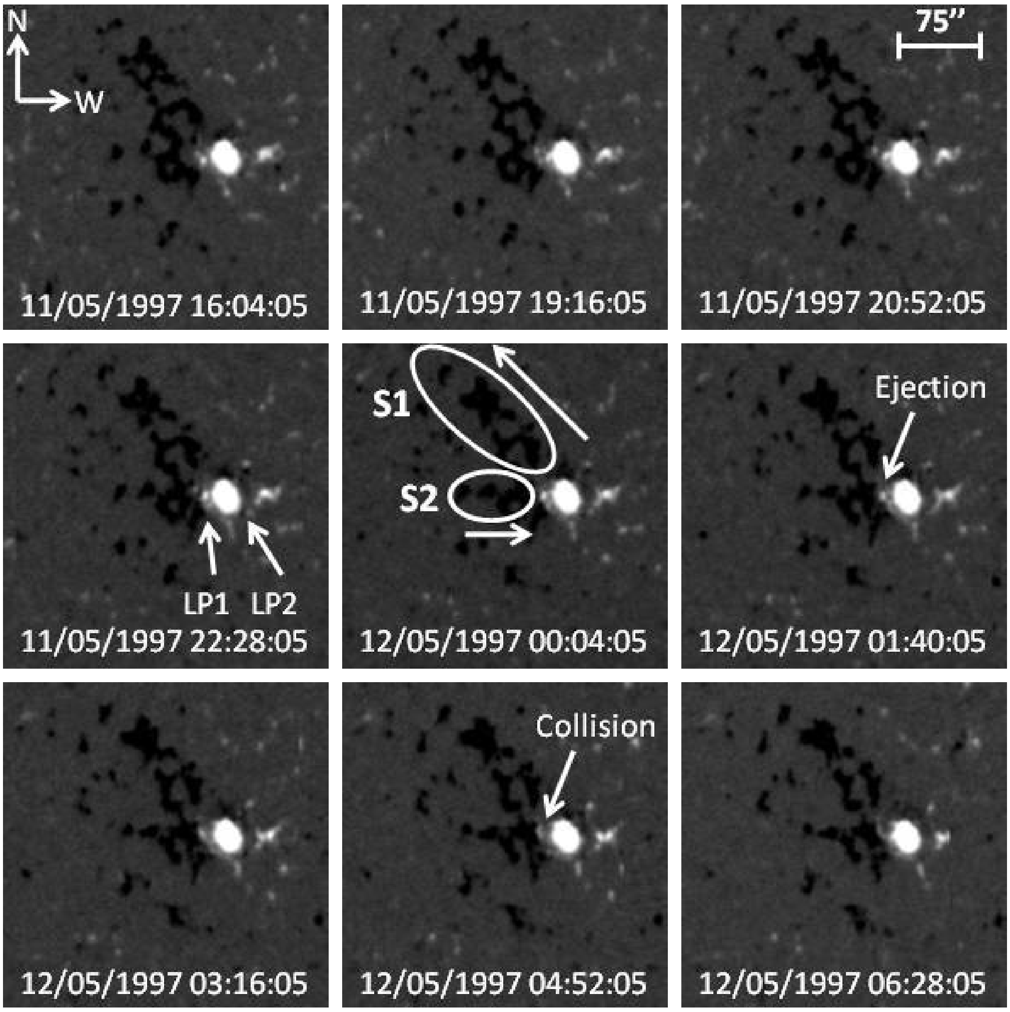

Figure 5.1: Sequence of a few selected high-resolution magnetograms of NOAA AR 8038 obtained by SOHO/MDI for the period 11-12 May 1997. The regions S1 and S2 are of following polarity, which are moving away and towards the leading polarity (sunspot), respectively. The ejection of north polarity flux from the sunspot is also shown. The onset of collision of north polarity flux, ejected from sunspot on 11 May around 20:52:30 UT, with a south polarity EFR in S2 began around 03:16 UT. The south polarity EFR in S1 is also intensified on 12 May.

1. Regular but discrete magnetic-field variations in the active region were taking place during the period under study in terms of emergence and cancellation of flux of both polarities, but predominantly of following

polarity. Previously, while studying this active region using observations from the Udaipur Solar Observatory (USO) and SOHO/MDI, Mathew and Ambastha (2000) showed appearances of emerging fluxes in this active region.

2. Negative flux region S2 (*cf.* Figure 5.1), the following polarity in the active region, was continually approaching the main positive leading polarity since 10 May, with resulting flux cancellations. However, the region S1 of following polarity (*cf.* Figure 5.1) was receding from the major leading polarity. In addition to the appearance of an emerging flux region (EFR) in S2, the magnetic fluxes were evolving, fragmenting, and merging indicating redistribution of fluxes in the active region (predominantly in trailing part). We confirmed appearances of EFRs in S2 as earlier reported by Mathew and Ambastha (2000) and Bharti et al. (2005). We found that among several EFRs observed in the active region, two EFRs of following polarity formed around 20:00 UT on 11 May, one each seen in S1 and S2. We believe these were of specific importance in the production of the solar flare on 12 May 1997.

3. Moving magnetic features (MMFs) of north polarity were ejecting out from the major leading polarity (sunspot) as shown in Figure 5.1 with a quasi-periodicity of about ten hours. A total seven MMFs were observed during 10-13 May. However, out of these seven MMFs five were seen during the interval from 00:04:30 UT on 10 May to 20:52:30 UT on 11 May. The other two were seen at 22:28:30 on 12 May and 06:28:30 UT on 13 May. We found the plane-of-the-sky velocity of these MMFs in the range of 200-500 m s^{-1}.

4. As shown in figure 5.1, one such moving magnetic feature of leading polarity flux (LP1), observed around 20:52:05 UT on 11 May began to collide with newly emerged south polarity flux in the S2 region that was approaching the major leading polarity (sunspot) around 03:16 UT on

12 May. In view of the poor temporal resolution of a few tens of minutes for magnetograms as well as CME observations (described in Section 5.3) it is not possible to arrive at a precise initiation time of the CME nor the collision time of the two opposite polarity fluxes observed in two magnetograms taken at 03:16 and 04:52 UT. However, we may estimate the initiation time of the CME within the temporal resolution limits of MDI and EIT as supported by signatures seen in EIT images. This collision of opposite polarity fluxes, i.e. cancellation of magnetic flux, is specifically important with regard to the production of the CME and the flare. About ten hours later to subsequent of collision in S2 the emerging flux regions were subsidizing. Conversely, the EFR of south polarity flux in S1 was significantly intensifying.

The above observations of the magnetic-field configurations of NOAA AR 8038 in terms of emerging flux regions, moving magnetic features, and cancellation of fields on short and long time scales provide a morphological picture of the ongoing process of magnetic-field variations in the active region. However, in order to understand among these factors of magnetic-field variations, which were predominant and responsible for triggering the flare and associated CME on 12 May 1997, we need a quantitative study of magnetic-field variations in relation to energy release by the active region. In next section, we describe a quantitative estimation of magnetic-field variations.

5.2.2 Measurement of Magnetic-Field Variations

5.2.2.1 Measurement of Magnetic Flux

The magnetic flux [ϕ] is estimated as the product of magnetic-field strength [H] and area [A] of a given active region as presented in the following relation (5.1).

$$\phi = \mathrm{H.A} \tag{5.1}$$

H is estimated using SOHO/MDI 96-minute full-disk observations with the help of functions provided in SolarSoft. The level-1.8 data from Stanford University [1] are processed for further measurements. We employ the Carrington Projection method for foreshortening correction using the *map_carrington.pro* routine provided in *SolarSoft*. The magnetic flux is estimated separately for regions of leading and following polarities identifying them distinctly as discussed below. The regime (pixels) having magnetic field strength $\geq$ 10% of the positive peak magnetic-field strength is considered as a leading polarity region. Similarly, the regime (pixels) belonging to the magnetic-field $\leq$ 10% of the negative peak magnetic field strength is considered as a following polarity region. The rest of the region is considered as background or quiet Sun. The size of the pixel is 1.97 arcsec, and therefore the area occupied by both the polarities is then estimated separately by total number of pixels multiplied by area of single pixel, i.e. 7252 $\times$ 1.972 $\times$ 1010 cm^3. The magnetic flux [ϕ] for the respective polarity is then estimated by multiplying the corresponding total magnetic-field strength with the above estimated area (c.f. Equation 5.1), and is plotted for each day as shown in Figure 5.2 (top panel).

5.2.2.2 Measurement of Magnetic-Field Gradient

The separation between leading and following polarities is considered as the distance between their respective centers of mass. The center of mass coordinates (xc, yc) of both the polarities are obtained with the aid of the following equations

$$\mathrm{x_c} = \frac{\sum_{\mathrm{i,j}} \mathrm{x(i,j)B_{los}(i,j)ds}}{\sum_{\mathrm{i,j}} \mathrm{B_{los}(i,j)ds}}$$

$$\mathrm{y_c} = \frac{\sum_{\mathrm{i,j}} \mathrm{y(i,j)B_{los}(i,j)ds}}{\sum_{\mathrm{i,j}} \mathrm{B_{los}(i,j)ds}}$$

Where B_{los}(i,j) is the line-of-sight magnetic field strength corresponding to the pixel with coordinate [x(i,j), y(i,j)] and ds = dx$\times$dy is the area of each pixel.

[1] http://soi.stanford.edu/magnetic/index5.html

The aforesaid sum runs over the all the pixels from region of interest (ROI). The estimated center of masses of leading and following polarities is then employed to get dz from:

$$\mathrm{dz} = \sqrt{(\mathrm{x_{cl}} - \mathrm{x_{cf}})^2 + (\mathrm{y_{cl}} - \mathrm{y_{cf}})^2}$$

Where, (x_{cl}, y_{cl}) are the coordinates of the center of mass of the leading polarity and (x_{cf}, y_{cf}) are of the following polarity. The magnetic field gradient is then estimated by dividing the difference of total magnetic-field strengths of leading and following polarities [dH] with the above estimated polarity separation [dz]. The variation of the estimated magnetic field gradient (dH/dz) over the passage of the active region on the disk is shown in Figure 5.2 (middle panel).

5.2.2.3 Measurement of angular rotation of leading polarity

The leading polarity LP2 is elliptical in shape (c.f. Figure 5.1). Its orientation can be described as an angle between its major axis and the Equator in the anti-clockwise direction. This angle is defined as the rotation angle of the sunspot (Zhang et al., 2008). In order to estimate the rotation of the leading polarity, we employ the *fit_ellipse.pro* procedure written in IDL and provided by the Coyote IDL programming package. The structure corresponding to the leading polarity is identified as the region (pixels) having magnetic field strengths (H) $\geq$ 10% of the peak magnetic field strength. This condition is the same as the condition defined for identifying the structure of the polarities as described in Section 5.2.3. The `fit_`ellipse.pro procedure is then applied on the identified region in order to obtain the parameters of the best fitted ellipse on the region. The output parameters of this procedure include the major and minor axes as well as their orientation from the Equator of the Sun in an anti-clockwise sense. The orientation angle of the major axis therefore gives the information of the rotation of leading polarity as shown in Figure 5.2 (bottom panel).

The eight hours averaged parameters viz. magnetic flux, gradient, and rotation are shown in Figure 5.2. The error in each parameter is estimated as standard deviation of five 96-minute observations comprising one eight hour data set, and is shown in each panel of Figure 5.2. Top panel of the Figure 5.2 shows the time variations of eight hour averaged magnetic fluxes of leading and following polarity. The variations show that the magnetic fluxes in the leading and following polarities have started to build from 7 May 1997. They attained a maximum value on 11 and 12 May 1997, however, it started to decrease afterwards. The middle panel of Figure 5.2 shows the time variation of the eight hour averaged magnetic field gradients.

The variation shows that magnetic-field gradient was significantly higher around 07 May but then it decreased until 10 May. The gradient started to increase on 11 May and attained a maximum value on 12 May 1997 - the day of CME/flare event. After the flare, the gradient started to decrease and continued to lower levels. The bottom panel of Figure 5.2 shows the temporal variation of eight hour averaged rotation angle of leading polarity. The variation indicates that the leading polarity was rotating anti-clockwise with $0.25°h^{-1}$ from 7 May 1997 until 01:40:05 UT on 12 May when the rotation angle reached to $\approx$ 100°. This finding is in contrast to Li et al. (2010) who reported minor clockwise rotation of $1°h^{-1}$ during 09-12 May 1997. We further found that the magnetograms beginning at 03:16:05 UT on 12 May showed a reversal of rotation in the leading polarity.

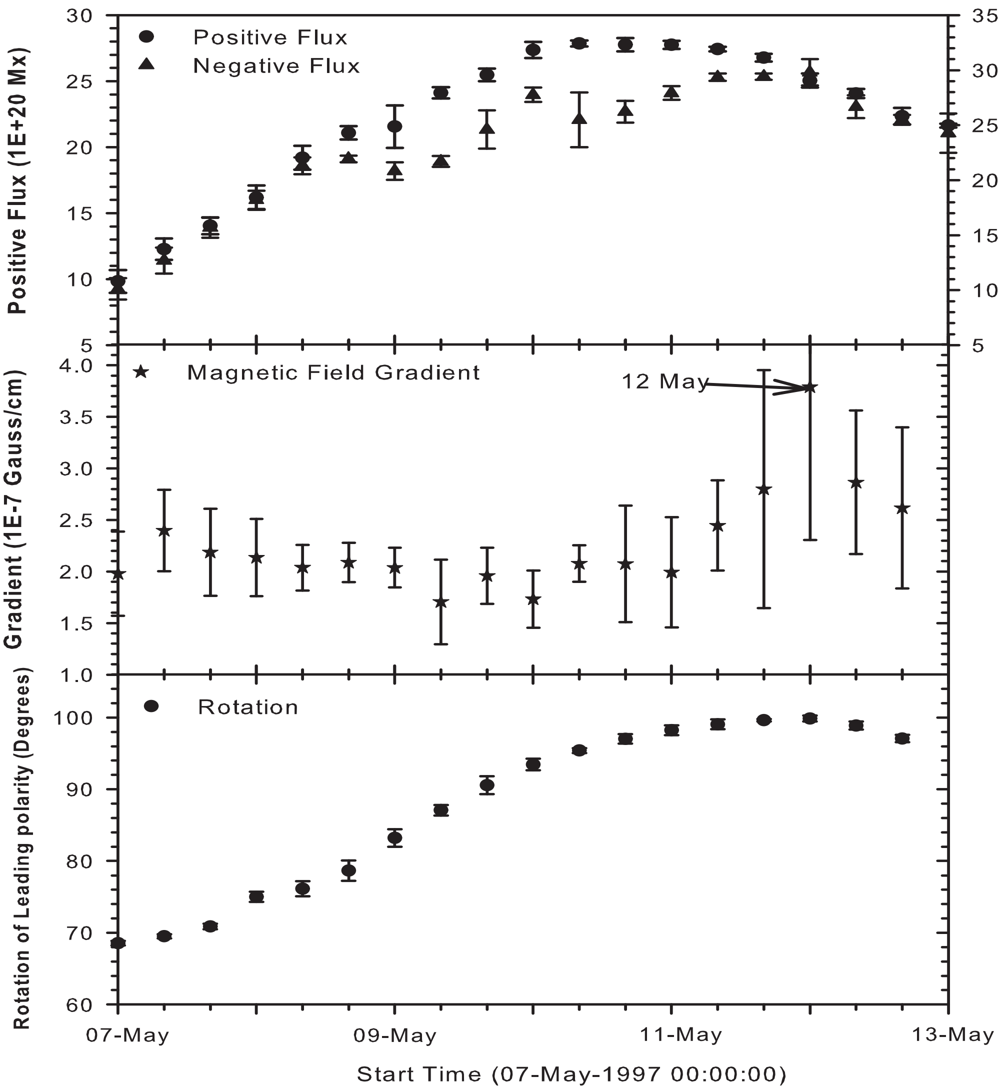

Figure 5.2: Temporal evolution of eight hour averaged magnetic fluxes of leading and following polarities of NOAA 8038 (top panel), the gradient (middle panel), and the rotation angle of leading polarity (bottom panel)

5.2.3 The H_α Observations

5.2.3.1 The Chromospheric Activity during 10-13 May 1997

Shown in Figure 5.3 is a sequence of high resolution Hα filtergrams obtained from USO during 10-13 May 1997. It may be noted that the filament that stretched over the active region and was visible on 10 May, was disrupted and was not visible on 11 May at 03:47 UT. However, it reformed around 06:30 UT on 11 May. This filament showed considerable activity in the active region during this period. In addition to filament activity, the plage intensity was also varying in the active region particularly during the period of appearance of emerging flux regions (EFR). The filament again appeared disrupted on 12 May from the beginning of our observations at 03:03 UT, which appears to be the potential candidate to brightening the EIT loops (*cf.* Section 5.2.6 and Figure 5.8 - right panel). However, as shown in figure 5.3, we could see several dark and bright surges from 03:03 to 04:40 UT on 12 May. It may also be noted that plage areas from following polarity fluxes and east of the dark leading sunspot brightened up on 12 May. Such chromospheric activities observed since beginning on 10 May in the active region are consistent with the appearances of EFRs and their growths and decays as seen in MDI observations.

5.2.3.2 The Filament Activity on 12 May 1997

Solar flares are associated with magnetic neutral lines where the vertical component of photospheric magnetic-field changes sign. These neutral lines are often marked by filaments, which become turbulent and disappear before the flare occurs (van Tend and Kuperus, 1978). We investigate the possible role of the filament in triggering the flare and CME that occurred on 12 May 1997 employing the Hα observations taken at a cadence of 30 seconds using the US Air Force Solar Observing Optical Network (SOON).

Figure 5.4 shows the temporal sequence of a few selected Hα images. The filament appearing as a dark curvilinear line and extending from North to South of the active region has been designated in four parts viz. F1, F2, F3, F4 as shown in Figure 5.4 (04:40:09 UT). This categorization is made based on their activity seen during the evolution of the region particularly before the occurrence of the flare and CME on 12 May 1997. For example, the part F1 is not visible at 04:29:09 UT, but it appeared at 04:34:09 UT and again disappeared at 04:35:09 UT.

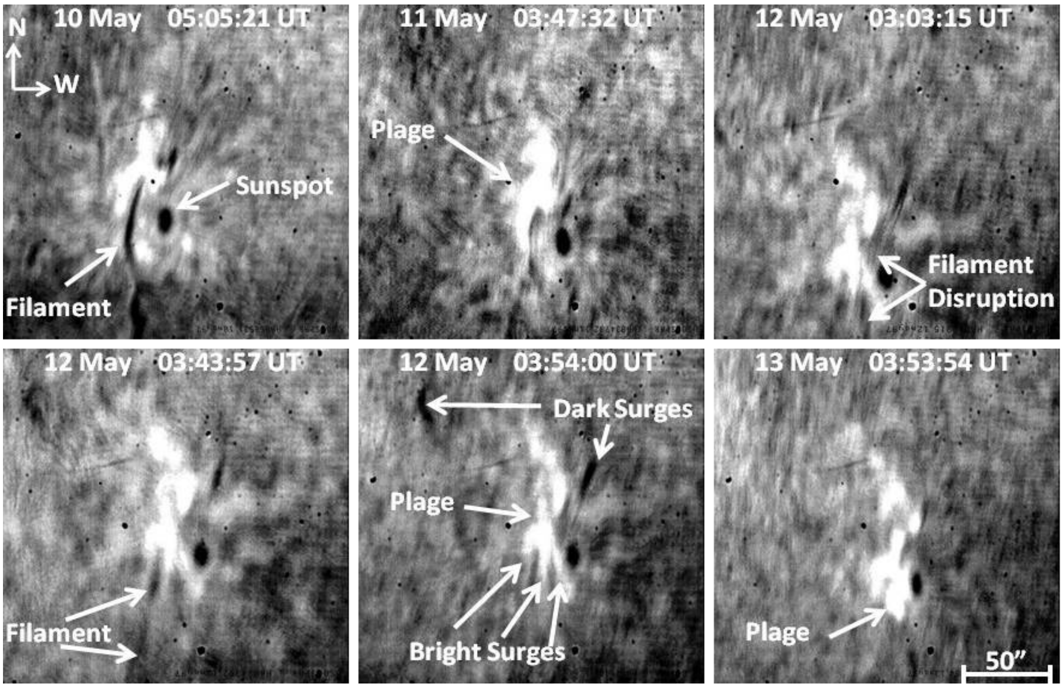

Figure 5.3: High resolution Hα filtergrams, one for each day for the period 10–13 May, 1997, showing bright and dark mass ejections and considerable filament activity and plage intensity variations in the active region. Significant filament activity may be noted between 03:03 and 03:54 UT.

We observed frequent disruptions of segment F1 and material moving out in the plane of the sky towards the Northwest above the leading sunspot LP2. This activity appears to be associated with frequent appearances of emerging fluxes of following polarity in the S2 region and flux cancellations with positive polarity. However, the disruption of the filament leads to upward motion of the filament due to enhanced gradients at the site of the filament. The magnetic-field gradient was observed to increase beginning on 11 May 1997 (*cf.* Figure 5.2). On the other hand, the longer F2 part of the filament, which was stable until 04:41:09 UT, started to detach from F3 around 04:41:39 UT. The breakup and eruption of F2 appears to be associated with the flare and CME. This time is also confirmed by GOES X-ray flux observation as the start time of flare (*cf.* Figure 5.6). The F3 and F4 parts of the filament, which almost remain connected with F2 in the pre-flare stage, significantly erupted at 04:43:39 UT, around the Hα flare time described in following Section.

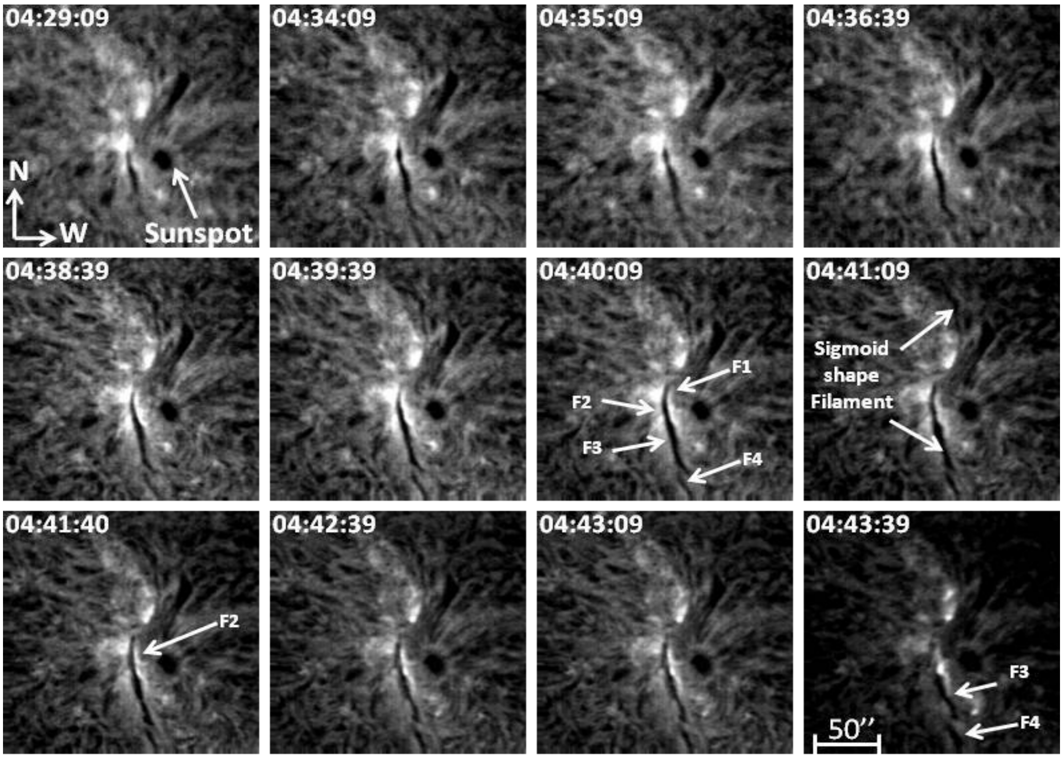

Figure 5.4: Sequence of Hα filtergrams showing filament activity on 12 May 1997 prior to CME-flare eruption. The F1 part of the filament shows frequent activity, while F2 and other parts were disrupted before the flare and CME around 04:43 UT. The filament also shows reverse-shaped sigmoidal structure.

5.2.3.3 The Hα Flare

In Figure 5.5 we show a sequence of Hα flare evolution observed by SOON. The Hα flare was first observed at 04:43:39 UT. The temporal cadence of observations was 30 seconds, and therefore the onset of the flare was between 04:43:09 and 04:43:39 UT. However, the GOES flare onset time in 1-8 Å was at 04:41:21 UT, consistent to F2 disruption. Nevertheless, taking 5σ enhancement above background as shown in Figure 5.6, we may confidently consider X-ray flare onset at 04:42:36 UT in 1-8 Å. On the other hand, the hard X-ray flare (25–50 keV) observed by BATSE, shown in Figure 5.6, started significantly later at 04:50 UT. It might be possible that either the sensitivity of the BATSE detector restricted the observations in the early phase or the hard X-ray component started significantly later around 04:50 UT. However, this event is found associated with interplanetary protons > 10 MeV. At both ends of the flare strands the bright material shot out as seen in the frame taken at 04:45:09 UT (Figure 5.5).

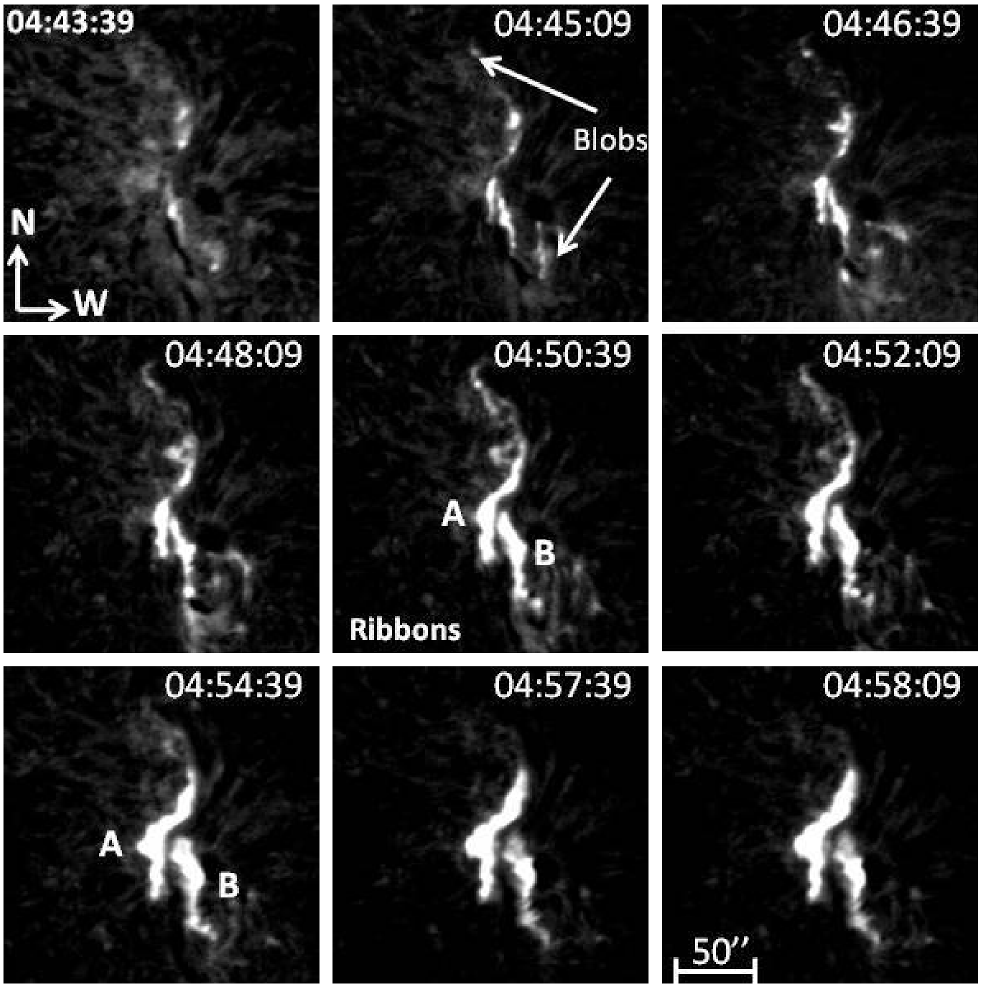

Figure 5.5: A sequence of high-resolution Hα filtergrams of the 1B flare observed in NOAA 8038 on 12 May 1997 by SOON. The bright mass ejection at both ends of flare ribbons may be seen at 04:45:09 UT. The flare ribbons move away from each other which may be noted by the separation of flare kernels A and B

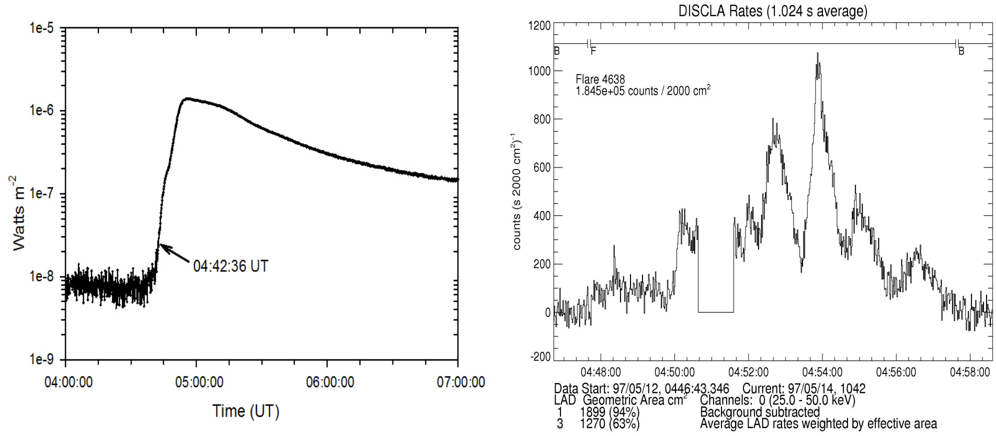

Figure 5.6: The three-seconds X-ray flux measurements in 1-8 Å by GOES 12 shows onset of the 12 May 1997 flare at 04:42:36 UT taken to be the 5 enhancement above pre-flare background, while the hard X-ray in 25-50 keV (right panel) shows the onset around 04:50 UT.

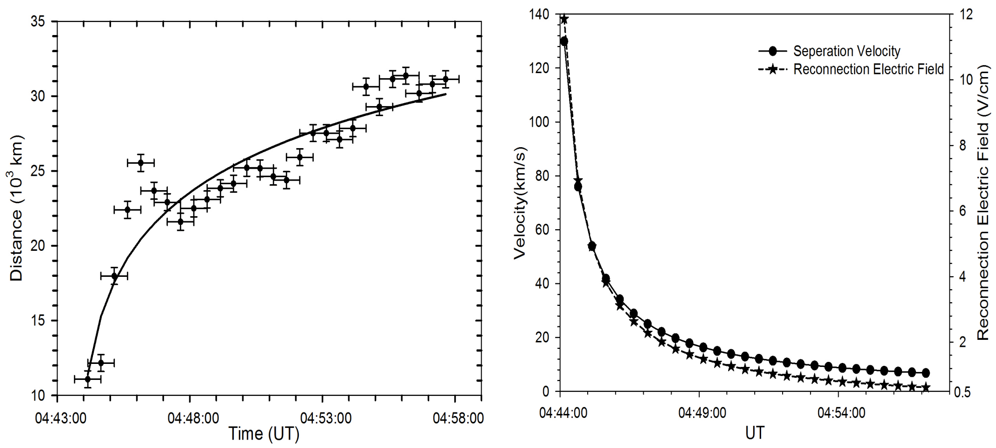

Figure 5.7: Left - The separation of flare kernels A and B of two opposite flare ribbons (*cf.* Figure 5.5-Left Panel) over time. The velocity decays exponentially from 120 to 10 km s^{-1} in a ten minute interval. Right - The deceleration of flare ribbons and the reconnection electric-field variation over time.

If these bright blobs are joined together then indicating that the mass ejection was of a spherical waveform resembling the blast wave seen by SOHO/ EIT at the initial phase of the CME. The speed of these bright blobs was in the range 200 to 300 km s^{-1}. The flare was composed of several bright/eruptive centers forming the ribbon structure. The ribbon structure in the flare was very clear beginning at 04:44:39 UT. The separation between the flare kernels A and B of the two opposite ribbons, shown in the frame taken at 04:50:39, has been measured as a function of time and is presented in Figure 5.7. The observations revealed that in the initial phase (04:44 – 04:46 UT) these kernels were separating away from each other with the speed of >80 km s^{-1}, which, however, slowed down exponentially to $\sim$ 20 km s^{-1} after 04:48 UT.

Further, we estimated the reconnection electric-field (ER) variation during flare as follows. We estimated the magnetic-field strength with the time cadence of 30 seconds with the aid of cubic spline interpolation technique employing the 96-minute full-disc MDI magnetic-field observations. The cubic spline interpolation algorithm for finding the interpolated magnetic field (B$_{int}$) is based on the smoothed interpolation described by Press et al. (1992) in their book "Numerical Recipes in C: The Art of Scientific Computing" considering first and second order derivatives as following.

$$\mathrm{B_{int}(t) = A.B(t_j) + C.B_{t_{j+1}} + D.B"(t_j) + E.B"_{t_{j+1}}} \tag{5.2}$$

Here $B(t_j)$ and $B(t_{j+1})$ are the observed values of photospheric magnetic field at time t_j and t_{j+1} respectively and t is the intermediate time for which magnetic field is to be estimated. A, C, D, and E are the parameters defined as following:

$$\mathrm{A \equiv \frac{t_{j+1} - t}{t_{j+1} - t_j}}$$

$$\mathrm{C \equiv 1 - A = \frac{t - t_j}{t_{j+1} - t_j}}$$

$$\mathrm{D \equiv \frac{1}{6}(A^3 - A)(t_{j+1} - t_j)^2}$$

$$\mathrm{E \equiv \frac{1}{6}(C^3 - C)(t_{j+1} - t_j)^2}$$

The estimated B_{int} is then multiplied with the corresponding ribbon-separation speed (V) so as to obtain the reconnection electric field (E_R) from the following relation.

$$E_R = V.B_{int} \tag{5.3}$$

The ribbon separation speed as well as the reconnection electric field mimics the passage of the CME. The flare kernel B of the west ribbon struck the leading sunspot around 04:54:39 UT and stopped further movement.

5.2.4 The Coronal Mass Ejection (CME)

According to Thompson et al. (1998) and Plunkett et al. (1998), beginning at about 04:35 UT, EIT recorded several CME signatures, including dimming regions close to the eruption, post-eruption arcade formation, and a bright wave-front propagating quasi-radially from the source region. However, the CME in the form of an EIT wave as shown in Figure 5.8 (left) was first observed in the difference images in 195 Å between 04:34 and 04:50 UT suggesting that the disturbance began at a time between these two times with an uncertainty of less than 18 minute. The CME was later observed by the *Large Angle Spectrometric Coronagraph* (LASCO) as a "halo" CME. In this investigation we consider analysis of plane-of-sky images of magnetograms, the Hα flare and the EIT images. We do not attempt to transfer or extrapolate a full 3D analysis. The CME emerged from its heliographic location N23 W07 and traveled outward as a spherical wave (*cf.* Figure 5.8 - left) with a speed of about 250±20 km s^{-1} (Plunkett et al., 1998). In Figure 5.8 (right) we further show the EIT 195 Å plane-of-sky images. We note explicitly that around 03:08 UT the first EUV emission started to brighten in the core of the reversed-S sigmoid configuration, which implies that slow magnetic reconnection was taking place there (Cheng et al., 2010) perhaps initiated as a consequence of the filament disruption observed on 12 May at 03:03 UT (*cf.* Figure 5.3).

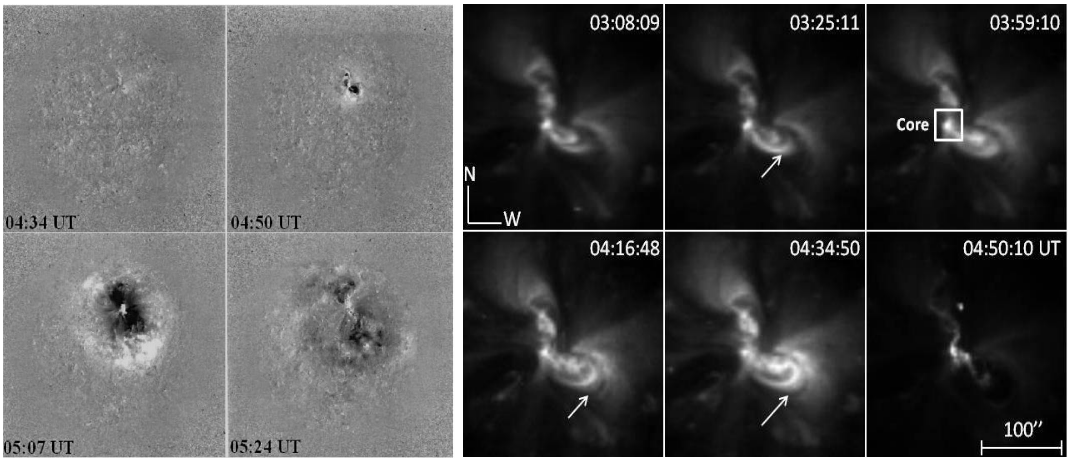

Figure 5.8: Left - SOHO/EIT 195 Å running-difference images of large-scale wave transient moving out as a CME. The wave-like structure began around 04:34 UT. Right - The time-series of SOHO/EIT 195 Å images. Loop brightening may be noted at 03:25:11 UT, which continued to brighten the whole active region at 04:34:50 UT.

We further note that as the field lines in the reversed-S sigmoid configuration continually reconnected, the filament (flux-rope) rose slowly and disrupted which unambiguously reveals the first brightening of the coronal loops around 03:25:11 UT (shown by arrow). The brightening of the coronal loops continued. As seen at 04:34:50 UT, all loops brightened, in close temporal agreement with the disruption of part F1 of the filament where mostly flux cancellation was taking place. In comparing this EIT image with the difference image (04:34 - 04:16 UT) in the left panel at 04:34 UT, we find a signature of dimming in the region but not the signature of blast wave. We consider this time as the onset of the filament rising due to loss of equilibrium in the active region. We believe the rising filament caused the dimming and then it continued to move up into the corona. Filament eruptions from the Sun are often accompanied by a dimming of the local coronal emission at many different wavelengths and appear to be associated with transient coronal holes (Harrison et al., 2003; Imada et al., 2007; Reinard and Biesecker, 2008, 2009; Jin et al., 2009; Dai et al., 2010; Robbrecht and Wang, 2010). The dimmings are in most cases caused by a decrease in the coronal density due to the opening up of the magnetic field and escape of the entrapped material into the heliosphere. The closing down of the flux proceeds from the inside outward, with the field lines rooted nearest to the photospheric polarity inversion line (PIL) pinching off first, giving rise to a progressively growing post-eruption loop arcade (Kopp and Pneuman, 1976). In the present case it appears that the disruption of the F2 part of the filament due to continuous loss of equilibrium (because of increasing gradients and rotation angle of LP2) initiated the flare and the CME starting around 04:43 UT as seen in GOES 1-8 Å and Hα observations. The CME can be seen in the difference image at 04:50 UT due to 18 min cadence of the EIT instrument. Thus, in contrast to Thompson et al. (1998) and Plunkett et al. (1998) we do not consider the onset of CME at 04:35 UT, rather we propose that the CME and flare began together around 04:42:36 UT (onset of the X-ray flare) as a consequence of opening of high altitude loops and consequently their reconnection. The filament detached from the photosphere and started to rise to the corona through the chromosphere perhaps with projected speed of 250 $\pm$ 20 km/s measured by Thompson et al. (1998) from EIT difference images, and by us from the bright mass ejection observed in H *alpha*. The rising filament motion caused continuous brightening of EIT loops as it was moving up into the corona starting from 03:25 UT seen in Figure 5.8 (right) and finally opened the loops around 04:42:36 UT so as to generate EIT wave seen later at 04:50 UT in EIT difference images. Due to the slow cadence of EIT image acquisition the reconnection time and hence the wave onset times were missed.

5.3 Discussions

We carried out a detailed study of the evolution of NOAA AR 8038 during its passage on the disk from 05 to 16 May 1997. In Figure 5.9, we attempt to use a schematic model to explain the full evolution of the flare-CME from early development to the ultimate eruption. It is well established that the full evolution of the CME is divided into four phases: i) the build-up phase, ii) the initiation phase, iii) the main acceleration phase, and iv) the propagation phase (Cheng et al., 2010). However, our current investigation is focused on the first three components of the CME, which include the flare and CME as two modes of a single energy release system.

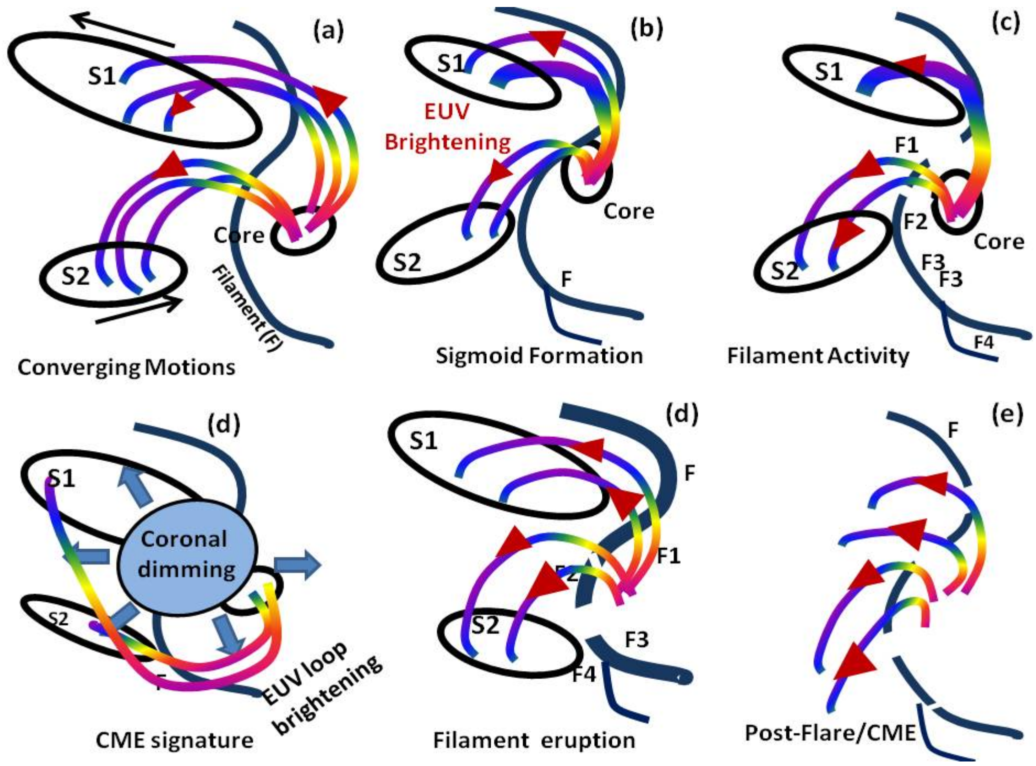

Figure 5.9: A schematic drawing of the evolution of the active region in the framework of Flare–CME event. Rainbow colored lines refer to the overlying magnetic-field lines. The leading and the following polarity regions are demarcated by black ellipse-shaped structures shown by core and S1 as well as S2 respectively. The dark blue line represents the filament overlying the polarity inversion line (PIL). The direction of magnetic-field lines is shown by magenta arrows. The light-blue arrows (d) represent the propagation of coronal dimming.

The build-up phase lasted five days, from 07 to 12 May 1997, before the CME. As discussed earlier, it is characterized by many precursor signatures: flux cancellation, filament activity, sigmoid, and Hα plage and EUV brightening, even though these signatures are neither necessary nor sufficient for an eruption. Formation and evolution of filaments have been extensively studied for many years. However, our observations of the filament formation and activation using two flux systems driven by the convergence of opposite polarities along the PIL confirms the simulation study carried out by Welsch et al. (2005). Chae et al. (2001) and Bharti et al. (2007) proposed that slow magnetic reconnection driven by converging motions may occur at all times in the chromosphere. The continuous reconnection can result in both the overlying field lines straddling the neutral line and the low-lying, core field lines (Chae et al., 2001; Welsch et al., 2005).

Furthermore, some EUV brightening/jets and small Hα eruptions/surges took place at the site of magnetic-flux cancellation (Liu, 2004). We propose that as the positive and negative fluxes moved close to each other near the PIL the anti-parallel inner ends of the two bundles of the loops reconnected slowly and continuously in the lower atmosphere (i.e. the chromosphere). These convergence motions almost perpendicular to the PIL (Cheng et al., 2010; Li et al., 2010) started to form sigmoidal structure (Figure 5.9a). At the same time, it also produced the low-lying field lines that are nearly parallel with the PIL. As time progresses, the lower field lines in the eastern part and the pre-existing field lines in the western part, being both J-shaped, moved closer to each other, driven by the continuous convergence motion along the PIL and formed a reversed-S sigmoid structure in the projection sky plane (Figure 5.9b). We conjecture that the ends of the two bundles of the J-shaped loops, on the opposite sides of the PIL, reconnected as tether cutting and formed the little twisted field lines, while the energy released through the reconnection heated the plasma in the middle part of the reversed-S sigmoid configuration, thus producing the EUV core brightening at 03:08 UT. The shortest field lines submerged into the sub-photosphere after the slow reconnection, which was manifested by the magnetic cancellation in the photosphere, and possibly produced the filament activity as seen in the chromosphere (Figures 5.9b-c). Recently, Tripathi et al. (2009) and Green and Kliem (2009) also reported such a sigmoid structure coming into existence after a pair of J-shaped arcs reconnected through flux cancellation in the photosphere. We propose that these sigmoid structures provide observational evidence of the flux rope existence prior to the flare-CME eruption. The active filaments condensed at the dip of these two J-shaped field lines, as indicated in Figure 5.9c. As the filament mass flew down from 10 May onwards along the field lines, more field lines rose and served as the overlying loops. These loops were heated slowly and remained invisible in the EUV until about an hour prior to the CME eruption on 12 May 1997. It is further proposed that as long as some open field lines exist at the reconnection site, part of the filament mass may erupt as EUV jets. However, although part of the filament mass (F1) flew down slowly or erupted, the rest of the filament appeared to be quite stable in the dip of the field lines at all times prior to the CME eruption (*cf.* Figure 5.4) as shown in Figure 5.9(c-d).

The initiation phase occurred when the upward force within the sigmoid was able to overcome the tension force of the overlying field lines. As more and more J-shaped loops reconnected by tether cutting, the twisted field lines in the reversed-S sigmoid configuration, beneath the overlying loops, moved up due to an increased upward magnetic hoop force and a decreased downward magnetic stress Moore et al. (2001b); Liu et al. (2007); Sterling et al. (2007). The rising, twisted field lines pushed the overlying loops upward. When the overlying loops were stretched to a certain extent due to the tether-cutting reconnection, a current sheet between the legs of the distended overlying field line was formed under the loops so that a fast, runaway reconnection was subsequently initiated, leading to the main energy-release phase and the impulsive acceleration of the CME; this is the standard model of eruptive flares (Hirayama, 1974). Another possibility leading to the main eruption is the triggering of MHD instability of the flux rope formed from the tether-cutting reconnection, through the kink and/or torus instability (Török and Kliem, 2005; Kliem and Török, 2006; Démoulin and Aulanier, 2010).

The subsequent main acceleration phase is believed to be caused by runaway magnetic reconnection, coupled with the explosive poloidal flux injection into the rising flux rope. Our observations show a fast reconnection rate (high speed of ribbon separation) and high reconnection electric fields in the main phase suggesting that the reconnection rapidly injects a large amount of poloidal flux into the twisted field lines, thus supplying a stronger upward driving force so as to impulsively accelerate the CME flux rope. On the other hand, the CME eruption led to a decrease in the magnetic pressure below the flux rope, which caused a faster inflow toward the current sheet and enhanced the runaway reconnection. This positive feedback process effectively released the magnetic free energy stored in the lower corona, which was converted into the kinetic energy of the CME and also produced the enhanced soft X-ray emissions (Li et al., 1993). On the contrary the HXR emission in 25–50 keV does not appear to be directly associated with the main phase of the flare as it is delayed by almost seven minutes from the onset of soft X-ray and Hα flare. It is possible that the instrumental sensitivity of BATSE might have restricted the early detection of HXR emission. Our proposal is strengthened by observed protons of > 10 MeV in association with this event, which, must have been accelerated along with the CME in the inner corona. However, this event failed to reach the NOAA *Space Weather Prediction Centers'* (SWPC) criteria to assure its place as a "qualified" proton event. On the other hand, the fact that interplanetary protons were seen at Earth is important. The other possibility might be that HXR emission is more associated with the CME propagation in the outer corona. This suggests early acceleration of the CME (in the inner corona) accelerated electrons to high energy during its propagation outwards and those runaway high energy electrons produced the hard X-ray emission. In the present case, a significant portion of the energy was carried by CME so the input energy for the flare was keep on decreasing over time as exhibited by reconnection electric field (see also Zhang et al., 2004; Qiu et al., 2004; Temmer et al., 2008). It suggests that the main acceleration phase of the CME in the inner corona is likely to be caused by fast runaway magnetic reconnection. Later on, the CME propagated with an almost constant velocity in the outer corona. In general, these observational results are consistent with the standard CME-flare model.

Moreover, EUV loops brightened around 04:34 UT in association with filament eruption activity. This led to a depletion of mass in the lower atmosphere near the active region and formed a coronal dimming (Thompson et al., 1998; Harra and Sterling, 2001) a few minutes before the main CME-flare eruption at 04:43 UT. As the magnetic reconnection progressed, the reconnection site rose gradually. The upward moving reconnection site induced the flare ribbons to separate horizontally at the base of the corona, as evident in Hα. Beneath the reconnection site, the newly reconnected magnetic loops were filled by the plasma that evaporated from the chromosphere and the sigmoid magnetic structure evolved into post-flare loop arcades (see also Liu et al., 2007), as shown in Figure 5.9 (f). After the main phase which lasted about seven minutes, the runaway reconnection came to a stop. The CME now entered into its simple propagation phase: the CME was propagating with a nearly constant speed or with a deceleration in the outer corona.

5.4 Conclusions

We studied the evolution of magnetic configuration for a few days prior to the flare and CME activity on 12 May 1997. During the build-up phase, we observed many precursors such as magnetic field cancellations, filament activation, bright and dark surges and plage brightening in the chromosphere, instantaneous EUV jets, and a reversed-S sigmoid structure. All the features were physically related to a persistent, slow, magnetic reconnection in the lower solar atmosphere, which was manifested as photospheric magnetic cancellations. Before the flare and CME eruption on 12 May 1997 there was a long period of reconnection occurring in the lower layers, resulting in the transfer and accumulation of magnetic free energy manifested as magnetic flux, as well as the formation of a magnetic structures favorable for eruption, i.e., the sigmoid structure of this event derived from the rotation of the leading sunspot. In addition to the process of flux cancellation, the emergence of magnetic flux may also play an important role in transferring magnetic free energy from the sub-photosphere into the corona (Tian et al., 2008; Archontis et al., 2009). We observed converging motions of opposite polarities in this active region beginning on 10 May 1997. The magnetic-field shear can be caused by the converging motion of opposite magnetic fluxes (Titov et al., 2008), which, in turn, produces the sigmoid-shaped structure as seen in Hα and EIT observations of 12 May 1997. The enhanced shear aided the accumulation of free energy in the corona. Therefore, the build-up phase accumulated sufficient magnetic free energy, beginning on 07 May 1997, for the eventual initiation and the final eruption of flare and CME event on 12 May 1997.

In the present event we found that the EUV emission started to brighten in the core of the reversed-S sigmoid configuration, which implies that slow magnetic reconnection was taking place in the active region. As the field lines in the reversed-S sigmoid configuration continually reconnected, the F1 part of the filament (flux-rope) rose slowly and then erupted. Furthermore, the convergence of opposite polarities resulted in increasing magnetic-field gradients. We believe that the loss of equilibrium began in this configuration suggesting an onset of the eruption at 04:34 UT seen as emission of loops in EIT images. However, the inner core magnetic reconnection prior to the eruption, combined with the bipolar magnetic structure in the active region and the absence of remote brightenings, seem to rule out the breakout model as the triggering mechanism of this flare associated CME event. Instead, we think that this eruption is most consistent with the tether-cutting initiation model.

Chapter 6

Self-organized criticality in the Solar corona

6.1 Introduction

The energy release in solar flares occurs as a consequence of destabilization of the coronal magnetic field lines. There are a number of flare models to explain the different magnetic topologies, which are based on specific instabilities or drivers viz. 1) standard 2D-flare model, 2) The Emerging Flux model, 3) The equilibrium loss model, 4) 2D Quadrupolar Flare model, 5) The Magnetic Breakout Model and 6) 3D Quadrupolar Flare Model. These models were later unified by (Shibata, 1998, 1999) envisioning a grand unified model of solar flares. The above stated models differ only in the driver mechanism of instability and dimensionality of magnetic reconnection geometry. In these models, multiple driver mechanisms have been proposed to explain the instabilities in the coronal magnetic field lines which give rise to energy release in the form of solar flares *viz.* prominence/ filament eruption, interaction of overlying magnetic field lines. Therefore, completely diverse mechanisms operating over solar flares account for several plasma processes in it.

In a statistical survey, Akabane (1956) discovered the scale-invariant power-law distribution of flare frequency versus respective energy released during the flares. Dennis (1985) revealed a power-law distribution with a slope of -1.8 in the occurrence of solar flares of magnitude of nano-flares to large X-class flares. This scale independent nature of solar flares has remained unexplained for long. For the very first time, Bak et al. (1987), the father of self-organizing criticality (SOC), provided an explanation to the "omnipresent" power-law distribution, observed also in many natural events such as sand-pile avalanches and earthquakes (Gutenberg-Richter law) with the help of the scale-free behavior to the 1/ f -flicker noise. Self-organized criticality (SOC) is defined as a natural state into which a dissipative system evolves into, independent of the nature of initial conditions. In general, various external forcing mechanisms may lead a system into criticality, where energy is dissipated in avalanche-like events. Lu and Hamilton (1991) were the first to apply the concept of SOC to solar flares to explain power-law nature of frequency distribution of various solar flare parameters with a cellular automaton model. They have proposed that the solar coronal magnetic field is in a state of self-organized criticality. In this model, pixilated coronal magnetic-field have been used as an analogy of lattice points of the sand-pile as shown in Figure 6.1 (Takalo et al., 1999). Further, magnetic-field destabilization is simulated with the condition when the gradient of ambient magnetic-field reaches a critical value, similar to the magnetic-field discontinuity angle as previously proposed by Parker (1988). With this kind of model, the observed power-law dependence of solar flare occurrence rate on flare size can be explained. Physically, solar flares may be understood as the avalanches of many small scale reconnection events, analogous to avalanches in the sand-pile model (Bak et al., 1987). Jain and Bhatnagar (1983) performed a statistical survey of the relationship between magnetic-field evolution and related X-Ray & Hα emission profile. They estimated a cut-off "magnetic complexity number" for flares of various intensities. It is very hard to illustrate the SOC observationally as the observing cadence of coronal magnetic-field is very small in comparison to the energy release rate in the solar flares. Many attempts have been made on the photospheric line-of-sight magnetograms as well as force-free extrapolated magnetic-fields in order to evaluate the parameters of criticality.

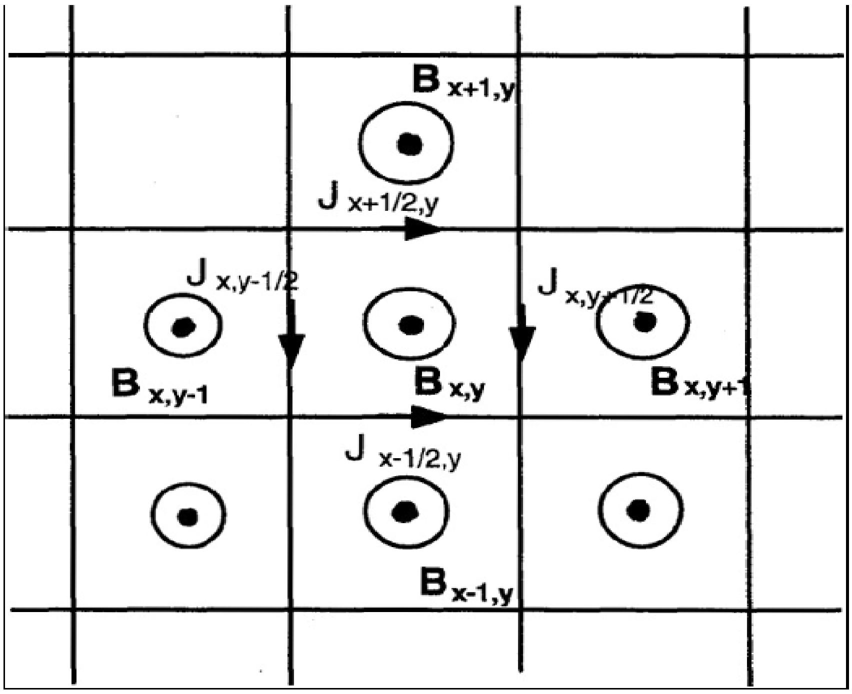

Figure 6.1: Cellular automaton model with magnetic fluxtubes as the lattice points where each one is characterized by a magnetic field B_z(x±1,y±1). The currents are shown at four sides with respective directions.

Since Giovanelli (1948) the role of magnetic-field destabilization, which follows up by reconnection to trigger the solar flare, is recognized. Parker (1963) described the magnetic-field annihilation as an underlying process of energy release during solar flares and since then, magnetic reconnection has become the only candidate which can satisfactorily explain solar flare energetics. Although the observations of coronal magnetic-fields are very difficult, Aulanier et al. (2000), Fletcher and Hudson (2001), Masson et al. (2009) have shown the evidence of coronal null points as a signature of reconnection during solar flares employing alternative methods of visualizing coronal magnetic-field topology. Thus, flare magnetic configuration may evolve through different topologies. To investigate the proxies for energy build-up, trigger and release, the role of magnetic field complexity triggering flare-CME system occurred on 12 May 1997 has been studied by Jain et al. (2011b). They attributed slow low-layer magnetic reconnection seen in the form of photospheric magnetic-field emergence and cancellation to be responsible for the storage of magnetic free energy in the corona. Thus we may note that the photospheric magnetic-field plays an active role in producing solar flares and can be regarded as a good test candidate for self-organization of corona evolving to criticality and leading to solar flare energy release. Till date, the problem of establishing this concept to the solar flare observations is very least attempted due to the lack of high-cadence solar observations in comparison to energy release rate in solar flares. Michelson Doppler Imager (MDI) instrument onboard SOHO observatory has provided 96-m cadence full-disk solar magnetograms for over one and half decades (Scherrer et al., 1995). Further to this, Helioseismic Magnetic Imager (HMI) onboard SDO mission, a successor of MDI/SOHO is continually providing excellent full-disk magnetograms with the temporal cadence of 45 s and thus provides a nice opportunity to study the evolution of photospheric proxies for coronal self-organization. Thus, the detailed investigation of SOC phenomenon in view of high cadence observations of photospheric magnetic field and coronal observations of solar flare may lead us to a better understanding of the driver mechanism of energy release in solar flares.

In this chapter, we investigate the relationship between evolution of photospheric magnetic-field with the coronal X-ray emission. Section 6.2 consists of the detailed observations used for this investigation. In section 6.3, we present the data analysis and results. We summarize and interpret the results obtained from the study in section 6.4.

6.2 Observations and Analysis Techniques

We investigate relationship between photospheric magnetic-field and coronal X-ray emission in order to understand the photosphere-corona coupling. We divide this study in two parts. Firstly, we undertake the investigation of full-disk magnetic-field observation and co-temporal disk-integrated coronal X-ray flux. Later, we study the magnetic-field parameters associated with the flare and co-temporal X-ray flux. In this way, we quantify both statistically independent and flare-dependent photosphere-corona coupling. In Table 6.1, we enlist the characteristics of the time duration selected for investigation of statistically independent relationship between photospheric magnetic flux and coronal X-ray flux. We also list the number of flares as a function of importance class for the selected duration. We estimate the photospheric magnetic-field parameters from synoptic magnetograms available from Michelson Doppler Imager (MDI) onboard SOHO mission.

Table 6.1: List of the observing duration selected for the study of photospheric magnetic flux and coronal X-ray flux

S.N	Duration	No. of ARs (AR Nos.)	No. of Flares (Class)
1	October 2003	29 (10464 - 10493)	59 (C) - 27 (M) - 3 (X)
2	August 2004	12 (10654 - 10666)	69 (C) - 21 (M) - 1 (X)
3	September 2005	09 (10803 - 10812)	51 (C) - 23 (M) - 8 (X)

The photospheric full-disc magnetic field observations are regularly obtained from MDI/SOHO instrument (Scherrer et al., 1995). MDI provides photospheric line-of-sight magnetic field (in gauss) of the Sun at every 96 minutes. The MDI instrument computes the magnetic field onboard employing the method of differencing dopplergrams obtained in right and left circular polarized light. Thirteen annual 14 Gb tar files are available with the time resolution of 96-minute observations during 1996 - 2010. We used the calibrated level 1.8

magnetograms for the durations listed in Table 6.1 as obtained from the MDI data archive at URL: `http://soi.stanford.edu/magnetic/level1.8`. The photospheric magnetic-flux has been estimated by employing the technique as discussed in Chapter 5 as well as in Jain et al. (2011a). The magnetic flux is estimated as the product of magnetic-field strength (H) and area of the corresponding polarity. H is estimated using SOHO/MDI 96-minute full-disk observations with the help of functions provided in SolarSoft, a library of algorithms written in IDL language. The level 1.8 data obtained from the archive are processed for further measurements. We employ the Carrington Projection method for foreshortening correction using the `map_carrington.pro` routine provided in SolarSoft. The magnetic flux is estimated separately for regions of leading and following polarities identifying them distinctly as discussed below. The regime (pixels) having magnetic field strength $\geq$ 10% of the positive peak magnetic-field strength is considered as a leading polarity region. Similarly, the regime (pixels) belonging to the magnetic-field $\leq$ 10% of the negative peak magnetic field strength is considered as a following polarity region. The rest of the region is considered as background or quiet Sun. The size of one pixel is 1.97 arcsec, and therefore the area occupied by both the polarities is then estimated separately by total number of pixels multiplied by area of single pixel, i.e. $725^2 \times 1.972 \times 10^{10}$ cm^2. The magnetic flux for the respective polarity is then estimated by multiplying the corresponding total magnetic-field strength with the above estimated area.

The Coronal X-ray flux is taken from the observations provided by full-disk X-ray sensors on-board the Geostationary Operational Environmental Satellites (GOES) operated by NOAA since 1974. GOES X-ray flux 3 s cadence data is available from the URL: `http://goes.ngdx.noaa.gov/data/avg` which is also processed through SolarSoft package. These observations are then averaged to 96 min time duration in order to achieve the same time cadence as that of photospheric magnetic field observations. Finally, this time averaged coronal X-ray flux is averaged over 8-hours to obtain 3 values in each day.

The standard deviation is termed as the uncertainty in this dataset as well as occurred due to averaging.

Further, in order to explore the evolution of photosphere-corona coupling $\sim$1 hour prior to a large (M and X class in this study) solar flare, we estimate magnetic-field parameters from Helioseismic Magnetic Imager (Scherrer et al., 2012, HMI) instrument onboard the Solar Dynamic Observatory (SDO) mission. HMI provides full-disk magnetograms at wavelength 6173 Å with spatial resolution of 0.5" per pixel and temporal cadence of 45 s. In Table 6.2, we list the timing of flare X-ray emission as well as the quiet time duration prior to the respective flare considered for current investigation. We have estimated the photospheric magnetic-flux and coronal X-ray flux for all the flares listed in this Table. Similar to the techniques discussed in the previous section, the magnetic flux is estimated separately for leading and following polarities. However, for this analysis, we have selected only that active region which was associated with the respective flare in contrast to previous analysis where we have selected all the ARs from the full solar disk. In this sub-magnetogram, the area occupied by both the polarities is then estimated separately by total number of pixels multiplied by area of single pixel, i.e. $725^2 \times 0.5 \times 10^{10}$ cm^2. The magnetic flux for each polarity is then estimated using above relation in the units of Gauss/cm^2 (Mx). For these events, coronal X-ray flux is also derived from the observations of GOES-15 satellite. The observing cadence of the GOES X-ray flux is 2 s. which has later been averaged to 45 s in view of photospheric magnetograms observation cadence.

6.3 Data analysis and Results

It has been proposed that magnetic free energy is stored in coronal loops and upon their self-organization leading to a criticality; it is released as flares/CMEs. In this regard, we explore the relationship between photospheric magnetic flux and associated co-temporal energy released in the form of X-rays from the corona.

6.3.1 Probing the photosphere-corona coupling

We use the photospheric magnetic-field observations from MDI/SOHO to estimate the signed and unsigned magnetic flux for very high flare productive months viz. October 2003, August 2004 and September 2005 as listed in Table 6.1. The techniques for estimation of the photospheric magnetic flux and coronal X-ray flux are described in previous section. Figure 6.2 shows the photospheric magnetic flux and coronal X-ray flux in the bottom and top panels, respectively for October 2003. The photospheric magnetic flux and coronal X-ray flux are varying in the range of 5×10^{28} - 3×10^{29} Mx and 1×10^{-7} - 2×10^{-4} Watts/m^2, respectively as may be noted from Figure 6.2. However, the dynamic range of photospheric magnetic flux variation is very smaller ($\sim$2 times) relative to the $\sim$3 orders of magnitude variation of coronal X-ray flux but co-temporal transient features in both the parameters may be noted in the Figure 6.2. This motivated us to undertake the correlation study between the aforesaid parameters.

We have plotted the coronal X-ray flux versus the respective photospheric magnetic flux as shown in Figure 6.3 for October 2003. The best-fit of parameters reveals strong power-law dependence between them with a linear regression of 0.82 and power law index of 4.24 as shown in Figure 6.3.

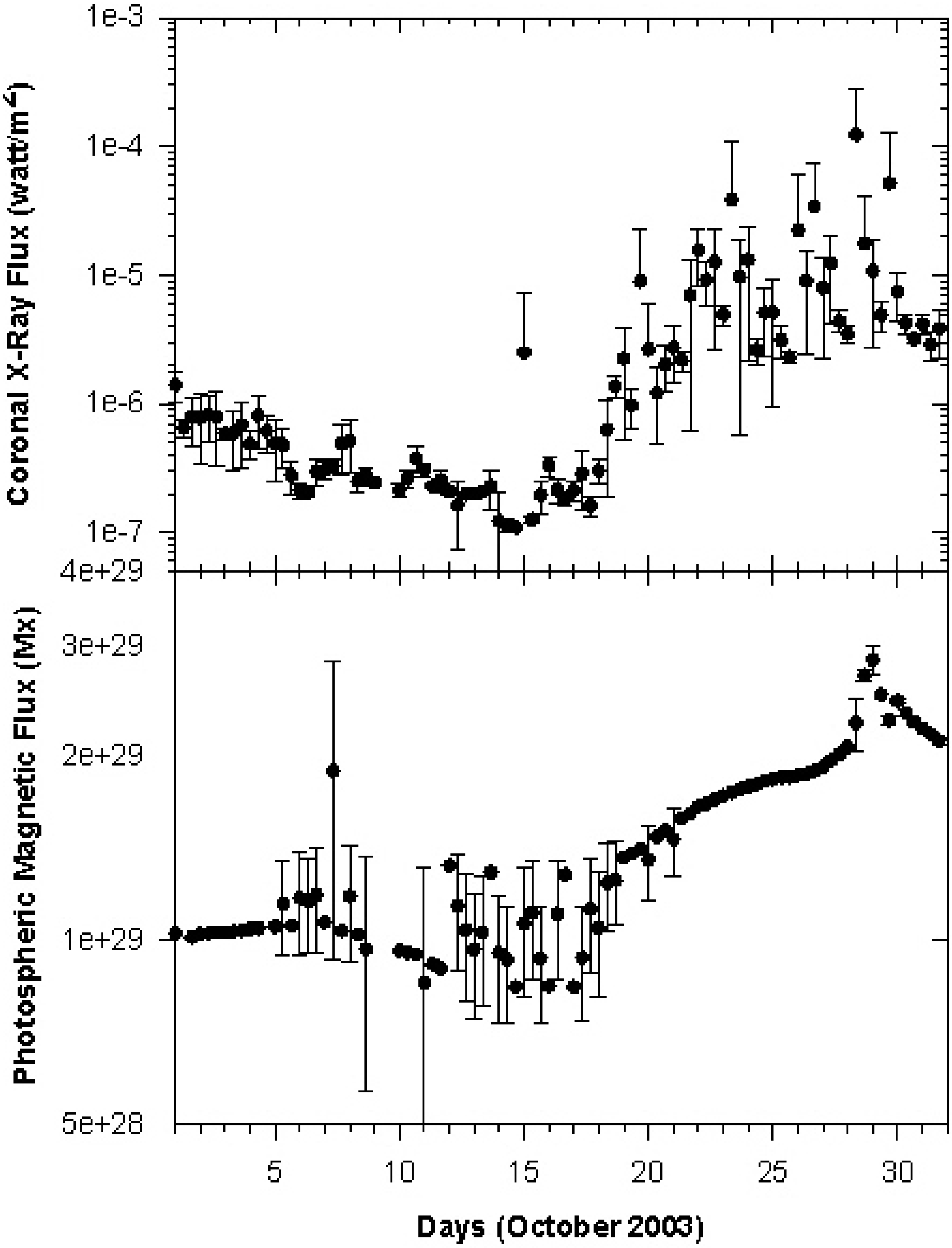

Figure 6.2: Top panel - Temporal evolution of coronal X-ray flux over the period of October 2003. Bottom panel- Time variation of Photospheric magnetic flux over the same period. Variation of the coronal X-ray flux in response to the temporal evolution of photospheric magnetic flux may be noted.

As the power-law relationship between photospheric magnetic flux and coronal X-ray flux holds for the observations for a whole month irrespective of the AR complexity, magnetic-field topology etc., we further explore the above correlation for observations for different durations. In this regard, we have estimated the aforesaid parameters for the months August 2004 and September 2005 with the same technique as discussed previously. As these months have also been observed to be high flare productive, we consider them too under the same selection criteria as for October 2003, for choosing the duration of analysis and listed in Table 6.1. Figure 6.4 shows the temporal evolution of photospheric magnetic flux and coronal X-ray flux for the months August 2004 (left) and September 2005 (right) in the top and bottom panels, respectively.

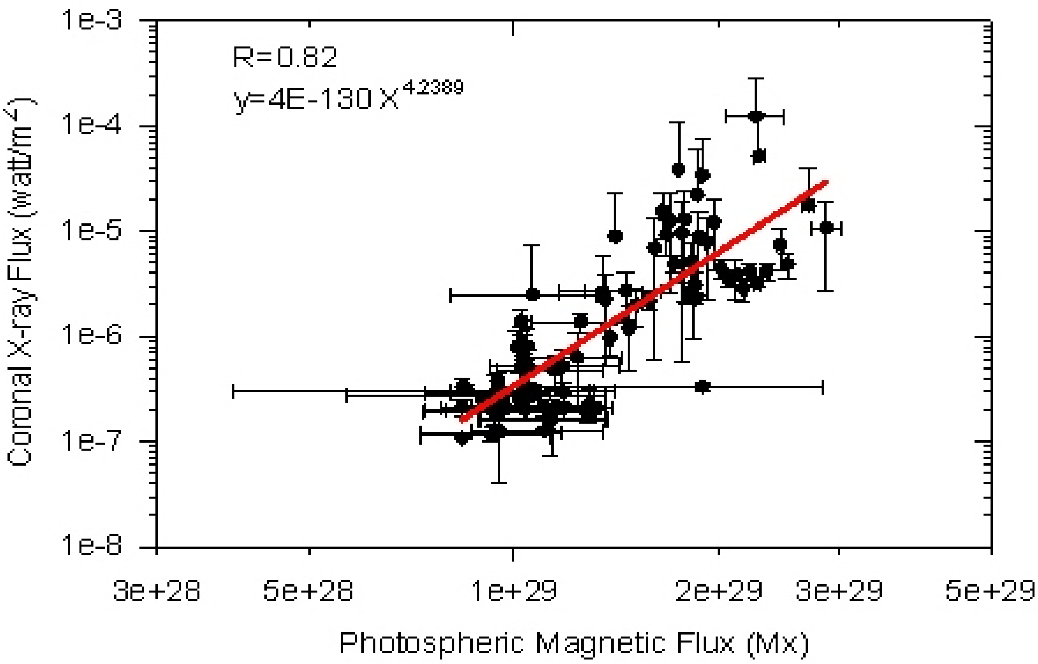

Figure 6.3: Coronal X-ray flux for October 2003 plotted as a function of photospheric magnetic flux. The error bars are shown in both the estimated parameters. Red line shows the power-law fit function with the strong correlation of R=0.82.

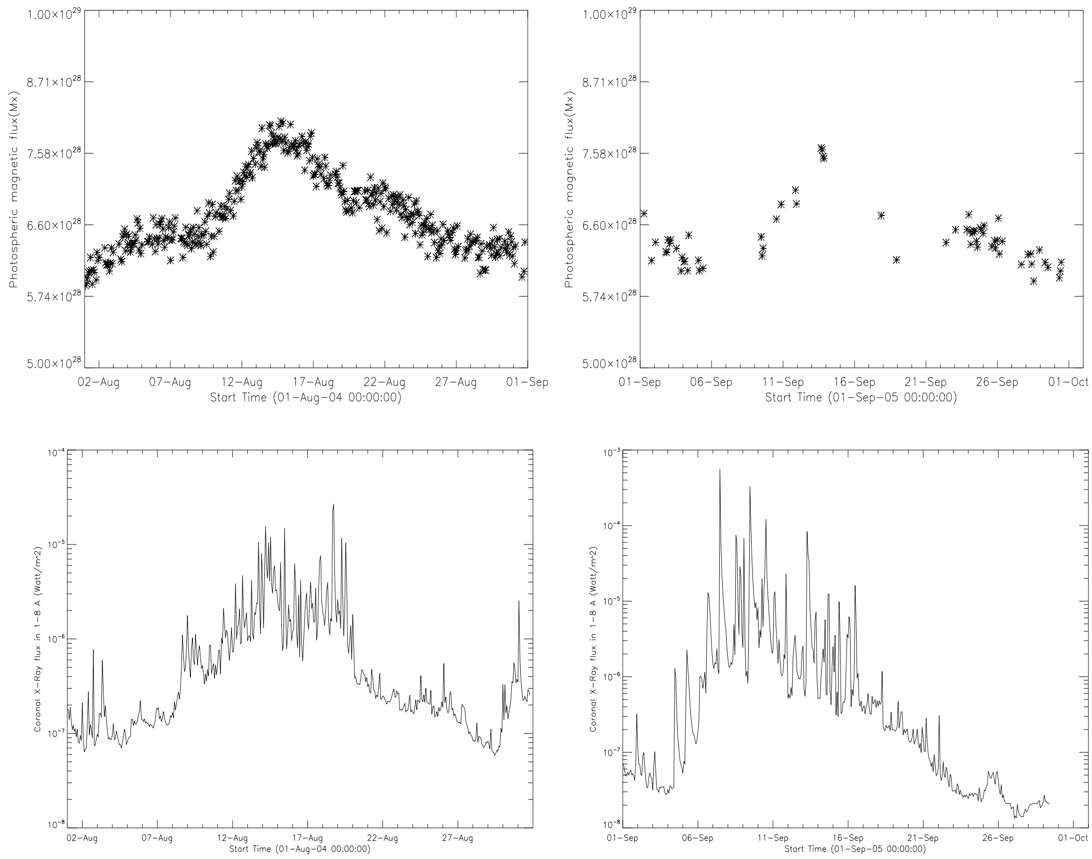

Figure 6.4: Top and bottom panels, respectively show the Photospheric magnetic flux and coronal magnetic flux plotted for the month August 2004 (left) and September 2005 (right).

From Figure 6.4, we may note that the photospheric magnetic flux and coronal X-ray flux are varying in the range of 5.7×10^{28} - 8.7×10^{28} Mx and 1×10^{-7} - 5×10^{-4} Watts/m^2, respectively. Thus the photospheric magnetic flux ranges similar to that estimated for October 2003. Further to this, we also note the co-temporal variations in both the parameters which confirm the interrelation of the two parameters irrespective of the duration of investigation. To demonstrate this, we combined and plotted the photospheric magnetic flux versus co-temporal coronal X-ray flux for both the months as shown in Figure 6.5. We find a power-law relationship between the parameters with the power-law index 9.98 and the linear correlation coefficient to be 0.65.

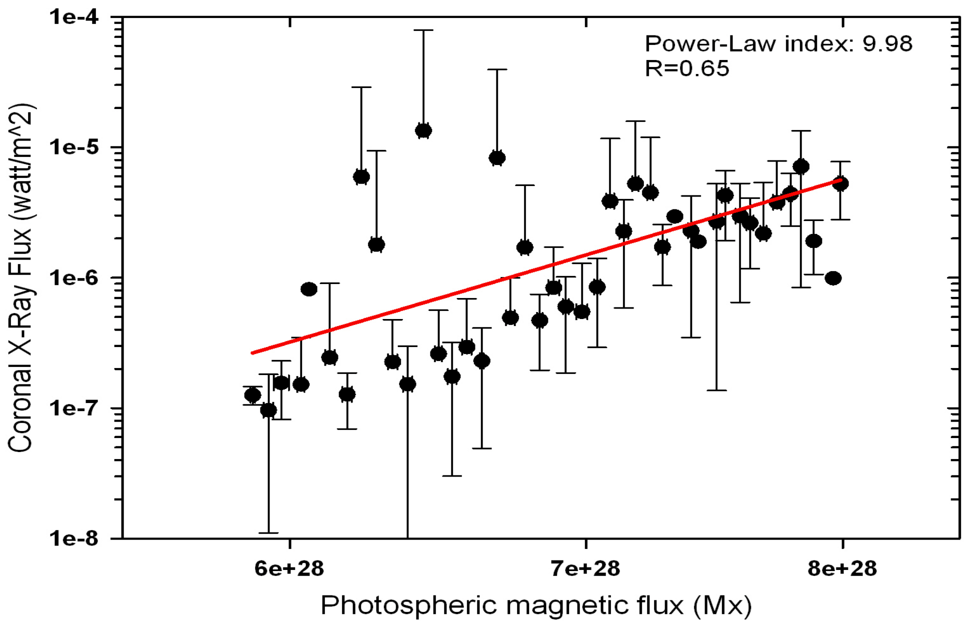

Figure 6.5: Photospheric magnetic flux plotted versus coronal x-ray flux combined for the months August 2004 and September 2005. The error bars are shown in both the estimated parameters. Red line shows the power-law fit function with the strong linear correlation coefficient of 0.65.

The above study suggests that the photosphere-corona coupling is intrinsic and invariant of the selection of the duration of investigation and nature of the individual flaring active region as well as its magnetic-field complexity. Our this result presents an observational evidence of the theoretical investigation earlier by Lu and Hamilton (1991). They suggested that energy release during solar flares can be understood as series of small scale magnetic reconnections where the intensity of typical flare is only dependent on number of reconnections during a flare. However, the current study is restricted to 96 minute cadence observations of the photospheric magnetic-field made from MDI but to improve our understanding we should employ multi-wavelength observations, which are recently being made available. In this context, we investigate the observations from Helioseismic Magnetic Imager (HMI) onboard SDO satellite, which provides the photospheric line-of-sight (LOS) magnetic-field observations with a superb time cadence of 45 seconds. In addition, Geostationary Orbital Environmental Satellite (GOES) - 15, a newcomer in the series of GOES satellites is observing the disk-integrated coronal X-ray flux with the cadence of 2 seconds. The above study employing data from MDI motivated us to probe the data from these high temporal cadence instruments to extend our investigation in order to explore photospheric parameters as a possible proxy of the evolution of criticality of the corona to give rise the large flaring activities as presented in the following section.

6.3.2 Evolution of photosphere-corona coupling

In order to explore the photospheric proxies leading to the criticality of the solar corona and subsequent flare, we study the temporal evolution of the photospheric and coronal parameters using high cadence observations. In this regard, we study the evolution of photospheric magnetic flux and associated coronal X-ray flux for 14 M class flares which occurred within $\sim$1 hour duration of X-ray quiet sun as listed in Table 6.2. For these 14 listed flares, we have estimated photospheric magnetic-flux of the leading and following polarities of the associated active region in contrast to the previous study where we employed the full-disk magnetograms. The full-disk coronal X-ray flux has been estimated from GOES-15 observations co-temporal to the photospheric magnetic flux. Here, although we employ disk-integrated coronal X-ray flux, it is made sure while selection of the active region that only single active region must be present on the whole solar disk. Thus the X-ray emission may be understood to be originated from the flare-associated active region only. Figure 6.6 shows the coronal X-ray energy loss rate in 1-8 Å and photospheric magnetic flux for the M4.2 flare occurred on September 08, 2011.

Table 6.2: Timing characteristics of Solar Flare

S.N	Date	AR No.	Quiet-time (UT)	Flare Time (UT)	Flare Location (6-12 keV)	Flare Class (GOES)
1	13-Feb-2011	11158	16:00 - 17:28	17:28 - 20:00	(-44, -220)	M6.6
2	16-Feb-2011	11158	12:30 - 14:19	14:19 - 15:00	(474, -245)	M1.6
3	18-Feb-2011	11162	19:30 - 20:56	20:56 - 22:30	(-2, 420)	M1.3
4	28-Feb-2011	11164	12:20 - 12:38	12:38 - 14:00	(-598, 525)	M1.1
5	11/12-Mar-2011	11166	23:30 - 04:33	04:33 - 05:00	(647, 224)	M1.3
6	14-Mar-2011	11169	17:00 - 19:30	19:30 - 23:00	(711, 341)	M4.2
7	15-Apr-2011	11190	16:30 - 17:02	17:02 - 18:30	(403, 290)	M1.3
8	22-Apr-2011	11195	03:00 - 04:35	04:35 - 06:00	(-639, -228)	M1.8
9	22-Apr-2011	11195	15:00 - 15:47	15:47 - 17:00	(-510, -212)	M1.2
10	06/07-Jun-2011	11226	22:30 - 06:16	06:16 - 12:30	(731, -346)	M2.5
11	27-Jul-2011	11260	14:00 - 15:48	15:48 - 18:00	(-561, 246)	M1.1
12	03-Aug-2011	11261	11:00 - 13:17	13:17 - 18:00	(445, 151)	M6.0
13	04-Aug-2011	11263	03:00 - 03:41	03:41 - 07:00	(554, 212)	M9.3
14	08-Sep-2011	11283	13:00 - 15:32	15:32 - 18:00	(615, 151)	M6.7

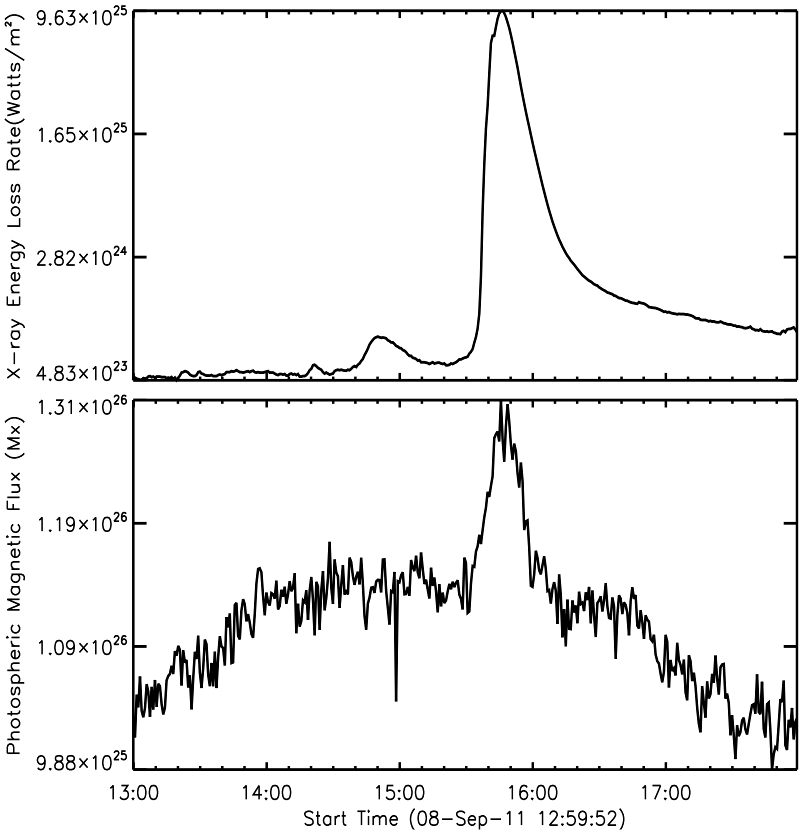

Figure 6.6: Coronal X-ray energy loss rate in 1-8 Å and photospheric magnetic flux plotted for the M6.7 flare occurred on September 08, 2011 in top and bottom panels, respectively.

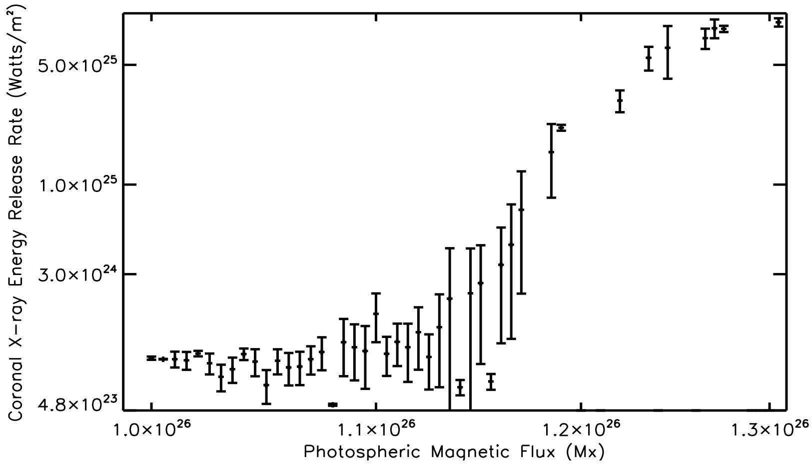

Figure 6.7: Coronal X-ray energy loss rate in 1-8 Å plotted versus photospheric magnetic flux for the M6.7 flare occurred on September 08, 2011.

Similar to the long cadence photospheric-corona coupling study, Figure 6.6 shows co-temporal variations in photospheric magnetic flux as well as in Coronal X-ray flux. Further, we plotted the coronal X-ray energy loss rate as a function of photospheric magnetic flux as shown in Figure 6.7. Here, we have averaged the coronal X-ray flux associated with the photospheric magnetic-flux bins of width 0.05×10^{26} Mx and the uncertainties have been estimated based on the standard deviation of the coronal flux in the respective bin. We may note from the Figure 6.7 that the correlation shows a power-law relationship, very similar to that obtained for the long-duration statistical investigation. In addition to this, we note that coronal X-ray flux remains unaltered for initial enhancements in the magnetic flux. This may be attributed to the fact that here we have also included the duration of quiet X-ray Sun to explore the evolution of the SOC in the corona. Thus, we may note from Figure 6.6 that the coronal X-ray flux has undergone to an avalanche as soon as the magnetic flux reached a value of $\sim 1.1 \times 10^{26}$ Mx. This magnetic flux may be termed as critical magnetic flux leading to the self-organized coronal magnetic fields towards criticality. Employing this technique, we have carried out the photosphere-corona evolution study of all the events listed in Table 6.2. We find the critical magnetic flux to be varying in the range of 1.0 - 3.5×10^{26} Mx with a median value of 2.05×10^{26} Mx and standard deviation of 0.9×10^{26} Mx. We may note from this analysis that the critical magnetic flux is not a statistically independent quantity and depends on the individual flare. To explore the significance of flare dependent critical magnetic flux, we have made a correlation study of critical magnetic flux with the flare intensity class as well as with the onset value of X-ray flux. However, we did not find convincing association. Further, the dynamic range of estimated photospheric magnetic flux and coronal X-ray flux for all the events listed in Table 6.2 is between 0.5 - 4.5×10^{26} Mx and between 4×10^{-6} - 9×10^{-4} Watts/m^2, respectively. In this study, we have also estimated the area of the positive and negative polarities and found them to be ranging in 1 - 9×10^{19} cm^2. Further, we have made a correction study of the area of positive and negative polarities with the flare intensity. In this case too, we did not find any relationship between both the parameters.

6.4 Summary, Discussion and Conclusion

In this chapter, we have carried out the investigation of the evolution of the photospheric magnetic flux and its correlation with the coronal X-ray flux in order to study the self-organization of the corona. In the following, we summarize and discuss the implications of the results obtained in this study.

6.4.1 Statistical study of Photosphere-corona coupling

We have estimated the integrated photospheric magnetic flux of all leading and following polarities on the solar disk for the duration of three very flare productive months viz. October 2003, August 2004 and September 2005. We also estimated the disk-integrated X-ray flux in 1-8 Å from GOES observations. Subsequently we have studied the correlation of the coronal X-ray flux with the co-temporal photospheric magnetic flux. We have found a strong power-law relationship between them. As the duration selected for the current investigation have been separated enough in time, this relationship can be understood statistically invariant. It also suggests that the photosphere-corona coupling does not depend on the individual flare AR complexity and flare plasma parameters. Interestingly, this relationship falls in the category of many other flare parameters which hold power law relationship viz. frequency distribution of hard X-ray peak count rates (Dennis, 1985; Christe et al., 2008), frequency distribution of non-thermal energies available during solar flare ($>$ 25 keV) (Crosby et al., 1993) etc. In this regard, this study provides a significant addition to the other studies. Apart from the general nature of this relationship, this result also has enormous applications in the energetic processes in the solar atmosphere. This is undoubtedly known that energy released during solar flares is not directly transferred from the photosphere to the corona during the flare but stored at coronal site a-prior to the flare occurs. The driver of this energy storage in the solar corona is the random motions of magnetic field-lines connecting throughout the photosphere to the corona. Thus the power-law relationship between the magnetic flux evolution and coronal X-ray flux suggests that the energy transmitted from the photosphere serves as an input to the energy released during flares. Further this also suggests that photospheric magnetic flux acts as a driver of energy storage which energizes the flare upon destabilization. Although we have successfully established the relationship of the photospheric magnetic flux to the coronal X-ray flux, the critical magnetic flux over which the X-ray flux avalanche occurs in the form flare is still not known. As the observing period undertaken for the current investigation has been very flare productive, there is a need of a period that includes both flare and the quiet time with high cadence observations.

6.4.2 Evolution of photosphere-corona coupling during and prior to the flare

In addition to the statistical investigation of the photosphere-corona coupling, we also undertook the study of photosphere-corona coupling for 14 M-class flares occurred during year 2010-2011. These flares are selected out of several well-observed flares from HMI/SDO as well as GOES-15 instruments in view of the following criteria of selection. All the events investigated in this study are M-class flares with ∼1 hour of X-ray quiet solar corona prior to the flare. The study of the evolution of photospheric magnetic flux and associated coronal X-ray flux has been carried out. The aim of this study has been to estimate the minimum photospheric magnetic flux essential to cause the flare. From this study, we have again found a power-law relationship between photospheric magnetic flux and coronal X-ray flux similar to the study conducted on long duration observations. In addition to this, from the plot of coronal X-ray flux versus photospheric magnetic flux, we have also marked a critical photospheric magnetic flux over which the coronal X-ray flux undergoes avalanche. We find that this critical magnetic flux is not an flare-independent quantity and varies in the range of 1.2 - 3.5 $\times$ 10^{26} Mx for the flares considered for current investigation. To explore further the physical significance of this critical magnetic flux in leading the self-organized corona towards criticality, we have made a correlation study of critical magnetic flux with the peak flare intensity, however, which does not result in any physically significant correlation. It may be noted that the dynamic range of estimated photospheric magnetic flux for all the events listed in Table 6.2 is 0.5 - 4.5 $\times$ 10^{26} Mx which is very small in comparison to the dynamic range of the coronal X-ray flux which ranges between 4 $\times$ 10^{-6} - 9 $\times$ 10^{-4} Watts/m^2. The magnetic flux estimated from all the events listed in Table 6.1 and 6.2 did not have a dynamic range as large as that in the coronal X-ray flux. Therefore, this study also shows a limitation of employing photospheric magnetic field observations in the study the self-organization of the corona. The study of correlation between area of the positive and negative polarities with the flare intensity has been made. We did not find significant correlation between them.

The study carried out in this chapter has led us to the very important finding of power-law relationship between photospheric magnetic flux and coronal X-ray flux. However, small dynamic range of the magnetic flux in contrast to large dynamic range of coronal X-ray flux does not allow us considering the photospheric magnetic flux a convincing proxy for the study of self-organized coronal magnetic-fields giving rise to solar flares. Therefore the future scope of the current study is to evaluate the other proxies of the photospheric magnetic complexity in addition chromospheric and/or coronal magnetic field correlation with coronal X-ray flux.

Chapter 7

Summary, Conclusions and Future Scope

7.1 Summary, Discussions and Conclusions

The aim of the investigations made in this thesis is to understand the less-understood, unexplained or debated phenomena of "Energy release processes in solar flares". Specifically, scientific objectives of this thesis have been 1) To understand the origin of the precursor phase emission and its association to the main phase emission; 2) To characterize the heating and cooling of the flaring plasma; 3) To explore the flare-CME relationship; and 4) To quantify the concept of self-organization of corona in view of observation of solar photosphere. In this chapter, we present the summary, discussion and future scope of the outcomes of the investigations made in thesis.

We have used multi-wavelength observations provided from several space and ground-based solar observatories to study the underlying processes of energy release. In chapter-2, we have presented a brief description of the instruments properties as well as data obtained from them. We also present the reduction techniques of the archived data used in this thesis.

7.1.1 Precursor phase emission in solar flares

In Chapter 3, we investigate the temporal, spatial and spectral evolutions of multi-wavelength emission during the precursor phase of solar flares to understand the physical processes occurring during this phase. We also aim to understand the association of physical processes occurred during this phase with those occurring in the well-understood main phase emission. In this regard, we performed statistical and quantitative characterization of the flare plasma parameters during the precursor as well as main phase in order to visualize their association during the main phase. Firstly, we estimated the flare plasma parameters viz. Temperature, Emission measure, non-thermal spectral index, and thermal non-thermal break energy employing a large dataset consisting of fifty flares attributing clear precursors prior to the main phase. From this study, we found that although the peak intensity count flux during the precursor phase is significantly smaller $\sim 10\%$ of that during the main phase, the estimated temperature during this phase attains substantially high value i.e. $\sim 80\%$ of the peak temperature attained during the main phase. On the other hand, emission measure estimated during the precursor phase was ~ 2 orders lesser than that attained during the main phase. Therefore, this statistical survey enables us to establish the fact that very high temperature plasma gives rise to the precursor phase. Although recent attempts to explore the origin of the precursor phase emission by Altyntsev et al. (2012); Falewicz et al. (2011); Battaglia et al. (2009) put forth a debate on the existence of thermal and non-thermal emission signatures during the precursor phase, they do agree on the existence of high temperature plasma during this phase which is in agreement to the current study. Further, spectral analysis of X-ray emission carried out during the precursor phase studied in this thesis clearly reveal thermal dominated distribution of the plasma responsible for the precursor emission. However, the trigger of this gradual energy release/leakage of energy in the form of precursors prior to impulsive explosion was still less explored. In this regard, we further explored the scenario of energy release during the precursor and main phases of twenty flares employing multi-wavelength observations. We carried out the investigation of the temporal and spatial evolution of photospheric magnetic-field parameters viz. signed and unsigned flux, gradient and shear. Although we noted small scale magnetic-field activities, no substantial evidences of magnetic-field emergence, submergence and/or cancellation was found to be temporally associated with the precursor phase emission. This result is not in complete agreement of the implications by Tandberg-Hanssen and Emslie (1988) and Chifor et al. (2007) who suggested significant signatures of magnetic-field evolution during the precursor emission. On the other hand, we found large scale flux cancellation during impulsive and gradual phase as previously revealed by Jain et al. (2011b). Further, in search of the trigger of the precursor and main phase, we carried out the investigation of spatial and temporal evolution of E/UV emission in conjunction with synthesized temperature and emission measure maps and filament evolution. We found clear signatures of slow-rising filament and/or partial eruption co-temporally associated with the precursor phase emission. In addition to this, we also noted the enhanced heated plasma as well as emission measure in the vicinity of the filament following polarity inversion line. This manifestation leads us to the scenario of filament activation adjoining both the phases of emission. We propose that during the precursor phase, small-scale magnetic reconnections in the vicinity of polarity inversion line heat the plasma which destabilizes the filament for eruption lately triggering the main phase emission.

7.1.2 Energy-dependent thermal emission and cooling in solar flares

In general, flare plasma parameters are derived from forward fitting of the modeled photon flux over the observed flare spectra. The observed emission has been widely treated with single temperature (isothermal) approximation in order to derive flare plasma parameters. However, multi-thermal nature of the plasma appears to be more physical. In addition, Aschwanden (2007) found the emission measure (EM) of the flare plasma to be varying as the function of the temperature. In this regard, we carried out the investigation of flare emission in 4-25 keV also understood as the regime of soft X-rays to characterize the thermal nature flare plasma in Chapter 4. Firstly, we model the spectro-temporal evolution of the photon flux in 4-15 keV energy band with a bremsstrahlung spectrum function integrating contributions from multi-temperatures ranging between 10-35 MK. A modeled photon spectrum in this way is best fitted by power-law distribution with index of -4.65. Aschwanden (2007) derived an analytical relationship between multi-thermal photon DEM index and power-law index of the flare spectrum in which multi-thermal photon index is 0.5 larger than the power-law index. Therefore, to compare the behavior of observations with the above established theoretical framework, we investigate ten M-class flares observed by SOXS mission. We derived solar flare plasma parameters *viz.* temperature, emission measure, multi-thermal DEM index etc. employing forward-fit of the 1-minute integrated observed photon spectra simultaneously with the multi-thermal and non-thermal functions. The multi-thermal DEM index obtained from this fitting is found to be ranging between -4.4 and -5.7 which is equivalent to the power-law index of -3.9 and -5.2 which is in close agreement to the derived power-law index of -4.65, derived from theoretically modeled multi-thermal spectrum. This result is a significant contribution to the field of flare X-ray spectroscopy in view of the fact that high energy X-ray emission (>10 keV) has already been explored by Aschwanden (2007) however the low-energy has never been studied for this characterization owing to lack of high spectral and high temporal observations.

The X-ray spectrum from flares follows a power-law function with energy and thus rapidly decreases with increasing photon energy. This indicates that the number of emitting electrons drastically increases with decreasing electron energy. Thus the energy carried by the accelerated electrons is very sensitive to the value of the low-energy cutoff or break energy point of thermal and non-thermal emission. The X-ray emission can be categorized in three types of emission depending on the underlying process viz. thermal emission (<10 keV), non-thermal emission (>25 keV) and hybrid emission (10-25 keV), however this classification is completely based on implication from flare spectral observations. Therefore, we also estimate the break-energy of thermal and non-thermal emission by energy-dependent delays in the peaks of emission time profile. Considering the fact that only thermal emission follows energy-dependent delay due to cooling effect, we model this delay to estimate conduction cooling time scales and found it to be varying in the range of 296 and 4640 s. This also enabled us to estimate the break energy to be varying between 14 - 21$\pm$1 keV which is in close agreement to the break energy estimated by Aschwanden (2007), however from the spectral analysis.

It is widely known that the energetic electrons responsible for the hard X-ray (HXR) emission by thick-target bremsstrahlung are the source of heating and thereby causing chromospheric evaporation seen in soft X-ray (SXR). This turns out to relate the temporal evolution of non-thermal and thermal emissions during solar flare. This relationship is also termed as the Neupert effect. Accordingly the time-derivative of thermal emission should co-vary as the non-thermal (HXR) emission. However, Neupert effect does not include the effect of cooling which is present in the flaring plasma simultaneous to heating. Thus this relationship is strictly valid for the asymptotic limit of very long cooling time scales. A physically more accurate model is needed to generalize Neupert effect over finite cooling time. In this regard, we investigate ten M-class flares observed by the SOXS. We employ exponentially decaying time-dependent cooling function in this regard as suggested by Aschwanden (2005). As a by-product of this study, we deduced a simple way of estimating cooling time scale directly from the observed flux-profile. The CZT detector onboard SOXS mission records observations in several energy bands viz. 7-10, 10-20, 20-50 and 4-56 keV with the temporal cadence as high as 1 sec. We employ 7-

10 keV as SXR and 20-30 keV band as HXR because they represent thermally and non-thermally originated emissions, respectively (Jain et al., 2011a). We model the time dependent cooling by estimating the ratio of time-derivative of SXR photon flux with that of HXRs. We fit the time evolution of the ratio by an exponentially decaying function in the rising phase and estimated cooling scale to be varying between 39-525s. The time-scales estimated in this way are in close agreement to the previous estimations by Aschwanden (2007) who, however, used spectral techniques. Due to the occurrence of the cooling effect in the rising phase of the flare, this scale may be attributed to conduction cooling time scale.

7.1.3 Role of Photospheric magnetic field in producing flare and CME

Solar eruptions viz. Flares, CMEs, SEPs etc. are fed by the energy available in the solar atmosphere in the form of non-potential magnetic-fields. However, these eruptions show both collective and independent behavior in their occurrence. In this regard, we carried out a detailed multi-wavelength investigation of a Coronal Mass Ejection (CME) and associated flare observed on 12 May 1997 in the NOAA Active Region 8038. This region was decaying, and produced only very small flare activity during its disk passage from 07-16 May 1997. However, on 12 May 1997 it produced a CME and associated medium size 1B/C1.3 flare. Detailed analyses of Hα filtergrams and MDI/SOHO magnetograms revealed continual but discrete surge activity, and emergence and cancellation of flux in this active region. Further, we note that the major opposite polarities of pre-existing region as well as in the emerging flux region were approaching towards each other and moving magnetic features (MMF) were ejecting out from the major north polarity at a quasi-periodicity of about 10 hours during 10-13 May 1997. These activities appear to be caused by the magnetic reconnection in the lower atmosphere driven by photospheric convergence motions, which were evident in magnetograms. The quantitative measurements of magnetic field variations such as magnetic flux, gradient, and sunspot rotation revealed that in this active region, free energy was slowly being stored in the corona. The slow low-layer magnetic reconnection may be responsible for the storage of magnetic free energy in the corona and the formation of a sigmoidal core field or a flux rope leading to the eventual eruption. The occurrence of EUV brightenings in the sigmoidal core field prior to the rise of a flux rope suggests that the eruption was triggered by the inner tether-cutting reconnection, but not via external breakout reconnection. We observe an impulsive acceleration from fast separation of the Hα ribbons for the first 150 seconds suggests the CME accelerated in the inner corona, which is also in consistence with the temporal profile of the reconnection electric field. Based on observations and analysis we propose a qualitative model, and we conclude that the mass ejections, filament eruption, CME, and subsequent flare were connected with one another and should be regarded within the framework of a solar eruption. This study revealed that the energy transport from solar photosphere to coronal sites starts many hours prior to the flare onset and magnetic-flux has turned out to be effective proxy in this regard. This study, if performed for a large series of active regions, may lead to the prediction of flare occurrence. Further, magnetic-field gradient and polarity rotation estimated in this study are found to be very good proxy of the trigger for stored energy. The quantitative estimation of the temporal evolution of polarity rotation angle has been found to possess the potential for a good proxy for the release of the stored energy.

7.2 Self-organizing critical state of the solar corona

Akabane (1956) discovered the statistical behavior of power-law distribution of flare frequency versus respective energy released to be scale-invariant i.e. independent of the magnitude of the flare, the complexity of the individual AR responsible for flares etc. Many more scale independent relations were further drawn by Dennis (1985). As each and every solar flare originates from a completely independent magnetic-field configuration from other flares, to explain this common behavior, Lu and Hamilton (1991) applied the concept of self-organizing criticality (SOC; Bak et al., 1987) and successfully explained the same by employing cellular automaton model. They have proposed that the solar coronal magnetic field which produces flare happens to be in a state of self-organized criticality.

As mentioned in the previous section, magnetic-field parameters are good proxy of flare energy release process. In this regard, to explore the SOC occurrence through observations, we have investigated relationship between photospheric magnetic-field and coronal X-ray flux in this thesis. We characterized this study in two parts. Firstly, we explored long-duration statistical relationship which includes the study of active region independent full-disk magnetic-field parameters as well as disk-integrated coronal X-ray flux. Secondly, the relationship between flare-associated active region's magnetic flux and coronal X-ray flux has been investigated. We found a strong power-law relationship between the photospheric magnetic flux and coronal X-ray flux in the case of long-duration study of photosphere-corona coupling. As the duration selected in our investigation were well separated in time, this result is statistically invariant i.e. does not depend on the complexity of ARs, chromospheric conditions and flare plasma parameters. In the latter case, where we investigated the evolution of photosphere-corona coupling during and prior to the flare, we again found a power-law relationship between photospheric magnetic flux and coronal X-ray flux similar to the results obtained in the former case. In addition, we have also noticed a photospheric magnetic flux over which the flare X-ray flux undergoes avalanche. This magnetic flux may be termed as critical magnetic flux.

7.3 Future Scope

The research never completes. We find ourselves in the ocean of problems and the research goes on with an attempt to solve them drop-by-drop. While the projected work in my thesis-synopsis has been accomplished as detailed in above sections, I find the following problems closely related to the energy release processes in solar flares. Few are extensions to the already accomplished ideas, others ask for more detailed investigation, however connected to the theme of my thesis. In this section, I will give a brief outline of the future plan of current research.

7.3.1 Evolution of the filament during the precursor and main phases of the flare

In this thesis, we have performed an extensive investigation of the spectral, spatial and temporal evolution of multi-wavelength emission during the precursor and main phases of flare. We have noted the evidences of partially erupted and/or slowly rising filament in due course of the precursor to the main phase emission. In this regard, high cadence multi-wavelength investigation of filament is necessary in order to lead to conclusive evidence of role of the filament as a trigerr or driver of instability.

7.3.2 Microwave emission during the precursor phase emission

Altyntsev et al. (2012), based on their study of precursor phase emission suggested that microwave emission is a better proxy of non-thermal emission than emission in HXR waveband. Although in the investigation carried out in this thesis, we have used the HXR emission available from the state-of-the-art instruments, it is desired to explore the non-thermal signatures during the precursor phase employing microwave emission. This study will enable us to understand the physical processes during the precursor phase in view of thermal or non-thermal origin.

7.3.3 Modeling the thermalization time of the flare plasma

We investigated Low energy X-ray emission in this thesis and found the emission to be originated from multi-thermal plasma. To achieve this, multi-thermal photon flux has been modeled theoretically with the assumption of uniform contribution from the temperatures. However, physically more realistic model would be to employ temperature weighted approach in modeling multi-thermal emission. Moreover, it also requires proper understanding of the thermalization time of the plasma. In this regard, we wish to exploit spectacular temporal and spectral cadence observation from SOXS mission in future.

7.3.4 Statistical survey of Magnetic-field parameters leading the corona to SOC

The photosphere corona coupling in the form of power-law relationship is obtained in this thesis. We further wish to explore the high cadence temporal and spectral evolution of photospheric magnetic field parameters in order to visualize the self-organizing criticality of the corona. Moreover, we will try to explore cellular automaton model over the observed photospheric magnetic field during solar flares. Statistical investigation of magnetic-field emergence, cancellation during the evolution of ARs will also be studied.

7.3.5 Instrumentation for observing multi-wavelength solar atmosphere

As detailed in chapter-2 and Appendix-A of this thesis, we have developed and operated an optical telescope, named as Thaltej Solar Flare Telescope (TSFT) to observe solar chromosphere. While developing this telescope, I learnt instrumentation, data analysis pipeline, data processing etc. In addition to this, I felt a great need of upgradation of this kind of facility in view of simultaneous multi-wavelength observation which may enable us to understand the tip-to-toe physical processes occurring in the solar atmosphere during flares. Therefore I am very much interested to develop a spectrograph to observe chromospheric and coronal lines. This will be a unique facility in view of tracing high-speed filaments, Mass ejections etc.

Appendix A

Thaltej Solar Flare Telescope (TSFT)-PRL

We installed a facility of observing full-disk chromosphere of the Sun with a 10-cm aperture refracting type telescope. The history of the study of solar atmosphere in Hα wavelength spans several decades and in this context various ground-based observatories in India are operational viz. ARIES, Nainital and Udaipur Solar Observatory (USO). Full-disk observations usually lack in the temporal cadence (best available is $\sim$1 min from GHN as explained above). On the other hand, a high-resolution observation of solar atmosphere viz. AR observations lacks the pointing accuracy as well as accurate co-ordinate which are very important for multi-wavelength study. In this regard, fast cadence full-disk observations are must to address science issues viz. filament evolution, and cooling of the solar flare plasma. Therefore, a unique facility with full-disk high temporal cadence observations with the specifications enlisted in Table A.1 is installed in PRL, Thaltej campus, Ahmedabad. This facility is named Thaltej Solar Flare Telescope (TSFT) which is installed at roof-top of Astronomy & Astrophysics division building, PRL. The TSFT current setup is shown in Figure A.1. This facility has been operational for synoptic observation of white-light Sun since April 2012.

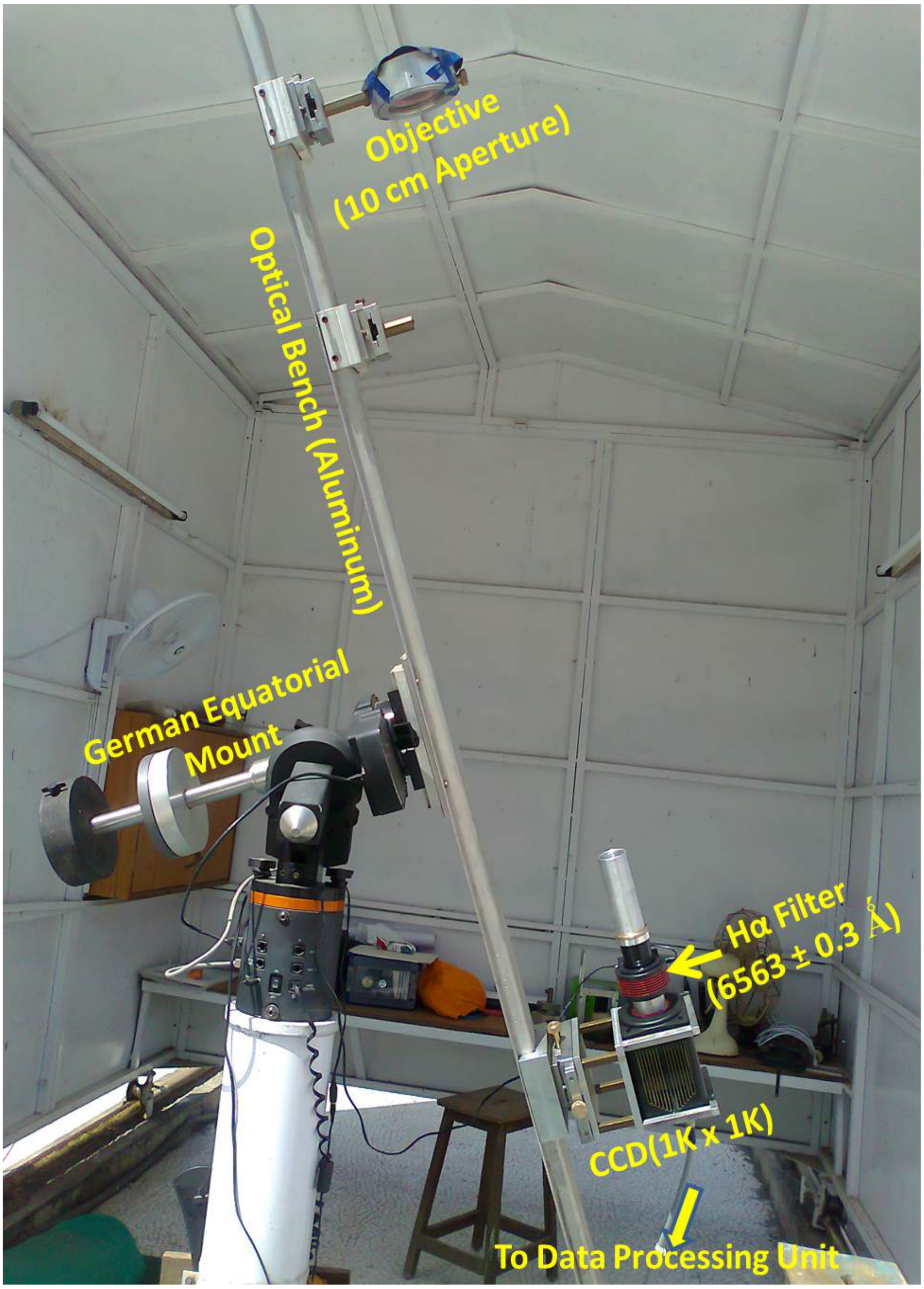

Figure A.1: Thaltej Solar Flare Telescope of Physical Research Laboratory operating at Thaltej campus. The 10-cm aperture refractor with f/16 focal ratio provides 13 mm image at prime focus. The quantum Hα filter coupled with CCD provides images with a cadence between 10ms to 5s as desired.

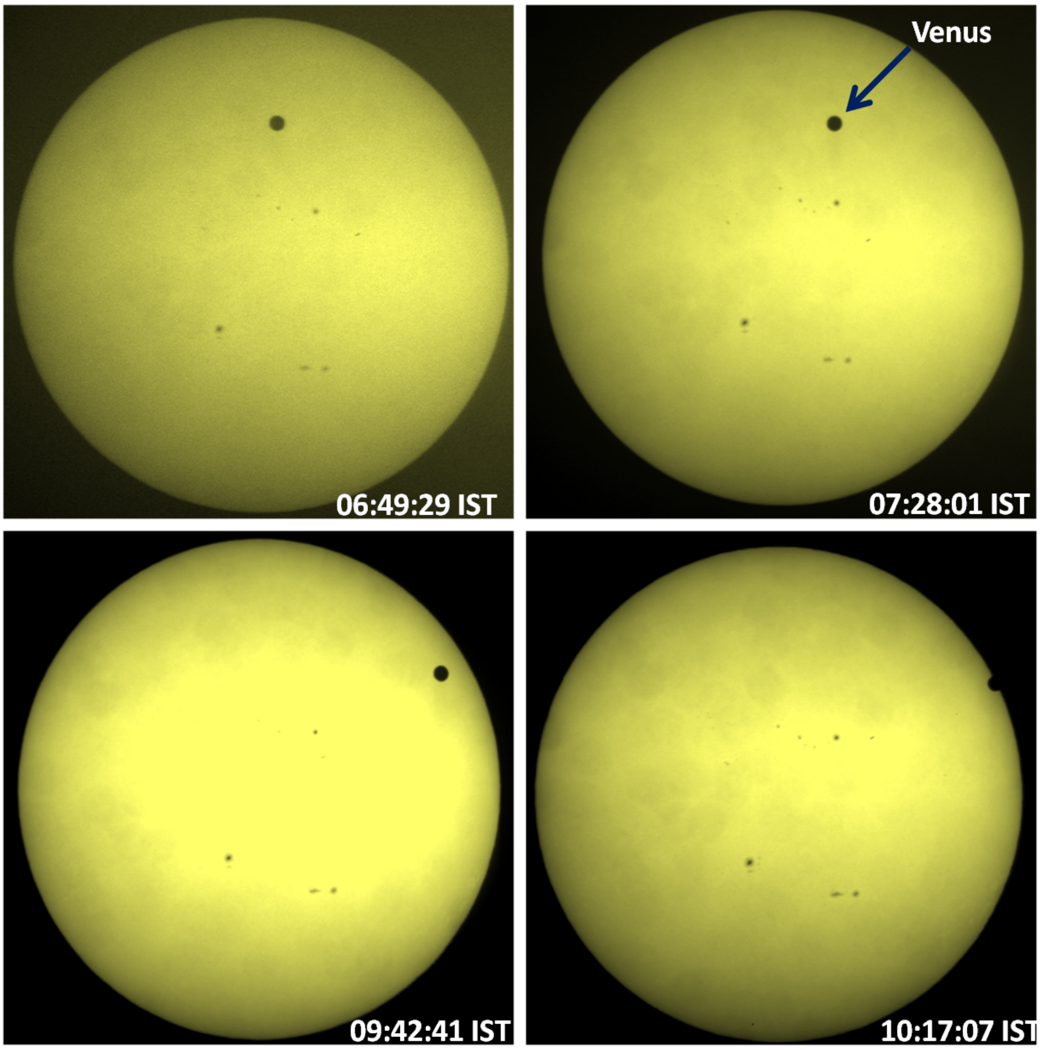

Figure A.2: The sequence of photographs of Venus Transit captured by Solar Flare Telescope at Thaltej campus of Physical Research Laboratory, Ahmedabad.

With this, we have observed a historical astronomical event of Venus transit occurred on 6th June 2012. Figure A.2 shows the time-series of images observed from TSFT during Venus transit event. Full-fledge Hα observations from TSFT started only since March 2013. Figure 1.3 (Chapter 1) shows full disk image (left panel) of the Sun taken by TSFT on 6th March 2013. The active region AR11689 on 6th March 2013 shown on right panel has been very complex with an M-shaped filament as shown by arrow. Prominences have been observed at the South-West limb. The observation of prominences structure shows the stability of the images with this telescope given a long exposure as high as ∼500ms. Regular observations have been started with auto-identification of the flare. We have been able to observe a number of C and M-class flares from this facility. The flare observation catalog is presented in table A.2.

Table A.1: Specifications of Thaltej Solar flare telescope

Aperture:	10 cm
F-ratio:	∼f/16
Spatial resolution:	2 arcsec/pixel (∼1500km)
Hα filter:	Daystar professional Quantum filter
CWL:	6562.8 Å (± 0.5 Å)
FWHM:	0.3 Å
Time cadence:	1.154 s

From the observation listed in table A.2, we may note that TSFT have been able to successfully observe 14 C and 2 M class flares. Figure A.3 shows the spatial evolution of AR11719 which was located almost in the center of the disk and produced a M6.5 flare at 07:16 UT. The magnetic-field configuration of this AR was $\beta\gamma$ type which is in favor of producing strong flare activities as discussed already in Chapter-1 of this thesis. This flare has been observed in multi-wavelength from multiple ground and space-based missions. The study of this event is of major interest as found associated with Coronal Mass Ejection observed by SoHO satellite.

Table A.2: Observation log of Thaltej Solar flare telescope

S. N.	Date	Observing Schedule (IST[a])	Flares Observed
1	05-Mar-2013	09:12 - 10:07	
2	06-Mar-2013	08:12 - 11:28	
3	07-Mar-2013	08:14 - 11:01	
4	08-Mar-2013	07:58 - 10:27	
5	12-Mar-2013	08:21 - 09:50	
6	15-Mar-2013	08:39 - 09:36	
		14:43 - 18:15	M1.1
7	16-Mar-2013	08:32 - 09:48	C2.6, C2.8, C2.7
8	18-Mar-2013	08:09 - 08:33	C1.4, C2.8
		14:38 - 14:47	C1.2
9	20-Mar-2013	07:59 - 10:29	
10	21-Mar-2013	07:59 - 10:44	
11	04-Apr-2013	08:17 - 09:58	
12	05-Apr-2013	07:45 - 11:00	
13	07-Apr-2013	08:42 - 08:58	
14	09-Apr-2013	08:28 - 09:53	
15	11-Apr-2013	12:39 - 16:27	M6.5
16	12-Apr-2013	08:01 - 08:36	
17	15-Apr-2013	08:10 - 08:21	
18	16-Apr-2013	07:34 - 07:45	
19	19-Apr-2013	10:35 - 11:30	
20	22-Apr-2013	10:46 - 12:00	C1.4, C2.7
21	28-Apr-2013	11:51 - 12:09	C2.1
22	29-Apr-2013	10:22 - 12:29	C3.0
23	30-Apr-2013	10:54 - 12:01	
24	01-May-2013	09:58 - 10:37	
25	02-May-2013	10:45 - 12:14	
26	13-May-2013	10:41 - 14:24	C1.2, C1.3
27	14-May-2013	09:26 - 12:47	C2.4, C2.0
28	15-May-2013	10:33 - 11:36	

[a]Indian Standard Time = 05:30 hrs + UT

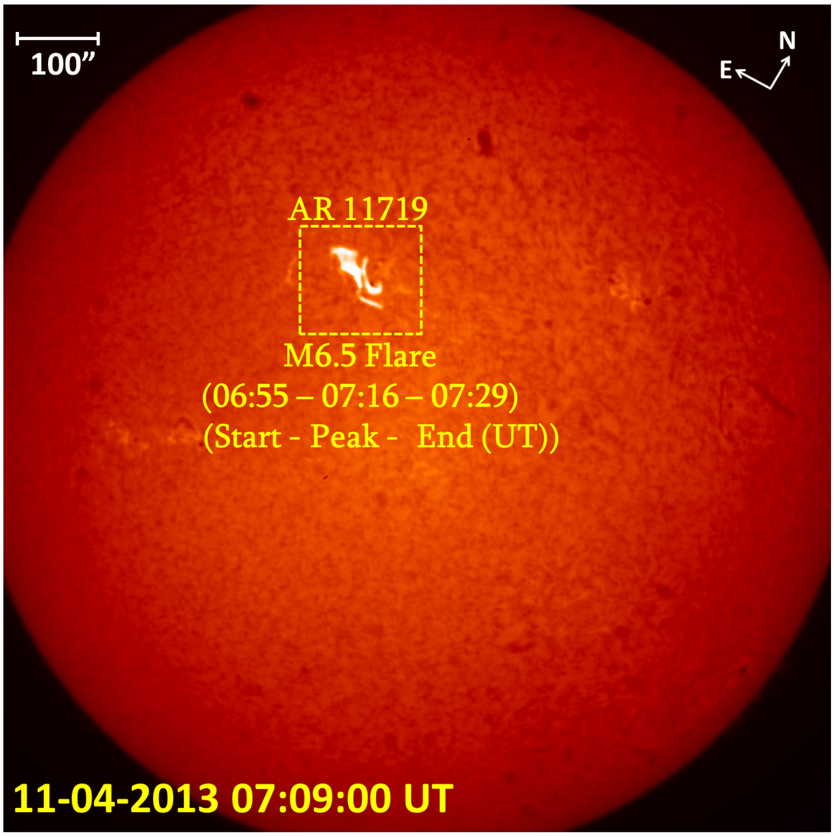

Figure A.3: Full disk image of the Sun obtained by TSFT/PRL on 11 April 2013 at 07:09:00 UT showing Hα emission from AR11719 in the form of two-ribbon during M6.5 flare.

References

Aarnio, A. N., Stassun, K. G., Hughes, W. J., and McGregor, S. L.: 2011, *Solar Phys.* **268**, 195 50

Akabane, K.: 1956, *Pub. Astron. Soc. Japan* **8**, 173 xxxi, 195, 221

Akioka, M.: 1998, in K. S. Balasubramaniam, J. Harvey, and D. Rabin (eds.), *Synoptic Solar Physics*, Vol. 140 of *Astronomical Society of the Pacific Conference Series*, p. 475 157

Altyntsev, A. A., Fleishman, G. D., Lesovoi, S. V., and Meshalkina, N. S.: 2012, *Astrophys. J.* **758**, 138 26, 42, 88, 138, 216, 223

Ambastha, A., Hagyard, M. J., and West, E. A.: 1993, *Solar Phys.* **148**, 277 14

Antiochos, S. K., DeVore, C. R., and Klimchuk, J. A.: 1999, in *American Astronomical Society Meeting Abstracts #194*, Vol. 31 of *Bulletin of the American Astronomical Society*, p. 868 45

Antiochos, S. K. and Sturrock, P. A.: 1978, *Astrophys. J.* **220**, 1137 30, 147

Archontis, V., Hood, A. W., Savcheva, A., Golub, L., and Deluca, E.: 2009, *Astrophys. J.* **691**, 1276 193

Asai, A., Yokoyama, T., Shimojo, M., and Shibata, K.: 2004, *Astrophys. J. Lett.* **605**, L77 27

Aschwanden, M. J.: 2002, *Space Sci. Rev.* **101**, 1 78

Aschwanden, M. J.: 2005, *Physics of the Solar Corona. An Introduction with Problems and Solutions (2nd edition)* xxx, 8, 29, 32, 38, 40, 41, 161, 219

Aschwanden, M. J.: 2007, *Astrophys. J.* **661**, 1242 104, 121, 145, 146, 149, 159, 163, 164, 166, 218, 220

Aschwanden, M. J.: 2008, *Journal of Astrophysics and Astronomy* **29**, 115 163

Aschwanden, M. J. and Alexander, D.: 2001, *Solar Phys.* **204**, 91 31, 147

Aschwanden, M. J., Benz, A. O., Dennis, B. R., and Schwartz, R. A.: 1995a, *Astrophys. J.* **455**, 347 24

Aschwanden, M. J., Boerner, P., Schrijver, C. J., and Malanushenko, A.: 2013, *Solar Phys.* **283**, 5 83, 132

Aschwanden, M. J., Dennis, B. R., and Benz, A. O.: 1998, *Astrophys. J.* **497**, 972 38, 104

Aschwanden, M. J., Schwartz, R. A., and Alt, D. M.: 1995b, *Astrophys. J.* **447**, 923 24

Aschwanden, M. J. and Shimizu, T.: 2013, *Astrophys. J.* **776**, 132 140

Aulanier, G., DeLuca, E. E., Antiochos, S. K., McMullen, R. A., and Golub, L.: 2000, *Astrophys. J.* **540**, 1126 45, 197

Aurass, H., Vršnak, B., Hofmann, A., and Rudžjak, V.: 1999, *Solar Phys.* **190**, 267 169

Awasthi, A. K. and Jain, R.: 2011, in *Astronomical Society of India Conference Series*, Vol. 2 of *Astronomical Society of India Conference Series*, pp 297–305 88

Bak, P., Tang, C., and Wiesenfeld, K.: 1987, *Physical Review Letters* **59**, 381 xxxi, 196, 222

Basu, S. and Antia, H. M.: 2003, *Astrophys. J.* **585**, 553 4

Batchelor, D. A.: 1989, in *Bulletin of the American Astronomical Society*, Vol. 21 of *Bulletin of the American Astronomical Society*, p. 850 42

Battaglia, M. and Benz, A. O.: 2006, *Astron. Astrophys.* **456**, 751 24

Battaglia, M., Fletcher, L., and Benz, A. O.: 2009, *Astron. Astrophys.* **498**, 891 26, 42, 88, 108, 130, 138, 141, 216

Benz, A. O.: 2008, *Living Reviews in Solar Physics* **5**, 1 19

Bharti, L., Jain, R., Joshi, C., and Jaaffrey, S. N. A.: 2005, in K. Sankarasubramanian, M. Penn, and A. Pevtsov (eds.), *Large-scale Structures and their Role in Solar Activity*, Vol. 346 of *Astronomical Society of the Pacific Conference Series*, p. 327 172, 173

Bharti, L., Rimmele, T., Jain, R., Jaaffrey, S. N. A., and Smartt, R. N.: 2007, *Mon. Not. Roy. Astron. Soc.* **376**, 1291 189

Bhatnagar, A. and Livingston, W.: 2005, *Fundamentals of solar astronomy* 9

Bhatt, N. J., Jain, R., and Awasthi, A. K.: 2013, *Res. in Astron. & Astrophys.* **13**, 978 13, 151

Biskamp, D.: 2005, *Magnetic Reconnection in Plasmas* 15

Blackman, E. G. and Chou, T.: 1997, *Astrophys. J. Lett.* **489**, L95 47

Brosius, J. W.: 2003, *Astrophys. J.* **586**, 1417 30

Brosius, J. W. and Holman, G. D.: 2012, *Astron. Astrophys.* **540**, A24 89, 91

Brown, J. C.: 1971, *Solar Phys.* **18**, 489 37

Brown, J. C., Spicer, D. S., and Melrose, D. B.: 1979, *Astrophys. J.* **228**, 592 41

Cameron, R.: 1999, in *American Astronomical Society Meeting Abstracts #194*, Vol. 31 of *Bulletin of the American Astronomical Society*, p. 914 14

Canfield, R. C. and Reardon, K. P.: 1998, *Solar Phys.* **182**, 145 44

Cargill, P. J., Mariska, J. T., and Antiochos, S. K.: 1995, *Astrophys. J.* **439**, 1034 31

Carmichael, H.: 1964, *NASA Special Publication* **50**, 451 39

Caspi, A.: 2010, *Ph.D. thesis*, Department of Physics, University of California, Berkeley, CA 94720-7450, USA 143

Chae, J., Wang, H., Qiu, J., Goode, P. R., Strous, L., and Yun, H. S.: 2001, *Astrophys. J.* **560**, 476 189

Chandra, R., Schmieder, B., Mandrini, C. H., Démoulin, P., Pariat, E., Török, T., and Uddin, W.: 2011, *Solar Phys.* **269**, 83 139

Chen, A.-Q. and Zong, W.-G.: 2009, *Research in Astronomy and Astrophysics* **9**, 470 50

Chen, F. F.: 1974, *Introduction to plasma physics* 18

Cheng, C.-C.: 1977, *Astrophys. J.* **213**, 558 44

Cheng, X., Ding, M. D., and Zhang, J.: 2010, *Astrophys. J.* **712**, 1302 185, 188, 189

Chifor, C., Mason, H. E., Tripathi, D., Isobe, H., and Asai, A.: 2006, *Astron. Astrophys.* **458**, 965 28, 89

Chifor, C., Tripathi, D., Mason, H. E., and Dennis, B. R.: 2007, *Astron. Astrophys.* **472**, 967 25, 28, 29, 89, 139, 217

Christe, S., Hannah, I. G., Krucker, S., McTiernan, J., and Lin, R. P.: 2008, *Astrophys. J.* **677**, 1385 211

Chumak, O.: 2005, *Astronomical and Astrophysical Transactions* **24**, 93 170

Chupp, E. L., Forrest, D. J., Higbie, P. R., Suri, A. N., Tsai, C., and Dunphy, P. P.: 1973, *Nature* **241**, 333 37

Colaninno, R. C. and Vourlidas, A.: 2009, *Astrophys. J.* **698**, 852 49

Craig, I. J. D. and Brown, J. C.: 1976, *Astron. Astrophys.* **49**, 239 144, 148

Crosby, N. B., Aschwanden, M. J., and Dennis, B. R.: 1993, *Solar Phys.* **143**, 275 211

Culhane, J. L.: 1969, *Mon. Not. Roy. Astron. Soc.* **144**, 375 34, 148

Culhane, J. L., Phillips, A. T., Inda-Koide, M., Kosugi, T., Fludra, A., Kurokawa, H., Makishima, K., Pike, C. D., Sakao, T., and Sakurai, T.: 1994, *Solar Phys.* **153**, 307 30, 31, 147

Culhane, J. L., Vesecky, J. F., and Phillips, K. J. H.: 1970, *Solar Phys.* **15**, 394 30, 31, 147, 153

Czaykowska, A., Alexander, D., and De Pontieu, B.: 2001, *Astrophys. J.* **552**, 849 42

Czaykowska, A., de Pontieu, B., Alexander, D., and Rank, G.: 1999, *Astrophys. J. Lett.* **521**, L75 30

Dai, Y., Auchère, F., Vial, J.-C., Tang, Y. H., and Zong, W. G.: 2010, *Astrophys. J.* **708**, 913 186

De Pontieu, B., McIntosh, S. W., Hansteen, V. H., and Schrijver, C. J.: 2009, *Astrophys. J. Lett.* **701**, L1 10

Delaboudinière, J.-P., Artzner, G. E., Brunaud, J., Gabriel, A. H., Hochedez, J. F., Millier, F., Song, X. Y., Au, B., Dere, K. P., Howard, R. A., Kreplin, R., Michels, D. J., Moses, J. D., Defise, J. M., Jamar, C., Rochus, P., Chauvineau, J. P., Marioge, J. P., Catura, R. C., Lemen, J. R., Shing, L., Stern, R. A., Gurman, J. B., Neupert, W. M., Maucherat, A., Clette, F., Cugnon, P., and van Dessel, E. L.: 1995, *Solar Phys.* **162**, 291 54

Démoulin, P. and Aulanier, G.: 2010, *Astrophys. J.* **718**, 1388 190

Deng, N., Xu, Y., Yang, G., Cao, W., Rimmele, T. R., Wang, H., and Denker, C.: 2005, *AGU Spring Meeting Abstracts* p. C5 14

Dennis, B. R.: 1985, *Solar Phys.* **100**, 465 xxxi, 196, 211, 222

Dennis, B. R. and Zarro, D. M.: 1993, *Solar Phys.* **146**, 177 33, 147, 155

Dere, K. P., Landi, E., Mason, H. E., Monsignori Fossi, B. C., and Young, P. R.: 1997, *Astron. Astrophys. Suppl.* **125**, 149 81, 98, 126, 149, 151

Desai, U. D., Pantazis, J., and Shah, K.: 1995, *Astrophys. Space Sci.* **231**, 487 63

Domingo, V., Fleck, B., and Poland, A. I.: 1995, *Solar Phys.* **162**, 1 54, 55

Dryer, M.: 1982, *Space Sci. Rev.* **33**, 233 50

Durouchoux, P., Hudson, H., Matteson, J., Hurford, G., Hurley, K., and Orsal, E.: 1983, *Astron. Astrophys.* **120**, 150 76

Falewicz, R., Siarkowski, M., and Rudawy, P.: 2011, *Astrophys. J.* **733**, 37 26, 42, 88, 89, 138, 216

Fárník, F., Hudson, H., and Watanabe, T.: 1996, *Solar Phys.* **165**, 169 25

Fárník, F., Hudson, H. S., Karlický, M., and Kosugi, T.: 2003, *Astron. Astrophys.* **399**, 1159 25

Fárník, F. and Savy, S. K.: 1998, *Solar Phys.* **183**, 339 25, 88, 93

Faurobert, M.: 2000, in W. Livingston and A. Özgüç (eds.), *Last Total Solar Eclipse of the Millennium*, Vol. 205 of *Astronomical Society of the Pacific Conference Series*, p. 156 12

Feynman, J. and Hundhausen, A. J.: 1994, *J. Geophys. Res.* **99**, 8451 50

Fisher, G. H.: 1989, *Astrophys. J.* **346**, 1019 89

Fisher, G. H., Canfield, R. C., and McClymont, A. N.: 1985, *Astrophys. J.* **289**, 425 89

Fisher, G. H., McClymont, A. N., and Chou, D.-Y.: 1991, *Astrophys. J.* **374**, 766 44

Fletcher, L., Dennis, B. R., Hudson, H. S., Krucker, S., Phillips, K., Veronig, A., Battaglia, M., Bone, L., Caspi, A., Chen, Q., Gallagher, P., Grigis, P. T., Ji, H., Liu, W., Milligan, R. O., and Temmer, M.: 2011, *Space Sci. Rev.* **159**, 19 18, 24, 25, 37, 144

Fletcher, L. and Hudson, H.: 2001, *Solar Phys.* **204**, 69 197

Forbes, T. G. and Acton, L. W.: 1996, *Astrophys. J.* **459**, 330 29, 30

Forbes, T. G. and Lin, J.: 2000, *Journal of Atmospheric and Solar-Terrestrial Physics* **62**, 1499 28

Forbes, T. G., Malherbe, J. M., and Priest, E. R.: 1989, *Solar Phys.* **120**, 285 30

Forbes, T. G. and Priest, E. R.: 1995, *Astrophys. J.* **446**, 377 14

Furth, H. P.: 1969, in D. G. Wentzel and D. A. Tidman (eds.), *Plasma Instabilities in Astrophysics*, p. 33 17

Gan, W.-Q., Li, Y.-P., and Chang, J.: 2001, *Chin. J. Astron. Astrophys.* **1**, 453 164, 165

Gan, W. Q., Li, Y. P., Chang, J., and Tiernan, J. M.: 2002, *Solar Phys.* **207**, 137 146, 165

Giovanelli, R. G.: 1939, *Astrophys. J.* **89**, 555 12

Giovanelli, R. G.: 1948, *Mon. Not. Roy. Astron. Soc.* **108**, 163 197

Green, L. M. and Kliem, B.: 2009, *Astrophys. J. Lett.* **700**, L83 189

Gronenschild, E. H. B. M. and Mewe, R.: 1978, *Astron. Astrophys. Suppl.* **32**, 283 34

Guidoni, S. and Longcope, D.: 2010, in *American Astronomical Society Meeting Abstracts No 216*, Vol. 41 of *Bulletin of the American Astronomical Society*, p. 320.04 141

Gupta, M., Jain, R., Trivedi, J., and Mishra, A. P.: 2008, *Journal of Astrophysics and Astronomy* **29**, 171 10

Hagyard, M. J.: 1984, *NASA STI/Recon Technical Report N* **84**, 35265 14

Hagyard, M. J., Teuber, D., West, E. A., and Smith, J. B.: 1984, *Solar Phys.* **91**, 115 43

Hagyard, M. J., Venkatakrishnan, P., and Smith, Jr., J. B.: 1990, *Astrophys. J. Supplement.* **73**, 159 43

Hara, H., Watanabe, T., Matsuzaki, K., Harra, L. K., Culhane, J. L., Cargill, P., Mariska, J. T., and Doschek, G. A.: 2008, *Pub. Astron. Soc. Japan* **60**, 275 29

Harra, L. K. and Sterling, A. C.: 2001, *Astrophys. J. Lett.* **561**, L215 26, 192

Harra, L. K., Williams, D. R., Wallace, A. J., Magara, T., Hara, H., Tsuneta, S., Sterling, A. C., and Doschek, G. A.: 2009, *Astrophys. J. Lett.* **691**, L99 26

Harrison, R. A., Bryans, P., Simnett, G. M., and Lyons, M.: 2003, *Astron. Astrophys.* **400**, 1071 186

Harrison, R. A., Waggett, P. W., Bentley, R. D., Phillips, K. J. H., Bruner, M., Dryer, M., and Simnett, G. M.: 1985, *Solar Phys.* **97**, 387 25

Harvey, J. W., Bolding, J., Clark, R., Hauth, D., Hill, F., Kroll, R., Luis, G., Mills, N., Purdy, T., Henney, C., Holland, D., and Winter, J.: 2011, in *AAS/Solar Physics Division Abstracts #42*, p. 1745 58

Hey, J. S.: 1983, *The radio universe (3rd edition)* 19

Heyvaerts, J. and Norman, C.: 2001, *Astronomical and Astrophysical Transactions* **20**, 295 10

Heyvaerts, J., Priest, E. R., and Rust, D. M.: 1977, *Astrophys. J.* **216**, 123 44

Hirayama, T.: 1974, *Solar Phys.* **34**, 323 39, 40, 190

Hogbom, J. A. and Brouw, W. N.: 1974, *Astron. Astrophys.* **33**, 289 77

Hollweg, J. V.: 1985, in B. W. Lites (ed.), *Chromospheric Diagnostics and Modelling*, pp 235–251 10

Holman, G. D., Aschwanden, M. J., Aurass, H., Battaglia, M., Grigis, P. C., Kontar, E. P., Liu, W., Saint-Hilaire, P., and Zharkova, V. V.: 2011, *Space Sci. Rev.* **159**, 107 34, 147

Hood, A. W. and Priest, E. R.: 1979, *Solar Phys.* **64**, 303 44

Hori, K., Yokoyama, T., Kosugi, T., and Shibata, K.: 1998, *Astrophys. J.* **500**, 492 31

Huber, A. C., Pantazis, J. A., and Jordanov, V.: 1995, *Nuclear Instruments and Methods in Physics Research B* **99**, 665 63

Hudson, H. S.: 1991, in *Bulletin of the American Astronomical Society*, Vol. 23 of *Bulletin of the American Astronomical Society*, p. 1064 32, 155

Hudson, H. S.: 2007, in P. Heinzel, I. Dorotovič, and R. J. Rutten (eds.), *The Physics of Chromospheric Plasmas*, Vol. 368 of *Astronomical Society of the Pacific Conference Series*, p. 365 23

Hudson, H. S. and Ohki, K.: 1972, *Solar Phys.* **23**, 155 37

Hurford, G. J., Schmahl, E. J., Schwartz, R. A., Conway, A. J., Aschwanden, M. J., Csillaghy, A., Dennis, B. R., Johns-Krull, C., Krucker, S., Lin, R. P., McTiernan, J., Metcalf, T. R., Sato, J., and Smith, D. M.: 2002, *Solar Phys.* **210**, 61 xvii, 75, 106, 121

Imada, S., Hara, H., Watanabe, T., Kamio, S., Asai, A., Matsuzaki, K., Harra, L. K., and Mariska, J. T.: 2007, *Pub. Astron. Soc. Japan* **59**, 793 186

Jain, R.: 1985, *Bulletin of the Astronomical Society of India* **13**, 253 91

Jain, R., Aggarwal, M., and Kulkarni, P.: 2010, *Research in Astronomy and Astrophysics* **10**, 473 13, 49, 50, 169

Jain, R., Aggarwal, M., and Sharma, R.: 2008, *Journal of Astrophysics and Astronomy* **29**, 125 95, 145, 148, 151, 163

Jain, R., Awasthi, A. K., Chandel, B., Bharti, L., Hanaoka, Y., and Kiplinger, A. L.: 2011a, *Solar Phys.* **271**, 57 13, 14, 20, 87, 104, 121, 139, 145, 200, 220

Jain, R., Awasthi, A. K., Rajpurohit, A. S., and Aschwanden, M. J.: 2011b, *Solar Phys.* **270**, 137 44, 109, 198, 217

Jain, R. and Bhatnagar, A.: 1983, *Bulletin of the Astronomical Society of India* **11**, 91 xxxi, 12, 169, 196

Jain, R., Dave, H., and Deshpande, M. R.: 2003, in *IAU Joint Discussion*, Vol. 17 of *IAU Joint Discussion* 63, 67

Jain, R., Dave, H., Shah, A. B., Vadher, N. M., Shah, V. M., Ubale, G. P., Manian, K. S. B., Solanki, C. M., Shah, K. J., Kumar, S., Kayasth, S. L., Patel, V. D., Trivedi, J. J., and Deshpande, M. R.: 2005, *Solar Phys.* **227**, 89 35, 54, 73, 87, 89, 92, 121, 148, 155, 164

Jain, R., Pradhan, A. K., Joshi, V., Shah, K. J., Trivedi, J. J., Kayasth, S. L., Shah, V. M., and Deshpande, M. R.: 2006, *Solar Phys.* **239**, 217 35

Jain, R., Rao, A. R., Deshpande, M. R., Dwivedi, B. N., Manoharan, P. K., Seetha, S., Vahia, M. N., Vats, H. O., and Venkatakrishnan, P.: 2000, *Bulletin of the Astronomical Society of India* **28**, 117 63, 87, 89, 146, 164

Jin, M., Ding, M. D., Chen, P. F., Fang, C., and Imada, S.: 2009, *Astrophys. J.* **702**, 27 186

Jing, J., Wiegelmann, T., Suematsu, Y., Kubo, M., and Wang, H.: 2008, *Astrophys. J. Lett.* **676**, L81 23

Joshi, B., Veronig, A. M., Lee, J., Bong, S.-C., Tiwari, S. K., and Cho, K.-S.: 2011, *Astrophys. J.* **743**, 195 28, 29, 89

Kaiser, M. L., Kucera, T. A., Davila, J. M., St. Cyr, O. C., Guhathakurta, M., and Christian, E.: 2008, *Space Sci. Rev.* **136**, 5 50

Kane, S. R.: 1974, in G. A. Newkirk (ed.), *Coronal Disturbances*, Vol. 57 of *IAU Symposium*, pp 105–141 24

Kane, S. R., Anderson, K. A., Evans, W. D., Klebesadel, R. W., and Laros, J.: 1979, *Astrophys. J. Lett.* **233**, L151 37

Karlický, M. and Kosugi, T.: 2004, *Astron. Astrophys.* **419**, 1159 30

Karpen, J. T., Antiochos, S. K., and DeVore, C. R.: 1991, *Astrophys. J.* **382**, 327 43

Karpen, J. T., Antiochos, S. K., and DeVore, C. R.: 1995, *Astrophys. J.* **450**, 422 43

Karpen, J. T., Antiochos, S. K., DeVore, C. R., and Golub, L.: 1998, *Astrophys. J.* **495**, 491 43

Kilner, J. R. and Nakano, G. H.: 1989, in C. J. Hailey and O. H. W. Siegmund (eds.), *EUV, X-Ray, and Gamma-Ray Instrumentation for Astronomy and Atomic Physics*, Vol. 1159 of *Society of Photo-Optical Instrumentation Engineers (SPIE) Conference Series*, pp 27–33 76

Kliem, B. and Török, T.: 2006, *Physical Review Letters* **96(25)**, 255002 190

Klimchuk, J. A., Patsourakos, S., and Cargill, P. J.: 2008, *Astrophys. J.* **682**, 1351 149

Kopp, R. A. and Pneuman, G. W.: 1976, *Solar Phys.* **50**, 85 28, 39, 187

Kraft, S., Bavdaz, M., Castelletto, B., Peacock, A., Scholze, F., Ulm, G., Gagliardi, M.-A., Nenonen, S., Tuomi, T., Juvonen, M., and Rantamäki, R.: 1998, *Nuclear Instruments and Methods in Physics Research A* **418**, 337 63

Krall, J., Chen, J., Howard, R. A., and Thompson, B. J.: 2000, in *AAS/Solar Physics Division Meeting #31*, Vol. 32 of *Bulletin of the American Astronomical Society*, p. 839 48

Lachish, U.: 1999, in R. B. James and R. C. Schirato (eds.), *Hard X-Ray, Gamma-Ray, and Neutron Detector Physics*, Vol. 3768 of *Society of Photo-Optical Instrumentation Engineers (SPIE) Conference Series*, pp 374–380 63

Landi, E. and Chiuderi Drago, F.: 2003, *Astrophys. J.* **589**, 1054 143

Landi, E., Del Zanna, G., Young, P. R., Dere, K. P., and Mason, H. E.: 2012, *Astrophys. J.* **744**, 99 81, 98, 126

Landi, E., Del Zanna, G., Young, P. R., Dere, K. P., Mason, H. E., and Landini, M.: 2006, *Astrophys. J. Supplement.* **162**, 261 143

Landi, E. and Klimchuk, J. A.: 2010, *Astrophys. J.* **723**, 320 143

Landi, E. and Phillips, K. J. H.: 2005, *Astrophys. J. Supplement.* **160**, 286 143

Leka, K. D., Canfield, R. C., McClymont, A. N., and van Driel-Gesztelyi, L.: 1996, *Astrophys. J.* **462**, 547 44

Lemaire, P., Gouttebroze, P., Vial, J.-C., Curdt, W., Schühle, U., and Wilhelm, K.: 2004, *Astron. Astrophys.* **418**, 737 37

Lemen, J. R., Title, A. M., Akin, D. J., Boerner, P. F., Chou, C., Drake, J. F., Duncan, D. W., Edwards, C. G., Friedlaender, F. M., Heyman, G. F., Hurlburt, N. E., Katz, N. L., Kushner, G. D., Levay, M., Lindgren, R. W., Mathur, D. P., McFeaters, E. L., Mitchell, S., Rehse, R. A., Schrijver, C. J., Springer, L. A., Stern, R. A., Tarbell, T. D., Wuelser, J.-P., Wolfson, C. J., Yanari, C., Bookbinder, J. A., Cheimets, P. N., Caldwell, D., Deluca, E. E., Gates, R., Golub, L., Park, S., Podgorski, W. A., Bush, R. I., Scherrer, P. H., Gummin, M. A., Smith, P., Auker, G., Jerram, P., Pool, P., Soufli, R., Windt, D. L., Beardsley, S., Clapp, M., Lang, J., and Waltham, N.: 2012, *Solar Phys.* **275**, 17 54, 83, 93

Li, H., Berlicki, A., and Schmieder, B.: 2005, *Astron. Astrophys.* **438**, 325 91, 132

Li, P., Emslie, A. G., and Mariska, J. T.: 1993, *Astrophys. J.* **417**, 313 191

Li, Y., Lynch, B. J., Welsch, B. T., Stenborg, G. A., Luhmann, J. G., Fisher, G. H., Liu, Y., and Nightingale, R. W.: 2010, *Solar Phys.* **264**, 149 177, 189

Li, Y. P. and Gan, W. Q.: 2006, *Astrophys. J. Lett.* **652**, L61 33

Liewer, P. C., de Jong, E. M., Hall, J. R., Howard, R. A., Thompson, W. T., Culhane, J. L., Bone, L., and van Driel-Gesztelyi, L.: 2009, *Solar Phys.* **256**, 57 135, 142

Lin, J. and Forbes, T. G.: 2000, in *AAS/Solar Physics Division Meeting #31*, Vol. 32 of *Bulletin of the American Astronomical Society*, p. 842 14

Lin, J., Soon, W., and Baliunas, S. L.: 2003, *New Astronomy Review* **47**, 53 45, 46

Lin, R. P., Dennis, B. R., Hurford, G. J., Smith, D. M., Zehnder, A., Harvey, P. R., Curtis, D. W., Pankow, D., Turin, P., Bester, M., Csillaghy, A., Lewis, M., Madden, N., van Beek, H. F., Appleby, M., Raudorf, T., McTiernan, J., Ramaty, R., Schmahl, E., Schwartz, R., Krucker, S., Abiad, R., Quinn, T., Berg, P., Hashii, M., Sterling, R., Jackson, R., Pratt, R., Campbell, R. D., Malone, D., Landis, D., Barrington-Leigh, C. P., Slassi-Sennou, S., Cork, C., Clark, D., Amato, D., Orwig, L., Boyle, R., Banks, I. S., Shirey, K., Tolbert, A. K., Zarro, D., Snow, F., Thomsen, K., Henneck, R., McHedlishvili, A., Ming, P., Fivian, M., Jordan, J., Wanner, R., Crubb, J., Preble, J., Matranga, M., Benz, A., Hudson, H., Canfield, R. C., Holman, G. D., Crannell, C., Kosugi, T., Emslie, A. G., Vilmer, N., Brown, J. C., Johns-Krull, C., Aschwanden, M., Metcalf, T., and Conway, A.: 2002, *Solar Phys.* **210**, 3 xx, 54, 73, 79, 92, 106, 164

Lin, R. P. and Hudson, H. S.: 1976, *Solar Phys.* **50**, 153 165

Lin, R. P. and Rhessi Team: 2003, *Advances in Space Research* **32**, 1001 14

Liu, C., Lee, J., Jing, J., Liu, R., Deng, N., and Wang, H.: 2010, *Astrophys. J. Lett.* **721**, L193 125

Liu, C., Lee, J., Yurchyshyn, V., Deng, N., Cho, K.-s., Karlický, M., and Wang, H.: 2007, *Astrophys. J.* **669**, 1372 51, 190, 192

Liu, W., Petrosian, V., and Mariska, J. T.: 2009, *Astrophys. J.* **702**, 1553 25

Liu, Y.: 2004, *Journal of Atmospheric and Solar-Terrestrial Physics* **66**, 1283 189

Liu, Y., Webb, D. F., and Zhao, X.: 2005, *AGU Fall Meeting Abstracts* p. A310 14

Lu, E. T. and Hamilton, R. J.: 1991, *Astrophys. J. Lett.* **380**, L89 xxxi, 196, 206, 222

MacCombie, W. J. and Rust, D. M.: 1979, *Solar Phys.* **61**, 69 30

Machado, M. E., Avrett, E. H., Vernazza, J. E., and Noyes, R. W.: 1980, *Astrophys. J.* **242**, 336 29

Mandrini, C. H., Demoulin, P., Henoux, J. C., and Machado, M. E.: 1991, *Astron. Astrophys.* **250**, 541 28

Markeev, A. K., Formichev, V. V., Chertok, I. M., Bhatnagar, A., Jain, R. M., Shelke, R. N., and Bhonsle, R. V.: 1983, *Bulletin of the Astronomical Society of India* **11**, 318 88

Martens, P. C. H. and Kuin, N. P. M.: 1989, *Solar Phys.* **122**, 263 169

Masson, S., Pariat, E., Aulanier, G., and Schrijver, C. J.: 2009, *Astrophys. J.* **700**, 559 78, 197

Mathew, S. K. and Ambastha, A.: 2000, *Solar Phys.* **197**, 75 173

Matteson, J. L., Coburn, W., Duttweiler, F., Heindl, W. A., Huszar, G. L., Leblanc, P. C., Pelling, M. R., Peterson, L. E., Rothschild, R. E., Skelton, R. E., Hink, P. L., and Crabtree, C.: 1997, in R. B. Hoover and F. P. Doty (eds.), *Hard X-Ray and Gamma-Ray Detector Physics, Optics, and Applications*, Vol. 3115 of *Society of Photo-Optical Instrumentation Engineers (SPIE) Conference Series*, pp 160–175 63

McIntosh, P. S. and Donnelly, R. F.: 1972, *Solar Phys.* **23**, 444 37

Mertz, L. N.: 1986, in *Bulletin of the American Astronomical Society*, Vol. 18 of *Bulletin of the American Astronomical Society*, p. 968 76

Metcalf, T. R., Hudson, H. S., Kosugi, T., Puetter, R. C., and Pina, R. K.: 1996, *Astrophys. J.* **466**, 585 77

Metcalf, T. R., Jiao, L., McClymont, A. N., Canfield, R. C., and Uitenbroek, H.: 1995, *Astrophys. J.* **439**, 474 23

Mierla, M., Inhester, B., Antunes, A., Boursier, Y., Byrne, J. P., Colaninno, R., Davila, J., de Koning, C. A., Gallagher, P. T., Gissot, S., Howard, R. A., Howard, T. A., Kramar, M., Lamy, P., Liewer, P. C., Maloney, S., Marqué, C., McAteer, R. T. J., Moran, T., Rodriguez, L., Srivastava, N., St. Cyr, O. C., Stenborg, G., Temmer, M., Thernisien, A., Vourlidas, A., West, M. J., Wood, B. E., and Zhukov, A. N.: 2010, *Annales Geophysicae* **28**, 203 50

Milligan, R. O., Gallagher, P. T., Mathioudakis, M., Bloomfield, D. S., Keenan, F. P., and Schwartz, R. A.: 2006, *Astrophys. J. Lett.* **638**, L117 27

Moore, R. L., Sterling, A. C., Hudson, H. S., and Lemen, J. R.: 2001a, *Astrophys. J.* **552**, 833 45, 46

Moore, R. L., Sterling, A. C., Hudson, H. S., and Lemen, J. R.: 2001b, *Astrophys. J.* **552**, 833 190

Neupert, W. M., Swartz, M., White, W. A., and Young, R. M.: 1969, in C. de Jager and Z. Svestka (eds.), *Solar Flares and Space Research*, p. 95 147

Ning, Z.: 2008a, *Solar Phys.* **247**, 53 31

Ning, Z.: 2008b, *Solar Phys.* **248**, 99 31

Ning, Z.: 2012, in M. Faurobert, C. Fang, and T. Corbard (eds.), *EAS Publications Series*, Vol. 55 of *EAS Publications Series*, pp 245–249 147

Ning, Z., Cao, W., Huang, J., Huang, G., Yan, Y., and Feng, H.: 2009, *Astrophys. J.* **699**, 15 105

Nishio, M., Nakajima, H., Enome, S., Shibasaki, K., Takano, T., Hanaoka, Y., Torii, C., Sekiguchi, H., Bushimata, T., Kawashima, S., Shinohara, N., Irimajiri, Y., Choi, Y.-S., Koshiishi, H., Shiomi, Y., Metcalf, T. R., and Canfield, R. C.: 1994, *Pub. Astron. Soc. Japan* **46**, L11 89

Nitta, N., Driel-Gesztelyi, L. V., Leka, K. D., Mickey, D. L., Metcalf, T. R., Wuelser, J.-P., Ichimoto, K., Sakurai, T., and Shibata, K.: 1994, in *Proceedings of Kofu Symposium*, pp 385–388 44

Nitta, N. V., Aschwanden, M. J., Boerner, P. F., Freeland, S. L., Lemen, J. R., and Wuelser, J.-P.: 2013, *Solar Phys.* 84, 121

Ohyama, M. and Shibata, K.: 1997, *Pub. Astron. Soc. Japan* **49**, 249 170

Parker, E. N.: 1958, *Astrophys. J.* **128**, 664 17

Parker, E. N.: 1963, *Astrophys. J. Supplement.* **8**, 177 16, 197

Parker, E. N.: 1988, *Astrophys. J.* **330**, 474 43, 196

Pesnell, W. D., Thompson, B. J., and Chamberlin, P. C.: 2012, *Solar Phys.* **275**, 3 54, 56, 83

Petschek, H. E.: 1964, *NASA Special Publication* **50**, 425 17

Phillips, K. J. H.: 2004, *Astrophys. J.* **605**, 921 34

Phillips, K. J. H., Aggarwal, K. M., Landi, E., and Keenan, F. P.: 2010, *Astron. Astrophys.* **518**, A41 143

Phillips, K. J. H., Chifor, C., and Dennis, B. R.: 2006, *Astrophys. J.* **647**, 1480 143

Phillips, K. J. H., Feldman, U., and Harra, L. K.: 2005, *Astrophys. J.* **634**, 641 144, 164

Phillips, K. J. H., Feldman, U., and Landi, E.: 2008, *Ultraviolet and X-ray Spectroscopy of the Solar Atmosphere*, Cambridge University Press 6

Phillips, K. J. H., Sylwester, J., Sylwester, B., and Landi, E.: 2003, *Astrophys. J. Lett.* **589**, L113 143

Plunkett, S. P., Thompson, B. J., Howard, R. A., Michels, D. J., St. Cyr, O. C., Tappin, S. J., Schwenn, R., and Lamy, P. L.: 1998, *Geophys. Res. Lett.* **25**, 2477 185, 187

Press, W. H., Teukolsky, S. A., Vetterling, W. T., and Flannery, B. P.: 1992, *Numerical recipes in C. The art of scientific computing* 184

Priest, E. R. and Forbes, T. G.: 2002, *Astron. Astrophys. Rev.* **10**, 313 14, 44

Qiu, J., Wang, H., Cheng, C. Z., and Gary, D. E.: 2004, *Astrophys. J.* **604**, 900 191

Radziszewski, K., Rudawy, P., and Phillips, K. J. H.: 2011, *Astron. Astrophys.* **535**, A123 91, 141

Raymond, J. C. and Smith, B. W.: 1977, *Astrophys. J. Supplement.* **35**, 419 31

Reeves, K. K. and Warren, H. P.: 2002, *Astrophys. J.* **578**, 590 31

Régnier, S. and Priest, E. R.: 2007, *Astron. Astrophys.* **468**, 701 38

Reinard, A. A. and Biesecker, D. A.: 2008, *Astrophys. J.* **674**, 576 186

Reinard, A. A. and Biesecker, D. A.: 2009, *Astrophys. J.* **705**, 914 186

Robbrecht, E. and Wang, Y.-M.: 2010, *Astrophys. J. Lett.* **720**, L88 186

Rust, D. M. and Kumar, A.: 1996, *Astrophys. J. Lett.* **464**, L199 44

Saint-Hilaire, P. and Benz, A. O.: 2005, *Astron. Astrophys.* **435**, 743 128, 130, 131, 146

Sato, J., Kosugi, T., and Makishima, K.: 1999, *Pub. Astron. Soc. Japan* **51**, 127 78

Scherrer, P. H., Bogart, R. S., Bush, R. I., Hoeksema, J. T., Kosovichev, A. G., Schou, J., Rosenberg, W., Springer, L., Tarbell, T. D., Title, A., Wolfson, C. J., Zayer, I., and MDI Engineering Team: 1995, *Solar Phys.* **162**, 129 54, 55, 198, 199

Scherrer, P. H., Schou, J., Bush, R. I., Kosovichev, A. G., Bogart, R. S., Hoeksema, J. T., Liu, Y., Duvall, T. L., Zhao, J., Title, A. M., Schrijver, C. J., Tarbell, T. D., and Tomczyk, S.: 2012, *Solar Phys.* **275**, 207 54, 56, 92, 201

Schmieder, B.: 2006, *Journal of Astrophysics and Astronomy* **27**, 139 169

Schmieder, B., Heinzel, P., Wiik, J. E., Lemen, J., Anwar, B., Kotrc, P., and Hiei, E.: 1995, *Solar Phys.* **156**, 337 29

Schrijver, C. J., De Rosa, M. L., Metcalf, T., Barnes, G., Lites, B., Tarbell, T., McTiernan, J., Valori, G., Wiegelmann, T., Wheatland, M. S., Amari, T., Aulanier, G., Démoulin, P., Fuhrmann, M., Kusano, K., Régnier, S., and Thalmann, J. K.: 2008, *Astrophys. J.* **675**, 1637 23, 38

Sharma, P., Bourgeois, M., Elmore, D., Granger, D., Lipschutz, M. E., Ma, X., Miller, T., Mueller, K., Rickey, F., Simms, P., and Vogt, S.: 2000, *Nuclear Instruments and Methods in Physics Research B* **172**, 112 73

Sheeley, N. R., Walters, J. H., Wang, Y.-M., and Howard, R. A.: 1999, *J. Geophys. Res.* **104**, 24739 49

Shibata, K.: 1998, in T. Watanabe and T. Kosugi (eds.), *Observational Plasma Astrophysics : Five Years of YOHKOH and Beyond*, Vol. 229 of *Astrophysics and Space Science Library*, p. 187 170, 195

Shibata, K.: 1999, *Astrophys. Space Sci.* **264**, 129 88, 103, 195

Shibata, K. and Magara, T.: 2011, *Living Reviews in Solar Physics* **8**, 6 87, 88

Shibata, K., Masuda, S., Shimojo, M., Hara, H., Yokoyama, T., Tsuneta, S., Kosugi, T., and Ogawara, Y.: 1995, *Astrophys. J. Lett.* **451**, L83 39, 170

Shibata, K. and Yokoyama, T.: 2001, *Advances in Space Research* **26**, 1753 87, 103

Shibata, K., Yokoyama, T., and Shimojo, M.: 1996, *Advances in Space Research* **17**, 197 170

Skumanich, A. and Lites, B. W.: 1987, *Astrophys. J.* **322**, 473 12

Smith, D. F.: 1979, in *Bulletin of the American Astronomical Society*, Vol. 11 of *Bulletin of the American Astronomical Society*, p. 660 41

Smith, D. M., Lin, R. P., Turin, P., Curtis, D. W., Primbsch, J. H., Campbell, R. D., Abiad, R., Schroeder, P., Cork, C. P., Hull, E. L., Landis, D. A., Madden, N. W., Malone, D., Pehl, R. H., Raudorf, T., Sangsingkeow, P., Boyle, R., Banks, I. S., Shirey, K., and Schwartz, R.: 2002, *Solar Phys.* **210**, 33 78

Somov, B. V.: 1978, *Solar Phys.* **60**, 315 147

Spirock, T. J., Yurchyshyn, V. B., and Wang, H.: 2002, *Astrophys. J.* **572**, 1072 14

Sterling, A. C., Harra, L. K., and Moore, R. L.: 2007, *Astrophys. J.* **669**, 1359 190

Sterling, A. C. and Moore, R. L.: 2005, *Astrophys. J.* **630**, 1148 25

Strong, K., Bruner, M., Tarbell, T., Title, A., and Wolfson, C. J.: 1994, *Space Sci. Rev.* **70**, 119 54, 82

Sturrock, P. A. and Coppi, B.: 1966, *Astrophys. J.* **143**, 3 16, 39

Subramanian, P. and Dere, K. P.: 2001, *Astrophys. J.* **561**, 372 171

Sui, L., Holman, G. D., and Dennis, B. R.: 2005, *Astrophys. J.* **626**, 1102 146

Svestka, Z.: 1976, *Solar Flares* 19

Svestka, Z., Hoyng, P., van Tend, W., Boelee, A., de Jager, C., Stewart, R. T., Acton, L. W., Bruner, E. C., Gabriel, A. H., Rapley, C. G., de Jager, C., LaFleur, H., Nelson, G., Simnett, G. M., van Beek, H. F., and Wagner, W. J.: 1982, *Solar Phys.* **75**, 305 30

Svestka, Z. F., Fontenla, J. M., Machado, M. E., Martin, S. F., and Neidig, D. F.: 1987, *Solar Phys.* **108**, 237 30

Sweet, P. A.: 1958, *The Observatory* **78**, 30 16, 17

Takalo, J., Timonen, J., Klimas, A., Valdivia, J., and Vassiliadis, D.: 1999, *Geophys. Res. Lett.* **26**, 1813 196

Tandberg-Hanssen, E. and Emslie, A. G.: 1988, *The physics of solar flares* 11, 31, 113, 139, 217

Temmer, M., Veronig, A. M., Kontar, E. P., Krucker, S., and Vršnak, B.: 2010, *Astrophys. J.* **712**, 1410 50

Temmer, M., Veronig, A. M., Vršnak, B., Rybák, J., Gömöry, P., Stoiser, S., and Maričić, D.: 2008, *Astrophys. J. Lett.* **673**, L95 191

Thompson, B. J., Plunkett, S. P., Gurman, J. B., Newmark, J. S., St. Cyr, O. C., and Michels, D. J.: 1998, *Geophys. Res. Lett.* **25**, 2465 185, 187, 192

Tian, L., Alexander, D., and Nightingale, R.: 2008, *Astrophys. J.* **684**, 747 193

Titov, V. S., Mikic, Z., Linker, J. A., and Lionello, R.: 2008, *Astrophys. J.* **675**, 1614 193

Török, T. and Kliem, B.: 2005, *Astrophys. J. Lett.* **630**, L97 190

Tousignant, O., Hamel, L.-A., Courville, J.-F., Paki, P., Macri, J. R., Larson, K., Mayer, M., McConnell, M. L., and Ryan, J. M.: 1997, in R. B. Hoover and F. P. Doty (eds.), *Hard X-Ray and Gamma-Ray Detector Physics, Optics, and Applications*, Vol. 3115 of *Society of Photo-Optical Instrumentation Engineers (SPIE) Conference Series*, pp 214–224 63

Tripathi, D., Kliem, B., Mason, H. E., Young, P. R., and Green, L. M.: 2009, *Astrophys. J. Lett.* **698**, L27 189

Tsuneta, S.: 1997, *Astrophys. J.* **483**, 507 39, 170

Tsuneta, S., Hara, H., Shimizu, T., Acton, L. W., Strong, K. T., Hudson, H. S., and Ogawara, Y.: 1992, *Pub. Astron. Soc. Japan* **44**, L63 29, 170

Uddin, W., Chandra, R., and Ali, S. S.: 2006, *Journal of Astrophysics and Astronomy* **27**, 267 93, 118

Uddin, W., Jain, R., Yoshimura, K., Chandra, R., Sakao, T., Kosugi, T., Joshi, A., and Despande, M. R.: 2004, *Solar Phys.* **225**, 325 14

Uddin, W., Schmieder, B., Chandra, R., Srivastava, A. K., Kumar, P., and Bisht, S.: 2012, *Astrophys. J.* **752**, 70 58

van Ballegooijen, A. A. and Martens, P. C. H.: 1989, *Astrophys. J.* **343**, 971 44

van Tend, W. and Kuperus, M.: 1978, *Solar Phys.* **59**, 115 179

Veronig, A., Vršnak, B., Dennis, B. R., Temmer, M., Hanslmeier, A., and Magdalenić, J.: 2002, *Astron. Astrophys.* **392**, 699 25, 33, 88, 93, 104

Veronig, A. M., Brown, J. C., Dennis, B. R., Schwartz, R. A., Sui, L., and Tolbert, A. K.: 2005, *Astrophys. J.* **621**, 482 30

Viswanatha, N., Simil, T. S., Prasad, N., Bhat, N. C., and Shankara Narayan, Y. S.: 2005, in B. Warmbein (ed.), *11th European Space Mechanisms and Tribology Symposium, ESMATS 2005*, Vol. 591 of *ESA Special Publication*, pp 211–215 68, 69

Vourlidas, A., Subramanian, P., Dere, K. P., and Howard, R. A.: 2000, *Astrophys. J.* **534**, 456 49

Wang, C., Burlaga, L. F., and Richardson, J. D.: 2002, *AGU Fall Meeting Abstracts* p. A484 14

Wang, H. and Tang, F.: 1993, *Astrophys. J. Lett.* **407**, L89 44

Wang, T., Sui, L., and Qiu, J.: 2007, *Astrophys. J. Lett.* **661**, L207 51

Wang, X., Chen, L., and Lin, Y.: 2004, *AGU Fall Meeting Abstracts* p. A498 14

Warren, H. P. and Warshall, A. D.: 2001, *Astrophys. J. Lett.* **560**, L87 25

Warren, H. P., Winebarger, A. R., and Hamilton, P. S.: 2002, *Astrophys. J. Lett.* **579**, L41 31

Welsch, B. T., DeVore, C. R., and Antiochos, S. K.: 2005, *Astrophys. J.* **634**, 1395 189

Wikstol, O., Judge, P. G., and Hansteen, V. H.: 1997, *Astrophys. J.* **483**, 972 9

Withbroe, G. L. and Noyes, R. W.: 1977, *Annual Rev. in Astron. & Astrophys.* **15**, 363 10

Woodgate, B. E., Shine, R. A., Poland, A. I., and Orwig, L. E.: 1983, *Astrophys. J.* **265**, 530 37

Yokoyama, T., Akita, K., Morimoto, T., Inoue, K., and Newmark, J.: 2001, *Astrophys. J. Lett.* **546**, L69 28, 29, 42, 46

Zarro, D. M., Canfield, R. C., Metcalf, T. R., and Strong, K. T.: 1988, *Astrophys. J.* **324**, 582 27, 30

Zhang, J., Dere, K. P., Howard, R. A., Kundu, M. R., and White, S. M.: 2001, *Astrophys. J.* **559**, 452 44, 50

Zhang, J., Dere, K. P., Howard, R. A., and Vourlidas, A.: 2004, *Astrophys. J.* **604**, 420 191

Zhang, Y., Liu, J., and Zhang, H.: 2008, *Solar Phys.* **247**, 39 170, 176

Zirin, H. and Liggett, M. A.: 1987, *Solar Phys.* **113**, 267 13